

MODIFICATION OF METAL-ORGANIC FRAMEWORKS FOR  
HYDROGEN SEPARATION/STORAGE AND CATALYSIS



A THESIS SUBMITTED IN PARTIAL FULFILLMENT OF THE REQUIREMENT FOR THE  
DEGREE OF DOCTOR OF PHILOSOPHY IN APPLIED CHEMISTRY  
DEPARTMENT OF CHEMISTRY SCHOOL OF SCIENCE  
KING MONGKUT'S INSTITUTE OF TECHNOLOGY LADKRABANG  
2022

KMITL-2022-SC-D-012-074

This material is reserved for educational use only, not allowed for commercial use.

Forbidden to modify the content, and cite the document when use.



**COPYRIGHT 2022**

**SCHOOL OF SCIENCE**

**KING MONGKUT'S INSTITUTE OF TECHNOLOGY LADKRABANG**

This material is reserved for educational use only, not allowed for commercial use.

Forbidden to modify the content, and cite the document when use.

|                   |  |
|-------------------|--|
| Thesis Title      | Modification of Metal-Organic Frameworks for Hydrogen Separation/Storage and Catalysis |
| Student Name      | Nuttapong Makmeesub  |
| Student ID        | 57605003   |
| Degree            | Doctor of Philosophy (Applied Chemistry)   |
| Department        | Chemistry  |
| Year              | 2022   |
| Thesis Advisor    | Prof. Dr. Tawan Sooknoi  |
| Thesis Co-advisor | Asst. Prof. Dr. Chonlada Ritvirulh   |

### Abstract

This thesis focuses on the post-synthetic modification of MOFs (HKUST-1 and MIL-101(Cr)) for H<sub>2</sub>/CO<sub>2</sub> separation, chemical hydrogen storage and catalytic oxidation. The unsaturated Cu<sup>2+</sup> sites in HKUST-1 acts as binding sites for strong CO<sub>2</sub> adsorption, which improve H<sub>2</sub>/CO<sub>2</sub> permselectivity up to 23.2 of 10wt% HKUST-1/HIPS membranes, prepared by solution casting. While, the unsaturated Cr<sup>3+</sup> sites in MIL-101(Cr) were grafted with acetylpyridine (AcP) and used as chemical hydrogen storage at atmospheric pressure, when Pd was incorporated. The chemical hydrogen storage of Pd-AcP-MIL-101(Cr) proceeded via hydrogenation/dehydrogenation of AcP, using Pd as catalyst and can be regulated by H<sub>2</sub> partial pressure and temperature. The chemical hydrogen storage of 0.33 mmol H<sub>2</sub>·g<sup>-1</sup> can be operated at 150 °C up to 10 cycles. In another approach, the ethylenediamine (en) was grafted at Cr<sup>3+</sup> unsaturated sites of MIL-101(Cr) and Pd<sup>2+</sup> was subsequently incorporated by double-solvent adsorption. Highly stable Pd<sup>2+</sup> species was anchored on en-MIL-101(Cr) by the strong interaction between Pd<sup>2+</sup> and en within MIL-101(Cr) confinement, preventing reduction to Pd<sup>0</sup>, even under H<sub>2</sub> at 150 °C. The catalysts with en: Pd<sup>2+</sup> molar ratios of 10 provided a higher activity for styrene oxidation (TOF ~30 h<sup>-1</sup>), compared to previous reports.

**Keywords :** Selective H<sub>2</sub>/CO<sub>2</sub> Permeation, Chemical Hydrogen Storage, Pd<sup>2+</sup> Catalyst, Oxidation, HKUST-1, MIL-101(Cr)

This material is reserved for educational use only, not allowed for commercial use.

Forbidden to modify the content, and cite the document when use.

## Acknowledgements

First of all, I would like to thank my advisor, Prof. Dr. Tawan Sooknoi and Asst. Prof. Dr. Chonlada Ritvirulh, for their guidance through my PhD research. I appreciate your precious time and valuable advice on my research and thesis. I would like to special thank Prof. Dr. Daniel E. Resasco for his excellent supervision and for valuable working experience at University of Oklahoma. I am very grateful to have his helpful suggestions during my research. Also, I would like to thank the valuable comments by examination committees Prof. Dr. Joongjai Panpranot, Asst. Prof. Dr. kittisak choojun, Assoc. Prof. Dr. Punnama Siriphannon and Assoc. Prof. Dr. Ekarat Detsri.

I would like to thank King Mongkut's Institute of Technology Ladkrabang and The University of Oklahoma for workplace and facility. I would like to acknowledge the Royal Golden Ph.D. Program (Grant No. PHD/0034/2557) for providing the financial support.

I am very grateful to our collaborators: Dr. Yingyot Poo-arporn and Dr. Suchinda Sattayaporn for their help with XAS analysis at Synchrotron Light Research Institute, Asst. Prof. Dr. Teng-Hao Chen for valuable experience in metal-organic framework synthesis. I also thank all the staff members of the School of Science at King Mongkut's Institute of Technology Ladkrabang and Chemical, Biological and Materials Engineering group at University of Oklahoma for their excellent service. Thanks to the Catalytic Chemistry Research members for your help, advice and discussion on my research.

At last, I would like to thank my family for their encouragement and support. I dedicate this work to my family with love because I could not have done it without you.

Mr. Nuttapong Makmeesub



## Table of Contents (Continued)

|  | Page |
|--|------|
| 2.2.1.3 Selective adsorption based on cooperative effects of size/shape exclusion and adsorbate–surface interactions | 22   |
| 2.2.2 MOFs membrane-based gas separation .....   | 22   |
| 2.2.3 MOFs based mixed-matrix membranes .....  | 24   |
| 2.2.3.1 Challenges in mixed matrix membranes fabrication .....   | 25   |
| 2.2.3.1.1 Selection of filler and polymer pair .....   | 25   |
| 2.2.3.1.2 Filler dispersion .....  | 26   |
| 2.2.3.1.3 Filler/polymer interface morphology .....  | 27   |
| 2.2.4 Mechanisms of gas transport in membrane materials .....  | 28   |
| 2.3 MOFs for hydrogen storage .....  | 30   |
| 2.3.1 MOFs as hydrogen storage .....   | 30   |
| 2.3.2 Hydrogen adsorption in MOFs .....  | 31   |
| 2.3.2.1 Hydrogen bonding strength .....  | 31   |
| 2.3.2.2 Surface area .....   | 32   |
| 2.3.2.3 Pore volume .....  | 33   |
| 2.3.2.4 Pore geometry .....  | 33   |
| 2.3.2.5 Catenation/interpenetration .....  | 34   |
| 2.3.3 MOFs supported inorganic hydride .....   | 35   |
| 2.4 MOFs for catalysis .....   | 36   |
| 2.4.1 MOFs with intrinsic catalytic activity .....   | 37   |
| 2.4.1.1 Catalysis on open metal sites and nondecorated frameworks .....  | 38   |
| 2.4.1.2 Catalysis on defects in MOFs .....   | 39   |
| 2.4.1.3 Catalysis on decorated MOFs .....  | 40   |
| 2.4.2 MOFs as supports for metal nanoparticles .....   | 41   |
| 2.4.2.1 Metal nanoparticles/MOF preparation .....  | 41   |
| 2.5 Overview of the thesis .....   | 45   |
| 2.6 Literature reviews .....   | 46   |
| 2.7 References .....   | 52   |



## Table of Contents (Continued)

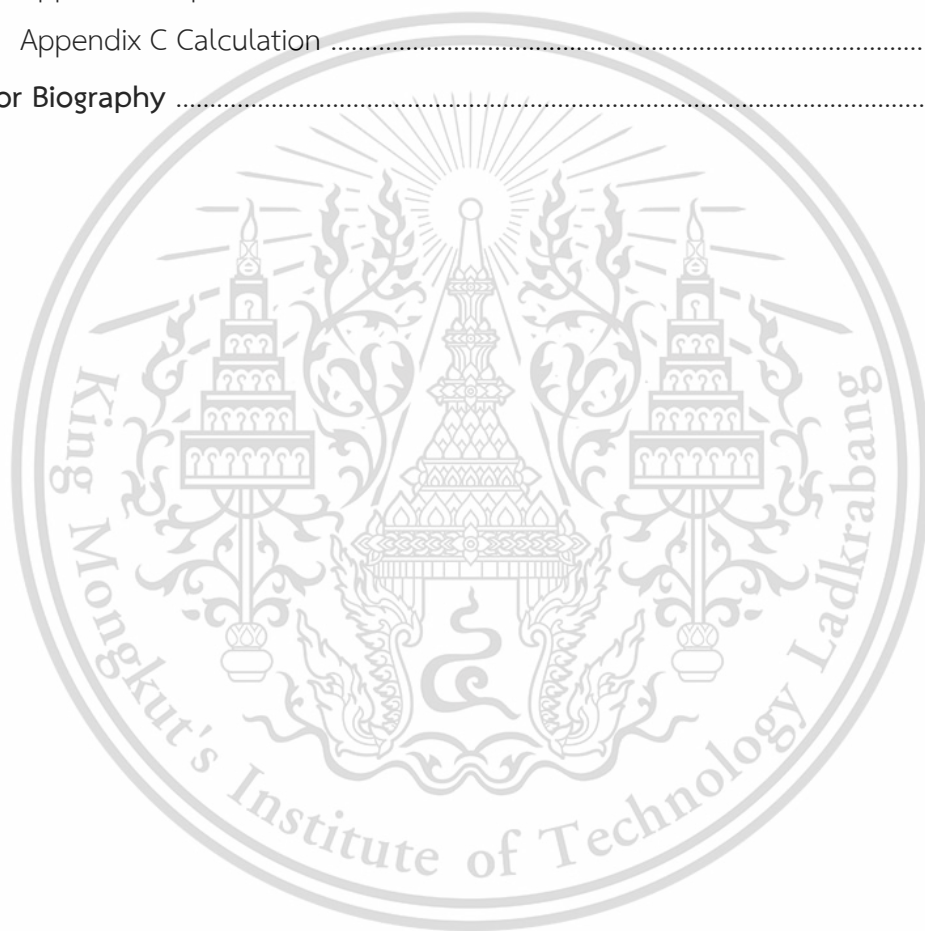
|   | Page       |
|---|------------|
| 3.3.4 Single gas permeation testing.....  | 69         |
| 3.3.5 Catalytic testing .....   | 70         |
| 3.3.5.1 Oxidation of styrene .....  | 71         |
| 3.3.5.2 Hydrogenation of phenylacetylene .....  | 71         |
| 3.3.5.3 Heck coupling of Iodobenzene with styrene .....   | 71         |
| 3.4 References .....  | 71         |
| <b>Chapter 4 Atmospheric H<sub>2</sub>/CO<sub>2</sub> permeability of HKUST-1/polymer mixed matrix membrane for hydrogen purification .....</b> | <b>73</b>  |
| 4.1 Results and discussion .....  | 74         |
| 4.1.1 Material characterization .....   | 74         |
| 4.1.2 Permeation testing .....  | 77         |
| 4.2 Conclusion .....  | 83         |
| 4.3 References .....  | 84         |
| <b>Chapter 5 Reversible Hydrogenation-Dehydrogenation of Acetylpyridine-Pd-MIL-101(Cr) for Chemical Hydrogen Storage .....</b>                  | <b>86</b>  |
| 5.1 Results and discussions .....   | 87         |
| 5.1.1 Material characterization .....   | 87         |
| 5.1.2 Hydrogen evolution and uptake .....   | 96         |
| 5.2 Conclusions .....   | 108        |
| 5.3 References .....  | 109        |
| <b>Chapter 6 Highly stable Pd<sup>2+</sup> species anchoring on ethylenediamine-grafted-MIL-101(Cr) as a robust oxidation catalyst .....</b>    | <b>111</b> |
| 6.1 Results and discussions .....   | 112        |
| 6.1.1 Synthesis and Characterization .....  | 112        |
| 6.1.1.1 Ethylenediamine grafted MIL-101(Cr) .....   | 112        |
| 6.1.1.2 Anchoring Pd <sup>2+</sup> species on ethylenediamine-grafted-MIL-101(Cr) .....   | 118        |
| 6.1.2 Catalytic testing .....   | 129        |
| 6.2 Conclusions .....   | 135        |
| 6.3 References .....  | 136        |

This material is reserved for educational use only, not allowed for commercial use.

Forbidden to modify the content, and cite the document when use.

## Table of Contents (Continued)

|  | Page |
|--|------|
| <b>Chapter 7 Conclusions and Suggestions</b> ..... | 139  |
| 7.1 Conclusions .....                              | 139  |
| 7.2 Suggestions .....                              | 141  |
| <b>Appendices</b> .....                            | 143  |
| Appendix A Temperature program condition .....     | 144  |
| Appendix B Spectra .....                           | 147  |
| Appendix C Calculation .....                       | 148  |
| <b>Author Biography</b> .....                      | 162  |



## List of Tables

| Table  | Page |
|--|------|
| <b>Chapter 3</b>   |      |
| 3.1 List of reagents .....   | 58   |
| 3.2 List of apparatuses .....  | 60   |
| <b>Chapter 4</b>   |      |
| 4.1 A summary of the H <sub>2</sub> /CO <sub>2</sub> separation performance of the reported MMMs .....   | 83   |
| <b>Chapter 5</b>   |      |
| 5.1 Composition and textural properties of the samples .....   | 89   |
| 5.2 Normalized areas of H <sub>2</sub> evolution after hydrogenation at 200 °C for 1 h .....   | 97   |
| 5.3 Normalized areas of H <sub>2</sub> consumption and H <sub>2</sub> evolution of samples from H <sub>2</sub> -TPR .....  | 100  |
| <b>Chapter 6</b>   |      |
| 6.1 Elemental composition and physical properties of the samples .....   | 114  |
| 6.2 Absorption edge energy of all samples under <i>in situ</i> reduction from 30 °C to 150 °C .....  | 124  |
| 6.3 R-factor of 0.03 wt%Pd over 1.2en-MIL-101(Cr), MIL-101(Cr) and SiO <sub>2</sub> samples and 0.2 wt%Pd loaded over 0.8en-MIL-101(Cr), MIL-101(Cr) and SiO <sub>2</sub> samples after linear combination fitting ..... | 126  |
| 6.4 Catalytic activities of Pd catalysts .....   | 129  |
| 6.5 Comparison of the catalytic activity of 0.03Pd-0.3en-MIL-101(Cr) with other catalysts reported in the literature for styrene oxidation .....   | 135  |

## List of Figures

| Figure  | Page |
|---|------|
| <b>Chapter 2</b>  |      |
| 2.1 Overview of MOFs chemistry .....  | 9    |
| 2.2 Constituents of metal-organic frameworks (MOFs); (a) Metal clusters (polyhedra demonstrate the metal coordination) and (b) organic molecules from which linkers are formed .....  | 10   |
| 2.3 Structures of different MOFs with the terephthalate (BDC) dianion as a linker....   | 11   |
| 2.4 Framework symmetry retention with an increase in the linker chain length .....  | 12   |
| 2.5 Examples of the change in the geometry of MOFs depending on the mutual arrangement of substituents in the linker molecule .....   | 12   |
| 2.6 The breathing effect of MIL-53 (Al, Ga or Fe) as a function of temperature above room temperature .....   | 14   |
| 2.7 Overview of synthesis methods, possible reaction temperatures, and final reaction products in MOF synthesis .....   | 14   |
| 2.8 Solvothermal synthesis of MOF .....   | 15   |
| 2.9 Microwave-assisted solvothermal synthesis of MOF structures .....   | 16   |
| 2.10 Electrochemical synthesis of MOF .....   | 16   |
| 2.11 Sonochemical synthesis of MOF .....  | 17   |
| 2.12 The example of layer-by-layer MOF synthesis method .....   | 17   |
| 2.13 Solvent activation of MOFs .....   | 18   |
| 2.14 Illustrative schematic of (i) covalent PSM using reactive groups on the MOF linker for modification by an organic reagent and (ii) coordinative PSM using a coordinating organic molecule to bind to the MOF SBU .....                               | 19   |
| 2.15 Illustrated covalent post-synthetic modification and subsequent polymerization synthesis of MOF–nylon hybrid materials .....   | 19   |
| 2.16 Illustration of the coordinative post-synthesis modification by grafting of ethylenediamine onto MIL-101(Cr) .....   | 20   |
| 2.17 Breathing behavior of the flexible MIL-53 MOF by application of an external mechanical pressure to provoke a molecular-sieving type separation, followed by regeneration from the unconstrained MOF after release of the mechanical constraint ..... | 23   |

This material is reserved for educational use only, not allowed for commercial use.

Forbidden to modify the content, and cite the document when use.

## List of Figures (Continued)

| Figure   | Page |
|--|------|
| 2.18 Schematic diagram of mixed matrix membrane .....  | 24   |
| 2.19 (a) Schematic shape of pre-functionalization, (b) hydrogen bonding between CO <sub>2</sub> molecule and -NH <sub>2</sub> functional group and (c) dipolar ion (zwitterion) formation by the acidic CO <sub>2</sub> and basic NH <sub>2</sub> groups ..... | 25   |
| 2.20 Covalently functionalized -NH <sub>2</sub> group of the MOF, with adipoyl chloride for post-synthetic polymerization of hybrid Nylon-MOF composites .....   | 26   |
| 2.21 Schematic diagram of interface void (a) and rigidified polymer (b) in MMMs  | 27   |
| 2.22 Illustration of gas transport across the membrane layer; (a) MMM with interfacial defect, (b) defect-free MMM .....   | 29   |
| 2.23 Crystal structure of MOF-210, the spheres represent the largest molecules, which could fit in the pore without touching the van der Waals surface of the framework atoms .....  | 31   |
| 2.24 Excess hydrogen uptake in MOFs at 77 K (left figure) and at room temperatures (right figure) plotted versus BET surface area .....  | 32   |
| 2.25 Theoretical values of hydrogen uptake calculated for different MOFs: a) at 0.1 bar plotted versus isosteric heat of adsorption, b) at 30 bar plotted versus accessible surface area and c) at 120 bar plotted versus pore volume                          | 32   |
| 2.26 Potential energy for adsorption within the free volume of Mg-C <sub>60</sub> @MOF .....   | 34   |
| 2.27 Schematic representation of the repeat unit of (a) single-framework MOF, catenation of two identical frameworks can be used to restrict the dimensions of the pore considerably by (b) interpenetration or to a lesser extent by (c) interweaving .....   | 35   |
| 2.28 Proposed interaction of LiBH <sub>4</sub> with the exposed Cu(II) sites in HKUST-1 .....  | 36   |
| 2.29 Assembly of (a) a functional MOF with catalytically active sites by direct assembly or post-synthetic modification (PSM) of a linker, (b) or a metal node, (c) nanoparticle encapsulation, or (d) MOF utilization as a carbon support .....               | 37   |
| 2.30 Open metal sites generation of MIL-100(Fe) for the aza-Michael reaction .....   | 38   |
| 2.31 (a) Chemical structure of H <sub>2</sub> tpdc-TEMPO, (b) X-ray crystallographic structure of UiO-68-TEMPO and (c) Zr-node contains one missing linker defect .....  | 39   |

This material is reserved for educational use only, not allowed for commercial use.

Forbidden to modify the content, and cite the document when use.

## List of Figures (Continued)

| Figure   | Page |
|--|------|
| 2.32 Generation of multivariate MOF catalysts via the dynamic spacer installation approach using proto-LIFM-28 and the resultant interconversions for different catalytic purposes ..... | 40   |
| 2.33 (a) Chemical vapor deposition of ZIF-8 thin films. The procedure consists of a metal oxide vapor deposition (Step 1) and a consecutive vapor-solid reaction (Step 2) .....          | 42   |
| 2.34 Encapsulation of MNPs into ZIF-8 via the mechanochemical strategy .....   | 43   |
| 2.35 Schematic illustration of the different process steps during solution impregnation .....  | 43   |
| 2.36 Schematic representation of the synthesis of MNP@MOF using the double solvent method .....  | 44   |
| <b>Chapter 3</b>   |      |
| 3.1 Diagram of hydrogen temperature program reduction .....  | 68   |
| 3.2 Gas permeation module and cell membrane diagram .....  | 70   |
| <b>Chapter 4</b>   |      |
| 4.1 XRD pattern of HKUST-1 .....   | 74   |
| 4.2 SEM image of HKUST-1 .....   | 75   |
| 4.3 N <sub>2</sub> adsorption-desorption isotherm of HKUST-1 .....   | 75   |
| 4.4 FTIR spectra of HKUST-1 .....  | 76   |
| 4.5 TGA thermogram of HKUST-1 .....  | 76   |
| 4.6 Gas flux and H <sub>2</sub> /CO <sub>2</sub> selectivity of different polymer membranes .....  | 78   |
| 4.7 Effect of HKUST-1 loading on (a) HKUST-1/HIPS and (b) HKUST-1/EVA MMMs on gas flux and H <sub>2</sub> /CO <sub>2</sub> selectivity .....   | 81   |
| <b>Chapter 5</b>   |      |
| 5.1 XRD patterns of all MOF samples .....  | 87   |

## List of Figures (Continued)

| Figure  | Page |
|---|------|
| 5.2 TEM image of AcP-0.5Pd-MIL (a, a'), AcP-2.5Pd-MIL (b, b'), AcP-4.0Pd-MIL (c, c') and 4.0Pd-MIL (d, d') at low and high magnification and their Pd particle size distribution (a''-d'') from approximately 200 Pd particles counted .....  | 88   |
| 5.3 N <sub>2</sub> adsorption and desorption isotherms of the samples at 77K .....  | 90   |
| 5.4 Peak-fitted core-line XPS spectra of MIL-101(Cr), 4.0Pd-MIL-101(Cr), AcP MIL 101(Cr) and AcP-4.0Pd-MIL-101(Cr) for (a) N(1s), (b) Cr(2p) and Pd(3d) .....   | 91   |
| 5.5 Demonstration of grafted organic hydrogen carrier (i.e., 3-acetylpyridine) in Pd encapsulated-MIL-101 (Cr) .....  | 92   |
| 5.6 <sup>1</sup> H NMR spectrum of as-prepared MIL-101(Cr) extract with DMSO-d <sub>6</sub> under sonication for 1 h .....  | 92   |
| 5.7 TGA thermograms of the samples under (a) Air and (b) N <sub>2</sub> .....   | 93   |
| 5.8 FTIR spectra of MOF samples .....   | 94   |
| 5.9 Interaction of AcP with the Lewis acid center at Cr <sup>3+</sup> nodes of the MIL-101(Cr) .....  | 94   |
| 5.10 Cr K-edge XANES spectra of MIL-101(Cr), 4.0Pd-MIL-101(Cr), AcP-MIL-101(Cr) and AcP-4.0Pd-MIL-101(Cr) and Cr <sub>2</sub> O <sub>3</sub> .....  | 95   |
| 5.11 Hydrogen evolution cycles of AcP-2.5Pd-MIL-101(Cr) under Ar after hydrogenation under H <sub>2</sub> at 200 °C for 1 h (normalized areas of H <sub>2</sub> evolution are tabulated in Table 5.2) .....   | 97   |
| 5.12 Chemical hydrogen storage of AcP-Pd-MIL-101(Cr) by hydrogenation and dehydrogenation of 3-Acetylpyridine (AcP) over Pd nanoparticles .....   | 98   |
| 5.13 <i>In situ</i> FTIR spectra of AcP-2.5Pd-MIL-101(Cr) from 30 to 200 °C with a heating rate of 5 °C·min <sup>-1</sup> (a) under H <sub>2</sub> (hydrogenation) and (b) under N <sub>2</sub> (dehydrogenation) .....   | 98   |
| 5.14 H <sub>2</sub> -TPR profiles of the sample testing under 10% H <sub>2</sub> in Ar from 70 to 200 °C with a heating rate of 5 °C·min <sup>-1</sup> and cooled under 10% H <sub>2</sub> in Ar to room temperature, and then the process was repeated for three times (normalized areas of H <sub>2</sub> evolution/consumption are tabulated in Table 5.3) | 100  |
| 5.15 Effect of hydrogenation temperature at 100, 130, 150 and 200 °C with time for H <sub>2</sub> evolution of AcP-2.5Pd-MIL-101(Cr) .....  | 101  |

This material is reserved for educational use only, not allowed for commercial use.

Forbidden to modify the content, and cite the document when use.

## List of Figures (Continued)

| Figure  | Page |
|---|------|
| 5.16 Effect of hydrogenation temperature (150 °C and 200 °C, for 1 h) on the stability of AcP-2.5Pd-MIL-101(Cr) when dehydrogenated at 200 °C for 1 h ....  | 103  |
| 5.17 XRD patterns of AcP-2.5Pd-MIL-101(Cr) (a) before hydrogenation and after four hydrogenation cycles (b) at 150 °C and (c) at 200 °C .....   | 103  |
| 5.18 Effect of dehydrogenation temperature on the sample stability of AcP-2.5Pd-MIL-101(Cr): hydrogenation at 150 °C, heating rate of 5 °C·min <sup>-1</sup> for 1 h, followed by dehydrogenation at different temperatures ..... | 104  |
| 5.19 Thermodynamic equilibrium as a function of temperature for hydrogenation of acetone and dehydrogenation of 2-propanol .....  | 105  |
| 5.20 Hydrogen evolution of AcP-2.5Pd-MIL-101(Cr) after hydrogenation at 150 °C, following dehydrogenation at different temperatures .....   | 105  |
| 5.21 Effect of Pd loading on H <sub>2</sub> evolution at Pd loading 0.5, 2.5 and 4.0 wt% by hydrogenation under H <sub>2</sub> and dehydrogenation under Ar flow at 150 °C for 1 h .....  | 106  |
| 5.22 Recyclability of AcP-4.0Pd-MIL-101(Cr) over hydrogenation and dehydrogenation cycles at 150 °C .....   | 107  |
| 5.23 TEM images of AcP-4.0Pd-MIL-101(Cr) before (a) and after (b) 10 <sup>th</sup> cycles for testing catalyst recyclability of hydrogenation at 150 °C for 1 h and then dehydrogenation at 150 °C for 1 h .....                  | 108  |
| <b>Chapter 6</b>  |      |
| 6.1 XRD intensity of MIL-101(Cr) when (a) grafted with ethylenediamine and introduced (b) 0.03 wt%Pd and (c) 0.2 wt%Pd over ethylenediamine-grafted samples .....   | 112  |
| 6.2 TGA and DTG thermograms of MIL-101(Cr) when (a, a') grafted with ethylenediamine and introduced (b, b') 0.03 wt%Pd and (c, c') 0.2 wt%Pd over ethylenediamine-grafted samples .....   | 113  |

## List of Figures (Continued)

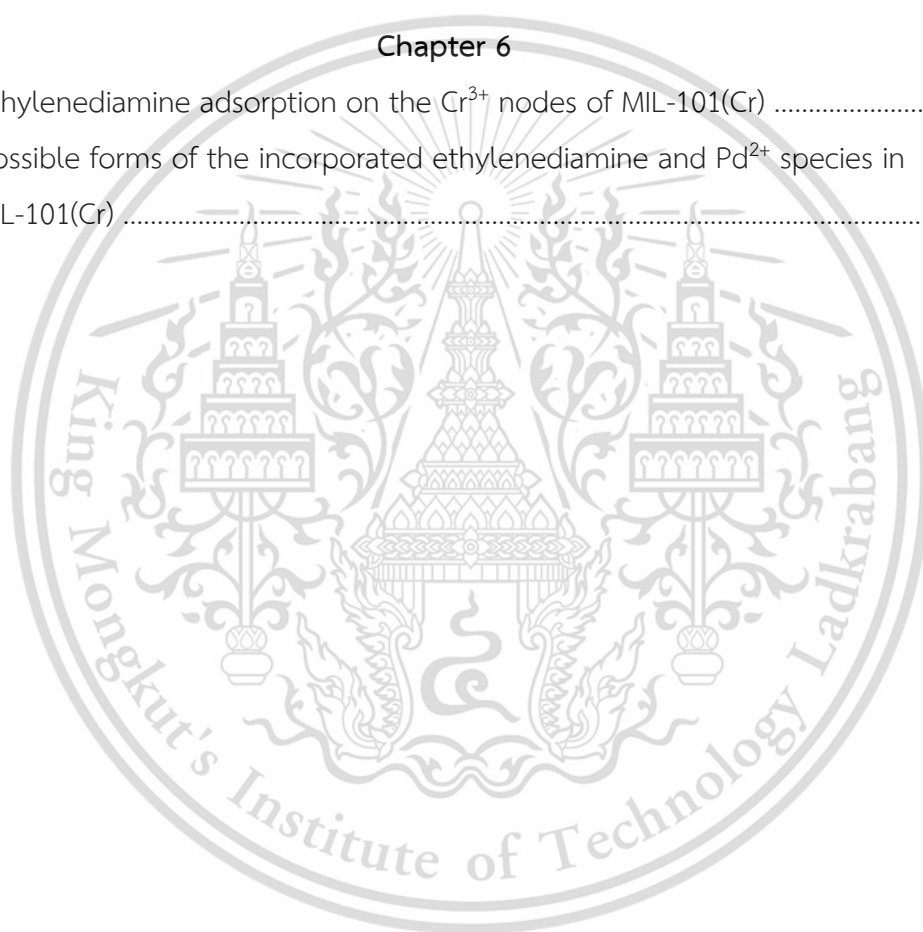
| Figure   | Page |
|--|------|
| 6.3 N <sub>2</sub> adsorption isotherm of (a) ethylenediamine-grafted MIL-101(Cr) with (b) 0.03 wt%Pd and (c) 0.2 wt%Pd loadings .....   | 113  |
| 6.4 High-resolution N 1s XPS spectra of (a) MIL-101(Cr), (b) 0.5en-MIL-101(Cr), (c) 0.03Pd MIL-101(Cr) and (d) 0.03Pd-0.5en-MIL-101(Cr) samples .....  | 114  |
| 6.5 Effect of ethylenediamine content on the relative XRD intensity ( $2\theta = 3.3^\circ$ ) of MIL 101(Cr) samples with and without Pd .....   | 115  |
| 6.6 FTIR spectra of (a) MIL-101(Cr), (b) 0.5en-MIL101(Cr), (c) 0.8en-MIL101(Cr), (d) 1.2en-MIL101(Cr) and (e) ethylenediamine (en) .....   | 116  |
| 6.7 High-resolution Cr 2p XPS spectra of (a) MIL-101(Cr), (b) 0.5en-MIL-101(Cr), (c) 0.03Pd-MIL-101(Cr) and (d) 0.03Pd-0.5en-MIL-101(Cr) samples .....   | 117  |
| 6.8 FTIR spectra of (a) ethylenediamine-grafted MIL-101(Cr) with (b) 0.03 wt%Pd and (c) 0.2 wt%Pd loadings .....   | 119  |
| 6.9 TEM images and Pd size distribution of (a, a', a'') 0.03Pd-MIL-101(Cr) and (b, b') 0.03Pd-0.5en-MIL-101(Cr). Note that in b', no particle could be detected ....   | 120  |
| 6.10 High-resolution Pd 3d XPS spectra of (a) non-reduced 0.03Pd-MIL-101(Cr), (b) 0.03Pd-MIL-101(Cr), (c) 0.03Pd-0.5en-MIL-101(Cr), (d) 0.03Pd-1.2en-MIL-101(Cr) and (e) 0.2Pd-1.2en-MIL-101(Cr) .....   | 121  |
| 6.11 High-resolution N 1s XPS spectra of (a) 0.8en-MIL-101(Cr), (b) 1.2en-MIL-101(Cr), (c) 0.03Pd-1.2en-MIL-101(Cr) and (d) 0.2Pd-1.2en-MIL-101(Cr) samples .....  | 122  |
| 6.12 Raman spectra of (a) ethylenediamine-grafted MIL-101(Cr) with (b) 0.03 wt%Pd and (c) 0.2 wt%Pd loadings .....   | 123  |
| 6.13 Normalized Pd L <sub>3</sub> -edge XANES spectra of (a)–(c) 0.03 wt%Pd over 1.2en-MIL-101(Cr), MIL-101(Cr) and SiO <sub>2</sub> samples and (d)–(f) 0.2 wt%Pd loaded over 0.8en-MIL-101(Cr), MIL-101(Cr) and SiO <sub>2</sub> samples after activation at 150 °C under N <sub>2</sub> , followed by reduction from 30 to 150 °C and holding at 150 °C for 20-60 min ..... | 124  |

## List of Figures (Continued)

| Figure   | Page |
|--|------|
| 6.14 Pd <sup>2+</sup> component of 0.03Pd-1.2en-MIL-101(Cr), 0.03Pd-MIL-101(Cr), and 0.03Pd-SiO <sub>2</sub> upon <i>in situ</i> reduction from 30 °C to 150 °C under 10%H <sub>2</sub> /N <sub>2</sub> , obtained from linear combination fitting (LCF) of Pd L <sub>3</sub> -edge XANES (Figure 6.13) using metallic Pd foil and PdCOCl <sub>2</sub> as references ..... | 125  |
| 6.15 Pd component from Pd L <sub>3</sub> -edge XANES linear combination fitting of 0.2Pd-0.8en-MIL-101(Cr), 0.2Pd-MIL-101(Cr) and 0.2Pd-SiO <sub>2</sub> upon <i>in situ</i> reduction at 150 °C under 10% H <sub>2</sub> /N <sub>2</sub> .....  | 125  |
| 6.16 Pd <sup>2+</sup> component from Pd L <sub>3</sub> -edge XANES linear combination fitting of 0.03Pd-1.2en-MIL-101(Cr), 0.03Pd-MIL-101(Cr) and 0.03Pd-SiO <sub>2</sub> upon <i>in situ</i> reduction at 150 °C during 0–60 min under 10%H <sub>2</sub> /N <sub>2</sub> .....  | 127  |
| 6.17 Pd component from Pd L <sub>3</sub> -edge XANES linear combination fitting of 0.03Pd-1.2en-MIL-101(Cr), 0.03Pd-MIL-101(Cr) and 0.03Pd-SiO <sub>2</sub> upon <i>in situ</i> reduction at 150 °C for 60 min under 10%H <sub>2</sub> in N <sub>2</sub> .....   | 127  |
| 6.18 Recycle of 0.03Pd-MIL-101(Cr) with or without ethylenediamine catalysts for oxidation of styrene .....  | 130  |
| 6.19 TEM images of (a) 0.03Pd-0.5en-MIL-101(Cr) and (b) 0.03Pd-MIL-101(Cr) after used for three cycles of styrene oxidation .....  | 132  |
| 6.20 Effect of ethylenediamine: Pd <sup>2+</sup> molar ratio on the turnover frequency (TOF) of styrene oxidation .....  | 133  |
| 6.21 Effect of ethylenediamine on Pd activity of Pd-en-MIL-101(Cr) and Pd(OAc) <sub>2</sub> .....  | 134  |

## List of Schemes

| Scheme   | Page |
|--|------|
| <b>Chapter 4</b>   |      |
| 4.1 Gas solution-diffusion mechanism in the polymer membrane and favorable diffusion of penetrant in amorphous region for semicrystalline polymer .....                        | 79   |
| 4.2 Strong interaction between CO <sub>2</sub> molecules and coordinatively unsaturated Cu <sup>2+</sup> sites in HKUST-1 and plausible gas transport in HKUST-1 channel ..... | 82   |
| <b>Chapter 6</b>   |      |
| 6.1 Ethylenediamine adsorption on the Cr <sup>3+</sup> nodes of MIL-101(Cr) .....  | 118  |
| 6.2 Possible forms of the incorporated ethylenediamine and Pd <sup>2+</sup> species in MIL-101(Cr) .....   | 128  |



## Abbreviations/Symbols

|                                |  |
|--------------------------------|--|
| °C                             | Celsius                                |
| %v/v                           | %Volume per volume                     |
| %w/v                           | %Weight per volume                     |
| ∅                              | Diameter                               |
| Å                              | Angstrom                               |
| AcP                            | Acetylpyridine                         |
| AcPh                           | Acetophenone                           |
| Al <sub>2</sub> O <sub>3</sub> | Aluminium oxide                        |
| APTES                          | (3-Aminopropyl)triethoxysilane         |
| Ar                             | Argon                                  |
| BAL                            | Benzaldehyde                           |
| BDC                            | Terephthalate                          |
| BET                            | Brunauer-Emmett-Teller                 |
| BF <sub>4</sub>                | Tetrafluoroborate                      |
| BJH                            | Barrett-Joyner-Halenda                 |
| BL                             | Beamline                               |
| bpdc                           | 4,4'-biphenyl dicarboxylic acid        |
| bpydc                          | 2,2'-bipyridine-5,5'-dicarboxylic acid |
| C <sub>4</sub> mim             | 1-n-butyl-3-methylimidazolium salts    |
| Ce                             | Cerium                                 |
| CH <sub>4</sub>                | Methane                                |
| cm                             | Centimeter                             |
| CO                             | Carbonmonoxide                         |
| CO <sub>2</sub>                | Carbondioxide                          |
| Cr                             | Chromium                               |
| Cu                             | Copper                                 |
| CVD                            | Chemical vapor deposition              |
| DMF                            | N,N-Dimethylformamide                  |
| DMSO                           | Dimethylsulfoxide                      |
| EDS                            | Energy Dispersive X-Ray Spectroscopy   |

This material is reserved for educational use only, not allowed for commercial use.

Forbidden to modify the content, and cite the document when use.

## Abbreviations/Symbols (Continued)

|                                |   |
|--------------------------------|---|
| en                             | Ethylenediamine   |
| eV                             | Electronvolt  |
| EVA                            | Ethylene vinyl acetate                                  |
| EXAFS                          | X-ray Absorption Fine Structure                         |
| FTIR                           | Fourier transform infrared                              |
| g                              | Gram  |
| GC                             | Gas chromatography                                      |
| h                              | Hour  |
| H <sub>2</sub>                 | Hydrogen  |
| H <sub>2</sub> -TPR            | Hydrogen-temperature programmed reduction               |
| H <sub>2</sub> -TPRe           | Hydrogen-temperature programmed reaction                |
| H <sub>2</sub> O               | Water   |
| H <sub>2</sub> O <sub>2</sub>  | Hydrogen peroxide                                       |
| H <sub>2</sub> SO <sub>4</sub> | Sulfuric acid   |
| HClO <sub>4</sub>              | Perchloric acid   |
| HEP                            | Hydroxyethylpyridine                                    |
| Hf                             | Hafnium   |
| HIPS                           | High Impact Polystyrene                                 |
| HKUST                          | Hong Kong University of Science and Technology          |
| IB                             | Iodobenzene   |
| ICP-OES                        | Inductively coupled plasma atomic emission spectroscopy |
| K                              | Kelvin  |
| K <sub>2</sub> CO <sub>3</sub> | Potassium carbonate                                     |
| LCF                            | Linear combination fitting                              |
| LiBH <sub>4</sub>              | Lithium borohydride                                     |
| LOHC                           | Liquid organic hydrogen carrier                         |
| m                              | Meter   |
| MeCN                           | Methanol  |
| mg                             | Milligram   |
| MgSO <sub>4</sub>              | Magnesium sulfate                                       |

This material is reserved for educational use only, not allowed for commercial use.

Forbidden to modify the content, and cite the document when use.

## Abbreviations/Symbols (Continued)

|                      |                             |
|----------------------|-----------------------------|
| MIL                  | Material Institut Lavoisier |
| min                  | Minute                      |
| mL                   | Milliliter                  |
| mm                   | Millimeter                  |
| MMMs                 | Mixed matrix membranes      |
| MOFs                 | Metal-organic frameworks    |
| MPa                  | Megapascal                  |
| N <sub>2</sub>       | Nitrogen                    |
| NaBH <sub>4</sub>    | Sodium borohydrode          |
| NaCl                 | Sodium chloride             |
| NB                   | Nitrobenzene                |
| nm                   | Nanometer                   |
| NMR                  | Nuclear magnetic resonance  |
| NPs                  | Nanoparticles               |
| O <sub>2</sub>       | Oxygen                      |
| OMS                  | Open metal sites            |
| OTf                  | trifluoromethanesulfonate   |
| PAA                  | Polyacrylic acid            |
| PBO                  | 1-pyridine-3-ylbutan-1-one  |
| PCN                  | Porous coordination network |
| Pd                   | Palladium                   |
| Pd(OAc) <sub>2</sub> | Palladium(II) acetate       |
| PdCl <sub>2</sub>    | Palladium(II) chloride      |
| PEI                  | Polyethylenimine            |
| PEM                  | Proton-exchange membrane    |
| PhEOH                | Phenylethanol               |
| PSf                  | Polysulfone                 |
| PSM                  | Post-synthetic modification |
| PVA                  | Polyvinylalcohol            |
| PVAc                 | Polyvinylacetate            |

This material is reserved for educational use only, not allowed for commercial use.

Forbidden to modify the content, and cite the document when use.

## Abbreviations/Symbols (Continued)

|                  |  |
|------------------|--|
| rpm              | Round per minute   |
| s                | Second   |
| S                | Surface area   |
| SBU              | Secondary building units   |
| SEM              | Scanning electron microscopy   |
| SiO <sub>2</sub> | Silica   |
| SLRI             | Synchrotron Light Research Institute   |
| Sty              | Styrene  |
| TCD              | Temperature conductivity detector  |
| TEM              | Transmission electron microscopy   |
| TEMPO            | (2,2,6,6-Tetramethylpiperidin-1-yl)oxyl or (2,2,6,6-tetramethylpiperidin-1-yl)oxidanyl |
| TGA              | Thermogravimetric analysis   |
| TOF              | Turnover frequency   |
| Tol              | Toluene  |
| UiO              | Universitetet i Oslo   |
| V                | Volume   |
| wt%              | Weight percent   |
| XANES            | X-ray absorption near-edge structure   |
| XAS              | X-ray absorption spectroscopy  |
| XPS              | X-ray photoelectron spectroscopy   |
| XRD              | X-ray powder diffraction   |
| Y                | Yttrium  |
| ZIF              | Zeolitic imidazolate framework   |
| $\alpha$         | Alpha  |
| $\beta$          | Beta   |
| $\gamma$         | Out of plane vibration   |
| $\delta$         | Bending vibration  |
| $\theta$         | Theta  |
| $\mu\text{L}$    | Microliter   |

This material is reserved for educational use only, not allowed for commercial use.

Forbidden to modify the content, and cite the document when use.

## Abbreviations/Symbols (Continued)

|               |                      |
|---------------|----------------------|
| $\mu\text{m}$ | Micrometer           |
| $\nu$         | Stretching vibration |
| $\pi$         | Pi                   |



This material is reserved for educational use only, not allowed for commercial use.

Forbidden to modify the content, and cite the document when use.

# Chapter 1

## Introduction

### 1.1 Research motivation

Over the past decades, metal organic frameworks (MOFs) have shown great potential for a wide-range of application in areas of energy and environmental sustainability.<sup>1</sup> With several advantages, including the ability to control the pore environment and tunable both terms of porosity and chemical functionality of MOFs, allow them to perform better over traditional porous materials.<sup>2</sup> Desirable and superior features such as chemical stability, binding affinity, and catalytic activity can be obtained by modifying MOF functionality, allowing more potential for improvement in response to the applications.

The formation of functional sites, including coordinatively unsaturated sites, Lewis acid or basic sites, on the internal surface of MOFs has played a crucial role in exploring MOFs for membrane-based selective gas separation. Since preferential adsorption of the functional sites has enabled to facilitate specific and selective recognition of gas molecules during the equilibrium process within MOF adsorbents,<sup>3</sup> providing high separation selectivity and productivity. There are numerous reports of MOFs being used as selective membrane to separate gas mixtures.<sup>4</sup> However, MOFs have been challenging to process continuous MOF membrane due to the presence of defects and chemical stability. Mixed matrix membranes (MMMs) attempt to solve this issue by using MOFs as a filler in the polymer matrix. It ideally leverages the membrane processability of polymers and the superior transport characteristics of MOFs. Numerous MOF-based MMMs (MOF-MMMs) have been investigated and specifically applied for H<sub>2</sub>/CO<sub>2</sub> separation.<sup>5-7</sup> Although most MOF-MMMs accomplish high gas separation, they require a lot of working pressure (typically >1 MPa).<sup>8</sup> Hence, permeability-selectivity trade-off at atmospheric pressure is still challenging. Accordingly, manipulation of MOF/polymer MMMs, including types of polymer matrix and MOF, have conducted for this study to improve the H<sub>2</sub> permeability and H<sub>2</sub>/CO<sub>2</sub> selectivity at atmospheric pressure.

Because of their huge internal surface area, high pore volume and low regeneration temperature, especially ease to activate strong adsorption sites, MOFs can be considered as candidate materials for hydrogen storage. Even though there are many MOFs that have high H<sub>2</sub> adsorption capacities at cryogenic temperatures and high pressure, typically at 77 K and 0.1 MPa,<sup>9</sup> the adsorption dramatically decreases as the temperature increases to room temperature. This is because the H<sub>2</sub> adsorption in MOFs is weak physisorption and the interaction energies between the H<sub>2</sub> molecules and frameworks are very low.<sup>10</sup> To increase the interaction energy between H<sub>2</sub> molecules and MOFs surface, there are numerous methods based chemisorption process have been employed such as ligand functionalization,<sup>11</sup> alkali metal ion<sup>12</sup> or alkaline-earth metal ion inclusion,<sup>13</sup> and embedding MOFs with Pd or Pt nanoparticles<sup>14</sup>. Nevertheless, high pressure and temperature are essentially required to obtain high efficiency. The chemical hydrogen storage of organic hydrogen carriers by hydrogenation and dehydrogenation of the functional group such as alkene/alkane (e.g. toluene/methylcyclohexane)<sup>15</sup>, catalyzed with Pd nanoparticles (Pd NPs), is an alternate solution to avoid the severe conditions. By grafting the organic hydrogen carrier function as an auxiliary ligand on metal node of MOFs, allows it to operate near-atmospheric condition. Further, the confined environment of MOFs could accommodate both the Pd NPs and the organic hydrogen carriers to be in close proximity, facilitating hydrogen transfer between H<sub>2</sub> and the carrier more readily. Thus, this leads to exceptionally stable storage material that allows long-term energy storage.

In addition to using the auxiliary ligand to function MOF as hydrogen storage material, it can also be used as an anchoring ligand for stabilizing Pd<sup>2+</sup>, heterogeneous catalyst, in the oxidation of styrene. Even though the Pd<sup>2+</sup> species is required as an active sites in this reaction, it is easily aggregate and form inactive Pd black, even at room temperature.<sup>16</sup> Thus, stabilization of Pd<sup>2+</sup> species by anchoring over the mesoporous support is essential to prevent the auto-reduction by feed upon reaction or at high temperature. Although the anchored Pd<sup>2+</sup> over SiO<sub>2</sub>,<sup>17</sup> polymer<sup>18</sup> and zeolites<sup>19</sup> have been extensively reported, the poor catalyst activity and stability were generally obtained since they were not stable at high reaction temperature. Moreover, the number of active sites

on these catalysts were relatively low due to limited anchoring sites on the external surface support. On this point, MOFs offer a chance to functionalize the anchoring sites over either organic linkers or unsaturated sites through their MOFs structure, resulting in the increase amount of Pd<sup>2+</sup> active species. Despite the fact that the decorated anchoring ligand on organic linker had better Pd<sup>2+</sup> activity,<sup>20</sup> the synthesis of special organic linkers is costly, and the preparation of these MOFs is somewhat complicated with low yields. Alternatively, grafting an electron-doner anchoring ligand at the coordinatively unsaturated sites around the metal nodes of MOFs is a more effective way to stabilize the Pd<sup>2+</sup> species within the MOFs. This would open an opportunity for immobilizing Pd<sup>2+</sup> species that can withstand reduction or decomposition at high temperatures, hence improving the catalyst stability.

Accordingly, this thesis focuses on the developments of modified MOFs (i.e. HKUST-1 and MIL-101(Cr)). The unsaturated metal sites in MOF were applied or modified post-synthetically to be used in the way of gas separation, chemical hydrogen storage and catalysis. The relationship between structural and chemical attributed of MOFs on their applications were described and discussed.

## 1.2 Objectives of the study

- 1) To obtain HKUST-1/polymer MMMs for H<sub>2</sub>/CO<sub>2</sub> separation at atmospheric pressure
- 2) To understand the effect of HKUST-1 on the gas permeability and H<sub>2</sub>/CO<sub>2</sub> permselectivity
- 3) To obtain acetylpyridine-Pd-MIL-101(Cr) as chemical hydrogen storage that can function by regulating temperature and hydrogen partial pressure
- 4) To investigate effect of hydrogenation/dehydrogenation temperature and Pd loading on material stability and H<sub>2</sub> capacity
- 5) To provide highly stable Pd<sup>2+</sup> species in ethylenediamine-MIL-101(Cr) that can withstand under high reduction temperatures and is able to catalyze in styrene oxidation
- 6) To study the role of MIL-101(Cr) and ethylenediamine-grafted for the stabilization of Pd<sup>2+</sup> species

### 1.3 Scopes of the study

#### 1.3.1 Atmospheric H<sub>2</sub>/CO<sub>2</sub> permeability of HKUST-1/MMMs for hydrogen purification

- 1) Synthesize HKUST-1 by solvothermal
- 2) Characterize the HKUST-1 with XRD, N<sub>2</sub> adsorption-desorption, TGA, FTIR and scanning electron microscopy (SEM)
- 3) Prepare the HKUST-1/MMMs (HIPS and EVA as polymer matrix) by solution casting and test their H<sub>2</sub> and CO<sub>2</sub> permeabilities

#### 1.3.2 Reversible Hydrogenation–Dehydrogenation of Acetylpyridine (AcP)-Pd-MIL-101(Cr) for Chemical Hydrogen Storage

- 1) Hydrothermally synthesize MIL-101(Cr), then sequentially modify with acetylpyridine by adsorption and incorporate Pd nanoparticles using double solvent technique
- 2) Characterize the AcP-Pd-MIL-101(Cr) sample by XRD, N<sub>2</sub> adsorption-desorption, CHN analysis, ICP-OES, TGA, TEM and XAS
- 3) Examine the acetylpyridine grafting on Cr<sup>3+</sup> nodes of MIL-101(Cr) by FTIR and XPS.
- 4) Test H<sub>2</sub> consumption (hydrogenation) and H<sub>2</sub> evolution (dehydrogenation) of AcP-Pd-MIL-101(Cr) by H<sub>2</sub>-TPR.
- 5) Optimize the hydrogenation/dehydrogenation conditions (hydrogenation temperature 100, 130, 150 and 200 °C for 0.5, 1 and 2 h and dehydrogenation temperature 150, 160, 170, 180, 190 and 200 °C for 1 h) on hydrogen storage performance and sample stability by H<sub>2</sub>-TPRe and *in situ* XAS in the region of XANES
- 6) Investigate the effect of Pd loading (0.5, 2.5 and 4.0 wt%) on hydrogen storage capacity
- 7) Study the hydrogen storage mechanism during hydrogenation and dehydrogenation of AcP-Pd-MIL-101(Cr) by *in situ* FTIR and H<sub>2</sub>-TPRe
- 8) Test the hydrogen storage recyclability by H<sub>2</sub>-TPRe

### 1.3.3 Highly stable Pd<sup>2+</sup> species anchoring on ethylenediamine-grafted-MIL-101(Cr) as a robust oxidation catalyst

1) Hydrothermally synthesize MIL-101(Cr) and then sequentially modify with ethylenediamine (en) by adsorption and incorporate Pd(OAc)<sub>2</sub> by double solvent technique.

2) Characterize the Pd-en-MIL-101(Cr) sample by XRD, N<sub>2</sub> sorption, CHN analysis, ICP-OES, TGA and TEM.

3) Examine the ethylenediamine grafting on Cr<sup>3+</sup> nodes of MIL-101(Cr) by FTIR and XPS.

4) Investigate the Pd-ethylenediamine coordination and Pd<sup>2+</sup> anchoring by XPS and Raman spectroscopy.

5) Study the effect of ethylenediamine (0.5, 0.8 and 1.2 mmol/g) and Pd (0.03 and 0.2 mmol/g) contents on the Pd<sup>2+</sup> irreducibility by *in situ* XAS in the region of XANES

6) Test the reactive Pd<sup>2+</sup> species with styrene oxidation, selective phenylacetylene hydrogenation and Heck coupling reactions

7) Study the effect of ethylenediamine: Pd<sup>2+</sup> contents (1.75, 2.15, 3.4, 10, 16, 20 and 31.3) on the Pd<sup>2+</sup> activity for styrene oxidation

## 1.4 Benefits of the study

This thesis provides a valuable knowledge mainly in MOFs modification for responding application in the field of gas separation, hydrogen storage and catalysis. In the first study, exhibits permselective H<sub>2</sub>/CO<sub>2</sub> separation for HKUST-1/polymer MMMs. Thanks to simple HKUST-1/MMMs preparation and the H<sub>2</sub>/CO<sub>2</sub> permselectivity comparable to other engineering polymer membrane, it would be possible to use in the industrial to reduce the operation costs and maintenance. For the second study, chemical hydrogen storage of Pd-AcP-MIL-101(Cr) offers new approach, which applying organic hydrogen carrier for material-based hydrogen storage. The simple operation by regulating temperature (less than 200 °C) and hydrogen partial pressure of hydrogenation and dehydrogenation processes present the cost-effective and less energy consumption than conventional hydrogen storage. In the third study, the anchoring of highly stable Pd<sup>2+</sup> species in ethylenediamine-MIL-101(Cr) presents the advantage of coordinatively

unsaturated sites in the MOF for grafting the ethylenediamine as an anchoring site to improve the active sites density and also stabilize the Pd<sup>2+</sup> species. This delicate and simple catalyst designs by using MOFs provide the guideline for preparation the Pd<sup>2+</sup> catalyst with high stability.

## 1.5 References

- (1) Julien, P. A.; Mottillo, C.; Fri, T. Metal–Organic Frameworks Meet Scalable and Sustainable Synthesis. *Green Chemistry* **2017**, *19*, 2729–2747.
- (2) Li, B. Porous Metal–Organic Frameworks: Promising Materials for Methane Storage. *Chem* **2016**, *4* (1), 557–580.
- (3) Lin, R.-B.; Xiang, S.; Zhou, W.; Chen, B. Microporous Metal–Organic Framework Materials for Gas Separation. *Chem* **2020**, *6* (2), 337–363.
- (4) Qian, Q.; Asinger, P. A.; Lee, M. J.; Han, G.; Mizrahi Rodriguez, K.; Lin, S.; Benedetti, F. M.; Wu, A. X.; Chi, W. S.; Smith, Z. P. MOF-Based Membranes for Gas Separations. *Chem. Rev.* **2020**, *120* (16), 8161–8266.
- (5) Hu, J.; Cai, H.; Ren, H.; Wei, Y.; Xu, Z.; Liu, H.; Hu, Y. Mixed-Matrix Membrane Hollow Fibers of Cu<sub>3</sub>(BTC)<sub>2</sub> MOF and Polyimide for Gas Separation and Adsorption. *Ind. Eng. Chem. Res.* **2010**, *49* (24), 12605–12612.
- (6) Wang, Y.; Yang, G.; Guo, H.; Meng, X.; Kong, G.; Kang, Z.; Guillet-Nicolas, R.; Mintova, S. Preparation of HKUST-1/PEI Mixed-Matrix Membranes: Adsorption-Diffusion Coupling Control of Small Gas Molecules. *J. Membr. Sci.* **2022**, *643*, 120070.
- (7) Dietzel, P. D. C.; Besikiotis, V.; Blom, R. Application of Metal–Organic Frameworks with Coordinatively Unsaturated Metal Sites in Storage and Separation of Methane and Carbon Dioxide. *J. Mater. Chem.* **2009**, *19* (39), 7362–7370.
- (8) Anjum, M. W.; Vermoortele, F.; Khan, A. L.; Bueken, B.; De Vos, D. E.; Vankelecom, I. F. J. Modulated UiO-66-Based Mixed-Matrix Membranes for CO<sub>2</sub> Separation. *ACS Appl. Mater. Interfaces* **2015**, *7* (45), 25193–25201.
- (9) Murray, L. J.; Dincă, M.; Long, J. R. Hydrogen Storage in Metal–Organic Frameworks. *Chem. Soc. Rev.* **2009**, *38* (5), 1294–1314.

- (10) Pareek, K.; Rohan, R.; Chen, Z.; Zhao, D.; Cheng, H. Ambient Temperature Hydrogen Storage in Porous Materials with Exposed Metal Sites. *Int. J. Hydrog. Energy* **2017**, *42* (10), 6801–6809.
- (11) Cao, W.; Li, Y.; Wang, L.; Liao, S. Effects of Metal Ions and Ligand Functionalization on Hydrogen Storage in Metal–Organic Frameworks by Spillover. *J. Phys. Chem. C* **2011**, *115* (28), 13829–13836.
- (12) Mulfort, K. L.; Hupp, J. T. Alkali Metal Cation Effects on Hydrogen Uptake and Binding in Metal–Organic Frameworks. *Inorg. Chem.* **2008**, *47* (18), 7936–7938.
- (13) Wahyu, W.; Ni'maturrohmah, D.; Putra, R.; Suwarno, H.; Fahrudin Arrozi, U. S. Enhanced Hydrogen Sorption Properties over Mg<sup>2+</sup> Modified Solvothermal Synthesized HKUST-1 (Mg<sup>2+</sup>/HKUST-1). *IOP Conf. Ser.: Mater. Sci. Eng.* **2019**, *509*, 012152.
- (14) Wang, L.; Stuckert, N. R.; Chen, H.; Yang, R. T. Effects of Pt Particle Size on Hydrogen Storage on Pt-Doped Metal–Organic Framework IRMOF-8. *J. Phys. Chem. C* **2011**, *115* (11), 4793–4799.
- (15) Zhu, Q.-L.; Xu, Q. Liquid Organic and Inorganic Chemical Hydrides for High-Capacity Hydrogen Storage. *Energy Environ. Sci.* **2015**, *8* (2), 478–512.
- (16) Iwasawa, T.; Tokunaga, M.; Obora, Y.; Tsuji, Y. Homogeneous Palladium Catalyst Suppressing Pd Black Formation in Air Oxidation of Alcohols. *J. Am. Chem. Soc.* **2004**, *126* (21), 6554–6555.
- (17) Borah, P.; Zhao, Y.  $\beta$ -Diketimine Appended Periodic Mesoporous Organosilica as a Scaffold for Immobilization of Palladium Acetate: An Efficient Green Catalyst for Wacker Type Reaction. *J. Catal.* **2014**, *318*, 43–52.
- (18) Islam, S. M.; Mondal, S.; Roy, A. S.; Mondal, P.; Mobarak, M.; Hossain, D.; Pandit, P. Synthesis and Characterization of a Polymer-Anchored Palladium(II) Schiff Base Complex and Its Catalytic Efficiency in Phosphine-Free Sonogashira Coupling Reactions. *Transit. Met. Chem.* **2010**, *35* (3), 305–313.
- (19) Ahn, J.-H.; Sherrington, D. C. Wacker Oxidation of Oct-1-Ene Using a Palladium(II) Complex Supported on Cyano-Functionalized Polyimide Beads. *Macromolecules* **1996**, *29* (11), 4164–4165.

- (20) Zhang, Y.; Wei, N.; Xing, Z.; Han, Z.-B. Functional Hexanuclear Y(III) Cluster-Based MOFs Supported Pd(II) Single Site Catalysts for Aerobic Selective Oxidation of Styrene. *Appl. Catal. A: Gen.* **2020**, *602*, 117668.



## Chapter 2

# Theories and Literature Reviews

### 2.1 Metal–organic framework

Metal–organic frameworks (MOFs), also known as porous coordination polymers, have recently emerged as a class of very promising organic–inorganic hybrid materials for diverse applications. MOFs are crystalline porous materials built from metal ions/polynuclear building units connected by polytopic organic linkers. An important feature of MOFs is that their framework structures, pore environment and functionality can be finely controlled by the choice of metal and organic building blocks and how they are connected. While high micropore volumes and large surface areas are desirable for many applications, such as narrow pores do not allow for hosting large objects and anchoring molecular functions, as well as fast mass diffusion and transfer, thereby providing possibility to use in a wide variety of applications (Figure 2.1).

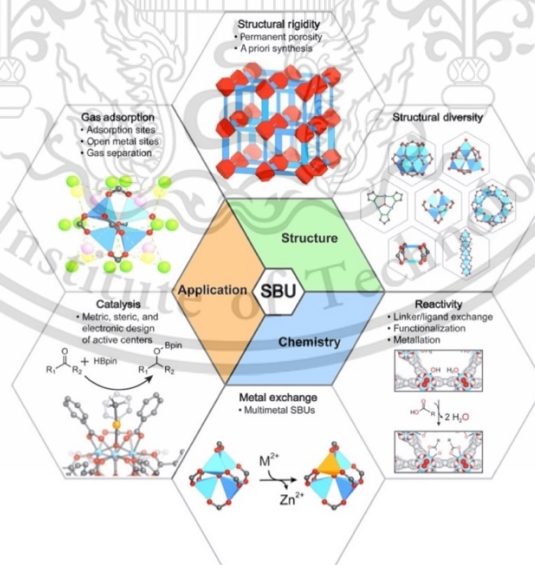
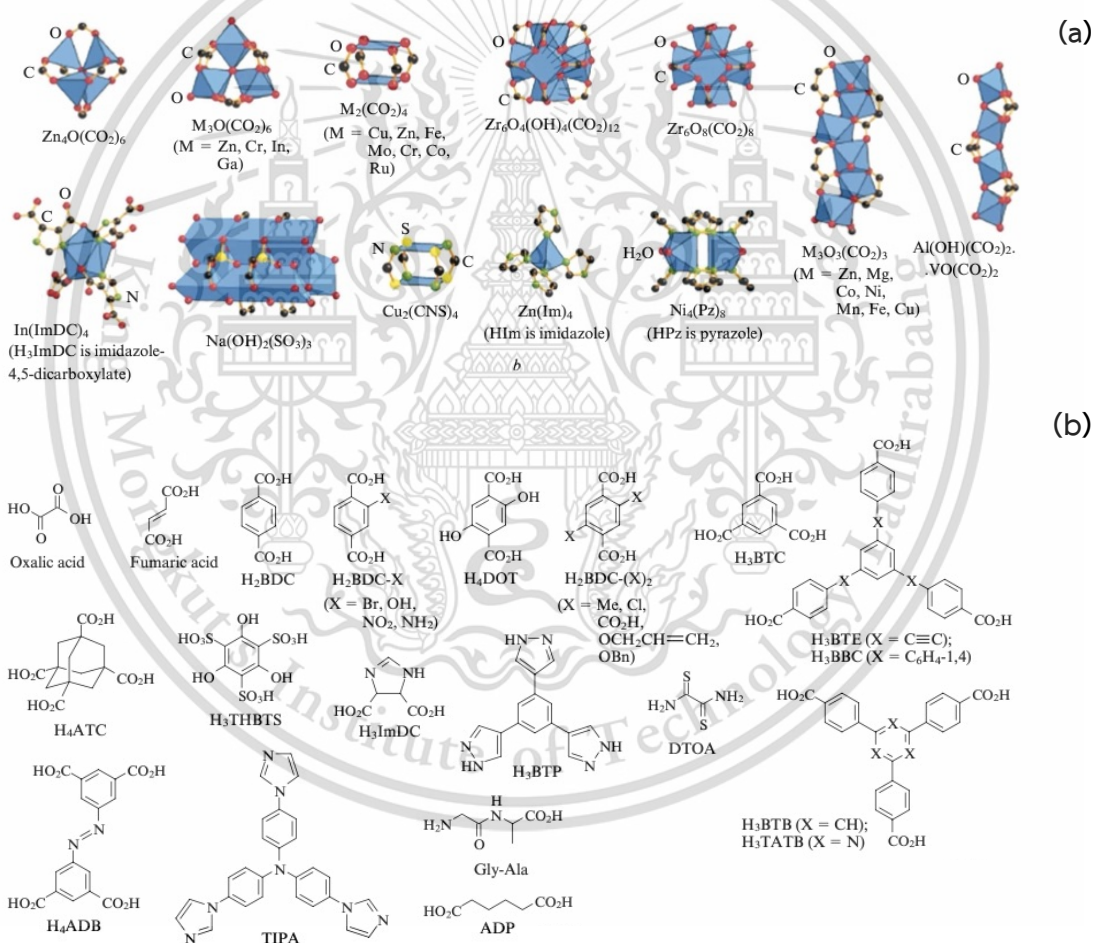


Figure 2.1 Overview of MOFs chemistry<sup>1</sup>

### 2.1.1 MOFs structure

MOFs are hybrid crystalline porous compounds materials that could be regarded as a highly assembled from the multinuclear inorganic building units, secondary building units (SBUs). The metal ions or their clusters are joint by chelating agents (ligand)<sup>2</sup> to result rigid structures with various dimensionalities<sup>3</sup>. Two components can be distinguished in MOFs: the SBU (Figure 2.2a) and organic molecules (Figure 2.2b) linking the former to give basically periodic porous structures. Different combinations of these structure elements lead to an enormous number of MOFs.



**Figure 2.2** Constituents of metal-organic frameworks (MOFs); (a) metal clusters (polyhedra demonstrate the metal coordination) and (b) organic molecules from, which linkers are formed<sup>4</sup>

In addition, in each geometry variant, the central metal atom can be substituted. In particular, the substitution of secondary building units, while the linker (terephthalic acid) is the same, can lead to quite different MOFs (Figure 2.3).

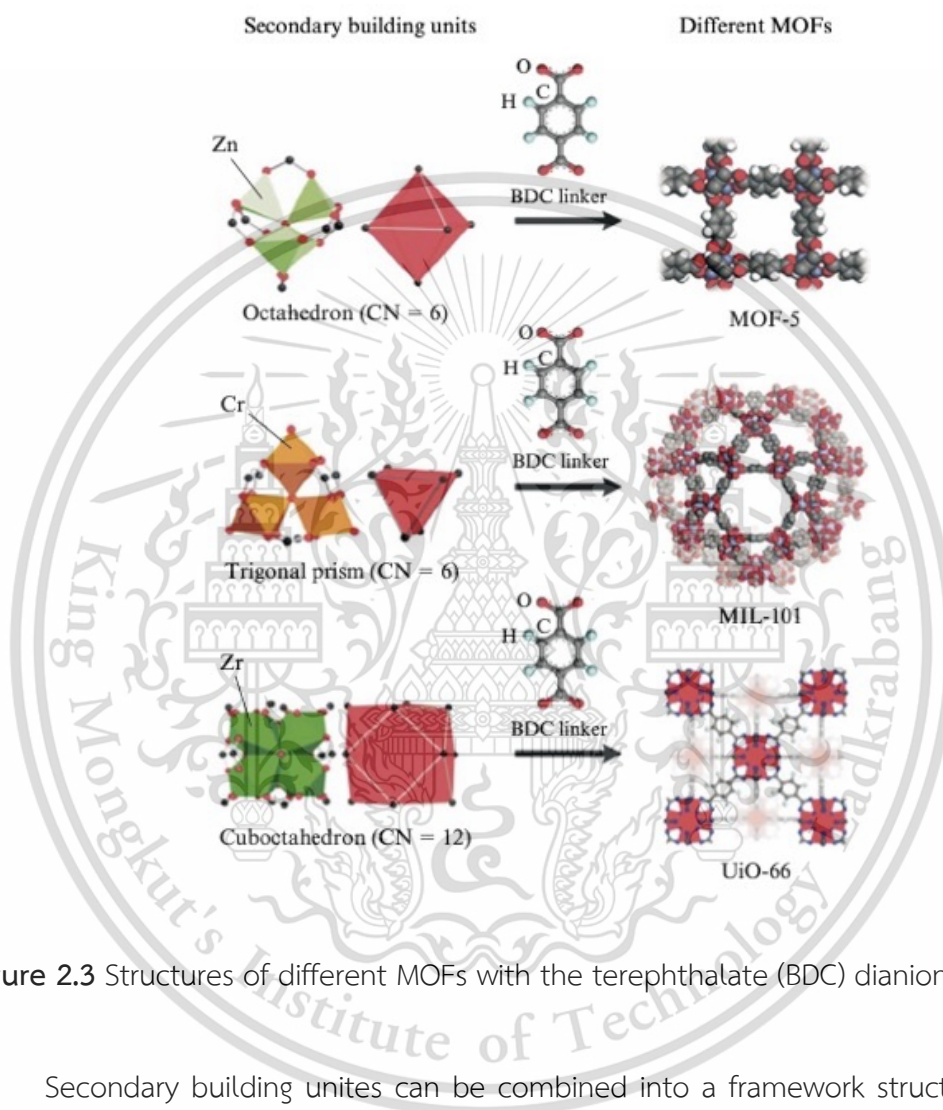


**Figure 2.3** Structures of different MOFs with the terephthalate (BDC) dianion as a linker

Secondary building units can be combined into a framework structure through different linkers. Selection and substitution of a linker can lead to two situations: either the symmetry of the structure is retained when another linker is used and only the unit cell parameters change because of the elongation of the carbon chain (for example, when going from UiO-66 to UiO-68) (Figure 2.4)<sup>5</sup> or the symmetry can also change because of the change in the mutual arrangement of functionalities (Figure 2.5).

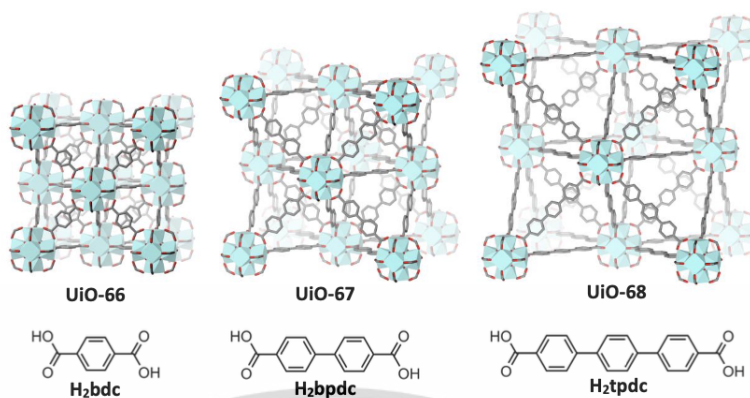


Figure 2.4 Framework symmetry retention with an increase in the linker chain length

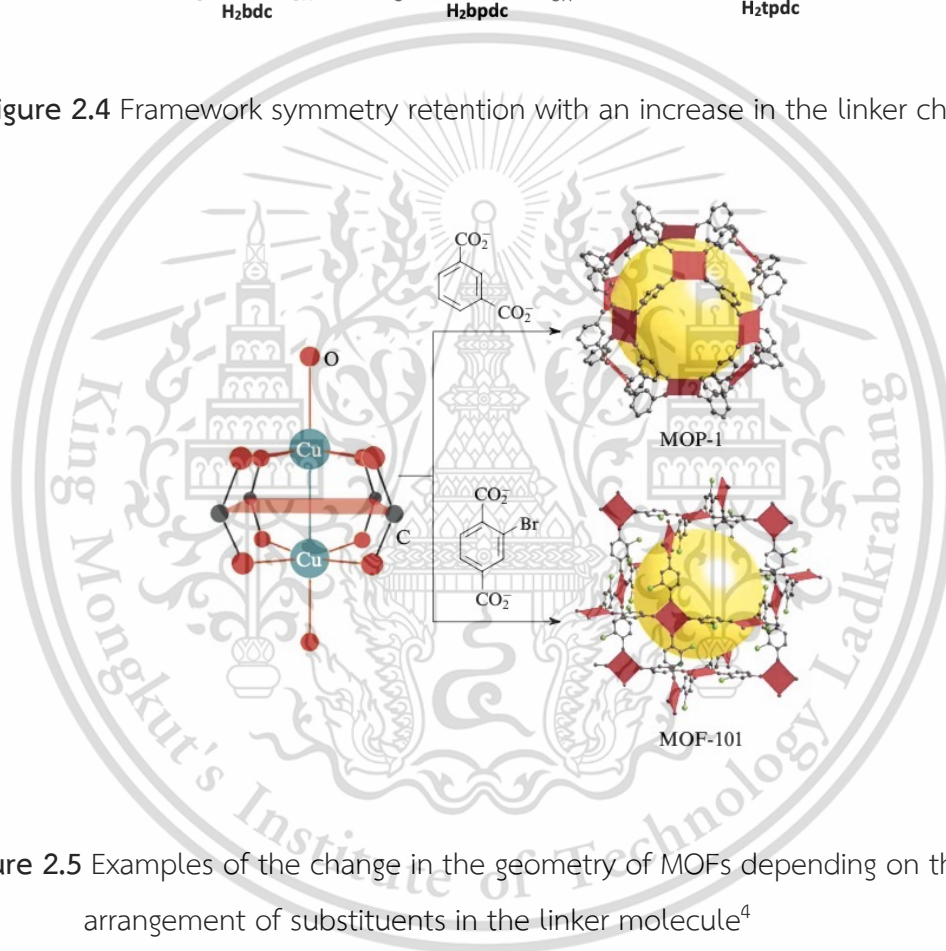


Figure 2.5 Examples of the change in the geometry of MOFs depending on the mutual arrangement of substituents in the linker molecule<sup>4</sup>

As already mentioned, MOFs are distinguished by the diversity of their structures, different symmetry and pore sizes and by their characteristics. The pore size is determined by the carbon chain length of the linker or the number of benzene rings in it, whereas the introduction of different substituents and functional groups into the linker is responsible for the additional selectivity and unique chemical properties of the pores.

## 2.1.2 General feature of MOFs

### 2.1.2.1 Porosity of MOFs

The porosities, or void spaces, in MOFs can be shaped in various forms. 1D channels or interconnecting channels of higher dimensionality can run through the solid. Free space inside pores can be accessible by entering pore windows that are of smaller diameter compared with that of the actual pore. Cavities can also be present in these materials. The void spaces in MOFs span from a few angstroms to tens of nanometers. The same material can contain pores of different sizes, both in the micro- and mesoscale region.<sup>6</sup> Size and shape selectivity can be accomplished using MOFs due to their tunable, well-defined pore size and shape. The most significant distinction compared to many other porous substances is their low density, which offers them extremely great surface areas and porosity.<sup>7</sup>

### 2.1.2.2 Flexibility of MOFs

Some MOFs are flexible yet robust enough to maintain their structures. Movements in the framework can occur upon change of external conditions, such as temperature, pressure, chemical medium.<sup>8</sup> The structure of MOF can adjust itself in order to accommodate incoming gases or liquids. The response is also dependent on host-guest and host interactions. Pores or channels can shrink and expand in a reversible manner, without breaking bonds, when gases or liquids are filling and evacuating from the pores/channels. This kind of response is called a dynamic or “breathing effect”.<sup>9</sup> A flexible network needs both enough free space to accommodate the guests and contain weak and less rigid ligand that make it possible for the network to change. The dynamic effects can depend on local flexibility at the linker and/or metal clusters that are flexible in their coordination to the linkers and change the bond angles slightly without breaking the bonds. The displacements can be of several angstroms, resulting in quite large changes in pore volume. An often-mentioned example is the MIL-53 as illustrated in Figure 2.6.

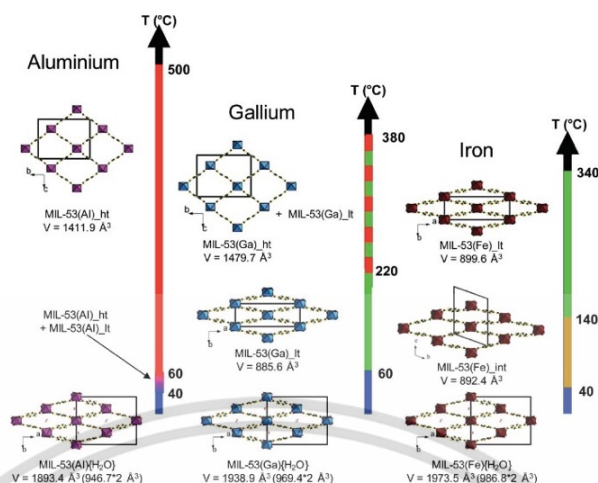


Figure 2.6 The breathing effect of MIL-53 (Al, Ga or Fe) as a function of temperature above room temperature

### 2.1.3 MOFs synthesis

Several efforts have been exploring diverse routes for the MOFs synthesis that are cost-effective, green, and rapid. Such routes can be classified as solvothermal, slow evaporation/direct precipitation, microwave assisted, electrochemical, mechanochemical, and sonochemical methods (Figure 2.7).

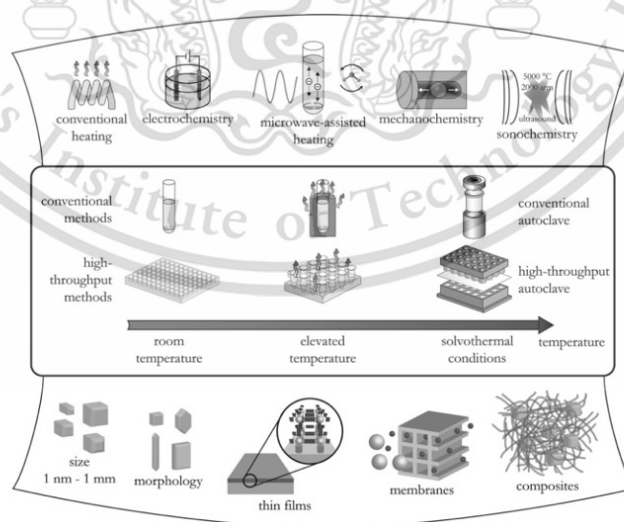


Figure 2.7 Overview of synthesis methods, possible reaction temperatures, and final reaction products in MOF synthesis

**Solvothermal approach;** In general, MOFs have been synthesized under solvothermal conditions via conventional electrical heating. The self-assembling process of MOFs usually starts from isolated metal ions and organic linkers (Figure 2.8). During the implementation of a solvothermal method, the chemical reaction proceeds in solvent at a temperature above its normal boiling point by containing the reaction mixture within a sealed vessel. These conditions increase the ability of solvent to dissolve solids and speed up reactions between solid species. The main advantage of this method is that almost any material can be dissolved in the solvent by increasing the temperature and pressure to its critical point.

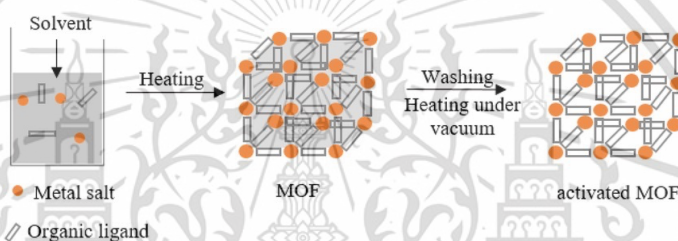


Figure 2.8 Solvothermal synthesis of MOF

**Microwave-assisted synthesis,** the energy for reaction is provided in the form of microwave (MW) radiation (Figure 2.9). It is generally used in organic syntheses, but it has wide application in rapid synthesis of nanoporous materials. Apart from fast crystallization, phase selectivity, narrow particle size distribution and morphological controls are some of the advantages of this method. Several MOFs containing  $\text{Fe}^{3+}$ ,  $\text{Al}^{3+}$ ,  $\text{Cr}^{3+}$ ,  $\text{V}^{3+}$ ,  $\text{Ce}^{3+}$  have been synthesized using MW assisted method. Formation of MOFs has been reported to carry out under MW radiation at a temperature over  $100\text{ }^{\circ}\text{C}$  with reaction time exceeding 1 h. Generally, MOFs can be formed quickly via MW irradiation with respect to conventional electrical heating process.

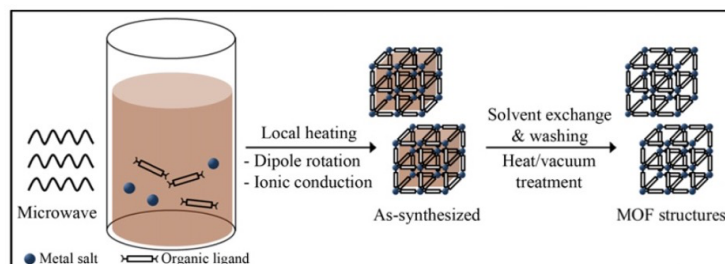


Figure 2.9 Microwave-assisted solvothermal synthesis of MOF structures

*Electrochemical synthesis* of MOF uses metal ions continuously supplied through anodic dissolution as a metal source instead of metals salts, which react with the dissolved linker molecules and a conducting salt in the reaction medium (Figure 2.10). Protic solvents are generally used to avoid deposition of metal on cathode, but during process  $H_2$  generation can be possibly observed.

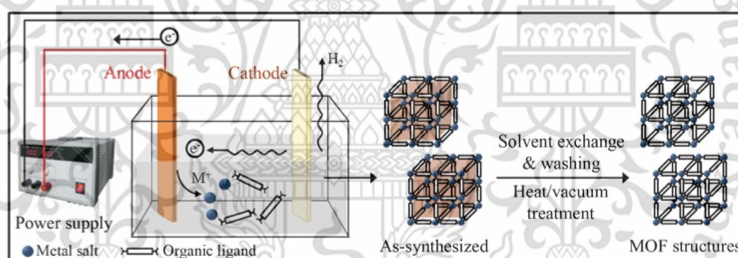


Figure 2.10 Electrochemical synthesis of MOF

*Sonochemical technique*, ultrasonic radiation (20 kHz – 10 MHz) is used for MOFs synthesis. This method can also achieve a reduction in crystallization time and significantly smaller particles size than those by the conventional solvothermal synthesis. When high energy ultrasound interacts with liquid, cavitation (process of bubble formation, growth and collapse under altering pressure) takes place and provides energy with high temperature of  $\sim 5000$  K and pressure of  $\sim 1000$  bar, creating hot spots to facilitate rapid crystallization of homogeneous crystals of MOFs (Figure 2.11).

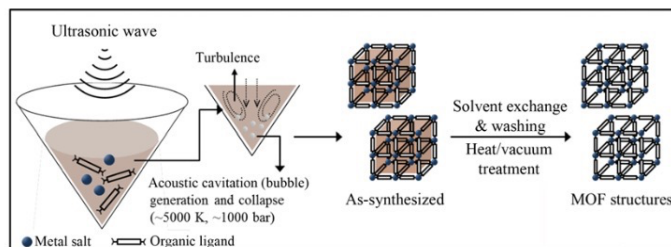


Figure 2.11 Sonochemical synthesis of MOF

*Layer by layer method* is used for the preparation of MOF thin films. The method is based on surface chemistry in which functionalized organic surface is immersed sequentially into the solutions of metal ion and organic linker. It was observed that orientation of thin film depends on that sequence through which the reactants are added (Figure 2.12). Metal source and surface termination are the two major factors that affect the rate of growth MOF film. Highly oriented growth was observed for substrates functionalized with different functional groups such as COOH, OH.<sup>10</sup>

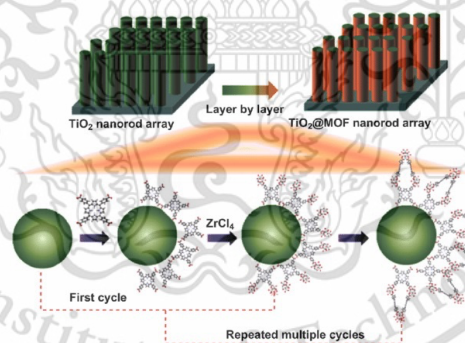


Figure 2.12 The example of layer-by-layer MOF synthesis method

In addition, an important step for post-synthetic treatment of MOFs is purification and activation. The purification is of crucial step for catalytic applications since the impurities, such as metal precursor, residue linkers and solvent, from synthesis reaction can mimic the catalytic activity and considerably deteriorate the absorption possibilities. The purification usually consists of treatment with a solvent at elevated temperature. The

activation implies pore emptying, which is often a difficult task. Since removal of inclusions from a porous structure by heating, can lead to collapse of the framework, especially if the guest molecules and the framework are bound by rather strong bonds or if inclusion removal requires high temperatures. There are different methods for simplifying the activation of MOFs. The most common among them is solvent activation, which is replacement of the solvent by a more volatile one that makes it possible to decrease the treatment temperature (Figure 2.13).

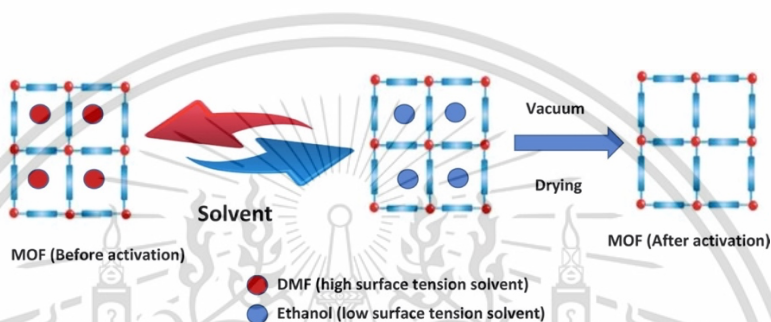
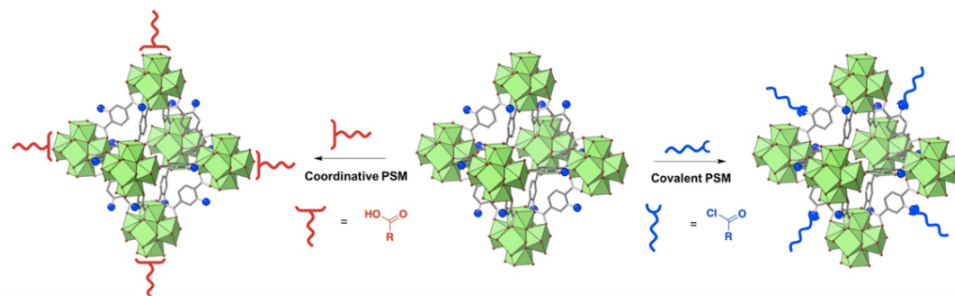


Figure 2.13 Solvent activation of MOFs

#### 2.1.4 Post-synthetic modification of MOFs

Compared with the conventional inorganic materials, hybrid nature of MOFs presents an opportunity for functionalizing their frameworks to expand their functional or structural diversity. Post-synthetic modification (PSM) usually involves chemical functionalization of organic linkers or metal clusters of a MOF to create a variation of the parent framework but still maintains the structural stability. The advantages of the PSM method include: (i) the ability to incorporate a wider range of functional groups, (ii) the ability to generate a series of functionally diverse MOFs with the same topology and (iii) the ability to introduce multiple kinds of functional groups into the same framework. The post-synthetic modification can be mainly divided into two categories as shown in Figure 2.14, including.

- **Covalent PSM**, in which the organic linkers of the MOF are modified with a reagent, resulting in new functional groups
- **Coordinative PSM**, where organic molecules containing metal ligating groups are introduced onto the inorganic SBUs of the MOF.



**Figure 2.14** Illustrative schematic of (i) covalent PSM using reactive groups on the MOF linker for modification by an organic reagent and (ii) coordinative PSM using a coordinating organic molecule to bind to the MOF SBU

#### 2.1.4.1 Covalent post-synthetic modification

The highly porosity and chemically rich components of MOFs provide excellent opportunities to perform covalent reactions on the surface, to extend their chemical complexity and functionality for various applications. Typically, the covalent post-synthetic modification usually involves organic linkers, containing a chemical functionality that does not interfere with MOF assembly but can be used as the site for modification in subsequent post-synthetic modification (Figure 2.15). Frequently, covalent PSM has been achieved using amine-, aldehyde- or azide-derivatized organic linkers, as these moieties are quite reactive and can be targeted with reasonable selectivity using specific reagents. The installation of these functional groups has led to the discovery of MOFs with interesting catalytic, gas separation, hydrophilic, and hydrophobic properties.

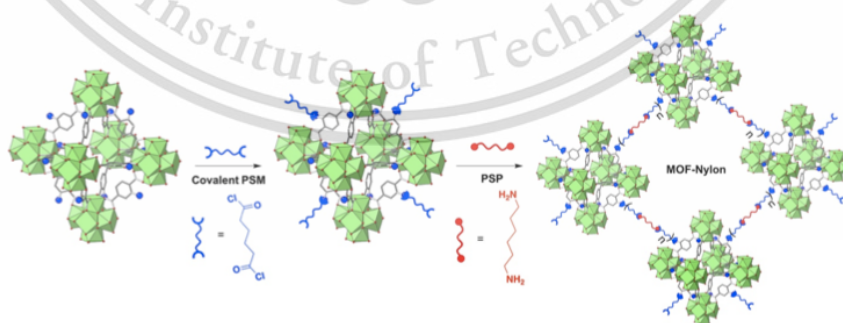


**Figure 2.15** Illustrated covalent post-synthetic modification and subsequent polymerization synthesis of MOF-nylon hybrid materials

### 2.1.4.2 Coordinative post-synthetic modification

In contrast to covalent modification, coordinative covalent modification involves changes in the coordination environment of the SBUs within the framework that do not alter the overall SBU or the framework topology. Many MOFs contain labile ligands, often coordinated solvent molecules, that are attached to the SBUs. These may be removed together with the solvent molecules included in the pores in the activation process to generate a porous material with open coordination sites, providing open metal sites (Figure 2.16). Alternatively, these labile ligands can be substituted by other ligands, and this substitution has often been used to enhance adsorption or catalytic properties.

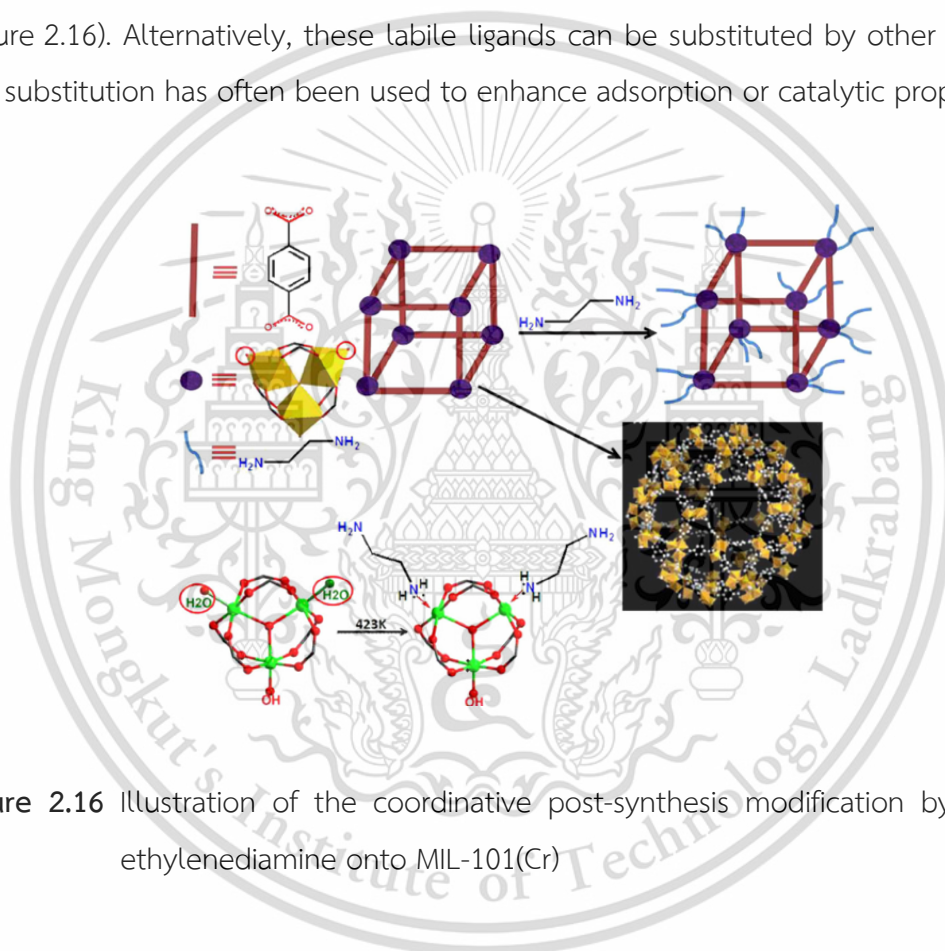


**Figure 2.16** Illustration of the coordinative post-synthesis modification by grafting of ethylenediamine onto MIL-101(Cr)

## 2.2 MOFs for gas adsorption and separation

Because of their enormous surface areas, adjustable pore diameters, and controllable surface characteristics, MOFs are excellent adsorbents for gas storage and separation. As potential adsorbents in gas separation and purification, MOFs offer unique advantages for specific applications based on their structural characteristics.

## 2.2.1 Selective gas adsorption in rigid MOFs

In rigid MOFs, much like in zeolites, the adsorption selectivity may be related to the molecular sieving effect and/or preferential adsorption based on the different strengths of the adsorbent–adsorbate and adsorbate–adsorbate interactions.

### 2.2.1.1 Selective adsorption based on size/shape exclusion

Selective adsorption based mainly on the molecular sieving effect has been confirmed in several MOFs. Structural analysis revealed that manganese formate, has a robust 3D framework structure with 1D channels. These channels contain larger apertures, which are connected to each other via a small window. Gas sorption experiments indicated that at 78 K this material can selectively adsorb H<sub>2</sub> over N<sub>2</sub> and Ar.<sup>11</sup> Thus, the selectivity was attributed to the small aperture of the channels. In another way, coordinatively linked interpenetrated MOF, PCN-17 which has a porous structure containing large cages linked by relatively small apertures and retains its porosity at temperatures as high as 480 °C. The interpenetration and sulfate bridging in PCN-17 reduce its pore (window) size to approximately 3.5 Å leading to selective adsorption of H<sub>2</sub> and O<sub>2</sub> over N<sub>2</sub> and CO.<sup>12</sup>

### 2.2.1.2 Selective adsorption based on adsorbate–surface interactions

Although the pore size and shape of an adsorbent are the major factors in determining the adsorption selectivity of guest molecules, the nature of the guest–surface interaction is also important. In some of the rigid MOFs, the adsorption selectivity can be attributed to the thermodynamic equilibrium effect or the kinetic effect in a given equilibrium time, namely the preferential adsorption but not the molecular sieving effect. In these cases, the selectivity was demonstrated to be related to adsorbate properties such as polarity, quadrupole moment, and H-bonding, as well as to the surface properties of the pores.

### 2.2.1.3 Selective adsorption based on cooperative effects of size/shape exclusion and adsorbate–surface interactions

The selective gas adsorption in some MOFs seems to be related to both the pore size and the interactions between adsorbate molecules and the pore walls. One example is Er<sub>2</sub>(pda)<sub>3</sub>, which has a 3D framework structure with 1D circular channels and

coordinatively unsaturated  $\text{Er}^{\text{III}}$  sites. The effective dimension of the channels is approximately  $3.4 \text{ \AA}$  in diameter. Adsorption measurements showed selective adsorption of  $\text{CO}_2$  over Ar and  $\text{N}_2$ , which was attributed to the combined effects of size and of host-guest interactions.<sup>13</sup> It was suggested that the host framework, with its coordinatively unsaturated  $\text{Er}^{\text{III}}$  ions, polar groups, and  $\pi$ -electrons, may give rise to an electric field, inducing a dipole in  $\text{CO}_2$ . Besides the induced dipole interaction, the quadrupole moment of  $\text{CO}_2$  would interact with the electric field gradient, contributing further to the adsorption potential energy.

### 2.2.2 MOFs membrane-based gas separation

For MOFs membrane-based gas separations, there are two main factors that play a role in the membrane separation performance: solubility and diffusivity of the feed gas in single or multi-component mixtures. The solubility of the targeted gas is governed through its thermodynamic affinity/interactions with the membrane, while its diffusivity is directed by its relative size with respect to the apertures and the pore sizes of the framework.

In principle, if the pore apertures and size are bigger than the dimensions of the penetrates, molecules in the gas mixture with a substantially stronger affinity/interaction with the pore system of the membrane would adsorb strongly and diffuse quicker through the membrane. If the interactions are moderate enough to allow for optimal desorption downstream, resulting in a permselectivity in favor of the highly absorbable gas, this case can lead to good separation (i.e., solubility-based separations). Accordingly, altering the pore system surface through ligand modification or chemical functionalization can improve solubility-based separation. This modification can lead to changes in the size and shape of the pore aperture, the pore volume, and the surface nature or functionality - polarity, hydrophilicity, or hydrophobicity - all of which can lead to either an improvement or a drop in the selectivity-permeability trade-off.

In the case of molecular sieving, i.e., size-selective separations, the kinetic diameters of the targeted molecules for separation usually govern the selection of the MOF candidates with the appropriate pore aperture for a given separation. However,

various studies reported that even gases with a kinetic diameter larger than that of the pore aperture are still able to permeate through the MOF membrane, which is plausibly governed by framework flexibility in MOFs (Figure 2.17).

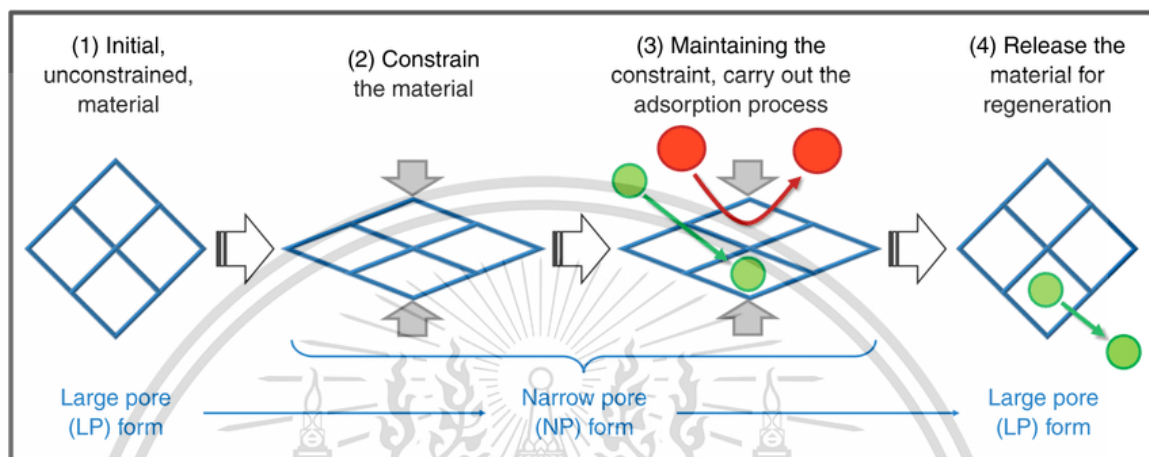


**Figure 2.17** Breathing behavior of the flexible MIL-53 MOF by application of an external mechanical pressure to provoke a molecular-sieving type separation, followed by regeneration from the unconstrained MOF after release of the mechanical constraint<sup>14</sup>

Although MOF-based membranes have shown the potential in high-quality performance for gas separation, it has been challenging to fabrication of thin-film MOF membranes such as poor substrate-film interactions, mechanical or thermal stability problems. The crystal growth as well as continuous process of MOF films need to be compromised with their gas selectivity due to the presence of defects in the films. In addition, simpler, cheaper, and high-yield synthesis methods are expected to lead to the preparation of MOF membranes on the large scale. MOF membranes with enhanced stability are required for practical separation conditions, such as high temperature and pressure. Thus, industrial application of MOFs in membranes will occur in composite membrane, where MOFs are used as filler particles in small amounts in polymer matrix.

### 2.2.3 MOFs based mixed-matrix membranes

Mixed-matrix membrane (MMMs, Figure 2.18) attempt to address the issues of MOF membrane by using MOFs as a filler in the polymer matrix, ideally leveraging the facile membrane processability of polymers and the superior transport characteristics of MOFs to form new composite materials. The employment of MOFs in MMMs provides potential advantages over other inorganic fillers: (i) the pore structure and pore size of MOFs can be tailored to specific applications through simply changing the recipe of precursor-metal salts and organic ligands, (ii) generally, MOFs display a better compatibility with the polymeric matrix since the organic linkers in MOFs have a stronger interaction with polymer chains.

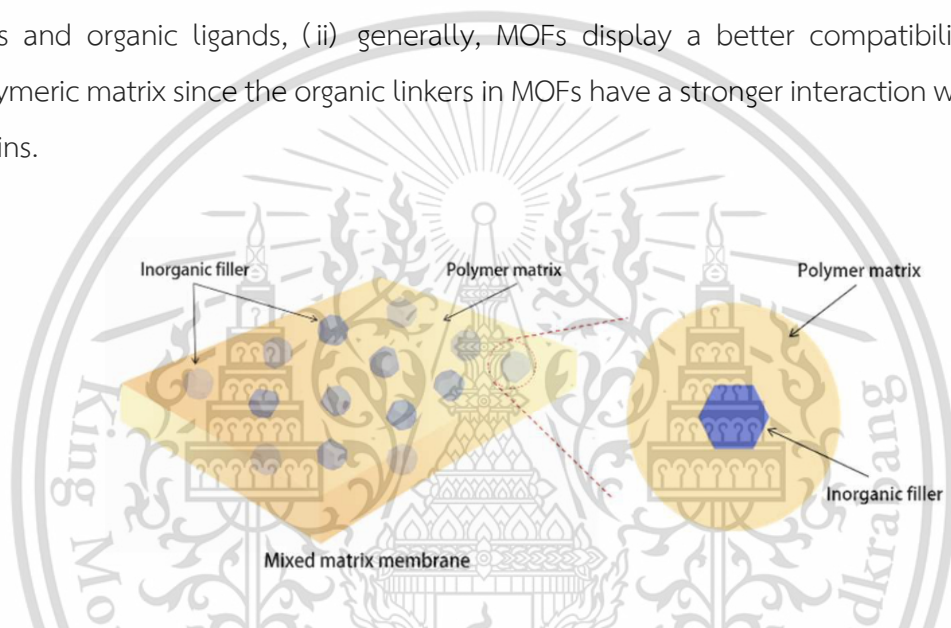


**Figure 2.18** Schematic diagram of mixed matrix membrane

The synthesis of MMMs is analogous to that of normal polymeric membranes, which can be developed to manufacture MMMs in an industrial scale by applying the current technology of polymeric membranes production. There are three main fabrication routes to prepare MMMs at lab scale:

- (i) Dispersion of filler particles into solvent before adding polymer
- (ii) Dissolution of polymer into solvent before the addition of the filler particles to the polymer solution
- (iii) Dissolution of polymer into solvent and dispersion of filler particles into solvent separately, then mix both suspensions

### 2.2.3.1 Challenges in mixed matrix membranes fabrication

#### 2.2.3.1.1 Selection of filler and polymer pair

Pair-wise selection is fundamentally important for MMMs fabrication, which is directly associated with the morphology and separation performance of the MMMs. In a defect-free mixed matrix membrane, the polymer phase determines the minimum separation performance and the filler determines the improvement of the membrane permeability and selectivity. As to the polymer, the free volume and composition of the polymer determine the gas solubility and diffusivity. Concerning the filler, the derived MMM properties are related to the chemical structure, pore geometry, surface chemistry and particle size distribution of the filler. Moreover, apart from all these material intrinsic properties, the membrane's interactions with the gases to separate must be considered. In general, due to their well-patterned pore structure, porous MOFs can serve as molecular sieves that contribute to high selectivity. The surface functionality of the filler (e.g.,  $-\text{NH}_2$ ) may also interact with the targeted gases (e.g.,  $\text{CO}_2$ ), enhancing gas solubility and selectivity in the MMM. An example for amine-functionalized MOF and their amine- $\text{CO}_2$  interactions presents in Figure 2.19.

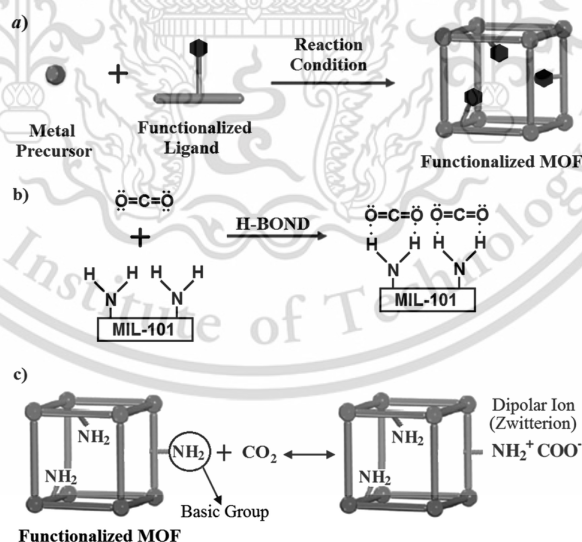


**Figure 2.19** (a) Schematic shape of pre-functionalization, (b) hydrogen bonding between  $\text{CO}_2$  molecule and  $-\text{NH}_2$  functional group and (c) dipolar ion (zwitterion) formation by the acidic  $\text{CO}_2$  and basic  $\text{NH}_2$  groups<sup>15</sup>

Furthermore, the compatibility between the filler phase and the polymeric matrix is of vital importance for the preparation of high performance MMMs. An appropriate approach is to use MOFs that contain organic linkers similar to the functional groups of polymer chains. In common practice, MOFs containing amino groups or surface ammonization can improve the interaction between the filler and the polymer, particularly for specific polymers such as polysulfone and polyamide, as shown in Figure 2.20.

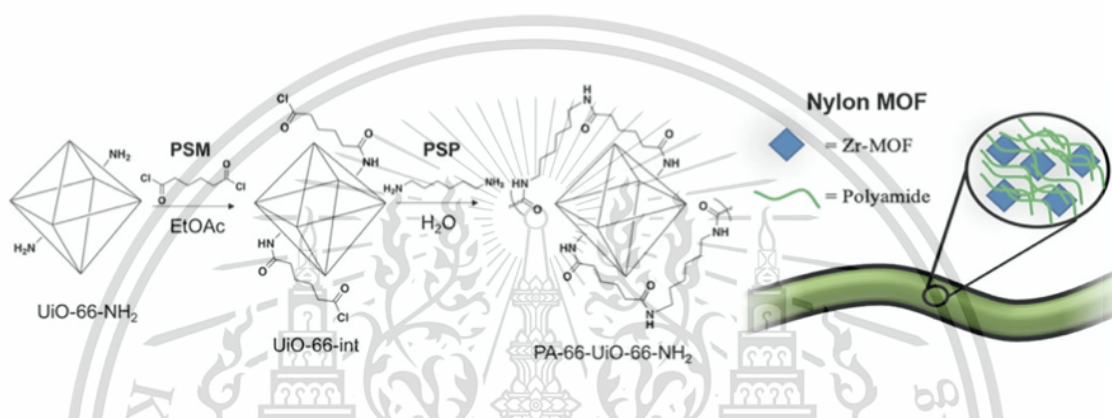


**Figure 2.20** Covalently functionalized -NH<sub>2</sub> group of the MOF, with adipoyl chloride for post-synthetic polymerization of hybrid Nylon-MOF composites<sup>16</sup>

#### 2.2.3.1.2 Filler dispersion

As the improvement in membrane performance is determined by the filler's content and size, an ideal MMM with optimum performance should consist of well-dispersed fillers at their maximum practical loading, and with an excellent filler/polymer contact. However, the aggregation of MOFs particles is difficult to avoid, while increasing the filler particle loading (>10%) due to the strong interaction between particles, or poor interaction between the filler and the polymer, so polymer chains are unable to enwrap all the particles. In addition, the aggregation of filler particles can lead to the formation of non-selective interfacial voids, deteriorating membrane separation efficiency. This circumstance can be more serious when using nano-sized MOFs with larger surface energy. The permeability and selectivity of MMM can increase simultaneously when increasing the size of ZIF-8 nanoparticle.<sup>17</sup> This may be due to the smaller external surface area of larger filler, leading to the lower degree of agglomeration.

### 2.2.3.1.3 Filler/polymer interface morphology

Poor adhesion between filler and polymer leads to the formation of defects at the filler/polymer interface. The organic compounds in MOFs can contribute to a better compatibility with the polymeric matrix compared to that yielded by typical inorganic fillers (e.g., zeolite,  $\text{SiO}_2$ ). However, the MOFs/polymer compatibility can often be overestimated in some cases, which by itself is still not sufficient to eliminate interfacial voids, especially when using micron-sized MOFs. Moreover, the surface organic functional groups (e.g., carboxyl) on MOFs are usually coordinated and not superficially exposed, unless special MOFs/polymer interactions are designed by modifying linkers for MOF synthesis or surface grafting by post-treatment. Poor interface morphology in MMM includes three major types: interfacial voids, rigidification of polymer around the filler particles, and blockage of filler's pores. Figure 2.21 displays schematic representations of interfacial voids (a) and of a rigidified polymer layer (b) at the polymer-particles interface. Low interface adhesion creates non-selective interfacial voids at the filler/polymer interface region, especially for some MMMs with micron-sized MOFs particles. Such voids will act as extra channels that allow non-selective gas transport, thus reducing the selectivity of the whole membrane, this kind of morphological features are known as “sieve-in-a-cage” morphology.

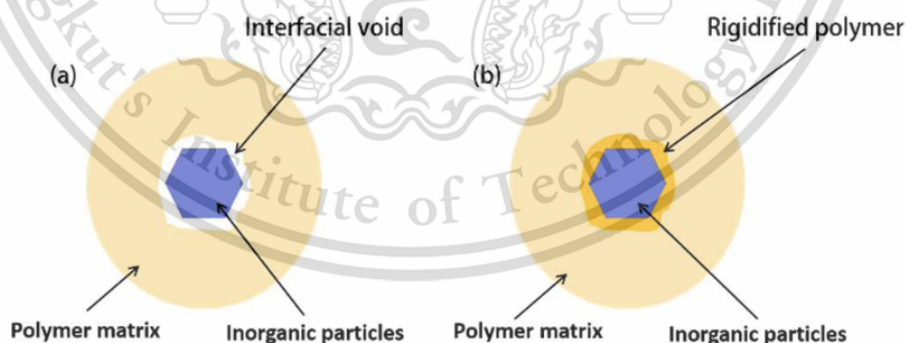


**Figure 2.21** Schematic diagram of interface void (a) and rigidified polymer (b) in MMMs

Rigidification of a polymer layer around the filler is caused by the immobilization of polymer chains at the filler/polymer interface. This phenomenon can also influence the gas transport behavior around the fillers. Although enhancement of the interface

adhesion between the filler and polymer is preferred, it decreases membrane permeability. Some studies found that when using some mesoporous materials as fillers, polymer chains were able to penetrate into the pores of the fillers, resulting in rigidity increase of the polymer matrix and improved filler/polymer contact.<sup>18</sup> Selectivity enhancement were observed in the membranes after incorporation of these mesoporous fillers, which should be corresponding to the chain rigidification and filler/polymer interaction in the MMMs.

In addition, particle pores can be blocked by sorbent, solvent, or polymer chains during the membrane fabrication. Pore blockage of the filler always leads to the decrease of membrane permeability, while its effect on selectivity depends on the pore dimension of the filler in the MMM. However, pore blockage is not always problematic, for the purpose of improving membrane selectivity, pore blockage method can be utilized to tailor the molecular sieving properties of porous fillers by confining a third agent (e.g., ionic liquid) to the pores of the fillers. This agent can act as a cavity occupant for manipulating MOFs' pore size.

#### **2.2.4 Mechanisms of gas transport in membrane materials**

The gas passage across MMM is illustrated in Figure 2.22. In this Figure, the possible mechanism is demonstrated in a defect-free MMM and MMM formed with interfacial defect surrounding the MOFs. Typically, the interfacial defect is associated with filler/polymer incompatibility or surface delamination of polymer chains during membrane fabrication.

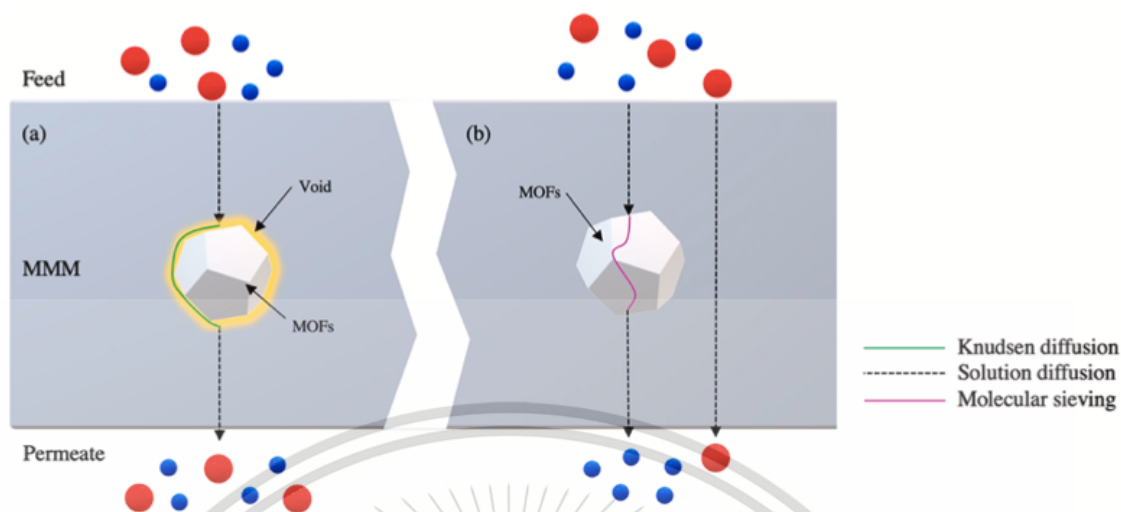


**Figure 2.22** Illustration of gas transport across the membrane layer; (a) MMM with interfacial defect, (b) defect-free MMM

The Knudsen-diffusion mechanism takes place at the interfacial voids. It is apparent that the interfacial void is undesired and reduces the selectivity of the system. In this case, the selectivity of a MMM drops as larger gas molecules can easily permeate through the voids. However, gas transportation through a dense layer membrane mainly relies on the solution-diffusion mechanism even though both the Knudsen diffusion as well as the solution diffusion transport can result in selective transport of gases in MMM, as shown in Figure 2.22a. The solution diffusion mechanism depends on the solubility and diffusivity of gas molecules. The following steps are followed for the gas molecules to move from the feed phase to the permeate;

- i) Sorption gas into the upstream face of the polymer
- ii) Diffusion of the gas through the polymer (along chemical or pressure gradient),
- iii) Desorption from downstream face of the polymer

The affinity of the component in the MMM towards the targeted gas molecules influences to the permeability coefficient. Another mechanism for gas passage in MMM is via size-exclusion (Figure 2.22b) in the presence of MOFs and this process is dependent on the pore dimensions and MOFs/polymer interface, besides the particle's aperture size. The molecular sieving mechanism is rather straight forward in which molecules with larger

kinetic diameters will be prohibited to pass through the particles in the matrix. The filler played a significant part in separating the gas due to its tortuous path, affinity, and adsorption capacity. Theoretically, the brutal way for the gas to travel through the small aperture size resulted in highly selective size-exclusion separation. Synergistics between solubility, diffusivity, affinity as well as size exclusion often being the factor that leads to the excellent separation performance by MOFs based MMM.

## 2.3 MOFs for hydrogen storage

### 2.3.1 MOFs as hydrogen storage

The physisorption mechanism suggests adsorption of molecular hydrogen on a surface via relatively weak van der Waals bonding. Several characteristic features of physisorption can be noted. The adsorption process is fast, i.e. the saturation is achieved within minutes after hydrogen pressure is stabilized, and fully reversible. Hydrogen is released when pressure is lowered and is adsorbed when pressure is increased again. Surface area is the main factor, which controls hydrogen adsorption capacity of the material. The more surface area, which is accessible for adsorbate molecules the more sorbate molecules, will be adsorbed on the adsorbent surface.

MOFs show some advantages as hydrogen adsorbents compared to other porous solids. They exhibited superior hydrogen adsorption properties at cryogenic temperatures (77 K). Combining different organic ligands and ion clusters, it is possible to synthesize MOFs with an almost infinite number of geometrical and chemical variations of the structure (Figure 2.23). Additional hydrogen adsorption sites can be introduced into the structure of MOFs by post-synthetic modifications improving their hydrogen adsorption properties.

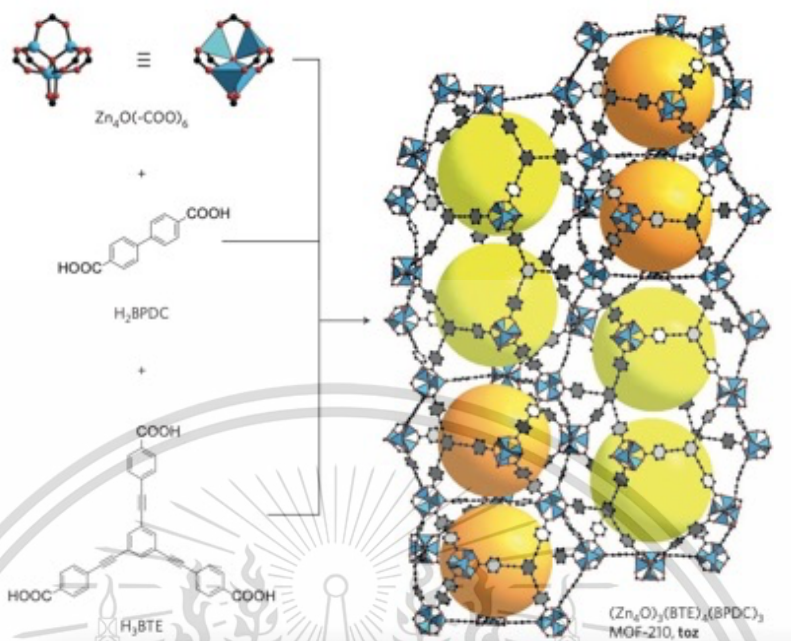


**Figure 2.23** Crystal structure of MOF-210, the spheres represent the largest molecules, which could fit in the pore without touching the Van der Waals surface of the framework atoms

However, at ambient temperatures, hydrogen adsorption in MOFs is relatively low and usually does not exceed 1 wt%.<sup>20</sup> Very strong research efforts have been focused on improving hydrogen storage in MOFs at ambient temperatures, which requires an understanding of the main factors influencing hydrogen adsorption. Some factors are the same as for most other materials where hydrogen is stored due to physisorption while other factors are inherent only for MOFs.

## 2.3.2 Hydrogen adsorption in MOFs

### 2.3.2.1 Hydrogen bonding strength

The most crucial factor is the bonding strength of H<sub>2</sub> molecules to the adsorbent surface, which is proportional to the isosteric heat of adsorption. H<sub>2</sub> molecules interact with the surface of MOFs via the weak Van Der Waals force, which results in low isosteric heat of adsorption in the range of 4-7 kJ/mol.<sup>21</sup> Several recently suggested ideas on how to improve the strength of hydrogen interaction with MOFs are the following:

- (i) reducing pore size
- (ii) introducing unsaturated metal adsorption sites
- (iii) doping MOFs with alkali metals
- (iv) changing organic ligands and metal clusters
- (v) using the hydrogen spillover effect

### 2.3.2.2 Surface area

An important factor influencing hydrogen adsorption in porous materials is surface area. Hydrogen adsorption is higher for MOFs with larger BET surface area (Figure 2.24). The relation between hydrogen uptake and BET surface area in MOFs is almost linear at 77 K and high hydrogen pressures. A similar linear relation between hydrogen uptake and BET surface area of MOFs is also observed at room temperatures, but to observe it MOFs need a proper activation. Such activation procedure is needed to remove solvent molecules and to produce unsaturated open metal sites which are important for hydrogen adsorption at room temperatures.

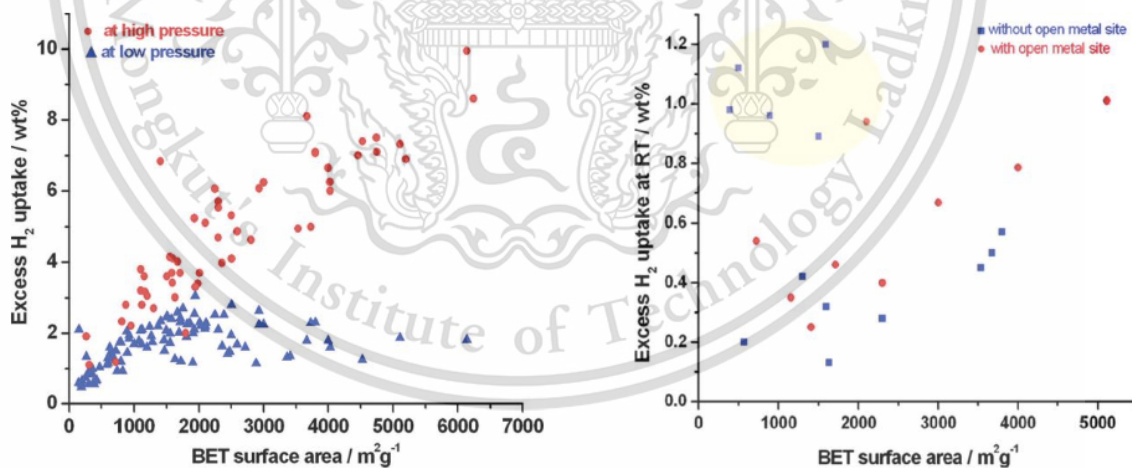


**Figure 2.24** Excess hydrogen uptake in MOFs at 77 K (left figure) and at room temperatures (right figure) plotted versus BET surface area<sup>22</sup>

### 2.3.2.3 Pore volume

Another important factor, which influences hydrogen adsorption is pore volume. Hydrogen adsorption in MOFs correlates with total pore volume though this correlation is more pronounced at 77 K.<sup>23</sup> Theoretical calculations performed for a family of MOFs with the same framework topology and the same surface chemistry but with different pore sizes showed that three different adsorption regimes exist at 77 K. It was found that at low pressure, hydrogen uptake correlates with the heat of adsorption, whereas at intermediate pressure uptake correlates with the surface area. For the highest pressures uptake correlates with pore volume.<sup>24</sup> A good example of how different factors determine hydrogen adsorption in different pressure ranges can be seen in Figure 2.25.

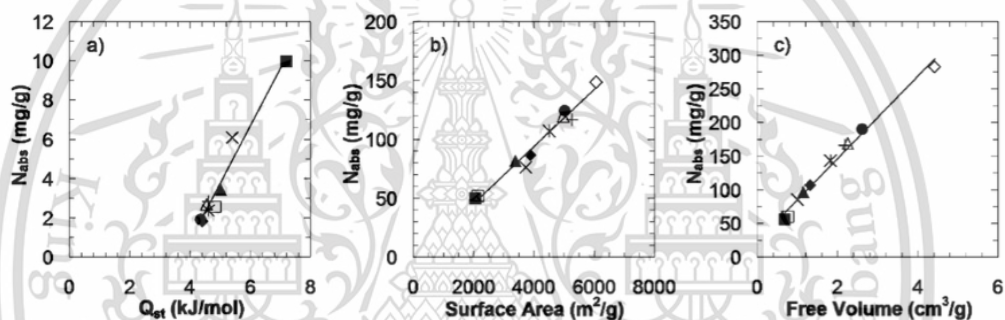


**Figure 2.25** Theoretical values of hydrogen uptake calculated for different MOFs: a) at 0.1 bar plotted versus isosteric heat of adsorption, b) at 30 bar plotted versus accessible surface area and c) at 120 bar plotted versus pore volume

### 2.3.2.4 Pore geometry

The shape and size of pores are also crucial for hydrogen adsorption. Due to the overlap of the potential fields from both sides of the pore walls and small pores should have higher affinity towards hydrogen and thus higher hydrogen uptake capacity comparing to pores with larger diameter. This theoretical assumption was confirmed by experimental results, using thermal desorption measurements. As reported by Panella et al. showed that hydrogen desorption from MOFs with smaller pore sizes, used the temperature higher than from MOFs with larger pore sizes.<sup>25</sup> There are few possible methods to reduce pore sizes in MOFs. One method is to introduce bulky groups into

organic ligands. Another method is catenation, or penetration, of two or more identical frameworks.<sup>26</sup> This technique was proven to work at low pressure and 77 K. However, the GCMC simulations predicted that it would not work at high pressures due to a reduced free volume.<sup>27</sup> Moreover, an impregnation of MOFs with organic molecules such as fullerene C<sub>60</sub>, free volume within pores can be reduced and additional hydrogen adsorption sites can be introduced inside the framework (Figure 2.26).<sup>28</sup>

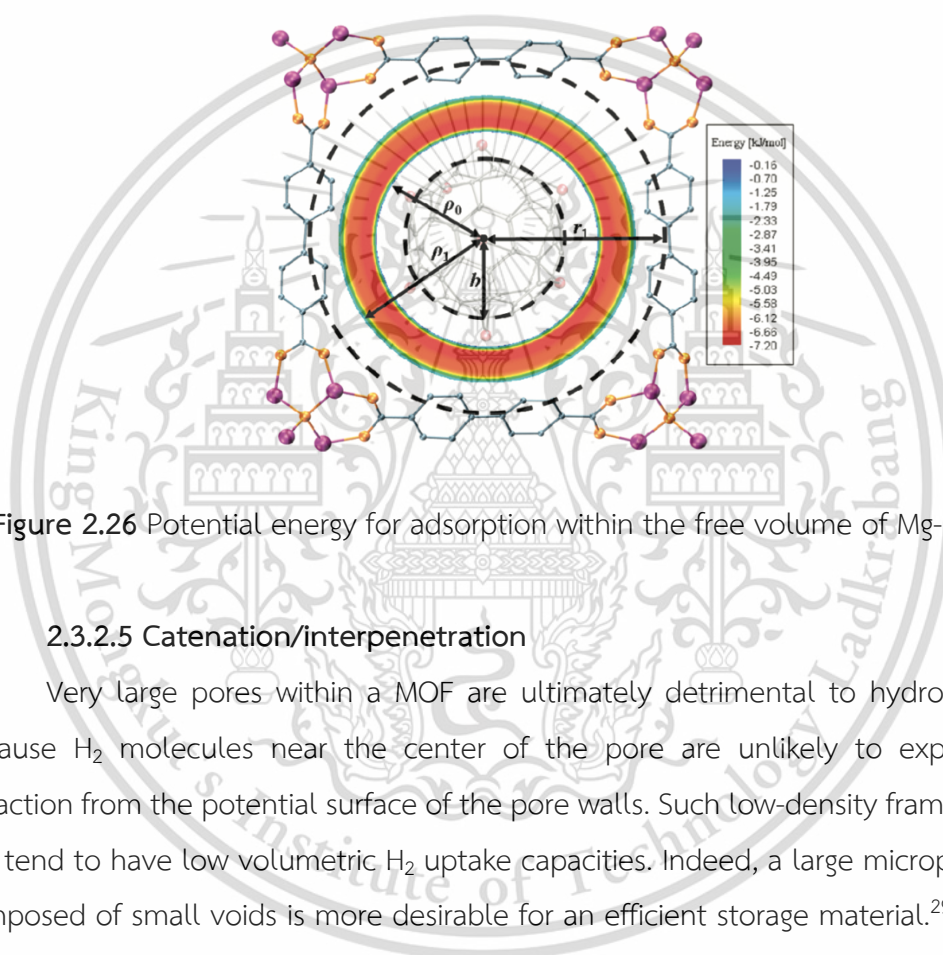
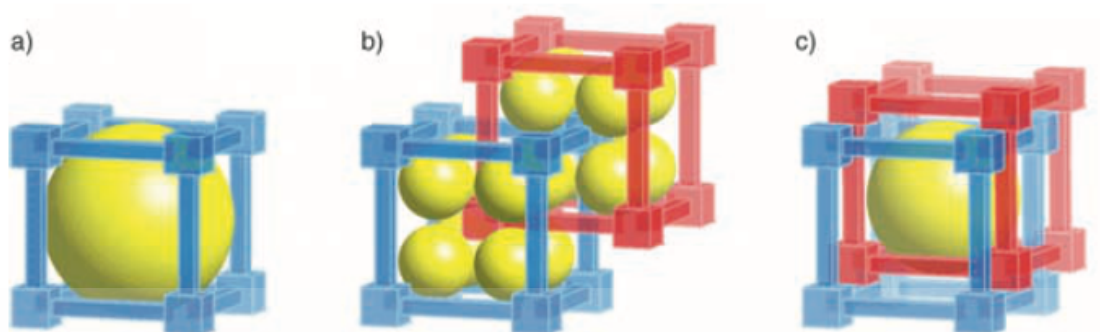


Figure 2.26 Potential energy for adsorption within the free volume of Mg-C<sub>60</sub>@MOF

### 2.3.2.5 Catenation/interpenetration

Very large pores within a MOF are ultimately detrimental to hydrogen storage, because H<sub>2</sub> molecules near the center of the pore are unlikely to experience any attraction from the potential surface of the pore walls. Such low-density framework solids will tend to have low volumetric H<sub>2</sub> uptake capacities. Indeed, a large micropore volume composed of small voids is more desirable for an efficient storage material.<sup>29</sup> Framework catenation has long been interest in MOF research. The intergrowth of two or more frameworks is allowed for many high-symmetry, default topologies and is often observed when long linkers are used. Catenation can take the form of interpenetration, where the frameworks are maximally displaced from each other, where they are minimally displaced and exhibit many close contacts. The most immediate consequence of catenation is a reduction of the free volume of the pores (Figure 2.27). Therefore, it is a viable strategy for improving hydrogen uptake.



**Figure 2.27** Schematic representation of the repeat unit of (a) single-framework MOF, catenation of two identical frameworks can be used to restrict the volume of the pore considerably by (b) interpenetration or to a lesser extent by (c) interweaving<sup>26</sup>

### 2.3.3 MOFs supported inorganic hydride

As hydrogen storage capacity of MOFs are found to decrease drastically near room temperature because of their weak interaction with  $H_2$  molecules, which results in low adsorption energy values not enough to meet the application requirements. To increase the interaction between adsorbed  $H_2$  molecules and a host material, the functionalization of host material by incorporating functional groups in the host material or by metal decoration of host materials are being explored. Several studies use the MOFs as a supported catalyst for hydrogen generation from chemical hydrides or hydrogen carriers. Reducing the size of metal hydrides to the nanometer range enables fast kinetics for both hydrogen release and subsequent uptake. Nanoscaling can also alter desorption thermodynamics by eliminating intermediate reaction steps, whereas surfaces and interfaces can also alter reaction pathways relative to bulk and enable reversibility. The strong interaction between unsaturated metal sites of MOFs and inorganic hydride also reported by Yu et al.<sup>30</sup> who used copper-based MOF as HKUST-1 to load lithium borohydride ( $LiBH_4$ ). The first dehydrogenation event of activated  $LiBH_4@HKUST-1$  occurred at 60 °C, much lower than that of pristine  $LiBH_4$  (380 °C). The direct interaction of the borohydride with the MOF copper unsaturated sites is invoked to explain this catalytic effect (Figure 2.28). No diborane by-product is formed during the borohydride

dehydrogenation, although no evidence of any B-containing by-product or of a clear decomposition mechanism was provided that the high catalytic activity of HKUST-1 is due to the interaction between  $\text{LiBH}_4$  and the Cu–O bonds in the MOF.

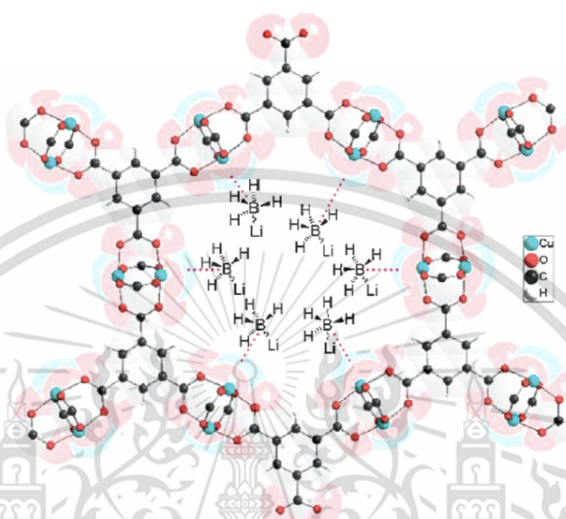


Figure 2.28 Proposed interaction of  $\text{LiBH}_4$  with the exposed Cu(II) sites in HKUST-1

## 2.4 MOFs for catalysis

MOFs have many properties that commend them as catalysts. Several features make MOFs as an excellent candidates for heterogeneous catalysts: (i) an unprecedented structural diversity, (ii) the intrinsic hybrid organic–inorganic nature, (iii) the presence of uncoordinated metal sites and readily accessible organic struts, (iv) the potential for rational design, and (v) a well-defined porosity. Several structural features of MOFs can be harvested for catalytic applications, as depicted in Figure 2.29.

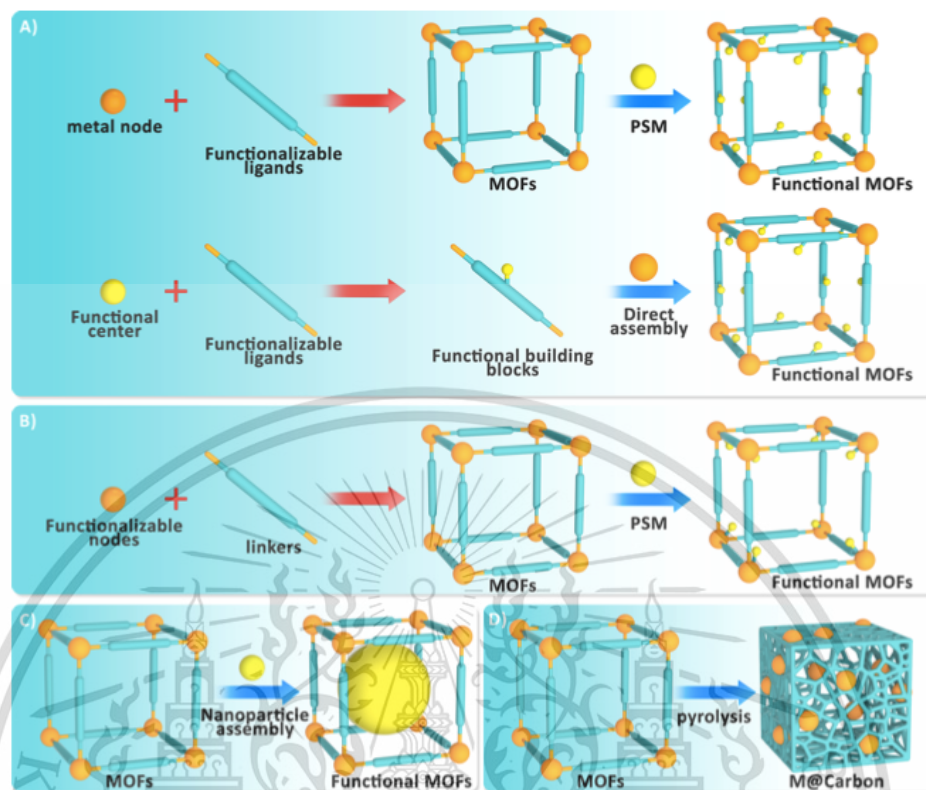


Figure 2.29 Assembly of (a) a functional MOF with catalytically active sites by direct assembly or post-synthetic modification (PSM) of a linker, (b) or a metal node, (c) nanoparticle encapsulation, or (d) MOF utilization as a carbon support<sup>28</sup>

#### 2.4.1 MOFs with intrinsic catalytic activity

MOFs have been proposed as ideal platforms for the heterogenization of homogeneous catalysts. MOFs can be understood as molecules arranged in a crystalline lattice, and as such, through crystal engineering, a given homogeneous catalyst could be extended through such a crystalline lattice, leading to solids with intrinsic catalytic activity. In this regard, many MOFs can be used as single-site catalysts. Mostly three different approaches have been proposed to achieve intrinsic catalytic activity (i) through the introduction of open metal sites (coordinationally unsaturated sites), (ii) through the creation of defects, and (iii) by using the organic linker as a catalyst or using it direct or indirect (post-synthetic modification) incorporation of such sites.

### 2.4.1.1 Catalysis on open metal sites and nondecorated frameworks

The earliest reports about catalytic activity of MOFs are those where the active site is an intrinsic part of the framework. For instance, mixed-valence open metal sites (OMSs) of MIL-100(Fe) for  $\text{Fe}^{2+}/\text{Fe}^{3+}$  as a catalyst were used for the aza-Michael addition of various amines with  $\alpha,\beta$ -unsaturated compounds (Figure 2.30).<sup>31</sup> The OMSs of MIL-100(Fe) were obtained by treatment under vacuum at 250 °C. It was found that the OMS-MIL-100(Fe) showed product yields up to 93% in the absence of any additive. In addition, the catalyst was recycled with no apparent loss of activity. The MIL-100(Fe), evacuated at different temperatures, was also used as a catalyst for selective ethylene tetramerization.<sup>32</sup> Depending on the evacuation temperature, both the surface area and the content of coordinatively unsaturated sites changed. They were found to be the main factors affecting the oligomerization performance. When evacuated at 250 °C, MIL-100(Fe), with an intact pore structure and high concentration of  $\text{Fe}^{2+}$  sites, reached the maximal catalytic activity of  $1.26 \times 10^5$  g/mol $_{\text{Fe}}$ ·h, and more than 80% of the products were branched and ringed  $\text{C}_8$  alkanes. The alkylaluminum (e.g.  $\text{Et}_2\text{AlCl}$ ) co-catalysts presented a clear influence on the oligomerization performance, not only via scavenging but also by creating additional open metal sites nearby.

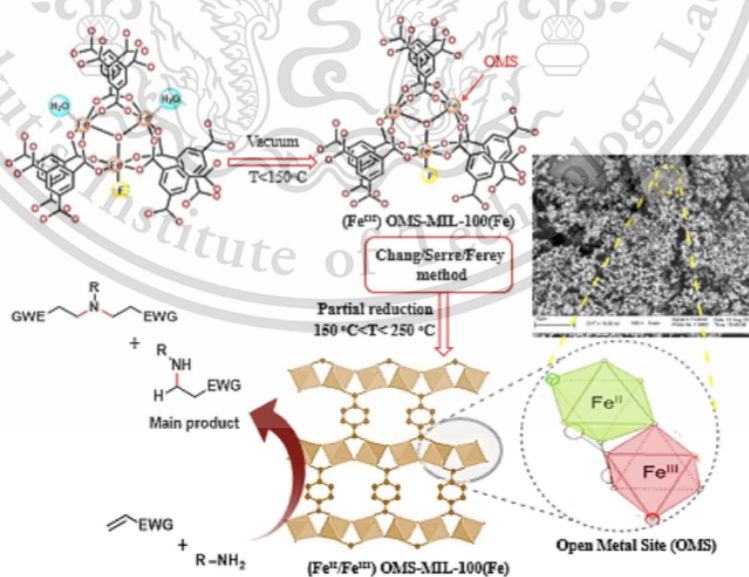


**Figure 2.30** Open metal sites generation of MIL-100(Fe) for the aza-Michael reaction

### 2.4.1.2 Catalysis on defects in MOFs

Defects in MOFs arise from the removal of either a linker, a cluster, or a coordinated solvent (e.g. water) molecule, which leads to nonstoichiometric metal to linker ratios. Missing linkers are often seen being compensated by formates, oxygen, hydroxyl groups, water, and/or chloride; however, due to the nonperiodicity of defects, comprehensive structural information is difficult to achieve, and molecular simulations play a key role in better understanding the nature of these catalytic sites. In case of UiO-66, the catalytic activity can be drastically increased by the introduction of defects. Since such defects have a significant impact on the porosity, mechanical properties, and Lewis and Bronsted acidities. Further, the additional coordinatively unsaturated Zr ions in the UiO-66 also created the presence of defects that leads to increase their Lewis acidity. This feature has largely been deployed on the synthesis of a robust TEMPO-radical-functionalized UiO-68-TEMPO with varied missing linker defects (Figure 2.31).<sup>33</sup> It revealed that a synergistic effect between the TEMPO radicals and hydrophilic defective Zr nodes affected the catalytic activity of UiO-68-TEMPO in aerobic oxidation of benzyl alcohol. The missing linker defects were controlled by using different amounts of a benzoic acid modulator. A higher benzoic acid concentration resulted in a single-crystalline UiO-68-TEMPO with fewer defects. Whereas a lower benzoic acid concentration led to highly defective microcrystals, resulting in higher catalytic activity.

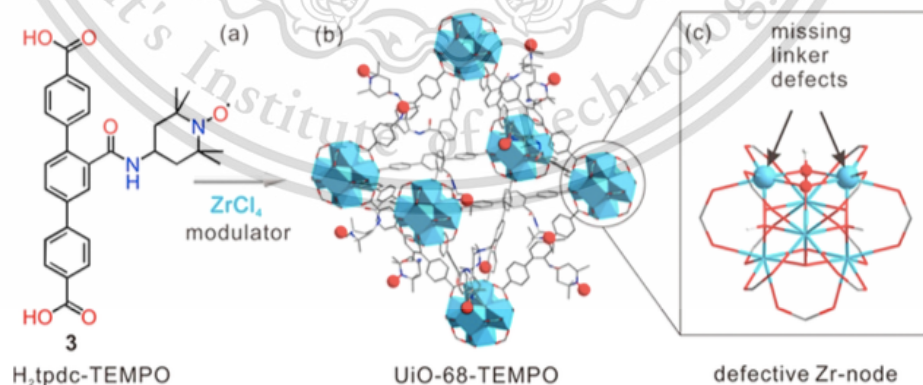


**Figure 2.31** (a) Chemical structure of H<sub>2</sub>tpdc-TEMPO, (b) X-ray crystallographic structure of UiO-68-TEMPO and (c) Zr-node contains one missing linker defect

### 2.4.1.3 Catalysis on decorated MOFs

In addition to the use of pristine and defective MOFs as catalysts, considerable efforts have been dedicated to the post-synthetic modification of these materials for catalytic applications. A multivariate MOF is a framework that contains two or more different functionalities. This can be achieved via mixed-linker one-pot synthesis or by post-synthetic modification. For example, LIFM-80 associated in the dynamic installation and uninstallation of functional secondary and ternary ligands in the primitive LIFM-28 as well as in metal-chelation and covalent-post modification processes (Figure 2.32).<sup>34</sup> Multiple active catalytic systems for oxidation, Knoevenagel condensation, click chemistry, and other reactions were obtained.

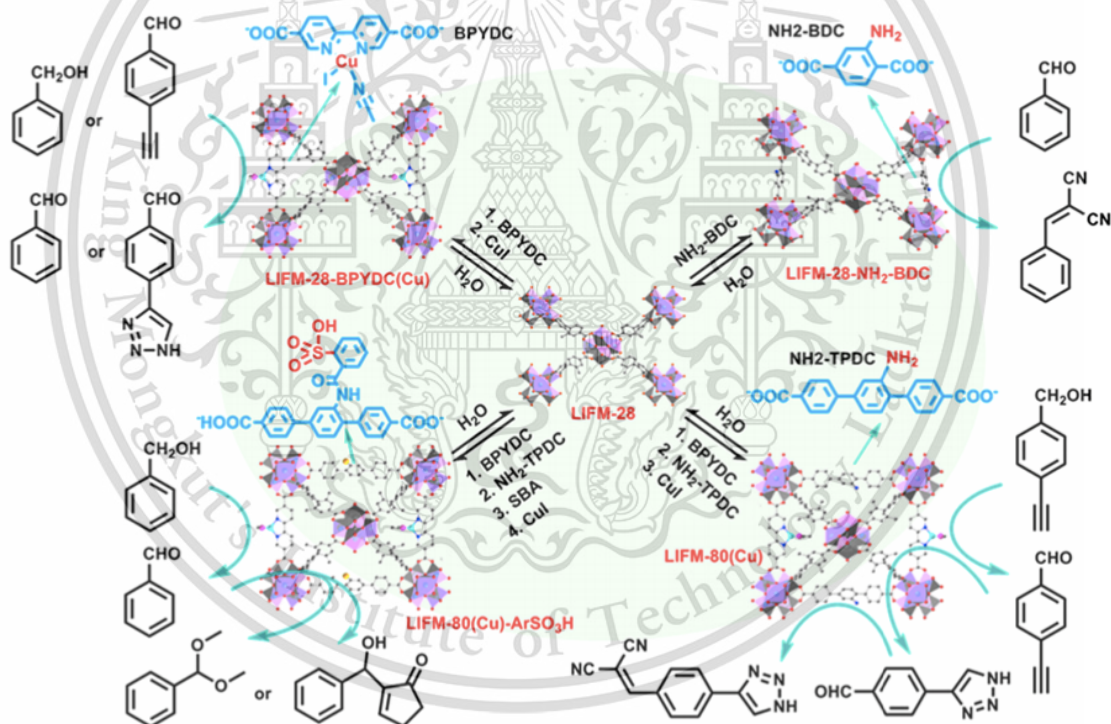


**Figure 2.32** Generation of multivariate MOF catalysts via the dynamic spacer installation approach using proto-LIFM-28 and the resultant interconversions for different catalytic purposes

## 2.4.2 MOFs as supports for metal nanoparticles

Metal nanoparticles (MNPs) are among the most important catalytic sites. A large number of relevant industrial processes rely on the use of MNPs. Special interest for using MOFs as supported MNPs in which catalytic performance in terms of selectivity is highly related with the size of the MNPs employed. The objective of the catalyst engineer is to achieve a particle size distribution close to that of the optimal particle size for the reaction, so that both activity and selectivity are maximized. Catalytic centers of MOFs are either metal ions, which can act as Lewis acids, and/or organic linkers. Both of these centers can be tuned or modified, e.g., dangling functional groups (such as  $-\text{NH}_2$ ,  $-\text{SH}$ ,  $-\text{SO}_3\text{H}$ ,  $-\text{OH}$ , etc.) on the linkers that can improve metal-support interactions. MOFs play different roles in these metal MNP/MOFs composites: they (i) stabilize MNPs within pores and control the uniform small particle size and distribution, (ii) assist in the selectivity of the reaction, e.g., by sieving small substrate molecules and/or blocking oversized molecules from catalytic interactions, (iii) alter the electronic properties of MNPs by controlling their electronic density and the electron charge transfer between the MOF and an MNP and (iv) catalyze one-pot tandem reactions in which both the MOF and MNPs act as separate active sites in their respective reactions.

### 2.4.2.1 Metal nanoparticles/MOF preparation

Assembling the active species within the pores of a preformed support is known as “ship in bottle” synthesis. This approach is supposed to prevent MNPs from aggregation and to limit their growth to the pore size of the host material. However, the task remains challenging due to many factors, such as the wettability of the internal MOF surface, the interactions between the metal precursor and pore environment, the thermal, chemical, and mechanical stabilities of the framework.

#### - Chemical vapor deposition

Usually, an activated MOF is placed together with a volatile metal precursor in the same vial under vacuum. During the evacuation, the metal precursor diffuses into the MOF channels but also remains on the external surface. After the subsequent reduction or thermal treatment, the precursor turns into nanoparticles. For instance, the preparation of ZIF-8 thin films via chemical vapor deposition (CVD) method presents in Figure 2.33.<sup>35</sup>

With this method, the particle size distribution fluctuates largely when such a protocol is employed. Currently, this method is rarely used for catalysis. Although this method allows for the synthesis of very small particles within MOFs, it requires a synthesis incorporating expensive and volatile complexes and high precision during the impregnation process to avoid MNP agglomeration on the external surface of the support.

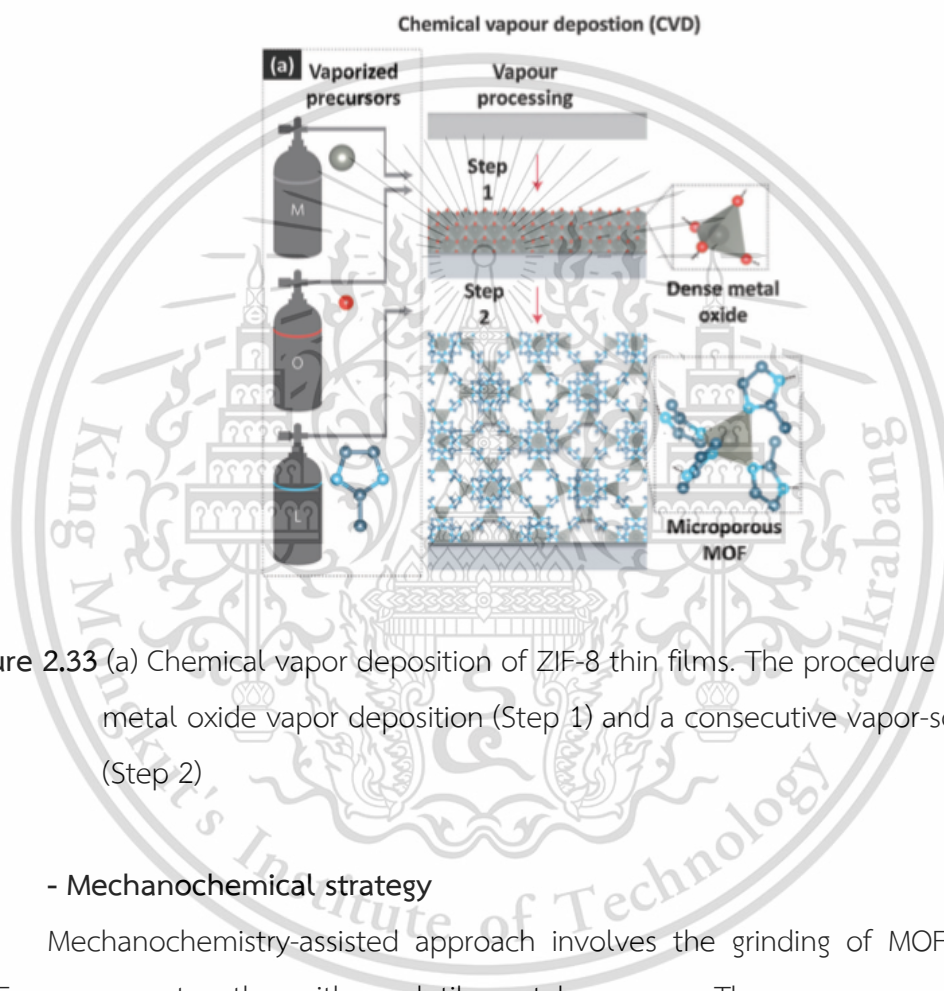


**Figure 2.33** (a) Chemical vapor deposition of ZIF-8 thin films. The procedure consists of a metal oxide vapor deposition (Step 1) and a consecutive vapor-solid reaction (Step 2)

#### - Mechanochemical strategy

Mechanochemistry-assisted approach involves the grinding of MOF powder or MOFs precursors together with a volatile metal precursor. The precursor penetrates into MOF channels and undergoes the subsequent reduction that leads to the formation of the composite material. The MNPs@ZIF-8 formation by this method showed in Figure 2.34.<sup>36</sup> The restrictions for this method are the same as those for CVD: the precursors are expensive and should be volatile, and the formation of nanoparticles on the external surface of the MOF is unavoidable.

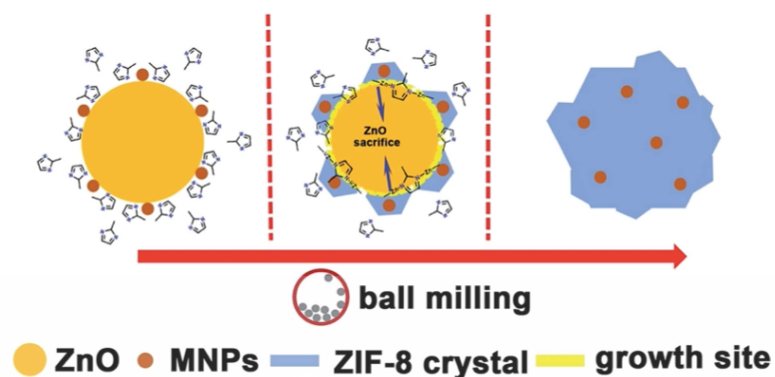


Figure 2.34 Encapsulation of MNPs into ZIF-8 via the mechanochemical strategy

#### - Solution impregnation

The solution impregnation method is based on dispersing and mixing a MOF powder with dissolved metal precursors as shown in Figure 2.35. The MOF pores become filled with the metal precursor solution because of the capillary effect. The reduction step of the precursor is required to form MNPs. The main disadvantage of this method is the lack of precursor location control, therefore the poor particle distribution on both the interior and exterior surfaces of MOFs.

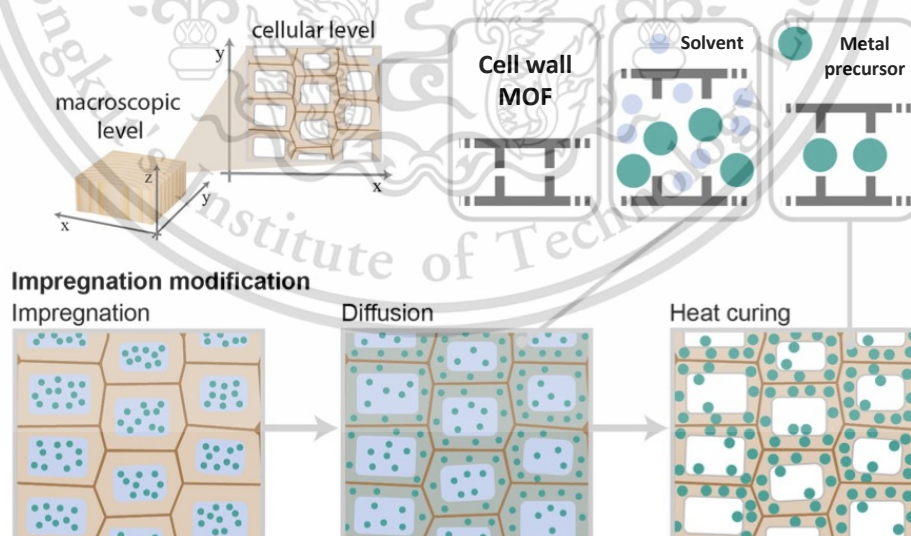


Figure 2.35 Schematic illustration of the different process steps during solution impregnation

### - Double solvent approach

The double solvent approach is a rational way for the synthesis of MNP@MOF composites. This method allows the conducting of the precise deposition of NPs on the internal surface of the pores. The driving force is the capillary effect, which limits the deposition of metal salts onto the outer space of frameworks. The double-solvent include the hydrophilic solvent (water) and the hydrophobic solvent (n-hexane). Usually, MOF powder is dispersed in a hydrophobic solvent. Subsequently, a small amount of the aqueous solution of the metal precursor salt is added to a vigorously stirred dispersion. It can be absorbed by the hydrophilic pores of MOF. After the reduction process, the small metal clusters are encapsulated within the MOF matrix (Figure 2.36).

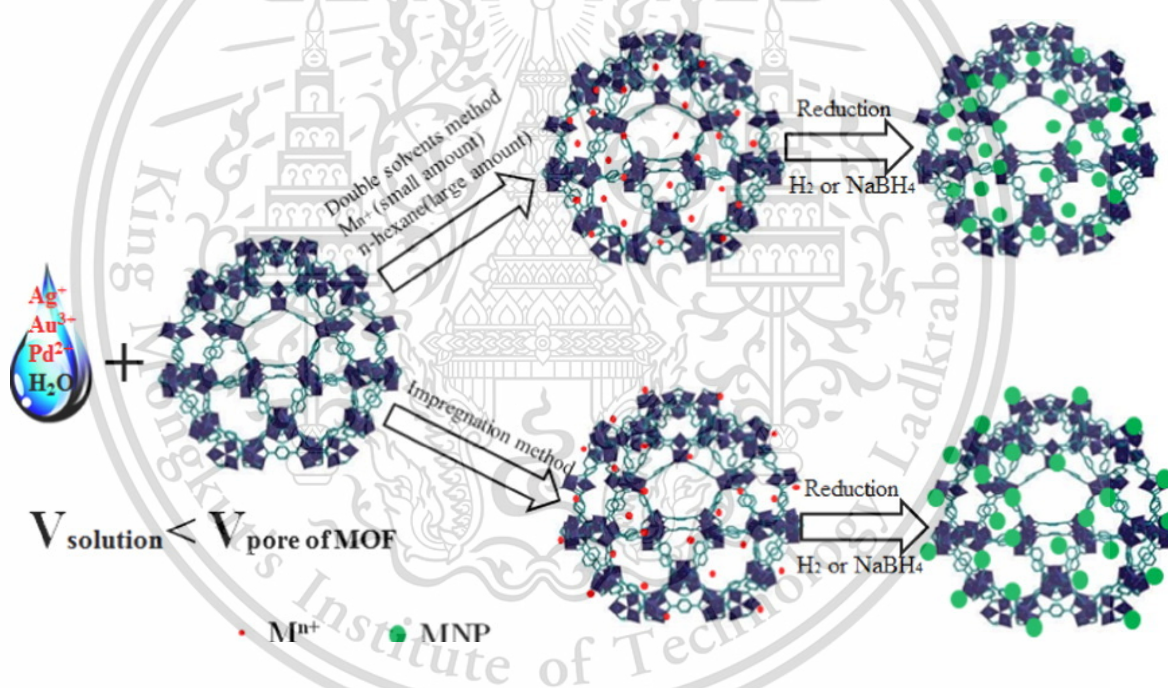


Figure 2.36 Schematic representation of the synthesis of MNP@MOF using the double solvent method<sup>37</sup>

## 2.5 Overview of the thesis

**Chapter 3**, MOF synthesis (MIL-101(Cr) and HKUST-1) and post-synthetic modification (e.g., organic compound grafting and metal incorporation) as well as characterization approaches were imparted. Experimental setting up and parameter for catalytic testing over those modified MOFs were explained.

Improving H<sub>2</sub>/CO<sub>2</sub> separation of polymer membrane by incorporating with HKUST-1 was mentioned in **Chapter 4**. The polymer matrixes such as high impact polystyrene (HIPS) and ethylene vinylacetate copolymer (EVA) were used for studying the effect of polymer on gas permeability. The HKUST-1 was used as filler for HKUST-1/polymer mixed matrix membrane. The effect of HKUST-1 loading on gas permeability and H<sub>2</sub>/CO<sub>2</sub> separation were inspected.

Attempts to introduce hydrogen storage function, through the grafting of acetylpyridine (AcP) into MIL-101(Cr) and subsequent loading of Pd, for chemical hydrogen storage at atmospheric pressure, was discussed in **Chapter 5**. The existence of AcP and Pd NPs in AcP-Pd-MIL-101(Cr) was studied by spectroscopic techniques. The hydrogenation–dehydrogenation of AcP-Pd-MIL-101(Cr) was evaluated over H<sub>2</sub>-TPRe, and the hydrogenated and dehydrogenated forms of AcP were addressed by *in situ* FTIR and <sup>1</sup>H NMR spectra. The effects of Pd content, operating temperature, hydrogen partial pressure for the hydrogenation–dehydrogenation cycle and hydrogen storage stability were investigated.

In addition, the stabilization of robust Pd<sup>2+</sup> species in MIL-101(Cr), contained ethylenediamine as an anchoring ligand was addressed in **Chapter 6**. The introduction of Pd<sup>2+</sup> species in the ethylenediamine-grafted MIL-101(Cr) carried out using double solvent approach to ensure the Pd<sup>2+</sup> dispersion in the MIL-101(Cr) framework. The interactions of ethylenediamine with both Cr<sup>3+</sup> nodes in MIL-101(Cr) and the incorporated Pd<sup>2+</sup>, were examined by various spectroscopic methods at high temperatures. The stability of Pd<sup>2+</sup> species under reducing conditions was studied by *in situ* XANES. In addition, activity for the Pd<sup>2+</sup> species within ethylenediamine grafted MIL 101(Cr) was tested by styrene oxidation. The effect of ethylenediamine: Pd<sup>2+</sup> molar ratios on the catalytic activity, stability and recyclability were examined.

The design and testing of developed MOFs were summarized in *Chapter 7*. The suggestions were also given for further development.

## 2.6 Literature review

### MOFs for gas separation

Guo H. et al<sup>38</sup> synthesized a thin HKUST-1 film via secondary-growth method. An oxide copper net was used as support to provide homogeneous nucleation sites for continuous HKUST-1 film growth. The copper net supported HKUST-1 membrane was fixed in a gas separation setup for separation studies of H<sub>2</sub>/CO<sub>2</sub>, H<sub>2</sub>/N<sub>2</sub>, and H<sub>2</sub>/CH<sub>4</sub> mixtures. It was found that the permeation flux of H<sub>2</sub> ( $2.2 \times 10^{-3} \text{ cm}^3/\text{m}^2\cdot\text{s}$ ) is much higher than those of other gases in the mixture systems, indicating that the membrane has a higher size selectivity preference for H<sub>2</sub>. In another word, it can be explained that the small H<sub>2</sub> molecule goes through the HKUST-1 membrane more easily than the strong adsorbing sorbates (CO<sub>2</sub>, N<sub>2</sub>, and CH<sub>4</sub>). The sorption capacity for CO<sub>2</sub>, CH<sub>4</sub>, and N<sub>2</sub> over HKUST-1 is much higher than that of H<sub>2</sub>. This is correlated to the structural and chemical features of the HKUST-1 favoring stronger interactions of CO<sub>2</sub>, CH<sub>4</sub>, and N<sub>2</sub>.

Kang Z. et al<sup>39</sup> prepared ultra-thin and flexible HKUST-1/graphene oxide (GO) intercalated membranes for studying separation of H<sub>2</sub>/CO<sub>2</sub> at near-atmospheric pressure. The GO plays a role of flexible matrix, and is sealed in the intergaps between the HKUST-1 crystals, to overcome solvothermal synthesis and interfacial defects of polycrystalline membrane. Whereas HKUST-1 acts as microporous fillers with uniform microporosity to improve the gas separation performance. CuO nanosheets/GO membranes are fabricated with layer-by-layer via repeated filtration cycles, then transformed to HKUST-1/GO membranes upon *in situ* reaction with linkers. The gas separation properties of the HKUST-1/GO membranes showed that after the doping of HKUST-1, heat of adsorption for CO<sub>2</sub> of HKUST-1/GO was improved due to the affinity between the Cu<sup>2+</sup> sites of HKUST-1 and CO<sub>2</sub>. These properties significantly enhanced performance for separation of H<sub>2</sub>/CO<sub>2</sub> mixtures. However, large layer gap between GO was found due to uneven distribution of HKUST-1 crystals, which leads to higher permeance and low selectivity. Thus, the membrane with more layer was required to achieve higher selectivity due to fewer defects

in the thicker membranes, even though the thicker membranes may result in lower H<sub>2</sub> permeance. After optimization, The HKUST-1/GO MMM can reach 73.2 of H<sub>2</sub>/CO<sub>2</sub> selectivity and achieve  $5.77 \times 10^{-7}$  mol/m<sup>2</sup>.s.Pa of H<sub>2</sub> permeance. The stability of separation performance was obtained up to 120 h without noticeable performance loss. Although a slight decline in H<sub>2</sub>/CO<sub>2</sub> selectivity was noted after bending and recovery, a similar H<sub>2</sub> permeance was obtained, which proves the flexibility of the composite membrane.

Lin R. et al<sup>40</sup> studied the effect of ionic liquid on an increase interfacial affinity between MOF filler and polymer for efficient membrane separation. The IL acts as the MOFs/polymer interfacial binder to enhance the adhesion between micron-sized HKUST-1 and polymer by taking advantage of the favorable MOF/IL and IL/ polymer interaction. Thin layer of 1-ethyl-3-methylimidazolium bis(trifluoromethylsulfonyl)imide (Emim[Tf<sub>2</sub>N] as IL) was immobilized on HKUST-1, then incorporated into 4,4'-(hexafluoroisopropylidene)-diphthalic anhydride-2,3,5,6-tetramethyl-1,3-phenyldiamine (6FDA-Durene) to fabricate HKUST-IL MMM. It was found that the sieve in a cage morphology of HKUST-IL in MMM was much less as compared to untreated HKUST-1, indicating excellent adhesion of HKUST-IL with the polymer. The volume fraction of filler, polymer, and voids calculated by image analysis showed that with the incorporation of IL, over 90 vol % interfacial void in derived MMM was eliminated with comparison to the MMM with untreated HKUST-1. This led to an improvement in selectivity for CO<sub>2</sub>/N<sub>2</sub> (27.1) and CO<sub>2</sub>/CH<sub>4</sub> (29.3) with a high CO<sub>2</sub> permeability of 1101.6 barrer.

Wang Y. et al<sup>41</sup> studied the effect of capping agent on HKUST-1/polyetherimide (PEI) MMM on the improvement of adsorption-diffusion of small gas molecule in the MMM. HKUST-1 nanocrystals were prepared with the addition of a capping agent (sodium formate) to control the average crystal size (~63 μm as seen by SEM) by regulating the overall rate of crystal growth, thereby allowing more nuclei to be formed and to prevent the agglomeration of HKUST-1 nanocrystals upon casting the HKUST-1/polymer suspension. The SEM images and EDS mapping of the cross-section of the HKUST-1/PEI membrane confirmed the homogeneous crystals dispersion with no obvious or major defects on the surface of the MMM. This also corresponded to the FTIR and XPS results showing that the Cu<sup>2+</sup> metal sites interact with the C=O of PEI polymer via electrostatic

interaction, thereby enhancing the interaction between PEI and HKUST-1. This leads to an improvement of H<sub>2</sub>/CO<sub>2</sub> separation. The PEI membrane loaded with 30 wt% HKUST-1 nanocrystals showed a high H<sub>2</sub> permeability (193.3 Barrer at 25 °C under 1.5 bar) with good H<sub>2</sub>/CO<sub>2</sub> selectivity factor of 20.6 in a single gas testing. This can be rationalized by the HKUST-1 embedded in PEI, which provides faster and low diffusion resistance through-pore channels for small and non-polar H<sub>2</sub> molecules. In addition, the presence of Cu metal sites ensures a strong adsorption effect and a slow desorption of CO<sub>2</sub> in MOFs' channels, ultimately controlling their transport properties.

### MOFs for hydrogen storage

Dong Y. et al<sup>42</sup> studied a catalytic hydrogenation and dehydrogenation of N-ethylindole (NEID), as liquid organic hydrogen carrier (LOHCs). The Hydrogenation of NEID was achieved over a 5 %w/w Ru/Al<sub>2</sub>O<sub>3</sub> catalyst in the temperature range of 160 – 190 °C at 9 MPa. The reaction results revealed that reaction rate strongly influenced by temperature. The consumption of NEID was found to follow first-order kinetics with an apparent activation energy of 62.4 kJ/mol. The process was found to undergo in sequential steps of NEID, 2H-NEID, 4H-NEID and 8H-NEID with rapid consumption of all intermediate species. Fully hydrogenated NEID (5.23 wt% hydrogen uptake) can be achieved at 190 °C within 80 min. The reverse process (hydrogen liberation), dehydrogenation of 8H-NEID was subsequently measured over 5 wt% Pd/Al<sub>2</sub>O<sub>3</sub> catalyst in the temperature range of 160 – 190 °C at 0.1 MPa. It was found that 8H-NEID was consumed quickly to form 4H-NEID and NEID upon the initiation of dehydrogenation. The 4H-NEID intermediate appeared to be kinetically stable and requires elevated temperatures to liberate hydrogen. Although full dehydrogenation could not be achieved, over 96% dehydrogenation was reached within 4 h with given the apparent activation energy of 8H-NEID dehydrogenation of 117.7 kJ/mol. In addition, the hydrogen gas produced in the dehydrogenation process was found to be of high purity, which is promising to apply this LOHC in a PEM fuel cell device.

Qin W. et al,<sup>43</sup> used MIL-101(Cr) doped with Pd NPs by sol-gel method for studying their hydrogen storage capability. The loaded Pd on MIL-101(Cr) at 1, 3, 5 wt%, provided the Pd particle size of 2.4, 2.9 and 5.8 nm, respectively, implying that higher Pd loading

tended to form agglomeration and larger-size particles. The hydrogen storage studies indicated that the presence of Pd NPs for Pd/MIL-101(Cr) sample could enhance the hydrogen storage capacities by a factor of 1.5–2.3 compared with that of the parent MIL-101. The maximum hydrogen uptake of 0.64 wt% at 7.3 MPa of H<sub>2</sub> pressure and 25 °C, was obtained over the 3 wt% Pd/MIL-101. This could attribute to spillover of atomic hydrogen from Pd particles to MIL-101(Cr) framework. However, a further increase of Pd content to 5 wt% remarkably reduced the hydrogen uptakes. This reduction in hydrogen capacity could be related to a decrease metal dispersion because of Pd metal aggregation at high Pd loading. Hence, high dispersion and small sizes of Pd particles on the MIL-101 were crucial factors for enhancing the hydrogen storage capacity.

Ding C. et al<sup>44</sup> prepared highly dispersed Pd NPs immobilized in MIL-101(Cr) for catalytic dehydrogenation of LOHC compound. The Pd NPs were loaded in MIL-101(Cr) by incipient-wetness impregnation and then reduction method. The catalytic activities of as-synthesized catalysts were investigated by the dehydrogenation of a representative LOHC compound, perhydro-N-propylcarbazole (12H-NPCZ) at 190 °C. The results indicated that 3wt%Pd/MIL-101 catalyst exhibited good catalytic activity for the dehydrogenation of 12H-NPCZ, which is superior to that of commercial 5 wt% Pd/Al<sub>2</sub>O<sub>3</sub> catalyst. This good catalytic activity ascribed to smaller and highly dispersed Pd NPs. Moreover, the 3wt%Pd/MIL-101 catalyst also showed good reusability by enabling to retain 88.7% conversion (4.81 wt% for H<sub>2</sub> release) up to five times of repeating use.

Stavila V. et al<sup>45</sup> presented reversible hydrogen storage of NaAlH<sub>4</sub> confined within the nanopores of a titanium-functionalized MOF-74(Mg). The MOF-74(Mg) possesses one-dimensional, 12 Å channels lined with Mg atoms having open coordination sites, which can serve as sites for Ti catalyst stabilization. The activated MOF was first exposed to gas-phase TiCl<sub>4</sub>, followed by melt infusion with NaAlH<sub>4</sub>, achieving loadings up to 21 wt%. The XRD, SEM-EDS and FTIR results confirmed that the hydride fills the pores of the intact MOF and is not merely a coating on the outside of the particles. The residual gas analysis demonstrated that the MOF-74(Mg) template was stable under repeated hydrogen desorption and hydride regeneration cycles (below 300 °C), allowing it to serve as a “nanoreactor”. The isothermal kinetic studies indicated that the activation energy for H<sub>2</sub>

desorption was reduced from 79.5 kJ/mol in bulk Ti-doped NaAlH<sub>4</sub> to 57.4 kJ/mol for nanoconfined NaAlH<sub>4</sub>. This corresponded to the onset of hydrogen desorption for NaAlH<sub>4</sub>@MOF-74(Mg), which was nearly 100 °C lower than that of bulk NaAlH<sub>4</sub>. The hydrogen releases from NaAlH<sub>4</sub>@MOF-74(Mg) that can reach a maximum value of 4.5 wt% at 200 °C. Moreover, it was found that confining NaAlH<sub>4</sub> within these pores changed the decomposition pathway by eliminating the stable intermediate Na<sub>3</sub>AlH<sub>6</sub> phase observed upon bulk NaAlH<sub>4</sub> decomposition and proceeding directly to NaH, Al, and H<sub>2</sub>. Although, the presence of titanium did not attribute to an increase in desorption kinetic, it enabled rehydrogenation of NaAlH<sub>4</sub> (at 160 °C under 10.5 MPa H<sub>2</sub> pressure for 2 h) to be almost fully reversible, by taking rehydrogenation time to be saturated hydrogen adsorption less than 20 min, faster than bulk the Ti-doped material. These results showed that both fast desorption kinetics and an exceptionally high degree of reversibility can be achieved by confining NaAlH<sub>4</sub> within the well-ordered pores of a MOF template.

#### MOFs for catalysis

Chen Y-Z. et al<sup>46</sup> used Pd/Ag nanoparticles in MIL-101(Cr) for the reductive amination of nitrobenzene, where the alloy NPs were included by the “double solvents” method. In this method the metal salt is dissolved in an aqueous solution while the MOF is dispersed in a non-polar solvent. Slowly adding an amount of aqueous solution less than the pore volume of the MOF allows the MOF to take up the metal salt within its hydrophilic pores by capillary action, while the non-polar solvent minimizes the metal salt depositing on the surface of the MOF. This deposition technique leads to small and highly dispersed metal nanoparticles. The selectivity of the reaction to the desired secondary amine was then tuned by varying the Pd/Ag ratio in the NPs. Using a Pd<sub>2</sub>Ag<sub>1</sub>@MIL-101(Cr) catalyst. It was found that 99% conversion was achieved with 85% selectivity to the desired 2° amine. This result indicates the efficacy of the double solvents method to prepare active bifunctional and tunable catalysts.

Alamgholiloo H. et al<sup>47</sup> presented a strategy to formation and stabilization of ultra-small palladium colloid on ethylenediamine(en)-modified MIL-101(Cr) catalyst for dehydrogenation of formic acid. The coordinatively unsaturated Cr<sup>3+</sup> sites of MIL-101(Cr)

was grafted with amine counterpart for preparing Pd catalyst. Afterward, a colloid of PVA/PdCl<sub>2</sub>/NaBH<sub>4</sub> generated the *in situ* Pd nanoparticles immediately loaded on to en/MIL-101(Cr). It was found that XRD intensities and shape-size morphology of the MIL-101(Cr) crystal do remain intact, implying that ethylenediamine-grafting and loading Pd processes did not damage to the MIL-101(Cr) crystal. In addition, the large-blueshift in N-H stretching vibration and ultra-small of 1.8 nm Pd particles size with high monodispersity profile for 1 wt% Pd loading could be attributed to the stabilization of Pd NPs by ethylenediamine. The catalyst was further tested catalytic activity of dehydrogenation of formic acid at room temperature. The resultant of Pd/en/MIL-101(Cr) catalyst indicated high catalytic activity with turnover frequency (TOF) of 583 h<sup>-1</sup> at 55 °C. Although small Pd NPs aggregation after the reuse was observed, the activity was almost maintained for the first three cycles, suggesting that the Pd@en/MIL-101(Cr) was stable during the decomposition of formic acid.

Otake K-I. et al<sup>48</sup>, prepared a Pd<sup>2+</sup> single-sites species in phosphoric-modified based Hf-MOF (Pd@Hf-MOF-808-PO<sub>4</sub>). The acidic phosphate group was aligned on the bridging position of the Hf<sub>6</sub>-oxide node. The oxyanions from the functionalized phosphate group can be utilized as anchoring Pd<sup>2+</sup> sites. TEM image analysis showed that no evidence of Pd nanoparticle formation was found in the oxyanion-functionalized MOF, while the unmodified MOF existed the Pd nanoparticles inside and outside of MOF crystals. Stability tests of these Pd<sup>2+</sup> sites under an H<sub>2</sub> atmosphere revealed that there was no significant decomposition to Pd<sup>0</sup> nanoparticles. It was suggested that the phosphate groups on the node improved the stability of Pd<sup>2+</sup> sites as compared to the parent MOF. The stabilized Pd<sup>2+</sup> sites in Hf-MOF-808-PO<sub>4</sub> showed better catalytic activity in the oxidative Heck reaction. The acid functionalization MOF node can stabilize the Pd<sup>0</sup> intermediate state during the catalytic reactions, thereby suppressing Pd<sup>0</sup> aggregation, leading to catalyst deactivation. In addition, the node functionalization increased the catalyst lifetime, compared to that of the pristine MOF, by reducing the mobility of Pd<sup>0</sup> atoms that can agglomerate into unreactive nanoparticles when generated as part of the catalytic cycle.

Zhang Y. et al<sup>49</sup>, presented a linker engineering strategy to synthesize single-site catalysts with tunable catalytic property. A series of PdCl<sub>2</sub> moiety-decorated Y<sub>6</sub>-MOFs were

synthesized, containing high densities of isolated active Pd<sup>2+</sup> sites for aerobic oxidation of styrene. The functional organic linker (H<sub>2</sub>bpydc), related bipyridine compound, was incorporated into Y<sub>6</sub>-cluster based MOF via post-synthetic ligand exchange. Then post-synthetic Pd<sup>2+</sup> metalation was performed to enhance the density of isolated single sites. XPS analysis verified that their Pd<sup>2+</sup> binding energy was aligned to oxidation state of metallized Y-bpydc<sub>x</sub>/bpdc<sub>1-x</sub> and the blue-shift of N binding appeared, indicating the coordination between N atom of bpydc group and the Pd<sup>2+</sup> site. This was confirmed the successful immobilization of PdCl<sub>2</sub> moieties on the framework. The obtained Pd<sup>2+</sup>-Y-bpydc<sub>x</sub>/bpdc<sub>1-x</sub> heterogeneous single-site catalysts can effectively promote selective oxidative cleavage of styrene to benzaldehyde, using O<sub>2</sub> as an oxidant, under solvent-free and mild reaction conditions (1 atm and 80 °C).

## 2.7 References

- (1) Kalmutzki, M. J.; Hanikel, N.; Yaghi, O. M. Secondary Building Units as the Turning Point in the Development of the Reticular Chemistry of MOFs. *Sci. Adv.* **2018**, *4* (10), eaat9180.
- (2) Yang, S.-Y.; Yuan, H.-B.; Xu, X.-B.; Huang, R.-B. Influential Factors on Assembly of First-Row Transition Metal Coordination Polymers. *Inorganica Chim. Acta* **2013**, *403*, 53–62.
- (3) Oisaki, K.; Li, Q.; Furukawa, H.; Czaja, A. U.; Yaghi, O. M. A Metal–Organic Framework with Covalently Bound Organometallic Complexes. *J. Am. Chem. Soc.* **2010**, *132* (27), 9262–9264.
- (4) Butova, V. V.; Soldatov, M. A.; Guda, A. A.; Lomachenko, K. A.; Lamberti, C. Metal–Organic Frameworks: Structure, Properties, Methods of Synthesis and Characterization. *Russ. Chem. Rev.* **2016**, *85* (3), 280–307.
- (5) Yuan, S.; Feng, L.; Wang, K.; Pang, J.; Bosch, M.; Lollar, C.; Sun, Y.; Qin, J.; Yang, X.; Zhang, P.; Wang, Q.; Zou, L.; Zhang, Y.; Zhang, L.; Fang, Y.; Li, J.; Zhou, H. Stable Metal–Organic Frameworks: Design, Synthesis, and Applications. *Adv. Mater.* **2018**, *30* (37), 1704303.

- (6) Dinca, M.; Long, J. R. Strong  $H_2$  Binding and Selective Gas Adsorption within the Microporous Coordination Solid  $Mg_3(O_2C-C_{10}H_6-CO_2)_3$ . *J. Am. Chem. Soc.* **2005**, *127* (26), 9376–9377.
- (7) Czaja, A. U.; Trukhan, N.; Müller, U. Industrial Applications of Metal–Organic Frameworks. *Chem. Soc. Rev.* **2009**, *38* (5), 1284.
- (8) Horike, S.; Shimomura, S.; Kitagawa, S. Soft Porous Crystals. *Nat. Chem.* **2009**, *1* (9), 695–704.
- (9) Férey, G.; Serre, C. Large Breathing Effects in Three-Dimensional Porous Hybrid Matter: Facts, Analyses, Rules and Consequences. *Chem. Soc. Rev.* **2009**, *38* (5), 1380.
- (10) Shekhan, O.; Wang, H.; Paradinas, M.; Ocal, C.; Schüpbach, B.; Terfort, A.; Zacher, D.; Fischer, R. A.; Wöll, C. Controlling Interpenetration in Metal–Organic Frameworks by Liquid-Phase Epitaxy. *Nat. Mater.* **2009**, *8* (6), 481–484.
- (11) Dybtsev, D. N.; Chun, H.; Yoon, S. H.; Kim, D.; Kim, K. Microporous Manganese Formate: A Simple Metal–Organic Porous Material with High Framework Stability and Highly Selective Gas Sorption Properties. *J. Am. Chem. Soc.* **2004**, *126* (1), 32–33.
- (12) Ma, S.; Wang, X.-S.; Yuan, D.; Zhou, H.-C. A Coordinatively Linked Yb Metal–Organic Framework Demonstrates High Thermal Stability and Uncommon Gas-Adsorption Selectivity. *Angew. Chem. Int. Ed.* **2008**, *47* (22), 4130–4133.
- (13) Pan, L.; Adams, K. M.; Hernandez, H. E.; Wang, X.; Zheng, C.; Hattori, Y.; Kaneko, K. Porous Lanthanide–Organic Frameworks: Synthesis, Characterization, and Unprecedented Gas Adsorption Properties. *J. Am. Chem. Soc.* **2003**, *125* (10), 3062–3067.
- (14) Chanut, N.; Ghoufi, A.; Coulet, M.-V.; Bourrelly, S.; Kuchta, B.; Maurin, G.; Llewellyn, P. L. Tailoring the Separation Properties of Flexible Metal–Organic Frameworks using Mechanical Pressure. *Nat. Commun.* **2020**, *11* (1), 1216.
- (15) Mahdipoor, H. R.; Halladj, R.; Ganji Babakhani, E.; Amjad-Iranagh, S.; Sadeghzadeh Ahari, J. Synthesis, Characterization, and  $CO_2$  Adsorption Properties of Metal Organic Framework Fe-BDC. *RSC Adv.* **2021**, *11* (9), 5192–5203.

- (16) Kalaj, M.; Denny, M. S.; Bentz, K. C.; Palomba, J. M.; Cohen, S. M. Nylon–MOF Composites through Postsynthetic Polymerization. *Angew. Chem. Int. Ed.* **2019**, *58* (8), 2336–2340.
- (17) Sánchez-Láinez, J.; Zornoza, B.; Friebe, S.; Caro, J.; Cao, S.; Sabetghadam, A.; Seoane, B.; Gascon, J.; Kapteijn, F.; Le Guillouzer, C.; Clet, G.; Daturi, M.; Téllez, C.; Coronas, J. Influence of ZIF-8 Particle Size in the Performance of Polybenzimidazole Mixed Matrix Membranes for Pre-Combustion CO<sub>2</sub> Capture and Its Validation through Interlaboratory Test. *J. Membr. Sci.* **2016**, *515*, 45–53.
- (18) Seoane, B.; Téllez, C.; Coronas, J.; Staudt, C. NH<sub>2</sub>-MIL-53(Al) and NH<sub>2</sub>-MIL-101(Al) in Sulfur-Containing Copolyimide Mixed Matrix Membranes for Gas Separation. *Sep. Purif. Technol.* **2013**, *111*, 72–81.
- (19) Schoedel, A.; Ji, Z.; Yaghi, O. M. The Role of Metal–Organic Frameworks in a Carbon-Neutral Energy Cycle. *Nat. Energy* **2016**, *1* (4), 16034.
- (20) García-Holley, P.; Schweitzer, B.; Islamoglu, T.; Liu, Y.; Lin, L.; Rodriguez, S.; Weston, M. H.; Hupp, J. T.; Gómez-Gualdrón, D. A.; Yildirim, T.; Farha, O. K. Benchmark Study of Hydrogen Storage in Metal–Organic Frameworks under Temperature and Pressure Swing Conditions. *ACS Energy Lett.* **2018**, *3* (3), 748–754.
- (21) Murray, L. J.; Dincă, M.; Long, J. R. Hydrogen Storage in Metal–Organic Frameworks. *Chem. Soc. Rev.* **2009**, *38* (5), 1294–1314.
- (22) Suh, M. P.; Park, H. J.; Prasad, T. K.; Lim, D.-W. Hydrogen Storage in Metal–Organic Frameworks. *Chem. Rev.* **2012**, *112* (2), 782–835.
- (23) Zhao, D.; Yuan, D.; Zhou, H.-C. The Current Status of Hydrogen Storage in Metal–Organic Frameworks. *Energy Environ. Sci.* **2008**, *1* (2), 222–235.
- (24) Frost, H.; Düren, T.; Snurr, R. Q. Effects of Surface Area, Free Volume, and Heat of Adsorption on Hydrogen Uptake in Metal–Organic Frameworks. *J. Phys. Chem. B* **2006**, *110* (19), 9565–9570.
- (25) Thomas, K. M. Adsorption and Desorption of Hydrogen on Metal–Organic Framework Materials for Storage Applications: Comparison with Other Nanoporous Materials. *Dalton Trans.* **2009**, *9*, 1487–1505.

- (26) Rowsell, J. L. C.; Yaghi, O. M. Strategies for Hydrogen Storage in Metal-Organic Frameworks. *Angew. Chem. Int. Ed.* **2005**, *44* (30), 4670–4679.
- (27) Frost, H.; Snurr, R. Q. Design Requirements for Metal-Organic Frameworks as Hydrogen Storage Materials. *J. Phys. Chem. C* **2007**, *111* (50), 18794–18803.
- (28) Thornton, A. W.; Nairn, K. M.; Hill, J. M.; Hill, A. J.; Hill, M. R. Metal–Organic Frameworks Impregnated with Magnesium-Decorated Fullerenes for Methane and Hydrogen Storage. *J. Am. Chem. Soc.* **2009**, *131* (30), 10662–10669.
- (29) Belof, J. L.; Stern, A. C.; Eddaoudi, M.; Space, B. On the Mechanism of Hydrogen Storage in a Metal–Organic Framework Material. *J. Am. Chem. Soc.* **2007**, *129* (49), 15202–15210.
- (30) Sun, W.; Li, S.; Mao, J.; Guo, Z.; Liu, H.; Dou, S.; Yu, X. Nanoconfinement of Lithium Borohydride in Cu-MOFs towards Low Temperature Dehydrogenation. *Dalton Trans.* **2011**, *40* (21), 5673–5676.
- (31) Han, Y.; Zhang, Y.; Zhang, Y.; Cheng, A.; Hu, Y.; Wang, Z. Selective Ethylene Tetramerization with Iron-Based Metal–organic Framework MIL-100 to Obtain C<sub>8</sub> Alkanes. *Appl. Catal. A: Gen.* **2018**, *564*, 183–189.
- (32) Rostamnia, S.; Alamgholiloo, H. Synthesis and Catalytic Application of Mixed Valence Iron (Fe<sup>II</sup>/Fe<sup>III</sup>)-Based OMS-MIL-100(Fe) as an Efficient Green Catalyst for the Aza-Michael Reaction. *Catal. Lett.* **2018**, *148* (9), 2918–2928.
- (33) Zhuang, J.-L.; Liu, X.-Y.; Zhang, Y.; Wang, C.; Mao, H.-L.; Guo, J.; Du, X.; Zhu, S.-B.; Ren, B.; Terfort, A. Zr-Metal–Organic Frameworks Featuring TEMPO Radicals: Synergistic Effect between TEMPO and Hydrophilic Zr-Node Defects Boosting Aerobic Oxidation of Alcohols. *ACS Appl. Mater. Interfaces* **2019**, *11* (3), 3034–3043.
- (34) Cao, C.-C.; Chen, C.-X.; Wei, Z.-W.; Qiu, Q.-F.; Zhu, N.-X.; Xiong, Y.-Y.; Jiang, J.-J.; Wang, D.; Su, C.-Y. Catalysis through Dynamic Spacer Installation of Multivariate Functionalities in Metal–Organic Frameworks. *J. Am. Chem. Soc.* **2019**, *141* (6), 2589–2593.
- (35) Stassen, I.; Styles, M.; Greci, G.; Gorp, H. V.; Vanderlinden, W.; Feyter, S. D.; Falcaro, P.; Vos, D. D.; Vereecken, P.; Ameloot, R. Chemical Vapour Deposition of Zeolitic Imidazolate Framework Thin Films. *Nat. Mater.* **2016**, *15* (3), 304–310.

- (36) Li, X.; Zhang, Z.; Xiao, W.; Deng, S.; Chen, C.; Zhang, N. Mechanochemistry-Assisted Encapsulation of Metal Nanoparticles in MOF Matrices *via* a Sacrificial Strategy. *J. Mater. Chem. A* **2019**, *7* (24), 14504–14509.
- (37) Liu, Y.; Jia, S.-Y.; Wu, S.-H.; Li, P.-L.; Liu, C.-J.; Xu, Y.-M.; Qin, F.-X. Synthesis of Highly Dispersed Metallic Nanoparticles inside the Pores of MIL-101(Cr) *via* the New Double Solvents Method. *Catal. Commun.* **2015**, *70*, 44–48.
- (38) Guo, H.; Zhu, G.; Hewitt, I. J.; Qiu, S. “Twin Copper Source” Growth of Metal–Organic Framework Membrane:  $\text{Cu}_3(\text{BTC})_2$  with High Permeability and Selectivity for Recycling  $\text{H}_2$ . *J. Am. Chem. Soc.* **2009**, *131* (5), 1646–1647.
- (39) Kang, Z.; Wang, S.; Fan, L.; Zhang, M.; Kang, W.; Pang, J.; Du, X.; Guo, H.; Wang, R.; Sun, D. *In Situ* Generation of Intercalated Membranes for Efficient Gas Separation. *Commun. Chem.* **2018**, *1* (1), 3.
- (40) Lin, R.; Ge, L.; Diao, H.; Rudolph, V.; Zhu, Z. Ionic Liquids as the MOFs/Polymer Interfacial Binder for Efficient Membrane Separation. *ACS Appl. Mater. Interfaces* **2016**, *8* (46), 32041–32049.
- (41) Wang, Y.; Yang, G.; Guo, H.; Meng, X.; Kong, G.; Kang, Z.; Guillet-Nicolas, R.; Mintova, S. Preparation of HKUST-1/PEI Mixed-Matrix Membranes: Adsorption-Diffusion Coupling Control of Small Gas Molecules. *J. Membr. Sci.* **2022**, *643*, 120070.
- (42) Dong, Y.; Yang, M.; Yang, Z.; Ke, H.; Cheng, H. Catalytic Hydrogenation and Dehydrogenation of N-Ethylindole as a New Heteroaromatic Liquid Organic Hydrogen Carrier. *Int. J. Hydrog. Energy* **2015**, *40* (34), 10918–10922.
- (43) Qin, W.; Cao, W.; Liu, H.; Li, Z.; Li, Y. Metal–Organic Framework MIL-101 Doped with Palladium for Toluene Adsorption and Hydrogen Storage. *RSC Adv.* **2014**, *4* (5), 2414–2420.
- (44) Ding, C.; Zhu, T.; Wang, F.; Zhang, Z.; Dong, Y.; Yang, M.; Cheng, G.; Ke, H.; Cheng, H. High Active Pd@mil-101 Catalyst for Dehydrogenation of Liquid Organic Hydrogen Carrier. *Int. J. Hydrog. Energy* **2020**, *45* (32), 16144–16152.
- (45) Stavila, V.; Bhakta, R. K.; Alam, T. M.; Majzoub, E. H.; Allendorf, M. D. Reversible Hydrogen Storage by  $\text{NaAlH}_4$  Confined within a Titanium-Functionalized MOF-74(Mg) Nanoreactor. *ACS Nano* **2012**, *6* (11), 9807–9817.

- (46) Chen, Y.-Z.; Zhou, Y.-X.; Wang, H.; Lu, J.; Uchida, T.; Xu, Q.; Yu, S.-H.; Jiang, H.-L. Multifunctional PdAg@MIL-101 for One-Pot Cascade Reactions: Combination of Host-Guest Cooperation and Bimetallic Synergy in Catalysis. *ACS Catal.* **2015**, *5* (4), 2062–2069.
- (47) Alamgholiloo, H.; Rostamnia, S.; Hassankhani, A.; Liu, X.; Eftekhari, A.; Hasanzadeh, A.; Zhang, K.; Karimi-Maleh, H.; Khaksar, S.; Varma, R. S.; Shokouhimehr, M. Formation and Stabilization of Colloidal Ultra-Small Palladium Nanoparticles on Diamine-Modified Cr-MIL-101: Synergic Boost to Hydrogen Production from Formic Acid. *J. Colloid Interface Sci.* **2020**, *567*, 126–135.
- (48) Otake, K.; Ye, J.; Mandal, M.; Islamoglu, T.; Buru, C. T.; Hupp, J. T.; Delferro, M.; Truhlar, D. G.; Cramer, C. J.; Farha, O. K. Enhanced Activity of Heterogeneous Pd(II) Catalysts on Acid-Functionalized Metal-Organic Frameworks. *ACS Catal.* **2019**, *9* (6), 5383–5390.
- (49) Zhang, Y.; Wei, N.; Xing, Z.; Han, Z.-B. Functional Hexanuclear Y(III) Cluster-Based MOFs Supported Pd(II) Single Site Catalysts for Aerobic Selective Oxidation of Styrene. *Appl. Catal. A: Gen.* **2020**, *602*, 117668.

## Chapter 3

### Research methodology

#### 3.1 Chemical and materials

Table 3.1 List of reagents

|    | Reagents                        | Grade/Purity     | Manufacturers       |
|----|---------------------------------|------------------|---------------------|
| 1  | Chromium nitrate nonahydrate    | 99%              | Acros               |
| 2  | Copper nitrate trihydrate       | 99.5%            | Carlo               |
| 3  | Palladium(II) acetate           | 98%              | Acros               |
| 4  | Sodium molybdate dihydrate      | 99.5%            | Carlo               |
| 5  | Terephthalic acid               | 98%              | Aldrich             |
| 6  | Trimesic acid                   | 95%              | Aldrich             |
| 7  | 3-acetylpyridine                | 98%              | Aldrich             |
| 8  | Ethylenediamine                 | 99%              | Aldrich             |
| 9  | Phenylacetylene                 | 98%              | Aldrich             |
| 10 | Iodobenzene                     | 98%              | Aldrich             |
| 11 | Styrene                         | 99.9%            | Aldrich             |
| 12 | Nitrobenzene                    | 99%              | Aldrich             |
| 13 | Ethylene vinylacetate copolymer | 28%VA<br>content | Exxon<br>Chemical   |
| 14 | High impact polystyrene         | STYRON™          | SIAM<br>POLYSTYRENE |
| 15 | Acetone                         | ACS reagent      | Carlo               |
| 16 | Acetonitrile                    | ACS reagent      | Carlo               |
| 17 | Methanol                        | ACS reagent      | Carlo               |
| 18 | Ethanol                         | ACS reagent      | Carlo               |
| 19 | 30% $H_2O_2$ solution           | -                | Aldrich             |
| 20 | Dimethyl sulfoxide- $d_6$       | 99.0%            | Aldrich             |
| 21 | Dimethyl sulfoxide              | ACS reagent      | Carlo               |

This material is reserved for educational use only, not allowed for commercial use.

Forbidden to modify the content, and cite the document when use.

Table 3.1 (Continued)

|    | Reagents                             | Grade/Purity | Manufacturers |
|----|--------------------------------------|--------------|---------------|
| 22 | <i>N,N</i> -Dimethylformamide        | ACS reagent  | Carlo         |
| 23 | Diethyl ether                        | ACS reagent  | Carlo         |
| 24 | Dichloromethane                      | ACS reagent  | Carlo         |
| 25 | n-Hexane                             | ACS reagent  | Carlo         |
| 26 | Toluene                              | ACS reagent  | Carlo         |
| 27 | n-Dodecane                           | ACS reagent  | Carlo         |
| 28 | Potassium carbonate                  | ACS reagent  | Carlo         |
| 29 | Sodium carbonate                     | ACS reagent  | Carlo         |
| 30 | Sodium hydroxide                     | ACS reagent  | Carlo         |
| 31 | Potassium hydroxide                  | ACS reagent  | Carlo         |
| 32 | 37% Hydrochloric acid                | ACS reagent  | Carlo         |
| 33 | 98% Sulfuric acid                    | ACS reagent  | Carlo         |
| 34 | 70% Nitric acid                      | ACS reagent  | Carlo         |
| 35 | 70% Perchloric acid                  | ACS reagent  | Sdfichem      |
| 36 | Calcium hydride                      | 99.9%        | Aldrich       |
| 37 | Magnesium sulfate                    | 99.5%        | Fluka         |
| 38 | Molecular sieve 4A, beads, 8-12 mesh | -            | Aldrich       |

### 3.2 Apparatuses

Table 3.2 List of apparatuses

| Apparatuses; specification                                    | Manufacturers; model            |
|---|---------------------------------|
| 1 Stainless-steel Autoclave                                   | TOPTION, TOPT-HT50              |
| 2 Stirred reactor and pressure vessel                         | Parr instrument, Series 4560    |
| 3 Hot plate stirrer   | Ohaus Guardian 5000             |
| 4 Mass flow controller  | Brook instrument LLC            |
| 5 Vertical tube furnace; 25mm chamber $\varnothing$ X 30cm    | Carbolite®; MTF 12/25/250       |
| 6 Tube furnace  | UTSAKAN, VF                     |
| 7 Gas chromatography with Flame ionized detector              | Agilent; HP5890, HP6890         |
| 8 HP-5 column; 0.25mm X 30m                                   | Agilent J&W                     |
| 9 DB-1 column; 0.25mm X 30m                                   | Agilent J&W                     |
| 10 DB-Wax column; 0.25mm X 30m                                | Agilent J&W                     |
| 11 Thermal conductivity detector with controller              | VICI®; TCD2-NIFED-220           |
| 12 CHN analyzer   | Thermo Fisher, FLASH 2000       |
| 13 Inductively coupled plasma - optical emission spectrometer | Perkin Elmer, 7300 DV           |
| 14 X-ray diffractometer                                       | Bruker AXS; D8 Advance          |
| 15 Fourier-transform infrared spectrometer                    | Thermo scientific; NICOLET 6700 |
| 16 X-ray photoelectron spectrometer                           | Kratos, Axis ultra DLD          |
| 17 X-ray absorption spectrometer                              | SLRI BL2.2 and 5.2              |
| 18 Gas absorption analyzer                                    | Quantachrome; Autosorb-1        |
| 19 Transmission electron microscope                           | FEI™; Tecnai G2                 |
| 20 Thermogravimetric analyzer                                 | Perkin Elmer®; Pyris            |
| 21 Nuclear Magnetic Resonance (500 MHz)                       | JEOL, Model JNM-ECZ-500R/S1     |
| 22 ODLAB Digester with Teflon trap                            | LABTER, ECO-PRE III             |
| 23 Flow meter   | Agilent; ADM1000                |
| 24 Ultrasonic bath  | Ultrasonik; 208H                |
| 25 Hot air oven   | Memmert; UF 110                 |

This material is reserved for educational use only, not allowed for commercial use.

Forbidden to modify the content, and cite the document when use.

### 3.3 Experimental methods

#### 3.3.1 MOFs synthesis

##### 3.3.1.1 MIL-101(Cr)

MIL-101(Cr) was synthesized, following the procedure reported by Bromberg et al.<sup>1</sup> Briefly,  $\text{Cr}(\text{NO}_3)_3 \cdot 9\text{H}_2\text{O}$  (2.0 g, 5 mmol), terephthalic acid (0.83 g, 5 mmol), and deionized water (20 mL) were mixed and sonicated, resulting in a dark, blue-colored suspension. The suspension was placed in a Teflon-lined autoclave and kept in an oven at 218 °C for 18 h without stirring. After cooling to room temperature, the MOF solids were separated by centrifugation (at 8000 rpm, 10 min) and washed with water, methanol and acetone, respectively. The solids were then sonicated in DMF (20 mL) for 10 min and stirred at 70 °C overnight. The resulting solids were separated by centrifugation and repeatedly washed with ethanol and acetone. Finally, a green solid was heated under  $\text{N}_2$  at 150 °C for 12 h.

##### 3.3.1.2 HKUST-1

HKUST-1 was synthesized, following the procedure reported by Chowdhury et al.<sup>2</sup> Briefly, 1,3,5-benzenetricarboxylic acid (1.0 g, 4.75 mmol) was dissolved in 30 mL of a 1:1 mixture of ethanol/DMF. In another beaker, copper (II) nitrate trihydrate (2.077 g, 8.59 mmol) was dissolved in 15 mL water. The two solutions were then mixed and stirred for 10 min. They were then transferred into Teflon-lined stainless-steel autoclave and heated at 100 °C for 10 h. The reaction vessel was cooled to room temperature normally. The resulting blue crystals were isolated by filtration and washing with methanol to remove solvated DMF. The product was then dried at room temperature and calcined at 150 °C for 12 h under  $\text{N}_2$  flow.

#### 3.3.2 MOFs modification

##### 3.3.2.1 Acetylpyridine grafting

Post-synthetic modification of MIL-101(Cr) by acetylpyridine (AcP) grafting followed the method described by Yang et al.<sup>3</sup> Briefly, 1 g of dehydrated MIL-101(Cr) was suspended in 120 mL of dry toluene. The system was purged with  $\text{N}_2$  for 30 min. To this suspension,

5 mL of AcP was added, and the mixture was refluxed overnight under N<sub>2</sub>. After cooling to room temperature, the mixture was centrifuged (at 8000 rpm, 10 min). The solid was then collected and thoroughly washed with dichloromethane. Thereafter, the obtained solids were dispersed in ethanol, ultrasonicated for 1 h, and centrifuged (8000 rpm, 10 min). The resulting solid was washed at least three times to remove the nongrafted AcP. Finally, the solid was heated under N<sub>2</sub> at 150 °C and labeled AcP-MIL-101(Cr).

### 3.3.2.2 Ethylenediamine grafting

Grafting of ethylenediamine on MIL-101(Cr) has followed the method described by Yang et al.<sup>3</sup> Briefly, 1 g of dehydrated MIL-101(Cr) was suspended in 120 mL of dry toluene. The system was purged with N<sub>2</sub> for 30 min. To this suspension, 19, 94 and 187 µL of ethylenediamine was added, and the mixture was refluxed for 12 h under N<sub>2</sub>. After cooling to room temperature, the solid was separated by centrifugation (at 8000 rpm for 10 min) and thoroughly washed with dichloromethane. After that, the obtained solids were dispersed in ethanol under sonication for 1 h and centrifuged at 8000 rpm for 10 min. The resulting solid was washed at least three times to remove non-grafted ethylenediamine. Finally, the solid was heated under N<sub>2</sub> at 150 °C and labeled as (x)en-MIL-101(Cr), where x specifies the amount of incorporated ethylenediamine in mmol/g.

### 3.3.2.3 Pd incorporation

Incorporation of Pd was carried out using the double solvent method reported by Anderson et al.<sup>4</sup> Typically, 1 g of dehydrated MIL-101(Cr) or modified-MIL-101(Cr) was suspended in 120 mL of dry n-hexane, as a hydrophobic solvent, and sonicated for 10 min. To this suspension, 1 mL of Pd(OAc)<sub>2</sub> solution in acetone (at desired concentration), as a hydrophilic solvent, was added dropwise, under vigorous stirring. After 3 h, the resulting solid was filtered, heated at 150 °C under N<sub>2</sub> overnight, and reduced at 150 °C under 10%H<sub>2</sub>/Ar for 2 h. For above 1.5 %w/v Pd concentration, the adsorption process needs to separate in the half of concentration and do repeat twice.

#### 3.3.2.4 Composite membrane fabrication

The composite membranes were prepared by solution casting. First, HKUST-1 was dispersed in the 50 mL of toluene in ultrasonic bath for 1 h. Then, 1 g of polymer pellet (HIPS and EVA) were stirred vigorously for 1 h. The HKUST-1/polymer solution was casted on the glass mold with the dimension of 210 mm x 297 mm. The polymer membrane was dried at room temperature overnight and then placed in the hot air oven at 80 °C for 1 h.

### 3.3.3 Characterization

#### 3.3.3.1 CHN analysis

To calculation amount of incorporated grafting agents, the modified MOF samples were determined by CHN analysis. The certain amount of sample was weighted. The tin capsule enclosing the samples fall into the reactor chamber where excess oxygen is introduced before. The complete oxidation is reached at a tungsten trioxide catalyst, which is passed by the gaseous reaction products. The resulting mixture gas should thus consist of CO<sub>2</sub>, H<sub>2</sub>O and NO<sub>x</sub>. Some excess O<sub>2</sub> passes the catalyst. The leaving gas stream includes the analytically important species CO<sub>2</sub>, H<sub>2</sub>O and N<sub>2</sub>. The gas mixture is brought to a defined pressure/volume state and is passed to a gas chromatographic system.

#### 3.3.3.2 Inductively coupled plasma-optical emission spectroscopy

The metal content determination was investigated using inductively coupled plasma-optical emission spectrometer. 100 mg of sample was firstly digested in HClO<sub>4</sub>:H<sub>2</sub>SO<sub>4</sub>:H<sub>2</sub>O (15:15:20 mL) solution, with the addition of 1 g of Na<sub>2</sub>MoO<sub>4</sub>·2H<sub>2</sub>O, at 210 °C with a heating rate of 10 °C/min for 6 h. The digested solution was filtered and adjusted with 5 v% H<sub>2</sub>SO<sub>4</sub> to 50 mL in volumetric flask. The solution is introduced into the plasma in a process that desolvates, ionizes, and excites them. The constituent elements can be identified by their characteristic emission lines and quantified against blank. The metal content was calculated using calibration curve.

### 3.3.3.3 X-ray diffraction

Crystal structure of the sample was examined by powder X-ray diffractometer (PXRD). The prepared sample as finely ground powder was packed into the holder. CuK $\alpha$  X-ray beam was used at 40kV and 30 mA. The sample was scanned in the range of 2-50° ( $2\theta$ ) with 2 deg/min and 0.02  $2\theta$ /step increment. The PXRD pattern of the sample were then compared with standard X-ray diffraction pattern for the determination of structure.

### 3.3.3.4 Fourier transform infrared spectroscopy

Functional group and their interaction in the sample were detected using Fourier Transform infrared spectrometer (FTIR). 2 mg sample and 100 mg KBr were grinded with agate mortar. The fine sample powder was compressed to get the sample pellet. FTIR spectra were collected with a resolution of 4 cm $^{-1}$  and 64 scans in the wavenumber range of 400-4000 cm $^{-1}$ .

### 3.3.3.5 *In situ* Fourier transform infrared spectroscopy

The change of functional group during hydrogenation/dehydrogenation was observed by *in situ* Fourier Transform infrared spectroscopy (*in situ* FTIR). 50 mg sample was packed in the holder, then activated at 150 °C under N $_2$  flow (30 mL/min) for 1 h. The system was flushed with H $_2$  pure (30 mL/min) at 30 °C for 30 min, followed by ramping temperature to 200 °C (5 °C/min) for hydrogenation. After cooling to 30°C under H $_2$  flow, the system was flushed with N $_2$  flow (30 mL/min) at 30°C for 30 min, then heating to 200 °C (5 °C/min) for dehydrogenation. The spectra were recorded in wavenumber range of 400-4000 cm $^{-1}$  with every 10 °C (64 scan/spectrum). The temperature profile shows in appendix A1.

### 3.3.3.6 Raman spectroscopy

Raman spectrometer was used to examine the functional groups that cannot be detected clearly by FTIR, such as  $\nu$ (Pd-N) and  $\nu$ (C-N). The sample was grinded and pelleted. The Raman spectra were obtained, using a microscope with an excitation wavelength of 514 nm in range of 100–4000 cm $^{-1}$ .

### 3.3.3.7 X-ray photoelectron spectroscopy

The chemical and electronic state of the C 1s, N 1s, Cr 2p, and Pd 3d was determined by X-ray photoelectron spectrometer (XPS), using a PHI 5800 ESCA (Physical Electronics) system, equipped with a standard achromatic Al K $\alpha$  X-ray source (1486.6 eV) operating at 300 W (15 kV, 20 mA) and a concentric hemispherical analyzer. The binding energies were calibrated to the C 1s peak at 284.8 eV. For spectra deconvolution, the obtained data was fitted using MagicPlot program with Gaussian-A type.

### 3.3.3.8 *In situ* X-ray absorption near-edge structure

The local geometric and electronic structure was investigated by *in situ* X-ray absorption near-edge structure (*in situ* XANES) equipped with a compact furnace. The *in situ* XAS measurements were performed in both transmission and fluorescence modes at BL 2.2 and 5.2 stations at the Synchrotron Light Research Institute, Thailand (SLRI). Electron beam energy was about 1.2 GeV and ring current ranged from 80 to 150 mA, while the maximum photon flux was  $1.1\text{--}1.7 \times 10^{11}$  photons/s at 100 mA. Double Ge (220) single crystals were utilized as a monochromator. An X-ray beam dimensions were 14 mm (width)  $\times$  1 mm (height) with a spatial resolution of 0.2 eV.

For preparation, the sample powder was mixed with binder (e.g., cellulose or boron nitride) and pelletized. The sample concentration needs to be optimized to find the best ratio for edge jump energy. To determine Cr<sup>3+</sup> species, the sample was *in situ* activated at 150 °C (5 °C/min) for 60 min. Then, the raw XANES data was recorded at room temperature (25 °C). The characteristic adsorption of Cr K-edge and molecular geometry of the samples were comparable with Cr<sup>3+</sup> standard (i.e. Cr<sub>2</sub>O<sub>3</sub> and K<sub>2</sub>Cr<sub>2</sub>O<sub>7</sub>). In case of determination the Pd composition, after activation, the raw XANES data was collected upon reduction under stream of 10%H<sub>2</sub>/Ar from 30 °C to 150 °C, then dwelling at 150 °C for 60 min. After XANES process, the resulted raw data was proceeded with the Athena software to obtain XANES spectra. PdCOCl<sub>2</sub> for Pd<sup>2+</sup> (3174.2 eV) and Pd foil for Pd<sup>0</sup> (3173.0 eV), as reference materials (Appendix B1), were used to determine the composition of Pd<sup>2+</sup> and Pd<sup>0</sup> species at different reduction temperature by linear combination fitting (LCF) of normalized samples. The temperature profile during *in situ* reduction showed in appendix A2.

### 3.3.3.9 Nuclear magnetic resonance spectroscopy

Nuclear magnetic resonance spectrometer ( $^1\text{H}$  NMR) was used to confirm molecular structure. 100 mg sample was immersed in  $\text{DMSO-}d_6$  at  $40\text{ }^\circ\text{C}$  for 1 h under ultrasonic condition. Then, the resulted solution was filtered by syringe filter. The obtained liquid was transferred to a 5 mm NMR glass tubes then mounted to the NMR machine. The experiment was performed on 500 MHz NMR system. The data was processed using TopSpin 4.0.6 software.

### 3.3.3.10 Gas adsorption analysis

Textural properties of the sample were investigated by gas adsorption analyzer. 10 mg of sample was loaded into a dried sample cell. The sample cell was loaded at the outgassing station at  $150\text{ }^\circ\text{C}$  for 12 h for catalyst surface cleaning. Then, the sample cell was moved to analysis station. Adsorption isotherm was measured in a pressure range of  $10^{-6}$  to  $1.0\text{ P/P}_0$  at  $-196\text{ }^\circ\text{C}$  cooling by liquid nitrogen. After the analysis, the cell was uninstalled and closed immediately. The sample cell was weighted and compared to the blank cell to obtain the certain sample weight. Surface area analysis was determined using Brunauer, Emmett, and Teller (BET) method, whereas pore volume and pore size analyses were obtained using Barrett-Joyner-Halenda (BJH) method.

### 3.3.3.11 Field emission scanning electron microscopy

Field emission scanning electron microscope (FESEM) was used to study surface morphology and measured crystallite size. 100 mg sample powder was deposited on the carbon tape which mounted on stub. The sputter coating with gold builds up on the specimen surface (around 10 nm) to prevent electron charging effect. The stub was loaded into the FESEM instrument. The image was collected with 1000-5000x magnification.

### 3.3.3.12 Transmission electron microscopy

Transmission electron microscope (TEM) was carried out to study metal particle size, morphology and crystallographic structure. For sample preparation, 5 mg sample powder was grinded by agate mortar. Fined powder was dispersed in the ethanol under ultrasonic condition. The suspension was dropped onto copper coated Formvar grid and

left to dry at room temperature overnight. The copper grid was loaded into the TEM instrument. The microscope performed using LaB<sub>6</sub> electron source with high tension electron of 200 kV (100000–300000x magnification). The particle size distribution was measured using Image J software.

#### 3.3.3.13 Thermogravimetric analysis

100 mg of sample was loaded into platinum pans then hanged from microbalance in the closed system of TGA. The analysis mode used under either nitrogen or air flows. Chamber purging at a flow rate of 30 mL/min was allowed for 5 min before the start of each run. All sample was used the TGA isothermal method followed by the high-resolution ramp method. The isothermal method involves heating the material up to 150 °C and holding for 60 min to remove remained solvent. The ramping method involves linearly heating to 900 °C at a constant rate 10 °C/min.

#### 3.3.3.14 Temperature program reduction

The hydrogen storage behavior was inspected using hydrogen temperature program reduction (H<sub>2</sub>-TPR, Figure 3.1). The evaluation of hydrogen consumption (hydrogenation) and hydrogen evolution (dehydrogenation) was observed upon ramping temperature and regulating hydrogen partial pressure. The signal was detected using temperature conductivity detector (TCD). 100 mg sample was packed in the glass tubes and mounted into the system. Prior experiment, the sample was undergone the *in situ* thermal treatment at 150 °C (5 °C/min) under N<sub>2</sub> flow (30 mL/min) for 12 h to get rid of an interference signal from solvent/humidity desorption upon operation. After cooling to ambient temperature, the system was switched to analyze mode. The sample was subjected to heat from 30 °C to 200 °C with constant rate of 5 °C/min under steam of 10% H<sub>2</sub>/Ar as reference gas. Subsequently, the temperature was decreased to ambient temperature under 10% H<sub>2</sub>/Ar atmosphere without any cooling equipment. The heating/cooling process was repeatedly carried out to investigate the hydrogen storage cycle. After each cycle, the system needs to be pulsed with 1% H<sub>2</sub>/Ar standard for

normalization. The calculation of hydrogen consumption and hydrogen evolution showed in appendix C1.

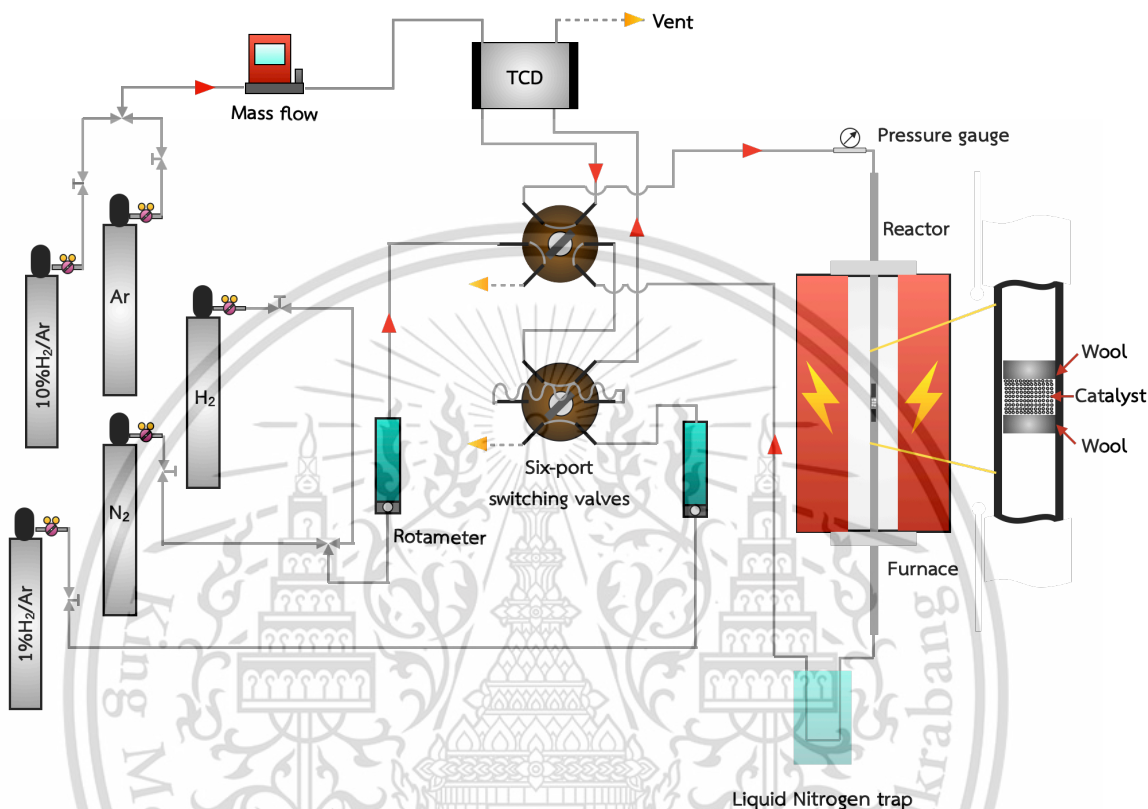


Figure 3.1 Diagram of hydrogen temperature program reduction

### 3.3.3.15 Temperature program reaction

The study of hydrogen storage performance was also carried out using the temperature program reaction ( $H_2$ -TPRe) experiment. The process was similar to the  $H_2$ -TPR system, but the reference gas was changed to Ar pure. At the first step, 100 mg sample was treated at 150 °C (5 °C/min) under  $N_2$  flow (30 mL/min) for 12 h. For hydrogenation, the sample was subjected to heat from 30 °C to target temperature (100, 130, 150 and 200 °C) with a heating rate of 5 °C/min under pure  $H_2$  flow (30 mL/min). After holding with desired hydrogenation time (e.g., 30, 50, 120 min), the sample was left to the ambient temperature under the  $H_2$  flow. The dehydrogenation process started by switching to the analyze mode and ramping the temperature from 30° to target

temperature (150, 160, 170, 180, 190 and 200 °C) with heating rate of 5 °C/min for 1 h. The system was cooled down to ambient temperature under Ar flow, then switching the system to the calcine mode. For normalization, the system must be pulsed with 1% H<sub>2</sub>/Ar standard at the end of cycle. The calculation of hydrogen uptake describes in appendix C2. To investigate the hydrogen storage recyclability, the hydrogenation-dehydrogenation cycle was repeatedly measured following the step discussed above.

#### 3.3.4 Single gas permeation testing

Gas permeability and selectivity of the polymer composite membrane was examined using gas permeation module as illustrated in Figure 3.2. The membrane was cut into 60 x 60 mm<sup>2</sup> and placed inside the permeation cell. This cell connects with feed gas (lower side) and carrier gas (upper side). At the feed gas, H<sub>2</sub> or CO<sub>2</sub> pure flows through the membrane at 30 mL/min. The permeated gas goes up on the upper side and then the carrier gas, e.g. Ar or He, (30 mL/min) brings the permeated gas to the sampling loop (1 mL). After the system achieves equilibration (30 min), the permeated gas was injected periodically to the thermal conductivity detector every 5 min for 30 min. For calibration, the mixed gas (1% H<sub>2</sub>/Ar or 10% CO<sub>2</sub>/He) was pulsed to the sampling loop and analyzed using TCD. In this system, the gas permeation was tested at atmospheric pressure, applying on both feed and permeated sides. To release pressure-drop existed upon permeation, the pressure at the feed sides was adjusted with needle valve to match up with the permeated side. The TCD signal was recorded after reaching equilibrium permeation for 60 min. The calculation of permeated flux addresses in appendix C3.

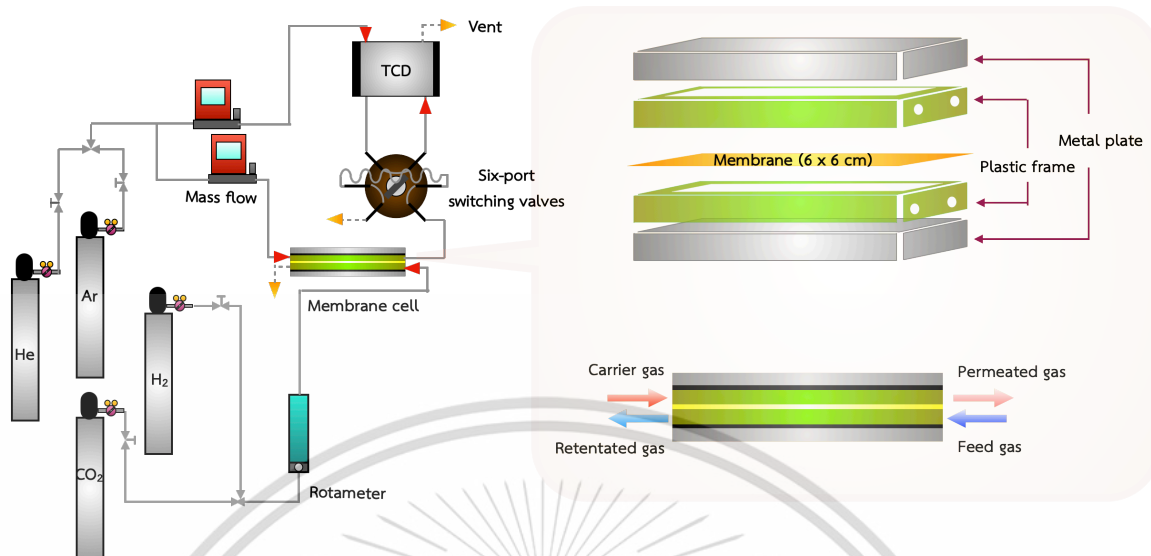


Figure 3.2 Gas permeation module and cell membrane diagram

### 3.3.5 Catalytic testing

#### 3.3.5.1 Oxidation of styrene

To a solution of styrene (1.0 mmol) in  $\text{CH}_3\text{CN}$  (10 mL), a Pd catalyst (0.49 mol%) and  $\text{H}_2\text{SO}_4$  (70 wt%, 10  $\mu\text{L}$ ) were added. The mixture was stirred for 15 min at room temperature. Then  $\text{H}_2\text{O}_2$  (30 wt%, 6.0 mmol) was added dropwise. The mixture was heated to 50  $^\circ\text{C}$  for 6 h. After completing the reaction, the catalyst was isolated using centrifugation (8000 rpm, 5 min). The resulting solution was neutralized with  $\text{Na}_2\text{CO}_3$ , then 5 mL of saturated NaCl solution was added. The reactant and products were extracted with diethyl ether (5 mL) three times. The organic phase was taken, diluted with diethyl ether, then analyzed by a gas chromatograph (HP-7890b) equipped with a DB-1 column and a flame ionization detector. The GC condition shows in appendix A3. The conversion and yields were calculated by calibrating with standards as indicates in appendix C4.

The catalyst was recycled by isolating the solid catalyst after use by centrifugation. Then, the catalyst was washed with acetonitrile, in an ultrasonic bath, for 1 h. The solid was separated and thoroughly washed with acetonitrile. After that, the obtained solid was dried ( $\text{N}_2$ , 150  $^\circ\text{C}$ , 12 h) before re-use in the next run.

### 3.3.5.2 Hydrogenation of phenylacetylene

47 g of ethanol and Pd catalyst (0.001 mol%) were added into a stainless-steel batch reactor (Parr series 4560, 300 mL). The mixture was equilibrated at 30 °C in N<sub>2</sub> with mild stirring. Next, the reactor was purged several times with H<sub>2</sub>, then 4 g of phenylacetylene was injected. The reaction was carried out at 30 °C, at 1.0 MPa H<sub>2</sub>, under vigorous stirring at 1000 rpm for 30 min. The product discharged from the reactor was analyzed by gas chromatograph (HP-6890) equipped with a DB Wax capillary column and a flame ionization detector. The GC condition indicates in appendix A4. The conversion and yields were calculated by calibrating with standards as presented in appendix C4.

### 3.3.5.3 Heck coupling of Iodobenzene with styrene

Iodobenzene (1 mmol), styrene (1.5 mmol), K<sub>2</sub>CO<sub>3</sub> (1.5 mmol), nitrobenzene (0.1g, internal standard) and Pd catalyst (0.5 mol%) were added to DMF (4 mL). The reaction mixture was stirred at 120 °C for 6 h. After the reaction was complete, the solution was centrifuged and washed with diethyl ether three times. The organic phase was subsequently washed with saturated NaCl solution, dried over anhydrous MgSO<sub>4</sub> and filtered. The reaction products were evaluated by a gas chromatograph (HP-6890) equipped with a DB-5 capillary column and a flame ionization detector. The GC condition expresses in appendix A5. The conversion and yields were calculated by calibrating with standards as indicates in appendix C4.

## 3.4 References

- (1) Bromberg, L.; Diao, Y.; Wu, H.; Speakman, S. A.; Hatton, T. A. Chromium(III) Terephthalate Metal-Organic Framework (MIL-101): HF-Free Synthesis, Structure, Polyoxometalate Composites, and Catalytic Properties. *Chem. Mater.* **2012**, *24* (9), 1664–1675.
- (2) Chowdhury, P.; Bikkina, C.; Meister, D.; Dreisbach, F.; Gumma, S. Comparison of Adsorption Isotherms on Cu-BTC Metal Organic Frameworks Synthesized from Different Routes. *Microporous Mesoporous Mater.* **2009**, *117* (1–2), 406–413.

- (3) Yang, F.; Yang, C.-X.; Yan, X.-P. Post-Synthetic Modification of MIL-101(Cr) with Pyridine for High-Performance Liquid Chromatographic Separation of Tocopherols. *Talanta* **2015**, *137*, 136–142.
- (4) Anderson, A. E.; Baddeley, C. J.; Wright, P. A. Tuning Pd-Nanoparticle@MIL-101(Cr) Catalysts for Tandem Reductive Amination. *Catal. Lett.* **2018**, *148* (1), 154–163.



## Chapter 4

# Atmospheric H<sub>2</sub>/CO<sub>2</sub> permeability of HKUST-1/polymer mixed matrix membrane for hydrogen purification

Herein, MMMs based on the combination of HKUST-1 and polymers were investigated for H<sub>2</sub> and CO<sub>2</sub> separation. Commercial polymers such as high impact polystyrene (HIPS) and ethylene vinylacetate copolymer (EVA) were used as a matrix for studying the effect of polymer types. To improve permeability and H<sub>2</sub>/CO<sub>2</sub> permselectivity, the HKUST-1 synthesized by hydrothermal and was used as filler. The characteristic of HKUST-1 crystal was examined with X-ray diffraction (XRD), N<sub>2</sub> sorption isotherm, Fourier-transform infrared spectroscopy (FTIR), Scanning electron microscopy (SEM) and Thermogravimetric analysis (TGA). Gas permeability and permselectivity were evaluated using single gas permeation. The effect of HKUST-1 loading on the gas separation performance for MMMs was also investigated.

## 4.1 Results and discussion

### 4.1.1 Material characterization

The XRD pattern of HKUST-1 possessed typical peaks at  $2\theta = 9.5^\circ, 11.7^\circ, 13.5^\circ, 14.7^\circ, 16.5^\circ, 17.5^\circ$  and  $19.1^\circ$  (Figure 4.1), which is in good agreement with the literature.<sup>1</sup> The SEM image of the HKUST-1 octahedral crystal was about  $\sim 10\text{-}30\ \mu\text{m}$  in particle size (Figure 4.2). The BET surface area of HKUST-1 was  $2027\ \text{m}^2/\text{g}$  with pore volume of  $0.68\ \text{cm}^3\ \text{g}^{-1}$ , indicating a typical  $\text{N}_2$  adsorption isotherms type I (Figure 4.3) - similar to the reported elsewhere.<sup>2</sup> The characteristic FTIR spectrum of HKUST-1 indicated the vibrational stretching of carboxylate ligands coordinated to the  $\text{Cu}^{2+}$  sites at  $1300\text{-}1700\ \text{cm}^{-1}$  (Figure 4.4). The doublet peak at  $1652\text{-}1450\ \text{cm}^{-1}$  was assigned to the  $\nu_{\text{as}}(\text{COO})$  and  $\nu_{\text{s}}(\text{COO})$  modes of carboxylate groups, which are located in the large pores of the framework, while the doublet at  $1419\text{-}1374\ \text{cm}^{-1}$  was attributed to the same vibrations of the groups placed in the smaller pores.<sup>3</sup>

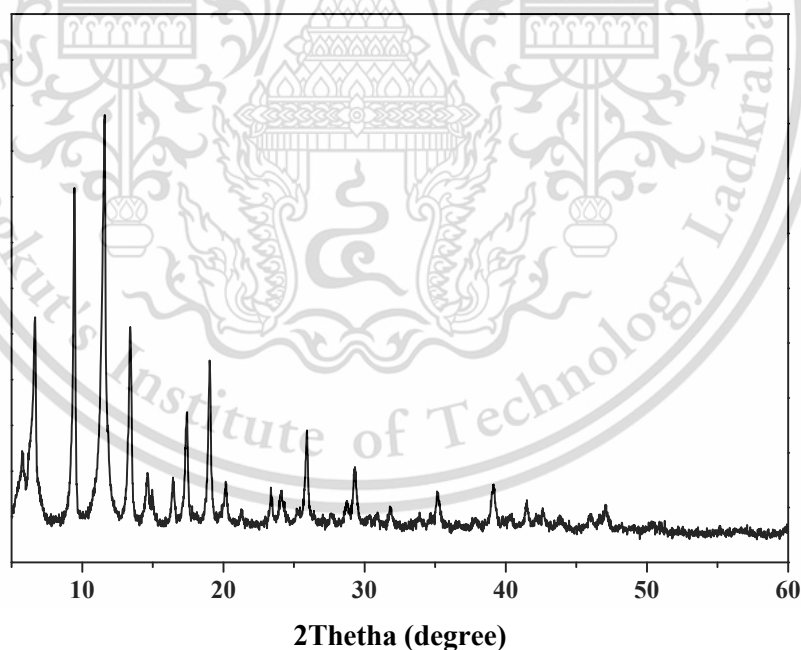


Figure 4.1 XRD pattern of HKUST-1

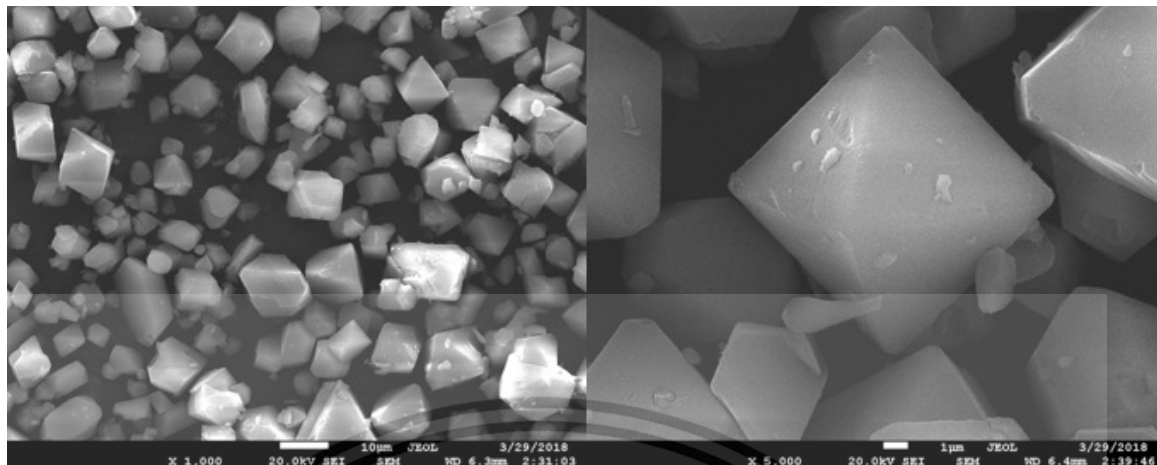


Figure 4.2 SEM image of HKUST-1

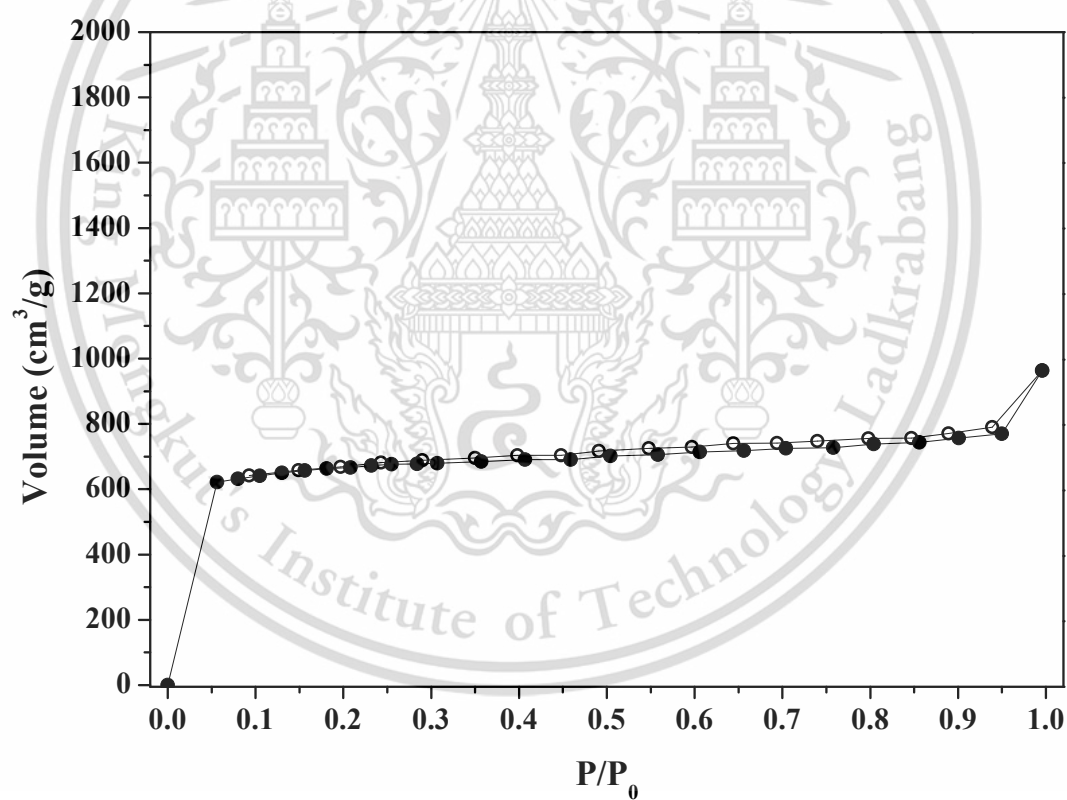


Figure 4.3  $\text{N}_2$  adsorption-desorption isotherm of HKUST-1

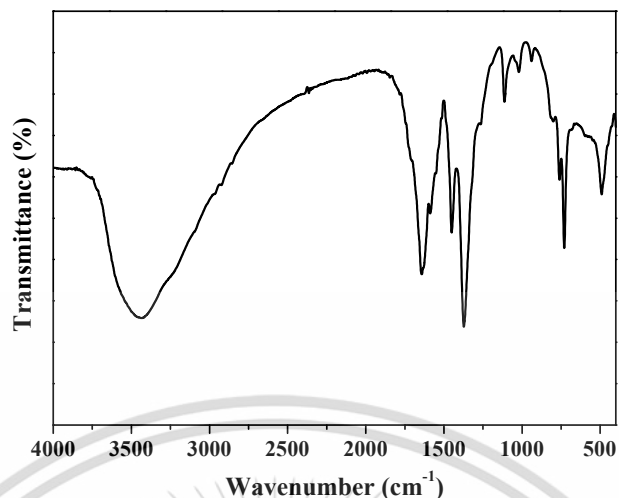


Figure 4.4 FTIR spectrum of HKUST-1

Thermogram curve in Figure 4.5 reveals that the weight loss behavior of HKUST-1 can be divided into two major stages. The first weight loss stage occurred at temperatures below 200 °C, which is attributed to the removal of water and solvent molecules from the surfaces and pores of HKUST-1. The onset decomposition temperatures of the frameworks started at around 270 °C and ended around 340 °C. According to the typical calculation of the relative weight loss of the HKUST-1 sample at this stage is approximately 60%, roughly corresponding to the theoretical weight loss caused by the decomposition of the organic ligands in HKUST-1 under air.<sup>4</sup>

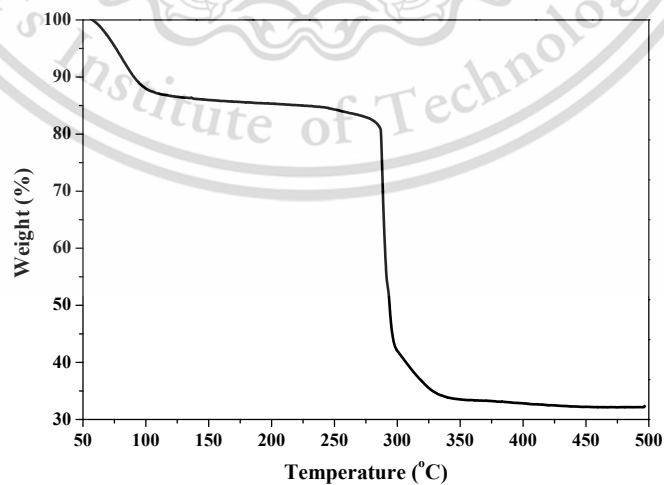


Figure 4.5 TGA thermogram of HKUST-1

#### 4.1.2 Permeation testing

The single gas permeability of the pure polymers and HKUST-1/polymer membranes was measured at 25 °C under atmospheric pressure. First, HIPS and EVA polymers were chosen to investigate the effect of polymer types on their H<sub>2</sub> and CO<sub>2</sub> permeabilities. The polymer membrane was prepared by solution casting with a fixed thickness at 70±5 μm. Figure 4.6 depicts the plot of different polymer membranes against their H<sub>2</sub> and CO<sub>2</sub> fluxes and the H<sub>2</sub>/CO<sub>2</sub> permselectivity. It showed that the HIPS membrane had H<sub>2</sub> flux of 1.67 cm<sup>3</sup> m<sup>-2</sup>s<sup>-1</sup>, whereas the EVA matrix was 0.27 cm<sup>3</sup> m<sup>-2</sup>s<sup>-1</sup>. The difference in gas permeability in both membranes could be explained by solution-diffusion mechanism,<sup>5</sup> as shown in scheme 4.1, which is driven by concentration gradient across the membrane. This mechanism starts by (i) sorption of the gaseous penetrants at the upstream side of the membrane, (ii) diffusion of the penetrants across the membrane and (iii) desorption of the penetrants at the downstream side of the membrane. On the basis of this mechanism, the key factors for determining gas permeability are their gas solubility and diffusivity in the membrane, which both sorption on the membrane surface and diffusion through the membrane define the molecular transport. As gas permeability in the membrane preferably occurs through the gap or pore occupied between polymer chains, defined as free volume. Thus, the polymer structure, which has higher fractional free volume, would have higher gas permeability, whereas the opposite trend could be observed for the polymer with high barrier properties i.e., degree of crystallinity or density of the polymer.<sup>6</sup> Accordingly, HIPS is an amorphous polymer, which is more abundant of fractional free volume than that of the semi-crystalline EVA polymer. Therefore, H<sub>2</sub> diffusivity was obtained for HIPS higher than EVA. Despite a substantial free volume being of HIPS membrane, leading to great H<sub>2</sub> diffusion, the CO<sub>2</sub> permeability of HIPS membrane (Figure 4.6) was obtained for 0.34 cm<sup>3</sup> m<sup>-2</sup>s<sup>-1</sup>, which was lower than that of EVA membrane (0.51 cm<sup>3</sup> m<sup>-2</sup>s<sup>-1</sup>). The opposite trend for CO<sub>2</sub> permeability was attributed to differential CO<sub>2</sub> solubility in both membranes. In general, gas solubility is related to the chemical affinity between gas and the polymer structure.<sup>7</sup> With this regard, the EVA polymer ought to have good CO<sub>2</sub> solubility due to the polar moiety like that of the acetate group, which is induced by dipole–quadruple interaction between CO<sub>2</sub> penetrant molecules and

polymer chains. The strong affinity between polar vinylactate segments (c.a.~28% vinylactate content)<sup>8</sup> and CO<sub>2</sub> molecules contributes to a higher CO<sub>2</sub> flux in EVA membrane. In case of HIPS membrane, the lower CO<sub>2</sub> permeability of 0.34 cm<sup>3</sup> m<sup>-2</sup> s<sup>-1</sup> could be derived from interfering CO<sub>2</sub> diffusion by bulky phenyl group in the HIPS polymer chain. Such large group might behave as the barrier segment, which prolongs the tortuosity of the diffusion path through the membrane. This might reduce CO<sub>2</sub> diffusivity in the HIPS membrane.

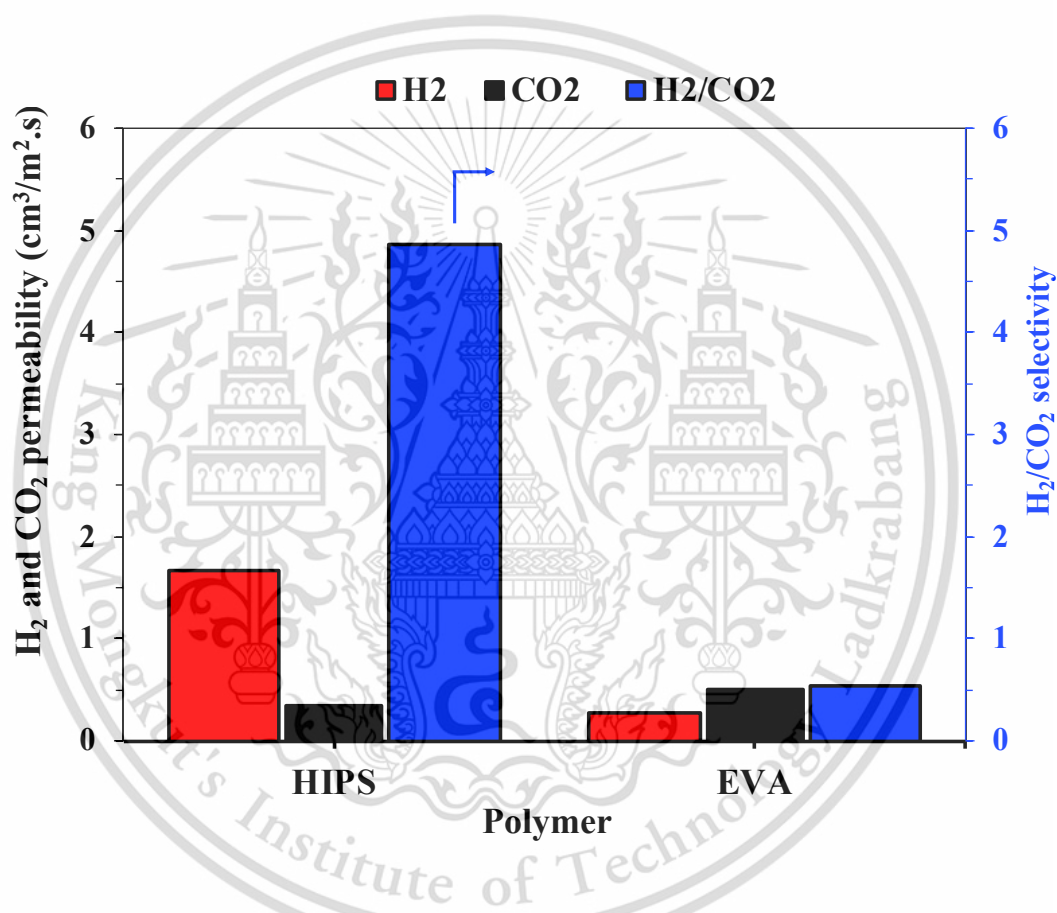
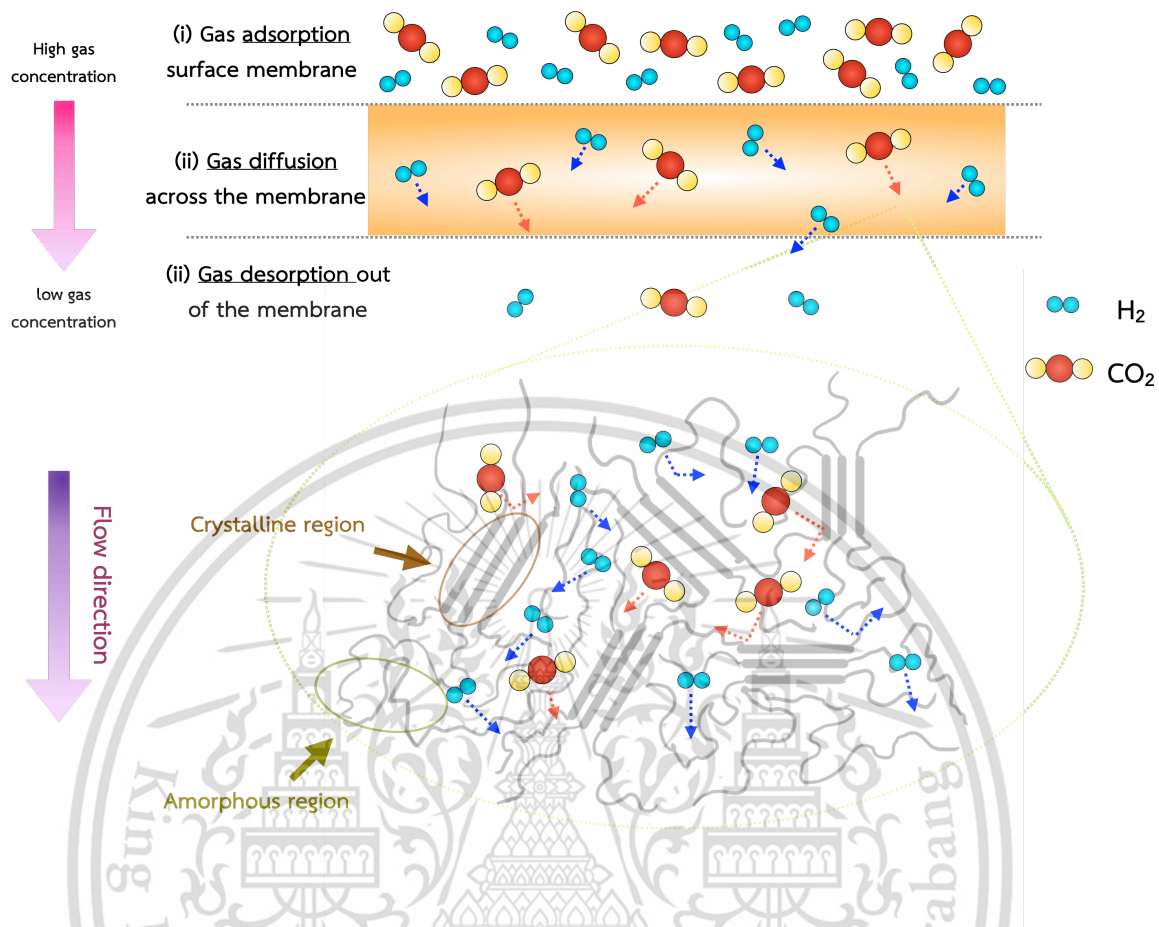


Figure 4.6 Gas flux and H<sub>2</sub>/CO<sub>2</sub> permselectivity of different polymer membranes



**Scheme 4.1** Gas solution-diffusion mechanism in the polymer membrane and favorable diffusion of penetrant in amorphous region for semicrystalline polymer

In addition, kinetic diameter of penetrant molecules would be another reason for considering the separation factor. As mobility of penetrant molecules in the polymer membrane is dependent by the gas kinetic diameter. Gas diffusibility decreases as the molecular size increases. The small  $\text{H}_2$  molecules (0.29 nm) could collide with segments of the polymer chain less than larger  $\text{CO}_2$  molecules (0.33 nm).<sup>9</sup> Thus, the low diffusion resistance of  $\text{H}_2$  molecules face within the membrane, leading to fast diffusion of smaller  $\text{H}_2$  molecules as compared to larger  $\text{CO}_2$ . From these reasons,  $\text{H}_2/\text{CO}_2$  permselectivity of the HIPS membrane would be greater than the EVA membrane (Figure 4.6). Based on these findings, HIPS membrane was chosen as the polymer matrix for further studying in the effect of HKUST-1 incorporation.

To achieve higher H<sub>2</sub> permeability and H<sub>2</sub>/CO<sub>2</sub> permselectivity, the addition of HKUST-1 in the polymer membranes was carried out. As high CO<sub>2</sub> adsorption in HKUST-1 (up to 18.5 wt% at 0.1 MPa and 27 °C as reported by Chen et al.),<sup>10</sup> It is expected to increase the H<sub>2</sub>/CO<sub>2</sub> permselectivity of HKUST-1-MMMs. Figure 4.7a reveals that an increase of HKUST-1 loading from 1 wt% to 10 wt% into HIPS membrane, the H<sub>2</sub> flux were enhanced significantly from 2.89 cm<sup>3</sup> m<sup>-2</sup>s<sup>-1</sup> to 17.19 cm<sup>3</sup> m<sup>-2</sup>s<sup>-1</sup>, whereas CO<sub>2</sub> flux was consistent. It was suggested that the H<sub>2</sub> molecule passes through the HKUST-1 pores more easily than CO<sub>2</sub> molecules as reported in the literature.<sup>11</sup> Such behavior could be rationalized by pore network of the HKUST-1 (0.41 and 0.69 nm for window sizes), which provides faster and resistance-less through-pore channels for small and non-polar H<sub>2</sub> molecules (0.29 nm). In contrast, the permeability of bigger CO<sub>2</sub> molecules decreased owing to their strong adsorption in the HKUST-1. The presence of coordinatively unsaturated Cu<sup>2+</sup> in HKUST-1 performs as strong CO<sub>2</sub> adsorption sites (scheme 4.2), which facilitates a slow desorption of CO<sub>2</sub> in the channels, thereby restricting its transport capabilities. These contributions lead to significantly improve of H<sub>2</sub>/CO<sub>2</sub> permselectivity from 4.87 to 23.17 at 10wt% HKUST-1 loading.

However, the improvement of gas separation was not observed for HKUST-1 loaded EVA membranes. Despite the increase of HKUST-1 loading, no obvious enhancement in terms of H<sub>2</sub> and CO<sub>2</sub> permeabilities was observed (Figure 4.7b). It could be suggested to blockage of the HKUST-1 pores by polymer penetration. This is presumably that the strong polymer-MOF interaction and good chain mobility of rubbery EVA polymer create a pore-blocking surface coating on the MOF particle surface and further infiltrate the polymer chain through the small pore of HKUST-1. Pore blockage of porous filler was generally observed for rubbery polymer as reported of ZIF-8/PDMS,<sup>12</sup> UiO-66/PEO,<sup>13</sup> MCM-41/PSF<sup>14</sup> and zeolite 5A/PES<sup>15</sup>. In contrast, lower chain mobility of the large bulky phenyl group in HIPS might not be affected. Accordingly, main contribution for gas permeability in case of HKUST-1/EVA could be solely from the diffusion in amorphous phase.

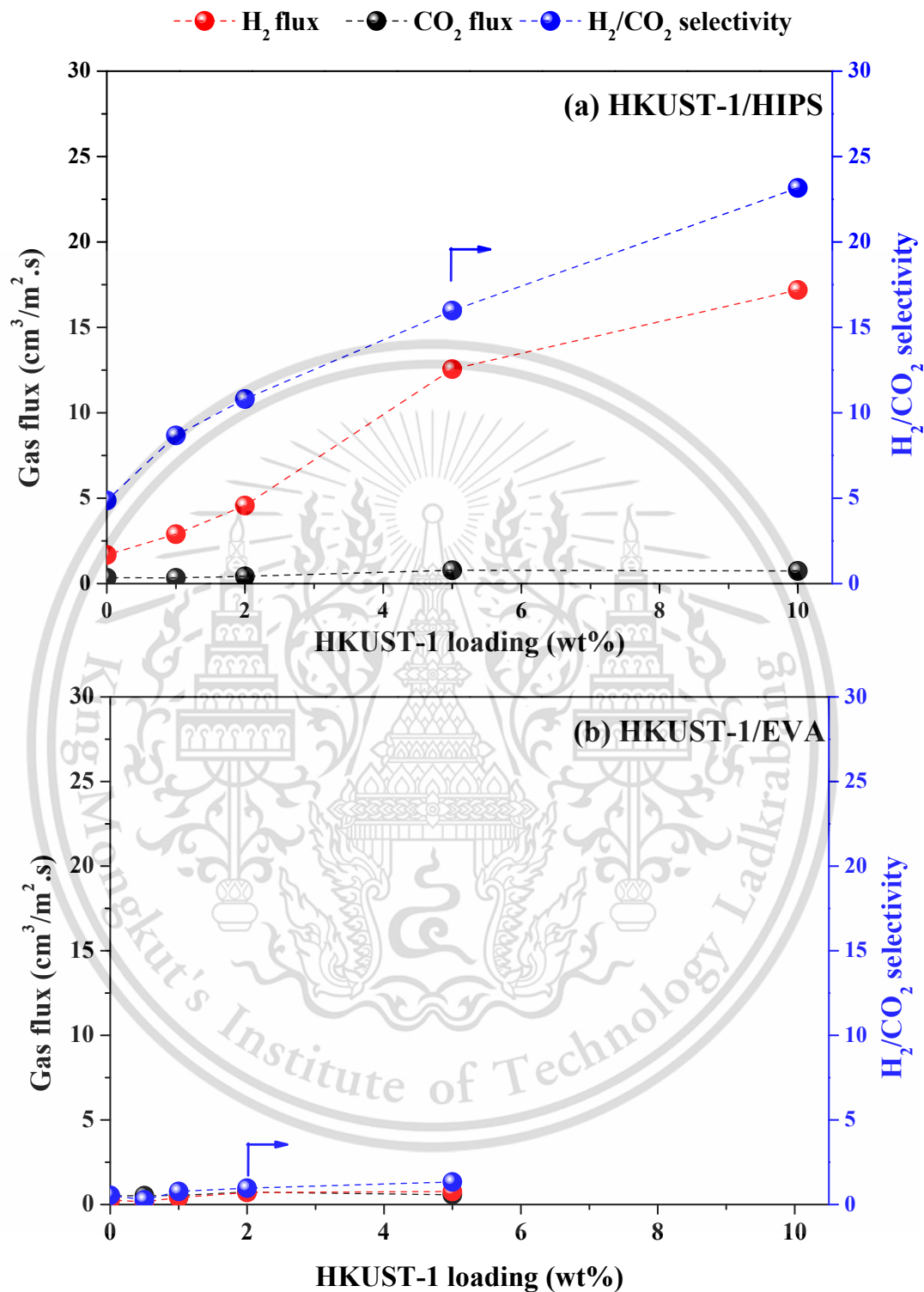
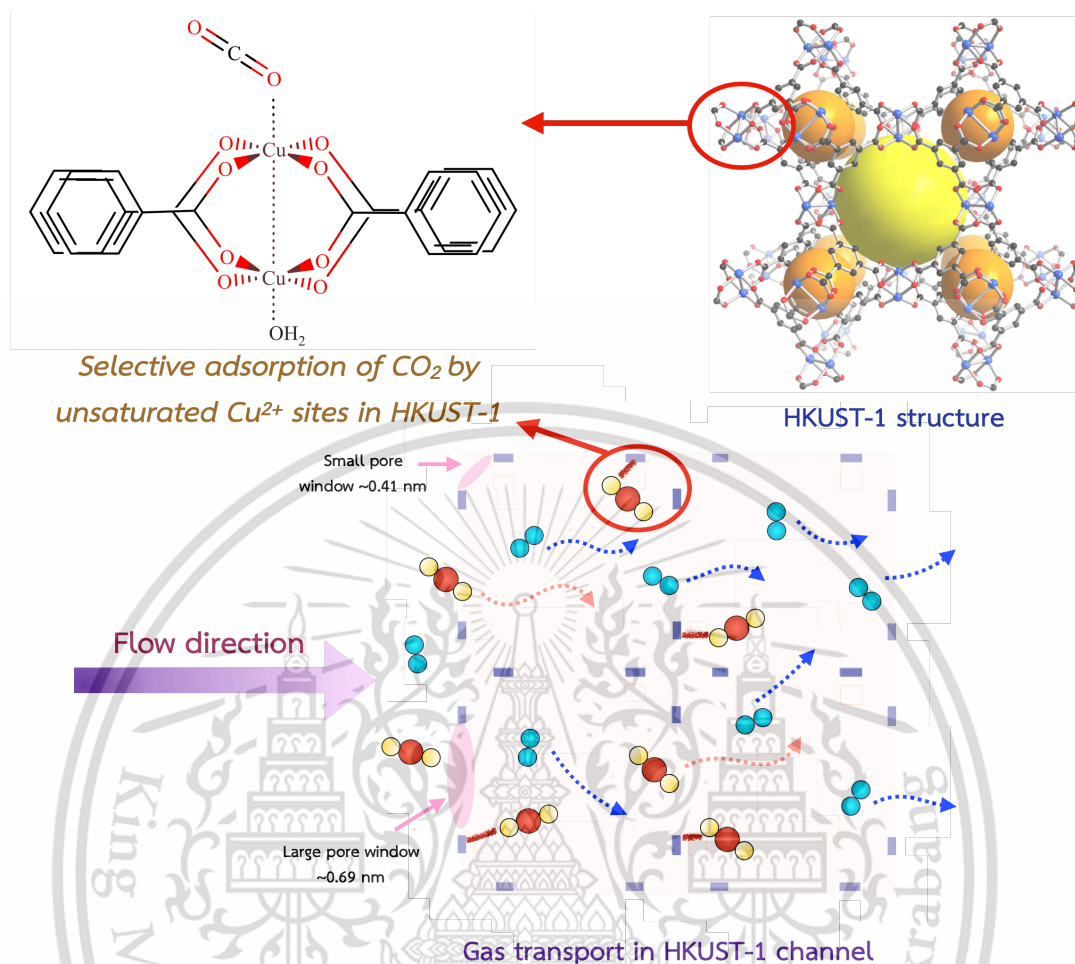


Figure 4.7 Effect of HKUST-1 loading on (a) HKUST-1/HIPS and (b) HKUST-1/EVA MMMs on gas flux and  $H_2/CO_2$  permselectivity



**Scheme 4.2** Strong interaction between CO<sub>2</sub> molecules and coordinatively unsaturated Cu<sup>2+</sup> sites in HKUST-1 and plausible gas transport in HKUST-1 channel

Compared to the reported MMMs (Table 4.1), the HKUST-1/HIPS MMM showed greater H<sub>2</sub>/CO<sub>2</sub> permselectivity than conventional inorganic porous fillers such as SiO<sub>2</sub> and Zeolite 4A (Table 4.1, entry 2-3).<sup>16,17</sup> Despite the fact that 30wt% UiO-66/PAA-PVP had a comparable permselectivity to this work (Table 4.1, entry 4),<sup>18</sup> the HKUST-1/HIPS MMM did not require high feed pressure. Even with a lower proportion of HKUST-1, the HIPS matrix has the superior permselectivity than engineering polymers like PEI (Table 4.1, entry 5).<sup>11</sup> Hence, the HKUST-1/HIPS MMM prepared in this work used simple process and showed highly promising for H<sub>2</sub>/CO<sub>2</sub> separation under atmospheric condition.

**Table 4.1** A summary of the H<sub>2</sub>/CO<sub>2</sub> separation performance of the reported MMMs

| Entry | Membrane                    | Temperature<br>(°C) | Pressure<br>(bar) | H <sub>2</sub> /CO <sub>2</sub><br>selectivity | Ref.      |
|-------|-----------------------------|---------------------|-------------------|--|-----------|
| 1     | 10wt% HKUST-1/HIPS          | 30                  | -                 | 23.2   | This work |
| 2     | 10wt% SiO <sub>2</sub> /PSf | 35                  | 3                 | 2.5  | 16        |
| 3     | 15wt% Zeolite 4A/PVAc       | 30                  | 0.75              | 5.0  | 17        |
| 4     | 30wt% UiO-66/PAA-PVP        | 40                  | 3                 | 19.2   | 18        |
| 5     | 30wt% HKUST-1/PEI           | 25                  | 1.5               | 15.8   | 11        |

## 4.2 Conclusion

The HKUST-1/polymer MMMs were prepared by solution casting, which was used for studying the effect of HKUST-1 on H<sub>2</sub> and CO<sub>2</sub> permeability. As compared to EVA, the HIPS membrane showed superior H<sub>2</sub> flux and H<sub>2</sub>/CO<sub>2</sub> permselectivity because of higher fractional free volume, facilitating small H<sub>2</sub> molecule diffusion and the bulky phenyl group of HIPS reduced their CO<sub>2</sub> diffusivity. The incorporation of HKUST-1 in the HIPS membrane indicated the significant improvement for H<sub>2</sub> permeability and H<sub>2</sub>/CO<sub>2</sub> permselectivity. This is because pore channel of the HKUST-1 provides faster and resistance-less pathway for small and non-polar H<sub>2</sub> molecules. In addition, strong interaction between CO<sub>2</sub> and coordinatively unsaturated Cu<sup>2+</sup> in HKUST-1, retards their CO<sub>2</sub> diffusivity. However, this effect was not observed for HKUST-1/EVA MMM, suggesting preferable diffusion in amorphous region over than the diffusion in HKUST-1 pore. The exceptional atmospheric separation performance of HKUST-1/HIPS MMM renders its attractive for hydrogen separation application.

### 4.3 References

- (1) Yang, A.; Li, P.; Zhong, J. Facile Preparation of Low-Cost HKUST-1 with Lattice Vacancies and High-Efficiency Adsorption for Uranium. *RSC Adv.* **2019**, *9* (18), 10320–10325.
- (2) Wahiduzzaman; Allmond, K.; Stone, J.; Harp, S.; Mujibur, K. Synthesis and Electrospinning of Nanoscale MOF (Metal-Organic Framework) for High-Performance CO<sub>2</sub> Adsorption Membrane. *Nanoscale Res. Lett.* **2017**, *12* (1), 6.
- (3) Gentile, F. S.; Pannico, M.; Causà, M.; Mensitieri, G.; Di Palma, G.; Scherillo, G.; Musto, P. Metal Defects in HKUST-1 MOF Revealed by Vibrational Spectroscopy: A Combined Quantum Mechanical and Experimental Study. *J. Mater. Chem. A* **2020**, *8* (21), 10796–10812.
- (4) Lin, K.-S.; Adhikari, A. K.; Ku, C.-N.; Chiang, C.-L.; Kuo, H. Synthesis and Characterization of Porous HKUST-1 Metal Organic Frameworks for Hydrogen Storage. *Int. J. Hydrog. Energy* **2012**, *37* (18), 13865–13871.
- (5) Kaldis, S. P.; Pantoleontos, G. T.; Koutsonikolas, D. E. Membrane Technology in IGCC Processes for Precombustion CO<sub>2</sub> Capture. *In Current Trends and Future Developments on (Bio-) Membranes*; Elsevier, **2018**; 329–357.
- (6) Kanehashi, S.; Kusakabe, A.; Sato, S.; Nagai, K. Analysis of Permeability; Solubility and Diffusivity of Carbon Dioxide; Oxygen; and Nitrogen in Crystalline and Liquid Crystalline Polymers. *J. Membr. Sci.* **2010**, *365* (1–2), 40–51.
- (7) Luo, J.; He, X.; Si, Z. Gas Permeation Properties of Polymer Membranes Containing Ethylene Glycol Monomers. *High Perform. Polym.* **2017**, *29* (2), 237–245.
- (8) Watasit, P.; Rukchonlatee, S.; Ausavasukhi, A.; Ritvirulh, C.; Sooknoi, T. Atmospheric CO<sub>2</sub>/CH<sub>4</sub> Permeability of EVA Copolymer/SiO<sub>2</sub> Composite Membrane for Biogas Purification. *J. Appl. Polym. Sci.* **2021**, *138* (42), 51229.
- (9) David, O. C. (**2012**), Membrane Technologies for Hydrogen and Carbon Monoxide Recovery from Residual Gas Streams. (Doctoral dissertation, Universidad De Cantabria)
- (10) Chen, Y.; Mu, X.; Lester, E.; Wu, T. High Efficiency Synthesis of HKUST-1 under Mild Conditions with High BET Surface Area and CO<sub>2</sub> Uptake Capacity. *Prog. Nat. Sci.* **2018**, *28* (5), 584–589.

- (11) Wang, Y.; Yang, G.; Guo, H.; Meng, X.; Kong, G.; Kang, Z.; Guillet-Nicolas, R.; Mintova, S. Preparation of HKUST-1/PEI Mixed-Matrix Membranes: Adsorption-Diffusion Coupling Control of Small Gas Molecules. *J. Membr. Sci.* **2022**, *643*, 120070.
- (12) Fang, M.; Wu, C.; Yang, Z.; Wang, T.; Xia, Y.; Li, J. ZIF-8/PDMS Mixed Matrix Membranes for Propane/Nitrogen Mixture Separation: Experimental Result and Permeation Model Validation. *J. Membr. Sci.* **2015**, *474*, 103–113.
- (13) Duan, P.; Moreton, J. C.; Tavares, S. R.; Semino, R.; Maurin, G.; Cohen, S. M.; Schmidt-Rohr, K. Polymer Infiltration into Metal–Organic Frameworks in Mixed-Matrix Membranes Detected *in situ* by NMR. *J. Am. Chem. Soc.* **2019**, *141* (18), 7589–7595.
- (14) Kim, S.; Marand, E. High Permeability Nano-Composite Membranes Based on Mesoporous MCM-41 Nanoparticles in a Polysulfone Matrix. *Microporous Mesoporous Mater.* **2008**, *114* (1–3), 129–136.
- (15) Li, Y.; Chung, T.; Cao, C.; Kulprathipanja, S. The Effects of Polymer Chain Rigidification, Zeolite Pore Size and Pore Blockage on Polyethersulfone (PES)-Zeolite A Mixed Matrix Membranes. *J. Membr. Sci.* **2005**, *260* (1-2), 45-55.
- (16) Pakizeh, M.; Moghadam, A. N.; Omidkhah, M. R.; Namvar-Mahboub, M. Preparation and Characterization of Dimethyldichlorosilane Modified SiO<sub>2</sub>/PSf Nanocomposite Membrane. *Korean J. Chem. Eng.* **2013**, *30* (3), 751–760.
- (17) Esmaili, N.; Boyd, S. E.; Brown, C. L.; Mac A. Gray, E.; Webb, C. J. Improving the Gas-Separation Properties of PVAc-Zeolite 4A Mixed-Matrix Membranes through Nano-Sizing and Silanation of the Zeolite. *ChemPhysChem* **2019**, *20* (12), 1590–1606.
- (18) Xiang, F.; Marti, A. M.; Hopkinson, D. P. Layer-by-Layer Assembled Polymer/MOF Membrane for H<sub>2</sub>/CO<sub>2</sub> Separation. *J. Membr. Sci.* **2018**, *556*, 146–153.

## Chapter 5

# Reversible Hydrogenation–Dehydrogenation of Acetylpyridine-Pd-MIL-101(Cr) for Chemical Hydrogen Storage

In this work, we report a new hydrogen storage material by modifying MIL-101(Cr) with 3-acetylpyridine (AcP), an organic hydrogen carrier with an N donor ligand for node anchoring and a carbonyl group as the hydrogen-carrying function. Pd nanoparticles (Pd NPs) were encapsulated in the AcP-grafted MIL-101(Cr), using a double-solvent method to ensure dispersion of the metal in the pockets. The existence of AcP and Pd NPs in Pd-AcP-MIL-101(Cr) was studied by various spectroscopic techniques. The hydrogenation-dehydrogenation of Pd-AcP-MIL-101(Cr) was evaluated over the temperature-programmed reaction (TPRe), and the hydrogenated and dehydrogenated forms of AcP were confirmed by *in situ* Fourier transform infrared (FTIR) and nuclear magnetic resonance (NMR) spectra. The effects of Pd content, temperature, and hydrogen partial pressure for the hydrogenation-dehydrogenation cycle were investigated. The hydrogen storage stability was also highlighted.

## 5.1 Results and discussions

### 5.1.1 Material characterization

Figure 5.1 shows the XRD patterns of all samples that similar to the pure MIL-101(Cr), as reported by Fer y et al.<sup>1</sup> The characteristic diffraction peaks of MIL-101(Cr) are assigned at  $2\theta = 2.81^\circ, 3.29^\circ, 3.98^\circ, 4.19^\circ, 5.92^\circ,$  and  $9.62^\circ$ . However, the relative peak intensity at  $2.81^\circ$  and  $3.29^\circ$  was lesser in AcP-MIL-101(Cr) and 4.0Pd-MIL-101(Cr), compared to that in MIL-101(Cr). This could be attributed to the grafting of AcP and incorporation of Pd NPs into the MIL-101(Cr) pore structure.<sup>2</sup> The decreased intensity became more pronounced with an increase in Pd loading (0.5–4.0 wt%). It should be noted that the diffraction peaks from Pd NPs were not observed in the wide-angle XRD patterns, presumably due to the small Pd loadings or high Pd dispersion.

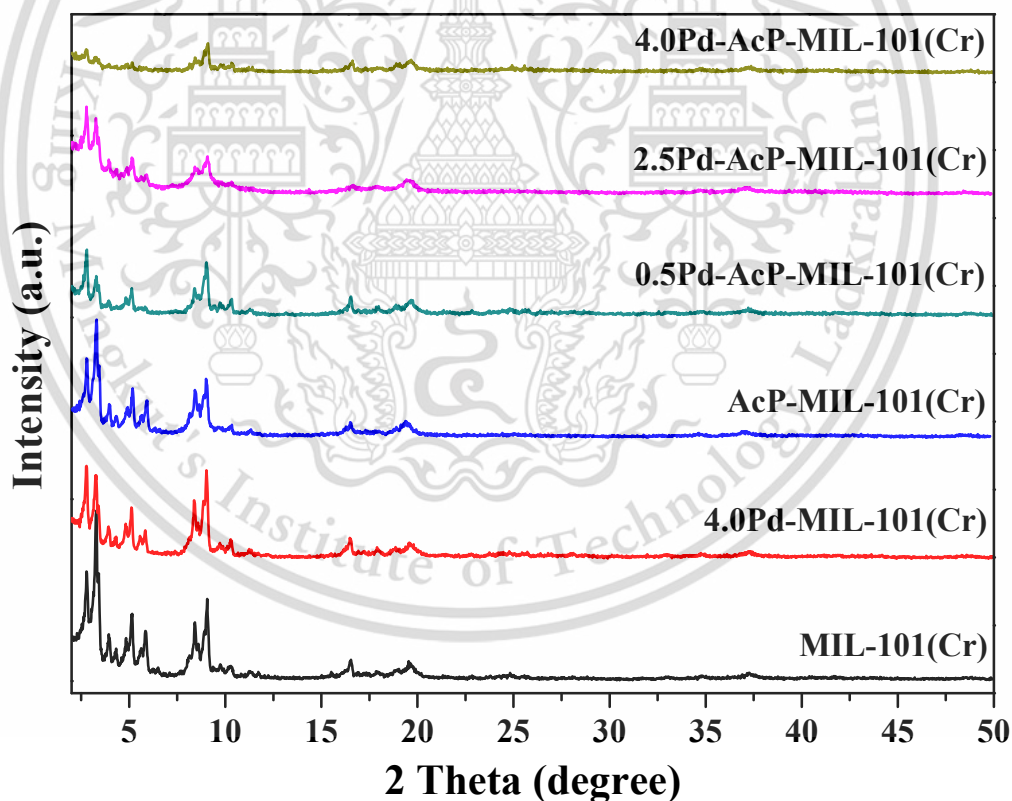
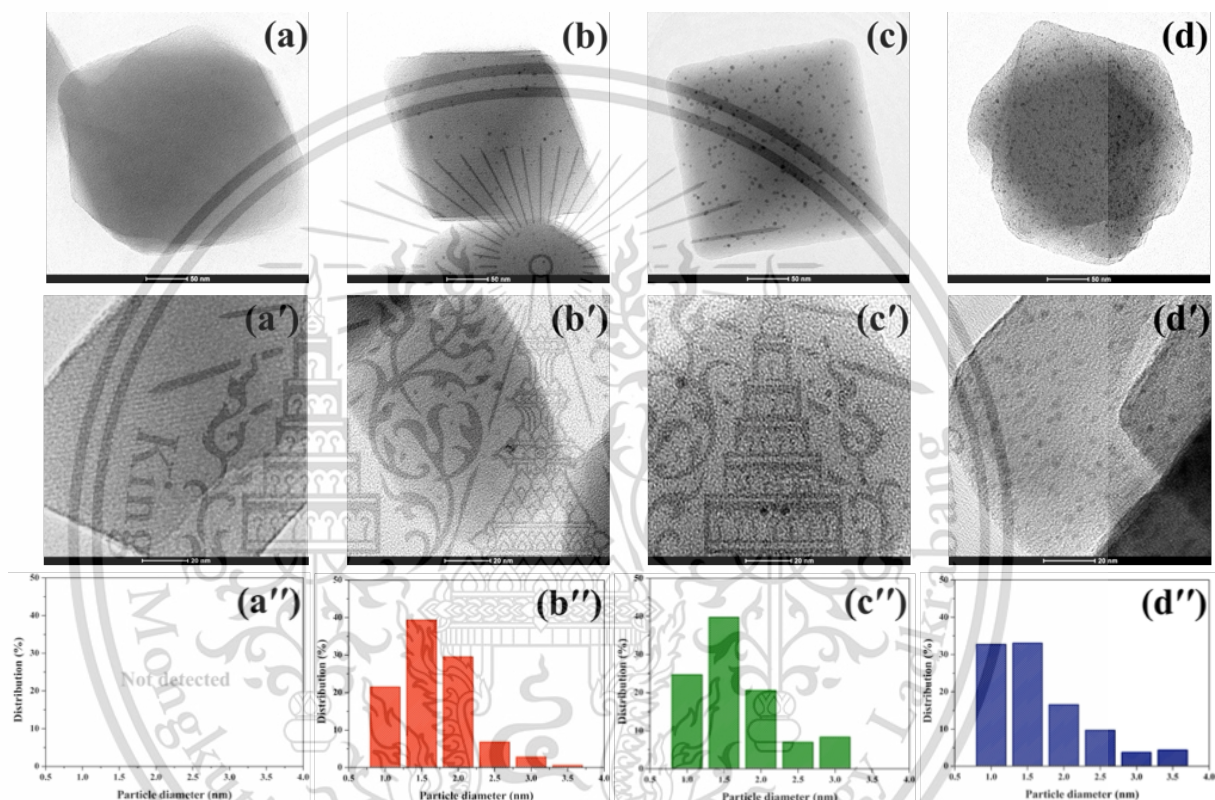


Figure 5.1 XRD patterns of all MOF samples

Figure 5.2 presents that the observed ultrafine Pd particles through the TEM analysis of 0.5Pd-AcP-MIL-101(Cr). As the Pd loading increased, the Pd nanoparticles were obviously seen with an average size of  $\sim 1.9$  nm for 2.5Pd-AcP-MIL-101(Cr), 4.0Pd-AcP-MIL-101(Cr), and 4.0Pd-MIL-101(Cr). It is likely that these Pd NPs (at loading  $>0.5$  wt%) would be dispersed on the external surface of MIL-101(Cr) crystals.



**Figure 5.2** TEM images of 0.5Pd-AcP-MIL (a, a'), 2.5Pd-AcP-MIL (b, b'), 4.0Pd-AcP-MIL (c, c') and 4.0Pd-MIL (d, d') at low and high magnification and their Pd particle size distribution (a''-d'') from approximately 200 Pd particles counted

All MOF samples exhibited high surface areas with typical type I isotherms, indicating the microporous materials, as shown in Table 5.1 and Figure 5.3. The grafted AcP and incorporation of Pd cause the lower surface area and pore volume, compared with MIL-101(Cr), as expected. The synthesized MIL-101(Cr) has a surface area of  $4440 \text{ m}^2\cdot\text{g}^{-1}$  and a pore volume of  $1.7 \text{ mL}\cdot\text{g}^{-1}$  - similar to those reported elsewhere.<sup>3</sup> Although the specific surface area dropped slightly, the pore volume was retained when AcP was grafted (Table 5.1, entry 3), whereas both the surface area and pore volume were decreased with Pd loading (Table 5.1, entry 2, 4–6). This suggests that some Pd NPs could position themselves inside the pore of MIL-101(Cr).

**Table 5.1 Composition and textural properties of the samples**

| Entry | Sample                | Pd loading (wt%) | $S_{\text{BET}}$ ( $\text{m}^2 \cdot \text{g}^{-1}$ ) | $V_{\text{pore}}$ ( $\text{cm}^3 \cdot \text{g}^{-1}$ ) | AcP loading <sup>(d)</sup> |                      | AcP/Cr <sup>3+</sup> ratio | Elemental composition (wt%) |     |     | Decomposition temperature ( $^{\circ}\text{C}$ ) | Weight loss (wt%) |
|-------|-----------------------|------------------|---|---|----------------------------|----------------------|----------------------------|-----------------------------|-----|-----|--|-------------------|
|       |                       |                  |   |   | wt%                        | $\text{mmol g}^{-1}$ |                            | C                           | H   | N   |  |                   |
| 1     | MIL-101(Cr)           | -                | 4440  | 1.7   | -                          | -                    | -                          | 28.2                        | 2.4 | 1.9 | 318  | 60.4              |
| 2     | 4.0Pd-MIL-101(Cr)     | 3.8              | 2380  | 1.2   | -                          | -                    | -                          | 27.5                        | 2.4 | 1.5 | 296  | 54.9              |
| 3     | AcP-MIL-101(Cr)       | -                | 3120  | 1.6   | 6.0                        | 0.5                  | 0.17                       | 28.3                        | 3.6 | 2.6 | 370  | 64.9              |
| 4     | 0.5Pd-AcP-MIL-101(Cr) | 0.5              | 2250  | 1.3   | 4.8                        | 0.4                  | 0.14                       | 28.7                        | 2.8 | 2.4 | 384  | 62.9              |
| 5     | 2.5Pd-AcP-MIL-101(Cr) | 2.5              | 2090  | 1.0   | 4.8                        | 0.4                  | 0.14                       | 30.1                        | 4.3 | 2.2 | 360  | 60.8              |
| 6     | 4.0Pd-AcP-MIL-101(Cr) | 4.0              | 2000  | 1.1   | 3.7                        | 0.3                  | 0.13                       | 23.7                        | 5.0 | 1.9 | 265  | 60.2              |

<sup>a</sup>ICP-OES, <sup>b</sup>Multipoint Brunauer-Emmett-Teller analysis, <sup>c</sup>Barrett-Joyner-Halenda method desorption, <sup>d</sup>Estimated from CHN analysis results, <sup>e</sup>CHN analysis, <sup>f</sup>Onset decomposition temperature under  $\text{N}_2$  atmosphere, <sup>g</sup>Weight loss at  $500 \text{ }^{\circ}\text{C}$  under air atmosphere.

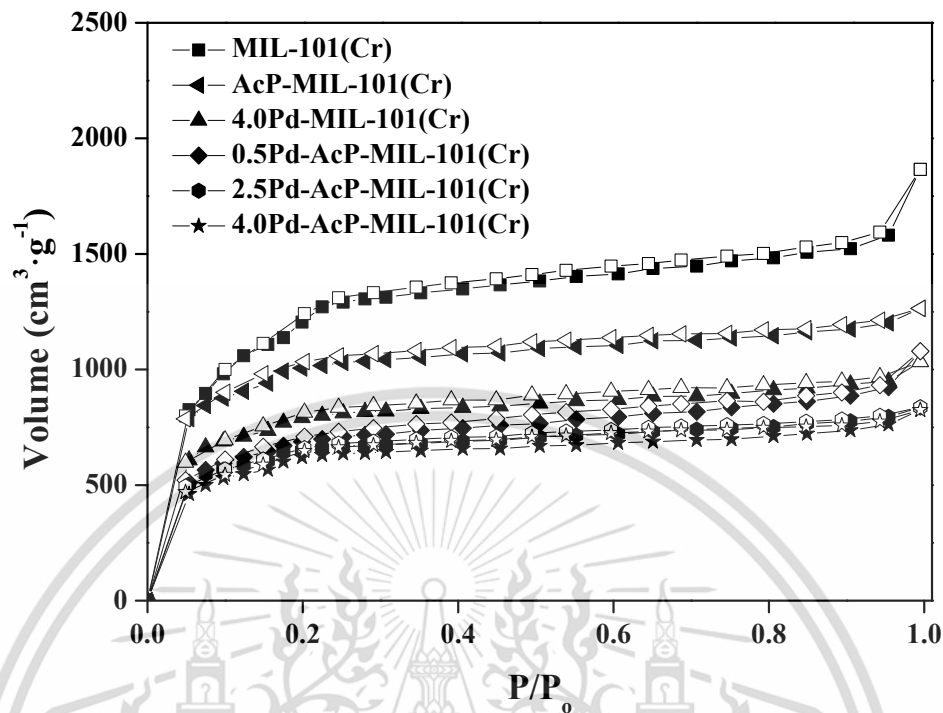
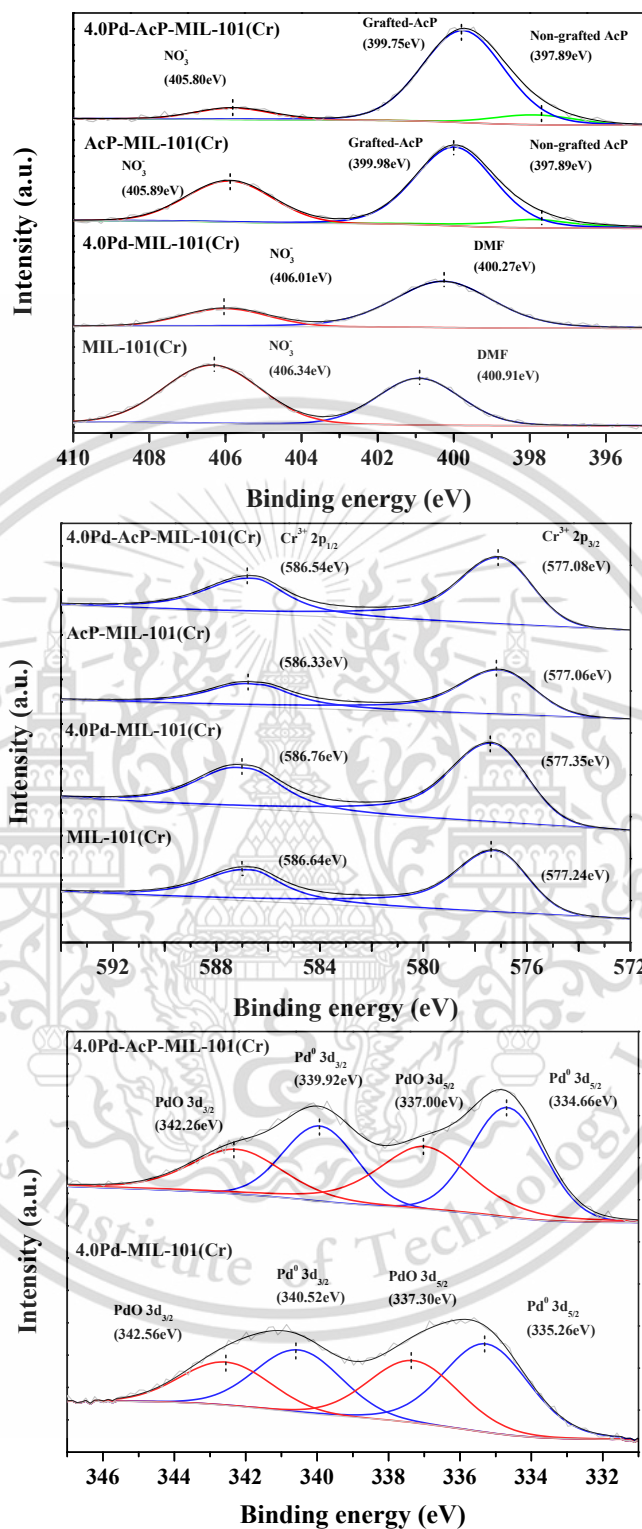
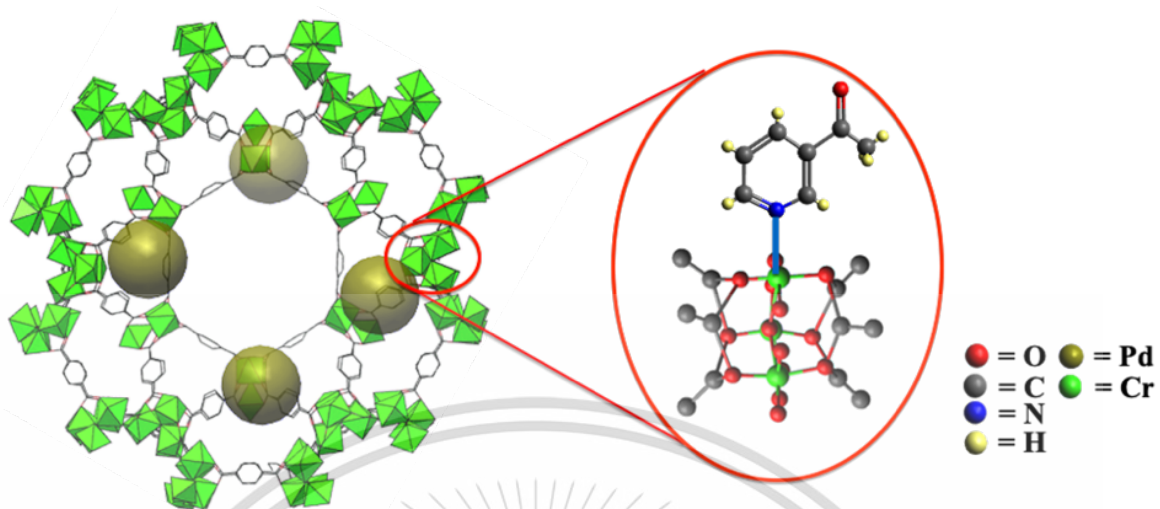


Figure 5.3  $N_2$  adsorption and desorption isotherms of the samples at 77 K

The organic composition of the prepared MIL-101(Cr) and the grafted AcP, Pd, and AcP-Pd on MIL-101(Cr), as determined by the CHN analysis, is also shown in Table 5.1. In addition to C, H, and O in MIL-101(Cr),  $\sim 1.9$  wt % of N was observed. This could be attributed to the nitrate anion ( $NO_3^-$ ), as evidenced (Figure 5.4) by the N 1s peak at 406 eV of  $NO_3^-$ .<sup>4</sup> The nitrate anion acts as a counter ion on one of the  $Cr^{3+}$  nodes in the MIL-101(Cr) framework, as shown in Figure 5.5.<sup>5</sup> However, trace amounts of DMF<sup>6</sup> may be retained on the surface, during XPS analysis, as seen by the signal at  $\sim 401$  eV<sup>7</sup> and also by the  $^1H$  NMR of the extracted sample (Figure 5.6). Once AcP was grafted in MIL-101(Cr), the N content increased, compared to its parent MIL-101(Cr). Accordingly, the N content (from the CHN analysis) could roughly indicate the AcP loading of approximately 6 wt% (Table 5.1, entry 3). Estimation of the AcP loading is described in the Appendix C5). The incorporation of Pd led to a decrease in the AcP content, as expected. TGA, in air, also suggested the same trend in the organic content (Figure 5.7a).



**Figure 5.4** Peak-fitted core-line XPS spectra of MIL-101(Cr), 4.0Pd-MIL-101(Cr), AcP-MIL-101(Cr) and 4.0Pd-AcP-MIL-101(Cr) for (a) N(1s), (b) Cr(2p) and Pd(3d)



**Figure 5.5** Demonstration of grafted organic hydrogen carrier (i.e., 3-acetylpyridine) in Pd-encapsulated-MIL-101 (Cr)

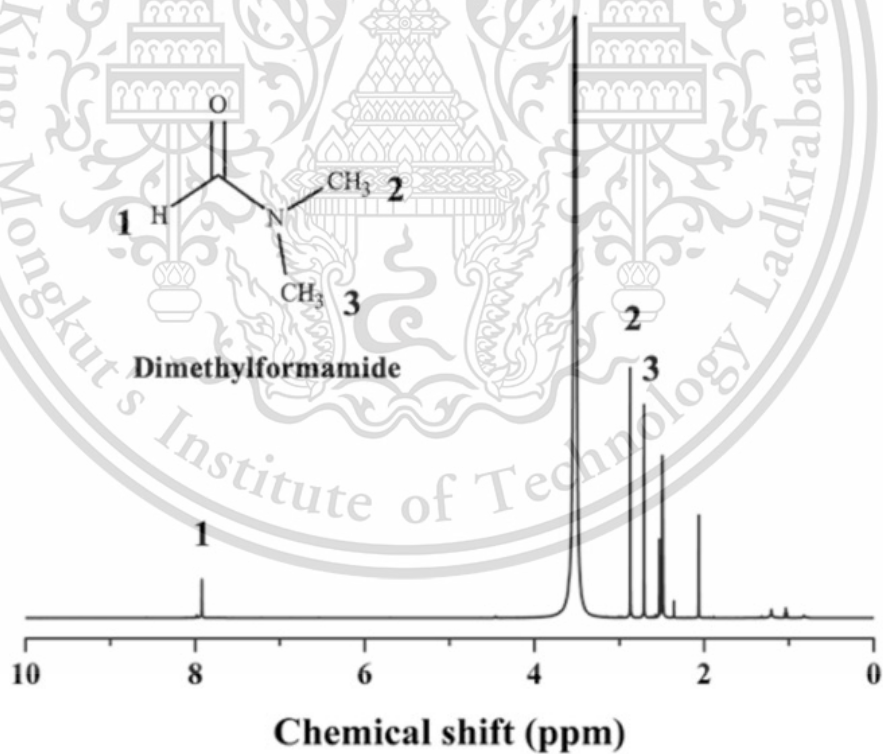


**Figure 5.6**  $^1\text{H}$  NMR spectrum of as-prepared MIL-101(Cr) extract with  $\text{DMSO-d}_6$  under sonication for 1 h

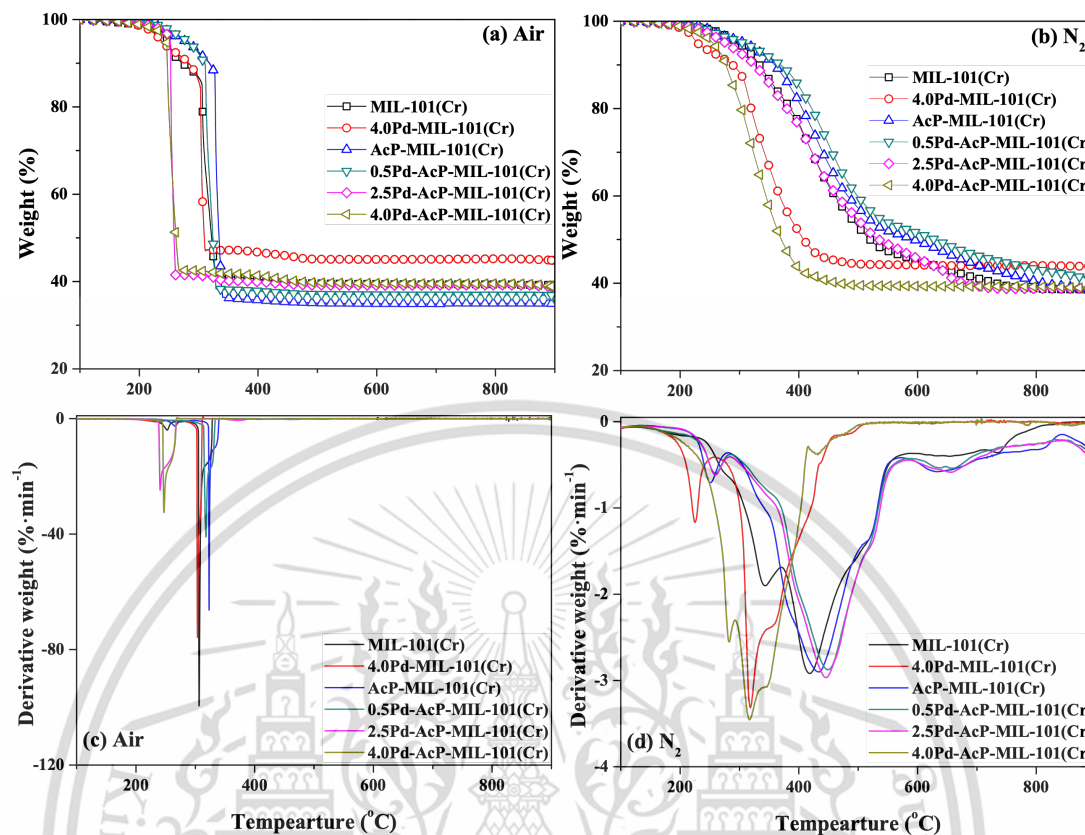


Figure 5.7 TGA thermograms of the samples under (a) Air and (b) N<sub>2</sub>

The IR spectra of MIL-101(Cr), Pd-MIL-101(Cr), and Pd-AcP-MIL-101(Cr) are shown in Figure 5.8. The characteristic bands of the symmetric ( $1401\text{ cm}^{-1}$ ) and asymmetric ( $1617\text{ cm}^{-1}$ ) vibrational stretching of carboxylate ligands,  $\nu(\text{COO}^-)$ ,<sup>8</sup> were observed in all samples. The weak and narrow bands at  $749$ ,  $1017$ , and  $1157\text{ cm}^{-1}$  can be assigned to the  $\delta(\text{C-H})$  and  $\gamma(\text{C-H})$  vibrations of the benzene rings.<sup>9</sup> The presence of these vibrational bands strongly confirm the successful formation of the MIL-101(Cr) framework. For all AcP-grafted samples, additional characteristic bands of AcP at  $702$ ,  $1273$ , and  $1695\text{ cm}^{-1}$  were detected. These bands are ascribed to the vibration of symmetric out-of-plane bending of 3-substituted pyridine,  $\delta(\text{C-H})$ , and  $\nu(\text{C=O})$ -conjugated ketone of AcP. It was also observed that the  $\nu(\text{C=O})$  vibration of the grafted AcP shifted to a higher frequency, suggesting an interaction of AcP with the Lewis acid center, presumably the  $\text{Cr}^{3+}$  nodes of the MIL-101(Cr) framework, as shown Figure 5.9.

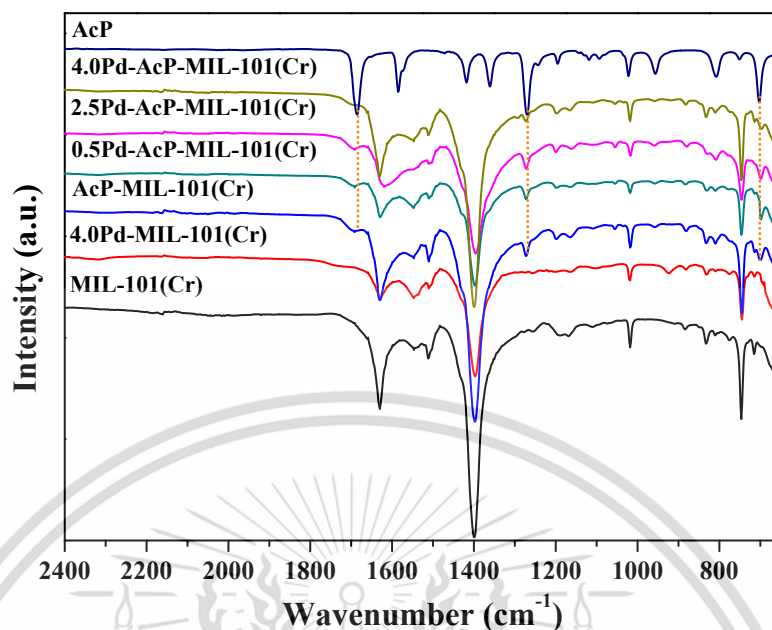


Figure 5.8 FTIR spectra of MOF samples

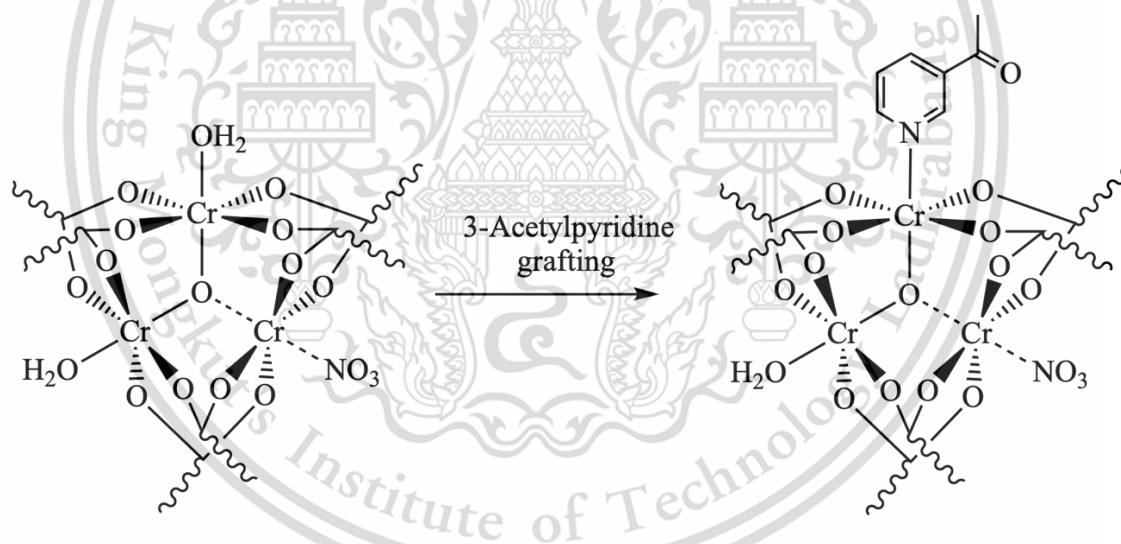
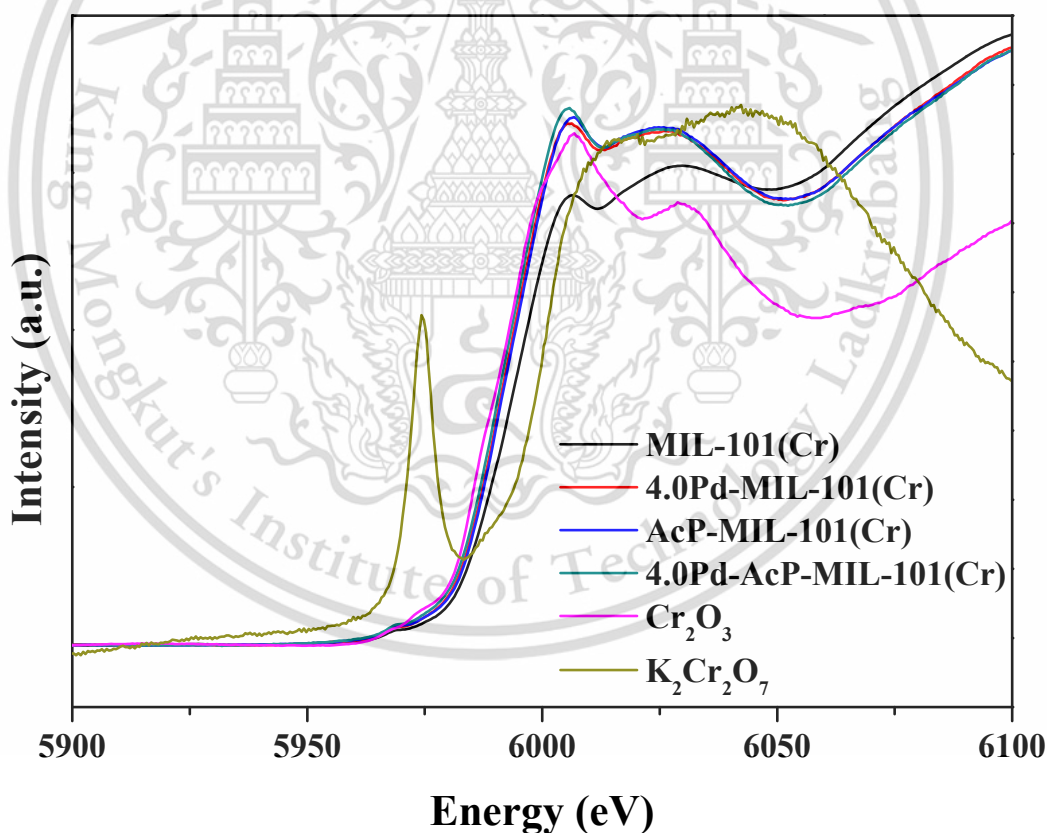


Figure 5.9 Interaction of AcP with the Lewis acid center at  $\text{Cr}^{3+}$  nodes of the MIL-101(Cr)

In a supporting manner, the N 1s binding energy of AcP shifted from 397.89 eV (nongrafted AcP) to 399.98 eV (Figure 5.4a). This significant shift (+2.1 eV) indicates that the grafted AcP could be bound to the  $\text{Cr}^{3+}$  Lewis acid center via N–Cr coordination.<sup>10</sup> In line with this view, the peak-fitted Cr 2p spectra of the AcP-grafted samples shifted from the typical binding energies of  $\text{Cr}^{3+}$  (577.24 eV)<sup>11</sup> to a lower energy (577.06 eV, Figure 5.4b).

The incorporated AcP interacts not only with  $\text{Cr}^{3+}$  nodes but also with Pd, as suggested by XPS results. Figure 5.4c clearly shows a red shift of binding energy (Pd  $3d_{5/2}$ ) from 335.26 to 334.66 eV (ca.  $\sim 0.6$  eV) for 4.0Pd-AcP-MIL-101(Cr).<sup>12</sup> This slight shift in the binding energy could be attributed to an increase in the electron density of Pd interacting with the grafted AcP. However, the incorporation of Pd had no effect on the local structure of MIL-101(Cr): no change in XPS and XANES spectra was observed when Pd was introduced (Figure 5.10). Figure 5.4b shows that the Cr 2p spectra of MIL-101(Cr) and 4.0Pd-MIL-101(Cr) appear the same. Also, Figure 5.10 exhibits that the edge energy at 6005 eV corresponding to  $\text{Cr}^{3+}$  remains intact. It is worth noting that the observed  $\text{Pd}^{2+}$  species from XPS could be derived from the surface oxidation of metallic Pd when exposed to air.<sup>13</sup>



**Figure 5.10** Cr K-edge XANES spectra of MIL-101(Cr), 4.0Pd-MIL-101(Cr), AcP-MIL-101(Cr) and 4.0Pd-AcP-MIL-101(Cr) and  $\text{Cr}_2\text{O}_3$

The interaction between AcP and  $\text{Cr}^{3+}$  nodes led to a higher stability of AcP-MIL-101(Cr), compared to the parent MIL-101(Cr) (Figure 5.7). In Table 5.1, the onset decomposition temperature shifted from 318 to 370 °C in the  $\text{N}_2$  atmosphere. However, after introducing Pd NPs, the thermal stability significantly decreased, especially at high Pd loadings (i.e., 265 °C for 4.0Pd-AcP-MIL-101(Cr), Table 5.1 entry 4–6). This could be derived from the presumption that the incorporated Pd NPs may activate the decarboxylation of the terephthalate linkers, leading to the deconstruction of the MIL-101(Cr) frameworks. Accordingly, the operating temperature for hydrogen uptake and evolution should not exceed 250 °C for these xPd-AcP-MIL-101(Cr) samples.

### 5.1.2 Hydrogen evolution and uptake

Evolution of  $\text{H}_2$  from 2.5Pd-AcP-MIL-101(Cr) (under Ar), after hydrogenation under  $\text{H}_2$  at 200 °C for 1 h, is shown in Figure 5.11. Hydrogen was initially released from the sample at ~180 °C (Figure 5.11, section a). This is presumably due to the dehydrogenation of 3-(1-hydroxyethyl)pyridine (HEP), the hydrogenated form of AcP. As the sample was treated in  $\text{H}_2$  at 200 °C for 1 h before the measurement, the incorporated AcP would be hydrogenated to HEP, anchoring on the  $\text{Cr}^{3+}$  node (as illustrated in Figure 5.12). The formation of HEP in 2.5Pd-AcP-MIL-101(Cr) can be evidenced by *in situ* FTIR spectroscopy as shown in Figure 5.13a. Upon heating under  $\text{H}_2$  from 30 to 200 °C, the intensities of the saturated  $\nu(\text{C-H})$  signals (~2840–2980  $\text{cm}^{-1}$ ) notably increased, together with the appearance of the O–H vibration band at 3265  $\text{cm}^{-1}$ , particularly at 150–200 °C. This is because additional methine (CH) would be formed along with the hydroxyls (OH) when the carbonyl group of AcP is hydrogenated to HEP. Accordingly, one could expect that the incorporated HEP would be dehydrogenated, liberating  $\text{H}_2$ , as observed upon heating in Ar. This is in line with the decrease in the intensity of saturated  $\nu(\text{C-H})$  vibrations with the disappearance of the  $\nu(\text{O-H})$  band in the *in situ* FTIR spectra of the hydrogenated 2.5Pd-AcP-MIL-101(Cr) sample (Figure 5.13b).

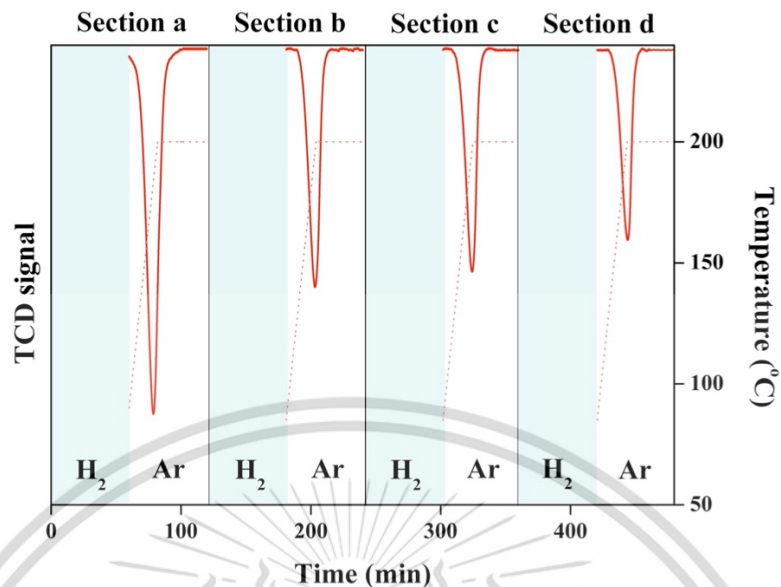


**Figure 5.11** Hydrogen evolution cycles of 2.5Pd-AcP-MIL-101(Cr) under Ar after hydrogenation under H<sub>2</sub> at 200 °C for 1 h (normalized areas of H<sub>2</sub> evolution are tabulated in Table 5.2)

**Table 5.2** Normalized areas of H<sub>2</sub> evolution after hydrogenation at 200 °C for 1 h

| <i>Sample</i>  | <i>Sections</i> |               |               |               |
|--|-----------------|---------------|---------------|---------------|
|  | <i>a</i>        | <i>b</i>      | <i>c</i>      | <i>d</i>      |
| <i>2.5Pd-AcP-MIL-101(Cr)</i>                                       | <i>1383.45</i>  | <i>753.24</i> | <i>666.08</i> | <i>561.27</i> |
| <i>Normalized Area</i>   |                 |               |               |               |
| <i>H<sub>2</sub> evolution (mmol H<sub>2</sub> g<sup>-1</sup>)</i> | <i>0.50</i>     | <i>0.27</i>   | <i>0.24</i>   | <i>0.20</i>   |

(a) Defined as the integrated area of H<sub>2</sub> evolution peak, divided by the integrated area of 1% H<sub>2</sub> in Ar pulse and (b) Calculated by multiplying the normalized area with molar concentration\* of 1% H<sub>2</sub>/Ar pulse under Ar carrier (0.019 μmolH<sub>2</sub>·pulse<sup>-1</sup>), then divided by the sample weight.

\*The molar concentration of 1% H<sub>2</sub> in Ar pulse was calibrated with the H<sub>2</sub> evolution peak from the decomposition of known-mass NaBH<sub>4</sub>. (by titration with standard KIO<sub>3</sub> solution), explained in Appendix C2.

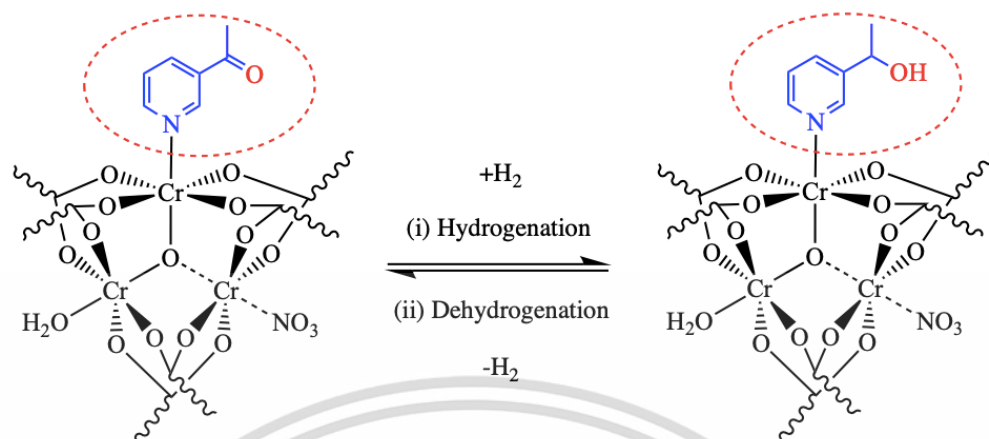


**Figure 5.12** Chemical hydrogen storage of Pd-AcP-MIL-101(Cr) by hydrogenation and dehydrogenation of 3-Acetylpyridine (AcP) over Pd nanoparticles

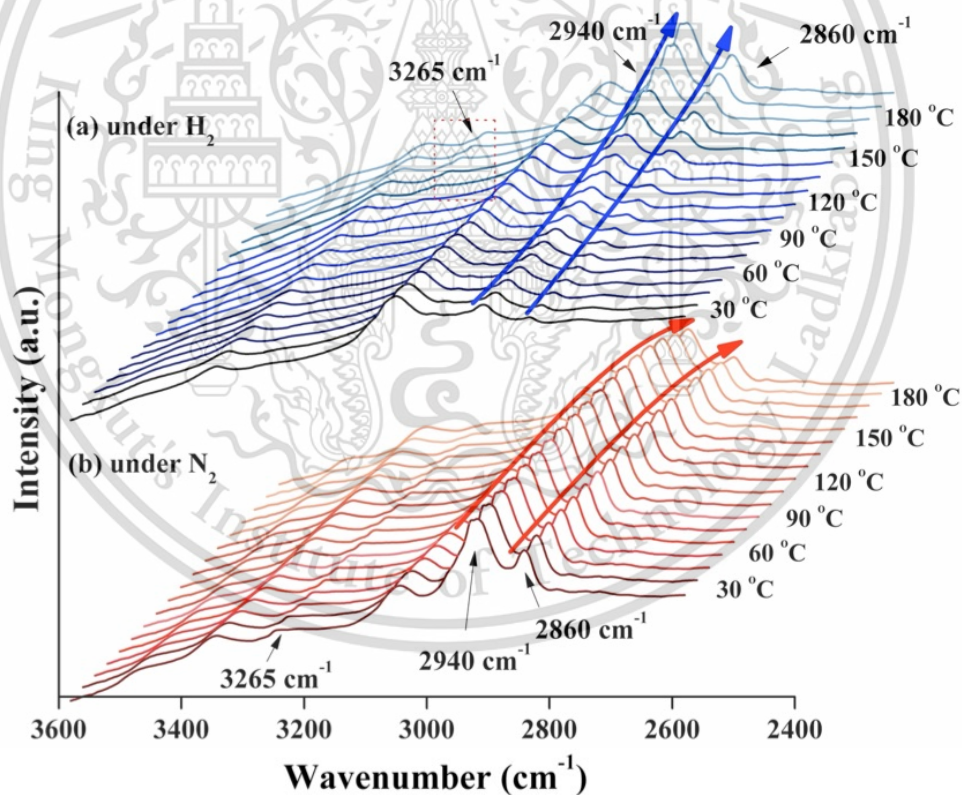


**Figure 5.13** *In situ* FTIR spectra of 2.5Pd-AcP-MIL-101(Cr) from 30 to 200 °C with a heating rate of 5 °C·min<sup>-1</sup> (a) under H<sub>2</sub> (hydrogenation) and (b) under N<sub>2</sub> (dehydrogenation)

After the first H<sub>2</sub> evolution was observed, the sample was subsequently treated under the flow of H<sub>2</sub> at 200 °C for another 1 h. The grafted AcP would be re-hydrogenated to HEP at this condition. Hence, another H<sub>2</sub> evolution can be observed again upon heating under Ar flow (Figure 5.11, section b). This clearly indicates that reversible hydrogenation and dehydrogenation of 2.5Pd-AcP-MIL-101(Cr) can be accomplished simply by changing the partial pressure of H<sub>2</sub> at an elevated temperature (~180 °C). In a supporting manner, the process was repeated for the other two cycles, and similar results were obtained (Figure 5.11, section c and d). This reproducible H<sub>2</sub> evolution clearly suggests that this sample may well act as a chemical hydrogen storage, in which “H<sub>2</sub> uptake” is achieved in the hydrogenation step, whereas the dehydrogenation leads to “H<sub>2</sub> release”.

In line with these results, H<sub>2</sub>-TPRe of 4.0Pd-AcP-MIL-101(Cr) shows both hydrogen consumption and evolution under 10% H<sub>2</sub> in Ar (Figure 5.14a). The hydrogen consumption of this sample was initially observed as the temperature was raised from 50 to 200 °C. This is attributed to the hydrogenation of AcP to HEP, presumably catalyzed by the incorporated Pd NPs. After cooling from the first cycle (hydrogenation), the hydrogen evolution (peak IV) was detected from 150 to 200 °C with 0.80 mmol H<sub>2</sub>·g<sup>-1</sup>, possibly from the dehydrogenation of HEP back to AcP. It is worth noting that, for the first dehydrogenation cycle, trace amounts of acetate that remained in the sample may decompose to other gases that also intensify the observed signal. The observed hydrogenation at 80–150 °C and dehydrogenation at 150–200 °C were not evidenced in samples without the incorporated Pd NPs (MIL-101(Cr) and AcP-MIL-101(Cr), Figure 5.14c–d). The trace amount of hydrogen (~0.02 mmol H<sub>2</sub>·g<sup>-1</sup>, Figure 5.14b) released from 4.0Pd-MIL-101(Cr), without AcP, is attributed to the  $\beta$ -hydride decomposition of Pd–H, as reported by Sandoval et al.<sup>14</sup> This indicates that the incorporated Pd NPs catalyzes both the hydrogenation and dehydrogenation of AcP, leading to the hydrogen uptake and subsequent release.

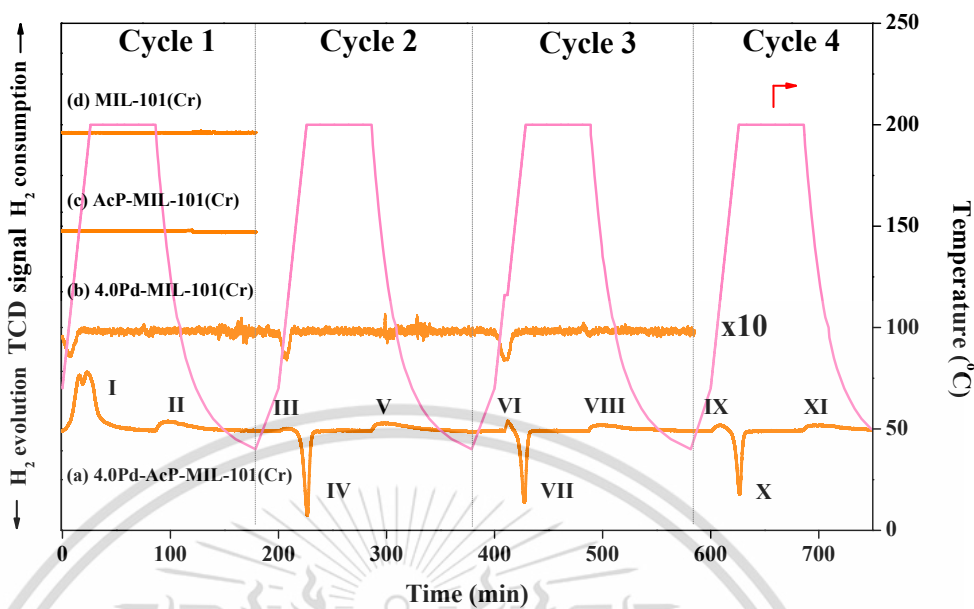


Figure 5.14  $H_2$ -TPR profiles of the sample testing under 10%  $H_2$  in Ar from 70 to 200 °C with a heating rate of 5 °C·min<sup>-1</sup> and cooled under 10%  $H_2$  in Ar to room temperature, and then the process was repeated for three times (normalized areas of  $H_2$  evolution/consumption are tabulated in Table 5.3)

Table 5.3 Normalized areas of  $H_2$  consumption and  $H_2$  evolution of samples from  $H_2$ -TPR

| Samples               | $H_2$ consumption - $H_2$ evolution (mmol $H_2$ g <sup>-1</sup> ) |       |       |       |       |       |       |       |       |       |       |
|-----------------------|---|-------|-------|-------|-------|-------|-------|-------|-------|-------|-------|
|                       | I   | II    | III   | IV    | V     | VI    | VII   | VIII  | IX    | X     | XI    |
| 4.0Pd-MIL-101(Cr)     | 0.023   | 0.019 | 0.021 |       |       |       |       |       |       |       |       |
| 4.0Pd-AcP-MIL-101(Cr) | 2.169   | 0.541 | 0.038 | 0.798 | 0.457 | 0.074 | 0.638 | 0.377 | 0.097 | 0.542 | 0.385 |

(a) Defined as the integrated area of  $H_2$  evolution peak, divided by the integrated area of 1%  $H_2$  in Ar pulse. (b) Calculated by multiplying the normalized area with molar concentration\* of 1%  $H_2$  in Ar pulse under 10%  $H_2$  in Ar carrier (0.799  $\mu\text{mol}H_2\cdot\text{pulse}^{-1}$ ), then divided by the sample weight.

\*The molar concentration of 1%  $H_2$  in Ar pulse was calibrated with the  $H_2$  consumption peak from the reduction of known-mass  $\text{CuO}$ , detailed in Appendix C2.

Interestingly, during cooling after the first hydrogenation step, another hydrogen consumption was detected (peak II, Figure 5.11a), suggesting that some of AcP may be retained after holding at 200 °C. This is presumably due to the thermodynamic limitation of AcP hydrogenation at 200 °C for typical ketones.<sup>15</sup> Accordingly, the remaining AcP can be hydrogenated at a relatively lower temperature (from 190 to 70 °C). However, the rate of hydrogenation would be relatively low at these temperature ranges, as seen from Figure 5.15. Hence, additional hydrogenation, with small hydrogen consumption (peak III, Figure 5.11a), was observed again upon heating from 80 to 150 °C during the second H<sub>2</sub>-TPRe cycle. At this stage, the incorporated organic hydrogen carrier would be virtually present in the hydrogenated form, HEP. Therefore, a consecutive dehydrogenation to AcP can take place (peak IV), as discussed earlier.

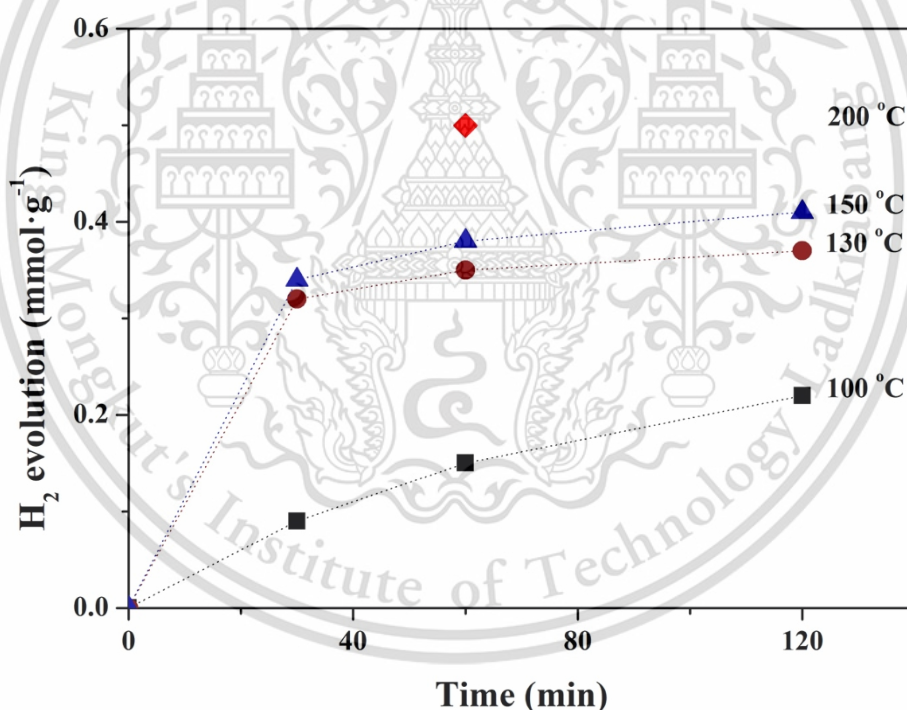


**Figure 5.15** Effect of hydrogenation temperatures at 100, 130, 150 and 200 °C with time for H<sub>2</sub> evolution of 2.5Pd-AcP-MIL-101(Cr)

The hydrogenation of AcP can be revealed again during cooling in the second cycle (peak V,  $0.46 \text{ mmol H}_2\cdot\text{g}^{-1}$ ) and also at the beginning of the third heating cycle, with a lesser extent (peak VI,  $0.07 \text{ mmol H}_2\cdot\text{g}^{-1}$ ). As the temperature rose over  $150 \text{ }^\circ\text{C}$ , dehydrogenation of HEP was repeatedly promoted, as seen by the hydrogen evolution in the third cycle (peak VII,  $0.64 \text{ mmol H}_2\cdot\text{g}^{-1}$ ). Similar phenomena can be replicated in the fourth cycle (peaks VIII and IX for hydrogenation and peak X for dehydrogenation). This clearly suggests that hydrogenation and dehydrogenation of the organic hydrogen carrier (AcP) can be reversibly facilitated by the cooling and heating cycles.

It is essential to state that the hydrogen evolution of the grafted AcP in Pd-MIL-101(Cr), for all experiments in Figures 5.11 and 5.14, decreased with the number of heating cycles. Especially in Figure 5.11 [2.5Pd-AcP-MIL-101(Cr)], the hydrogen evolution decreased from 0.50, 0.27, 0.24, to  $0.20 \text{ mmol H}_2\cdot\text{g}^{-1}$  for the first to the fourth cycles (see Figure 5.16). One could expect that the decline of the hydrogen evolution was caused by the partial destruction of the MIL-101(Cr) framework, presumably via the hydrogenolysis of organic linkers<sup>16</sup> during the hydrogenation at  $200 \text{ }^\circ\text{C}$  for 1 h. This was evidenced by a decrease in the crystallinity of 2.5Pd-AcP-MIL-101(Cr) after four heating cycles, as shown in Figure 5.17c. Accordingly, a lower hydrogenation temperature at  $150 \text{ }^\circ\text{C}$  was tested, and the hydrogen evolution was recorded for four cycles, as also illustrated in Figure 5.16. It was clear that hydrogenation at  $150 \text{ }^\circ\text{C}$  led to a lower hydrogen evolution ( $0.38 \text{ mmol H}_2\cdot\text{g}^{-1}$  as compared to  $0.50 \text{ mmol H}_2\cdot\text{g}^{-1}$  at  $200 \text{ }^\circ\text{C}$ ). This suggests that a relatively less HEP is produced after the hydrogenation of AcP at  $150 \text{ }^\circ\text{C}$ , presumably due to a lower hydrogenation rate at this temperature. It is deduced from Figure 5.15 that the hydrogenation rate is a function of temperature, where hydrogen evolution rises steadily from 0.15 to  $0.50 \text{ mmol H}_2\cdot\text{g}^{-1}$  after hydrogenation at temperatures from  $100$  to  $200 \text{ }^\circ\text{C}$  for 1 h. Nevertheless, the hydrogen evolution for the following cycles was somewhat similar to the initial value (i.e.,  $0.31\text{--}0.34 \text{ mmol H}_2\cdot\text{g}^{-1}$ ) when the sample was hydrogenated at  $150 \text{ }^\circ\text{C}$ . This implies a higher stability of the sample, compared to that hydrogenated at  $200 \text{ }^\circ\text{C}$ . In a supporting manner, the sample crystallinity after four heating cycles at  $150 \text{ }^\circ\text{C}$  was retained (Figure 5.17b).

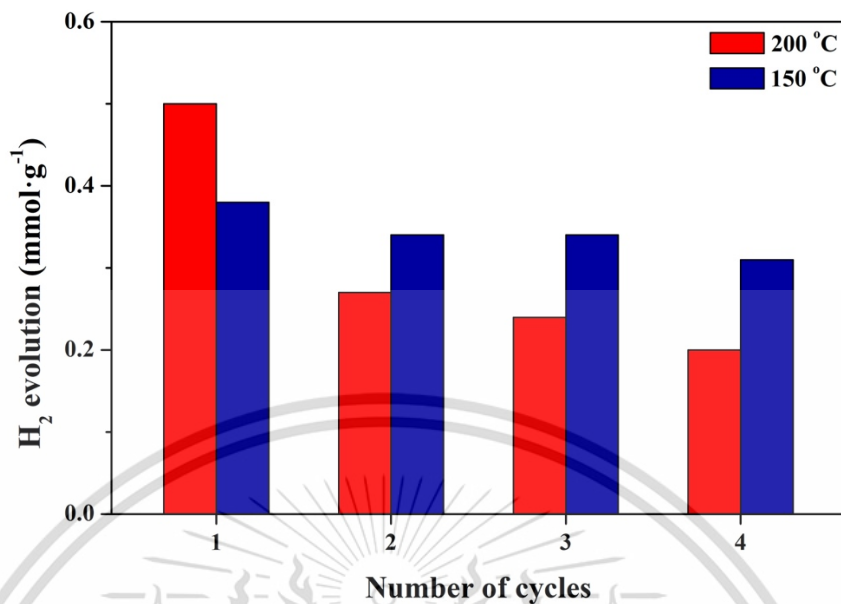


Figure 5.16 Effect of hydrogenation temperature (150 °C and 200 °C, for 1 h) on the stability of 2.5Pd-AcP-MIL-101(Cr) when dehydrogenated at 200 °C for 1 h

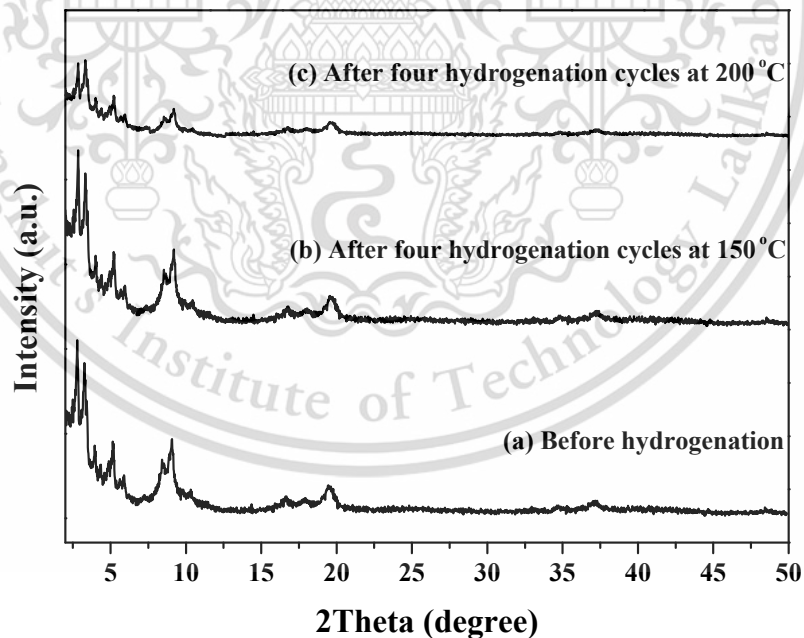
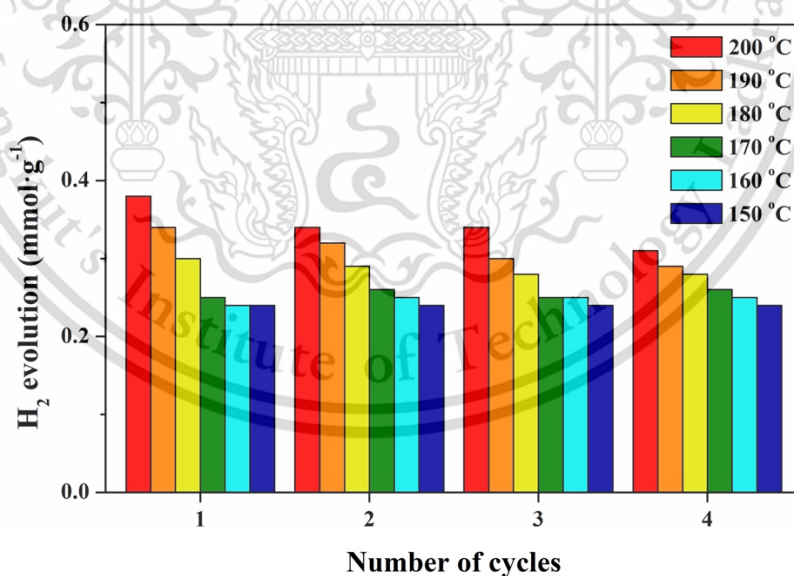


Figure 5.17 XRD patterns of 2.5Pd-AcP-MIL-101(Cr) (a) before hydrogenation and after four hydrogenation cycles (b) at 150 °C and (c) at 200 °C

In addition to the hydrogenation temperature, the stability of 2.5Pd-AcP-MIL-101(Cr) was affected by the final temperature for the dehydrogenation cycle. When the final temperature for dehydrogenation decreased from 200 to 150 °C a lower hydrogen release was measured (0.38 down to 0.24 mmol H<sub>2</sub>·g<sup>-1</sup>), as shown in Figure 5.18. This could be presumably due to a thermodynamic limitation, as dehydrogenation is an endothermic process (see in Figure 5.19).<sup>15</sup> Despite the similar rate of dehydrogenation, Figure 5.20 clearly shows that a considerable extent of hydrogen evolution is observed at a higher temperature. However, at a temperature higher than 150 °C, the hydrogen evolution decreased with the number of cycles, especially at 200 °C - from 0.38 to 0.31 mmol H<sub>2</sub>·g<sup>-1</sup> - after four cycles (see Figure 5.18). This suggests that dehydrogenation above 150 °C could possibly damage the MOFs in a manner similar to that observed for the hydrogenation process (Figures 5.15 and Figure 5.16). However, the observed hydrogen release remained the same for dehydrogenation at 150 °C. Accordingly, the optimum dehydrogenation temperature would be less than 150 °C, in order to maintain the stability of 2.5Pd-AcP-MIL-101(Cr).



**Figure 5.18** Effect of dehydrogenation temperature on the sample stability of 2.5Pd-AcP-MIL-101(Cr): hydrogenation at 150 °C, heating rate of 5 °C·min<sup>-1</sup> for 1 h, followed by dehydrogenation at different temperatures

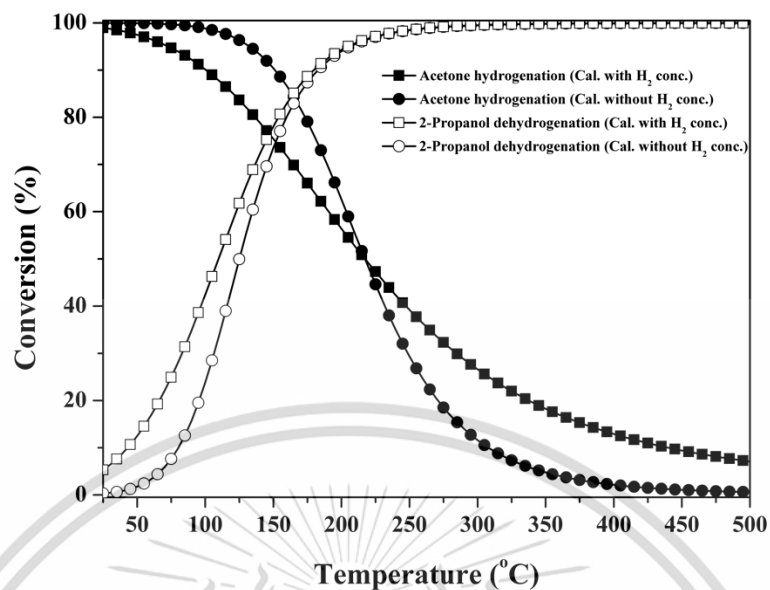


Figure 5.19 Thermodynamic equilibrium as a function of temperature for hydrogenation of acetone and dehydrogenation of 2-propanol

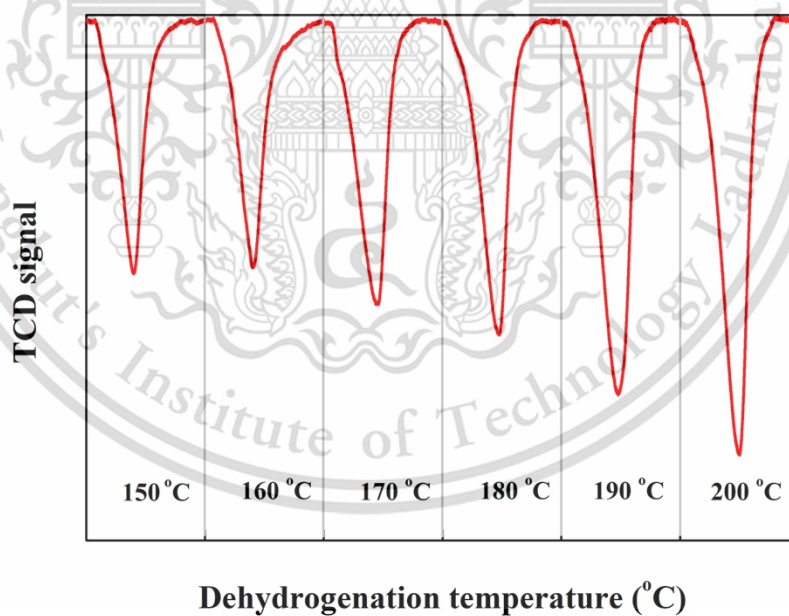
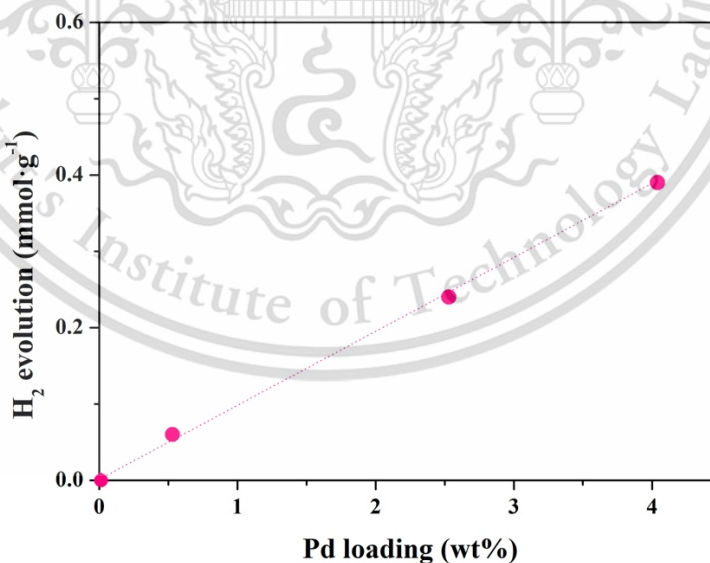


Figure 5.20 Hydrogen evolution of 2.5Pd-AcP-MIL-101(Cr) after hydrogenation at 150 °C, following dehydrogenation at different temperatures

Although the hydrogen uptake and evolution were relatively lower when the sample was hydrogenated and dehydrogenated at 150 °C, the same amount of hydrogen consumed and released was reproduced. This key behavior clearly shows the hydrogen storage ability of 2.5Pd-AcP-MIL-101(Cr). To improve the hydrogen storage capacity, the rate of both hydrogenation and dehydrogenation should be enhanced. This can be achieved by increasing the Pd content (Figure 5.21). H<sub>2</sub> evolution linearly depended on the incorporated Pd. This was not the result of the hydrogen dissociation by Pd NPs, as only a trace amount of hydrogen evolution was observed in 4.0Pd-MIL-101(Cr), as shown previously in Figure 5.14b. Moreover, an excessive amount of grafted AcP (0.50 mmol·g<sup>-1</sup>) was present in all samples, compared to Pd loading (0.04–0.37 mmol·g<sup>-1</sup>). Therefore, with the same amount of AcP, the observed increase in the hydrogen evolution with Pd loading would be derived from the higher rate of hydrogenation and dehydrogenation catalyzed by Pd. Despite the fact that only the dispersed Pd NPs were evidenced on the external surface of MIL-101(Cr) by TEM (Figure 5.2), the interaction between Pd and AcP hinted by XPS (Figure 5.4) and the observed catalytic activity suggested that some of Pd would coexist with AcP inside the MIL-101(Cr) pocket.



**Figure 5.21** Effect of Pd loading on H<sub>2</sub> evolution at Pd loading 0.5, 2.5, and 4.0 wt% by hydrogenation under H<sub>2</sub> and dehydrogenation under Ar flow at 150 °C for 1 h

With appropriate hydrogenation and dehydrogenation temperatures (i.e., 150 °C) and Pd loading, chemical hydrogen storage can be demonstrated over 4.0Pd-AcP-MIL-101(Cr) for at least 10 cycles, with a consistent storage capacity of 0.33 mmol H<sub>2</sub>·g<sup>-1</sup> per cycle, as shown in Figure 5.22. Under these conditions, the Pd particle size remained in the same range (1.91 ± 0.7 nm), as compared to the fresh sample (Figure 5.23). This suggests that Pd agglomeration may be inhibited by the interaction between Pd and the MOFs, as discussed earlier. Compared to LOHCs, 4.0Pd-AcP-MIL-101(Cr) can be readily operated at constant temperature and atmospheric pressure for both hydrogen uptake and release. Despite the low hydrogen storage capacity (<0.1 wt %), this noncryogenic storage material can be feasibly handled, compared to other atmospheric cryo-adsorption materials (~1 wt %) operating at an extremely low temperature (77 K). Nevertheless, further investigation for a higher hydrogen storage capacity will be necessarily required, especially by increasing the organic hydrogen carrier loading in the MOFs.

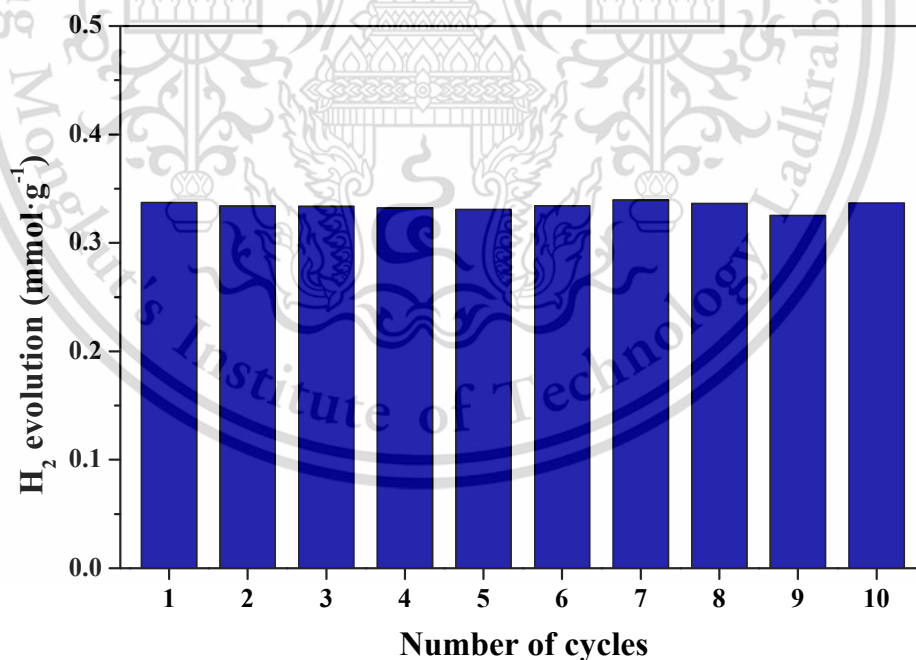


**Figure 5.22** Recyclability of 4.0Pd-AcP-MIL-101(Cr) over hydrogenation and dehydrogenation cycles at 150 °C

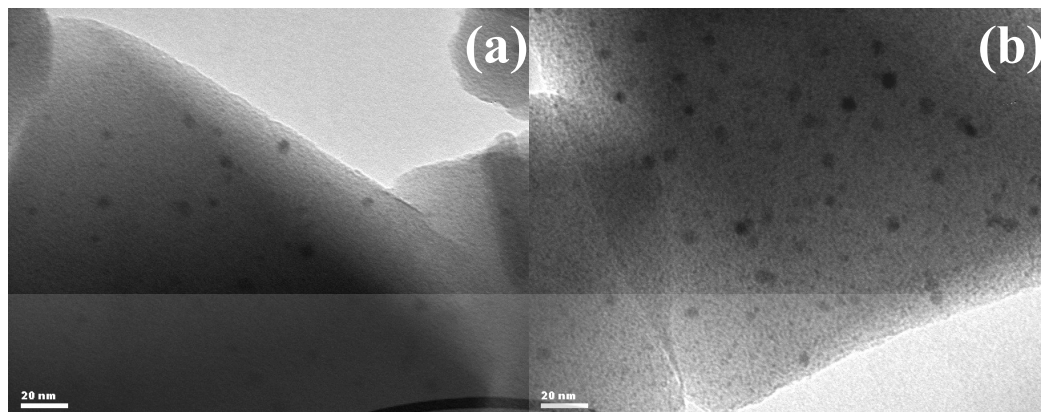


**Figure 5.23** TEM images of 4.0Pd-AcP-MIL-101(Cr) before (a) and after (b) 10<sup>th</sup> cycles for testing catalyst recyclability of hydrogenation at 150 °C for 1 h and then dehydrogenation at 150 °C for 1 h

## 5.2 Conclusions

In this study, Pd-AcP-MIL-101(Cr) can be successively used as a hydrogen storage material, where AcP acts as an organic hydrogen carrier. The grafted AcP interacts with the Cr<sup>3+</sup> nodes in MIL-101(Cr), via coordinative covalent bonding with the N-pyridine ring. The incorporated Pd is well dispersed and interacts with the grafted AcP in MIL-101(Cr). Hydrogen uptake efficiently proceeds via hydrogenation at the carbonyl group of AcP to HEP, whereas the hydrogen release is accomplished by the dehydrogenation of HEP to AcP. The incorporated Pd NPs catalytically drive both processes at atmospheric pressure. The hydrogen uptake and release can be regulated either by (i) the operating temperature or (ii) the hydrogen partial pressure at a constant temperature. Over 150 °C, the MIL-101(Cr) frameworks can be damaged by the heating cycle, whereas the optimum operating temperature at 150 °C provides a consistent hydrogen storage of 0.33 mmol H<sub>2</sub>·g<sup>-1</sup> per cycle. Pd-AcP-MIL-101(Cr) reported herein is one of the noncryogenic chemical hydrogen storage material with a measurable hydrogen storage capacity. More importantly, this new hydrogen storage material can be operated at constant temperature and pressure (atmospheric), simply by tuning the hydrogen partial pressure. However, the hydrogen storage in terms of weight capacity (<0.1 wt %) is too low from a practical point of view. Further investigation for higher hydrogen storage capacity will be necessarily required.

This material is reserved for educational use only, not allowed for commercial use.

Forbidden to modify the content, and cite the document when use.

### 5.3 References

- (1) Ferey, G. A Chromium Terephthalate-Based Solid with Unusually Large Pore Volumes and Surface Area. *Science* **2005**, *309* (5743), 2040–2042.
- (2) Zhang, J.-Y.; Zhang, N.; Zhang, L.; Fang, Y.; Deng, W.; Yu, M.; Wang, Z.; Li, L.; Liu, X.; Li, J. Adsorption of Uranyl Ions on Amine-Functionalization of MIL-101(Cr) Nanoparticles by a Facile Coordination-Based Post-Synthetic Strategy and X-Ray Absorption Spectroscopy Studies. *Sci. Rep.* **2015**, *5* (1), 13514.
- (3) Zhao, T.; Jeremias, F.; Boldog, I.; Nguyen, B.; Henninger, S. K.; Janiak, C. High-Yield, Fluoride-Free and Large-Scale Synthesis of MIL-101(Cr). *Dalton Trans.* **2015**, *44* (38), 16791–16801.
- (4) Hu, B.; Xue, Z.; Wang, H.; Cai, L.; Xiong, H.; Jiang, X.; Du, Z. Biomimetic Syntheses of Pure or Doped Metal Hydroxide Nitrate Thin Films by a Dual-Template Approach. *J. Mater. Chem.* **2009**, *19* (16), 2373–2379.
- (5) Maksimchuk, N. V.; Zalomaeva, O. V.; Skobelev, I. Y.; Kovalenko, K. A.; Fedin, V. P.; Kholdeeva, O. A. Metal–Organic Frameworks of the MIL-101 Family as Heterogeneous Single-Site Catalysts. *Proc. R. Soc. A.* **2012**, *468* (2143), 2017–2034.
- (6) Liu, X.; Zhao, Y. Y. Adsorption Kinetics of Methylene Blue on Synthesized DMF-MIL-101(Cr), a DMF-Functionalized Metal-Organic Framework. *Key Eng. Mater.* **2015**, *671*, 419–424.
- (7) Gu, J.; Li, X.; Hu, D.; Liu, Y.; Zhang, G.; Jia, X.; Huang, W.; Xi, K. Green Synthesis of Amphiphilic Carbon Dots from Organic Solvents: Application in Fluorescent Polymer Composites and Bio-Imaging. *RSC Adv.* **2018**, *8* (23), 12556–12561.
- (8) Maksimchuk, N.; Timofeeva, M.; Melgunov, M.; Shmakov, A.; Chesalov, Y.; Dybtsev, D.; Fedin, V.; Kholdeeva, O. Heterogeneous Selective Oxidation Catalysts Based on Coordination Polymer MIL-101 and Transition Metal-Substituted Polyoxometalates. *J. Catal.* **2008**, *257* (2), 315–323.
- (9) Yang, K.; Sun, Q.; Xue, F.; Lin, D. Adsorption of Volatile Organic Compounds by Metal–Organic Frameworks MIL-101: Influence of Molecular Size and Shape. *J. Hazard. Mater.* **2011**, *195*, 124–131.

- (10) Yang, F.; Yang, C.-X.; Yan, X.-P. Post-Synthetic Modification of MIL-101(Cr) with Pyridine for High-Performance Liquid Chromatographic Separation of Tocopherols. *Talanta* **2015**, *137*, 136–142.
- (11) Zhang, Z.; Shi, W.; Wang, W.; Xu, Y.; Bao, X.; Zhang, R.; Zhang, B.; Guo, Y.; Cui, F. Interfacial Electronic Effects of Palladium Nanocatalysts on the By-Product Ammonia Selectivity during Nitrite Catalytic Reduction. *Environ. Sci.: Nano* **2018**, *5* (2), 338–349.
- (12) Gniewek, A.; Trzeciak, A.; Ziolkowski, J.; Kepinski, L.; Wrzyszczyk, J.; Tylus, W. Pd-PVP Colloid as Catalyst for Heck and Carbonylation Reactions: TEM and XPS Studies. *J. Catal.* **2005**, *229* (2), 332–343.
- (13) Zhao, X.; Jin, Y.; Zhang, F.; Zhong, Y.; Zhu, W. Catalytic Hydrogenation of 2,3,5-Trimethylbenzoquinone over Pd Nanoparticles Confined in the Cages of MIL-101(Cr). *Chem. Eng. J.* **2014**, *239*, 33–41.
- (14) Sandoval, V. H.; Gigola, C. E. Characterization of Pd and Pd-Pb/c -A1203 Catalysts. A TPR-TPD Study. *Appl. Catal. Gen.* **1996**, *148*, 81–96.
- (15) *Lange's Handbook of Chemistry*, 15. ed.; Dean, J. A., Lange, N. A., Eds.; McGraw-Hill handbooks; McGraw-Hill: New York, NY, 1999.
- (16) Moon, H. R.; Lim, D.-W.; Suh, M. P. Fabrication of Metal Nanoparticles in Metal–Organic Frameworks. *Chem. Soc. Rev.* **2013**, *42* (4), 1807–1824.

## Chapter 6

# Highly stable Pd<sup>2+</sup> species anchoring on ethylenediamine-grafted-MIL-101(Cr) as a robust oxidation catalyst

In this chapter, a robust Pd<sup>2+</sup> species in MIL-101(Cr) containing ethylenediamine as an anchoring ligand was synthesized. The Pd<sup>2+</sup> species was introduced in the ethylenediamine-grafted MIL-101(Cr), using double solvent adsorption to ensure the Pd<sup>2+</sup> dispersion in the MIL-101(Cr) framework. The interactions of ethylenediamine with both Cr<sup>3+</sup> nodes in MIL-101(Cr) and the incorporated Pd<sup>2+</sup>, were examined by various spectroscopic methods at high temperatures. The stability of Pd<sup>2+</sup> species under reducing conditions was studied by *in situ* X-ray absorption near edge structure (*in situ* XANES). In addition, activity of the Pd<sup>2+</sup> species within ethylenediamine grafted MIL-101(Cr) was tested for styrene oxidation. The effect of ethylenediamine: Pd<sup>2+</sup> molar ratio on the catalytic activity and stability was also investigated.

## 6.1 Results and discussions

### 6.1.1 Synthesis and Characterization

#### 6.1.1.1 Ethylenediamine grafted MIL-101(Cr)

The XRD patterns of all samples matched well with the pure MIL-101(Cr), reported by Ferey et al.<sup>1</sup> with characteristic peaks at  $2\theta = 2.81^\circ, 3.29^\circ, 3.97^\circ, 5.16^\circ, 5.88^\circ, 8.44^\circ, 9.06^\circ, 10.34^\circ, 11.26^\circ, 16.5^\circ, 16.92^\circ, 17.27^\circ$  and  $19.56^\circ$  (Figure 6.1). Trace amount of  $\text{Cr}_2\text{O}_3$  was observed by the diffraction peaks at  $24.77^\circ$  and  $37.29^\circ$ . The MIL-101(Cr) sample exhibited corresponding metal/organic content (Figure 6.2) and typical  $\text{N}_2$  adsorption isotherms type I (Figure 6.3) with a high surface area of  $4210 \text{ m}^2/\text{g}$  and a pore volume of  $2.6 \text{ cm}^3/\text{g}$  - similar to those reported elsewhere<sup>2</sup> (Table 6.1). In addition to C and H,  $\sim 1.9 \text{ wt}\%$  N was observed by CHN analysis (Table 6.1, entry 1) for pure MIL-101(Cr). This could be attributed to (i) the nitrate counterion of the  $\text{Cr}^{3+}$  nodes<sup>3</sup> and (ii) DMF retained by solvent substitution on the  $\text{Cr}^{3+}$  nodes upon washing. Both species can be evidenced by N 1s XPS at  $406 \text{ eV}$  (nitrate ion)<sup>4</sup> and  $401 \text{ eV}$  (DMF) (Figure 6.4a). Estimation of the ethylenediamine loading is described in appendix C6.

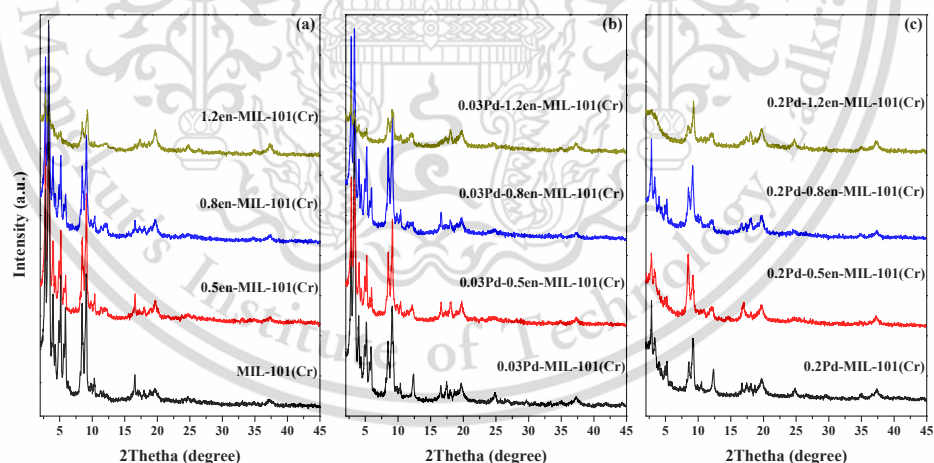


**Figure 6.1** XRD intensity of MIL-101(Cr) when (a) grafted with ethylenediamine and introduced (b) 0.03 wt%Pd and (c) 0.2 wt%Pd over ethylenediamine-grafted samples

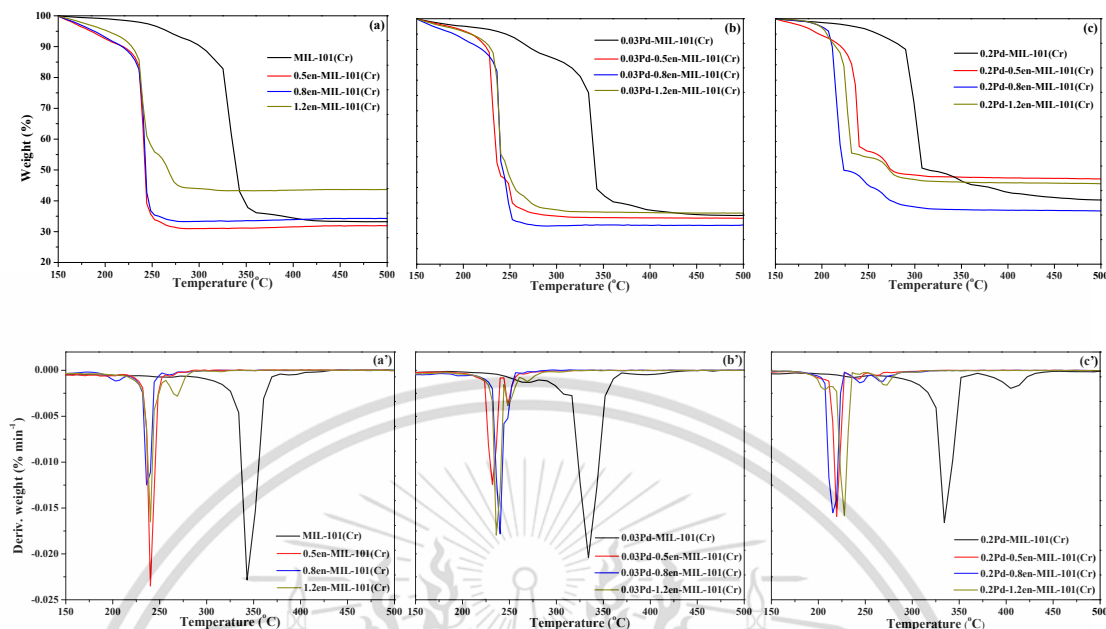


Figure 6.2 TGA and DTG thermograms of MIL-101(Cr) when (a, a') grafted with ethylenediamine and introduced (b, b') 0.03 wt%Pd and (c, c') 0.2 wt%Pd over ethylenediamine-grafted samples

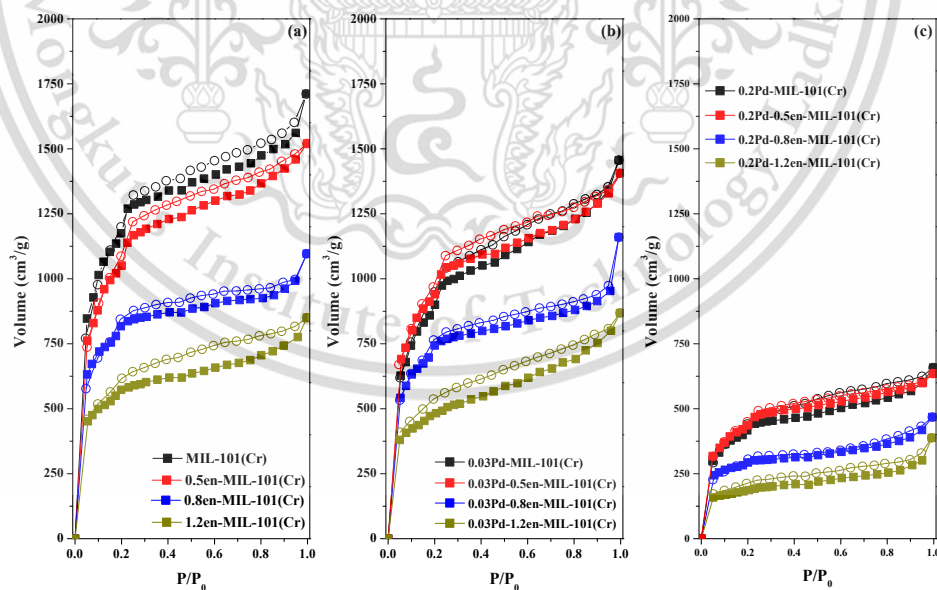


Figure 6.3 N<sub>2</sub> adsorption isotherm of (a) ethylenediamine-grafted MIL-101(Cr) with (b) 0.03 wt%Pd and (c) 0.2 wt%Pd loadings

Table 6.1 Elemental composition and physical properties of the samples

| Entry | Sample                   | $S_{\text{BET}}^a$<br>( $\text{m}^2/\text{g}$ ) | $V_{\text{pore}}^b$<br>( $\text{cm}^3/\text{g}$ ) | Element composition (wt%) |              |              |              | Ethylenediamine loading <sup>e</sup> |        | Pd loading <sup>e</sup> |        | Ethylenediamine/<br>Pd<br>molar ratio |
|-------|--------------------------|---|---|---------------------------|--------------|--------------|--------------|--------------------------------------|--------|-------------------------|--------|---------------------------------------|
|       |                          |   |   | $\text{Cr}^{3+c}$         | $\text{C}^d$ | $\text{H}^d$ | $\text{N}^d$ | wt%                                  | mmol/g | wt%                     | mmol/g |                                       |
| 1     | MIL-101(Cr)              | 4210  | 2.6   | 21.9                      | 28.2         | 2.4          | 1.9          | -                                    | -      | -                       | -      | -                                     |
| 2     | 0.5en-MIL-101(Cr)        | 3790  | 2.3   | 23.5                      | 30.4         | 3.7          | 3.2          | 1.63                                 | 0.58   | -                       | -      | -                                     |
| 3     | 0.8en-MIL-101(Cr)        | 2650  | 1.7   | 21.5                      | 32.3         | 3.2          | 4.0          | 2.04                                 | 0.73   | -                       | -      | -                                     |
| 4     | 1.2en-MIL-101(Cr)        | 1890  | 1.3   | 26.8                      | 27.2         | 4.5          | 5.3          | 3.23                                 | 1.15   | -                       | -      | -                                     |
| 5     | 0.03Pd-0.5en-MIL-101(Cr) | 3390  | 2.2   | 22.4                      | 29.9         | 2.3          | 2.5          | 1.35                                 | 0.48   | 0.26                    | 0.03   | 16.0                                  |
| 6     | 0.03Pd-0.8en-MIL-101(Cr) | 2450  | 1.7   | 21.4                      | 29.5         | 2.8          | 3.4          | 1.67                                 | 0.60   | 0.25                    | 0.02   | 20.0                                  |
| 7     | 0.03Pd-1.2en-MIL-101(Cr) | 1600  | 1.3   | 22.4                      | 31.8         | 2.8          | 4.6          | 2.62                                 | 0.94   | 0.29                    | 0.03   | 31.3                                  |
| 8     | 0.2Pd-0.5en-MIL-101(Cr)  | 1540  | 0.9   | 22.7                      | 30.5         | 2.4          | 2.1          | 0.97                                 | 0.35   | 1.95                    | 0.18   | 1.8                                   |
| 9     | 0.2Pd-0.8en-MIL-101(Cr)  | 930   | 0.7   | 22.1                      | 25.9         | 2.5          | 2.2          | 1.20                                 | 0.43   | 2.09                    | 0.19   | 2.2                                   |
| 10    | 0.2Pd-1.2en-MIL-101(Cr)  | 610   | 0.6   | 25.7                      | 29.9         | 2.5          | 3.3          | 1.91                                 | 0.68   | 1.94                    | 0.18   | 3.4                                   |
| 11    | 0.03Pd-MIL-101(Cr)       | 3235  | 2.2   | 23.5                      | 29.9         | 2.3          | 1.6          | -                                    | -      | 0.31                    | 0.03   | -                                     |
| 12    | 0.2Pd-MIL-101(Cr)        | 1800  | 1.2   | 28.2                      | 25.3         | 2.4          | 1.3          | -                                    | -      | 2.39                    | 0.22   | -                                     |

<sup>a</sup>BET multipoints, <sup>b</sup>BJH method desorption, <sup>c</sup>ICP-OES, <sup>d</sup>CHN analyzer, <sup>e</sup>Calculated from CHN analysis (as details in appendix C6)

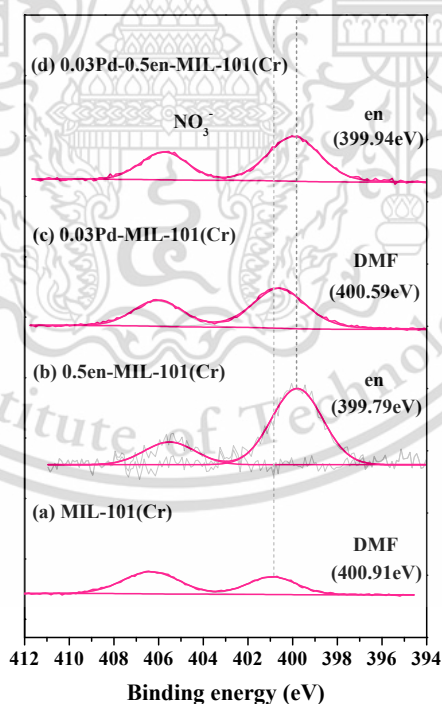
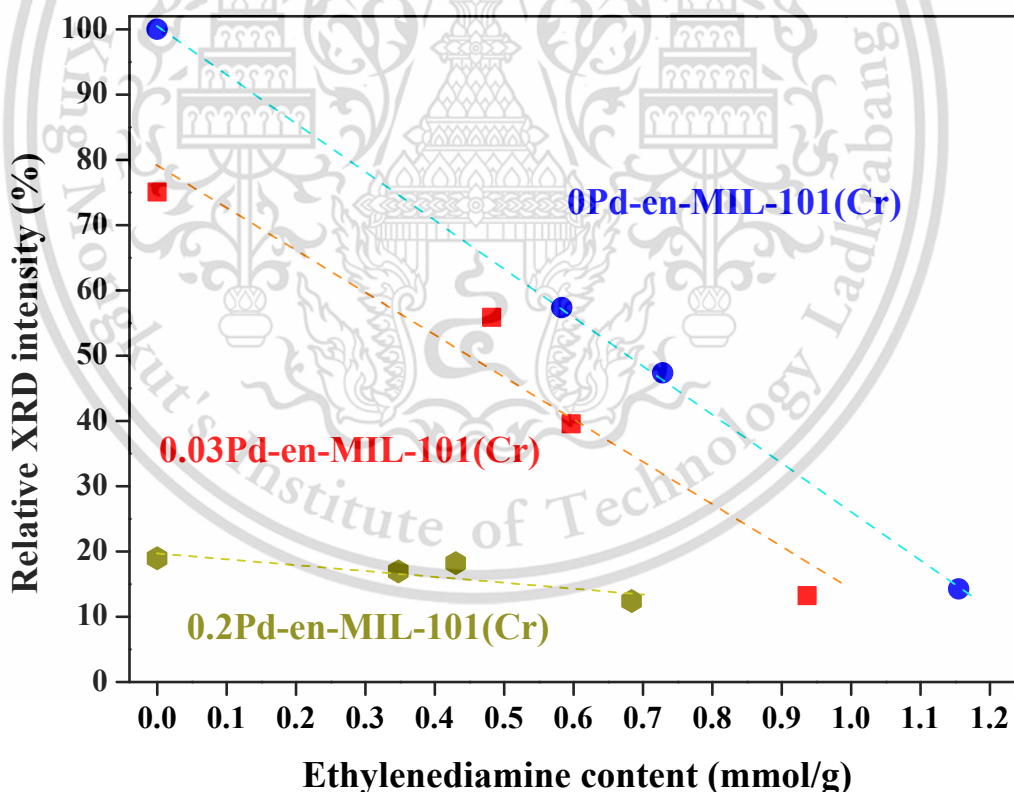


Figure 6.4 High-resolution N 1s XPS spectra of (a) MIL-101(Cr), (b) 0.5en-MIL-101(Cr), (c) 0.03Pd MIL-101(Cr) and (d) 0.03Pd-0.5en-MIL-101(Cr) samples

When the samples were modified with 0.5 to 1.2 mmol/g of ethylenediamine, the N content (from CHN analysis) clearly increased, compared to its parent MIL-101(Cr) (Table 6.1). Whereas the crystallinity, the surface area and pore volume decreased (Table 6.1, entry 1-3). This implies that the incorporated ethylenediamine partially occupied in the micropores,<sup>5</sup> as seen by the decrease in both relative intensity at  $2\theta = 3.3^\circ$  (Figure 6.5) and micropore volume (Figure 6.3a) with ethylenediamine content. A notable decrease in the crystallinity and N<sub>2</sub> adsorption volume were observed when excessive amounts of ethylenediamine (up to 1.2 mmol/g) were introduced. This indicates the partial collapse of the framework due to the ligand substitution at Cr<sup>3+</sup> nodes by the ethylenediamine, that has a ligand strength greater than the terephthalate linker. In support with this view, a hysteresis loop was observed in the N<sub>2</sub> adsorption isotherm of 1.2en-MIL-101(Cr) (Figure 6.3), suggesting a rise in mesoporosity of this sample.



**Figure 6.5** Effect of ethylenediamine content on the relative XRD intensity ( $2\theta = 3.3^\circ$ ) of MIL 101(Cr) samples with and without Pd

Grafting with ethylenediamine led to a rise of new peak at 399.8 eV<sup>6</sup> as seen from N 1s XPS spectra of 0.5en-MIL-101(Cr), for example (Figure 6.4b). While, the NO<sub>3</sub><sup>-</sup> counterion peak (~406 eV) remained unchanged, DMF peak (~400.5 eV) disappeared, presumably due to ligand substitution at Cr<sup>3+</sup> node by ethylenediamine. In a supporting manner, the band intensity at 1055 cm<sup>-1</sup> increased with ethylenediamine content (Figure 6.6a-d), in addition to characteristic MIL-101(Cr) bands assigned to symmetric vibrational stretching of carboxylate ligands  $\nu(\text{COO}^-)$  located at 1401 cm<sup>-1</sup>,<sup>7</sup> and weak bands at 749, 1017 and 1157 cm<sup>-1</sup>, assigned to  $\delta(\text{C-H})$  and  $\gamma(\text{C-H})$  vibrations of the benzene rings.<sup>8</sup> The 1055 cm<sup>-1</sup> band corresponded to the C-N stretching vibration of aliphatic amine.<sup>9</sup> Especially at 0.8 and 1.2 mmol/g of ethylenediamine samples, a slight blue-shift of this band (~5 cm<sup>-1</sup>) was noted - compared to the pure ethylenediamine, suggesting a particular interaction of the amine group with the Cr<sup>3+</sup> node, as discussed earlier.

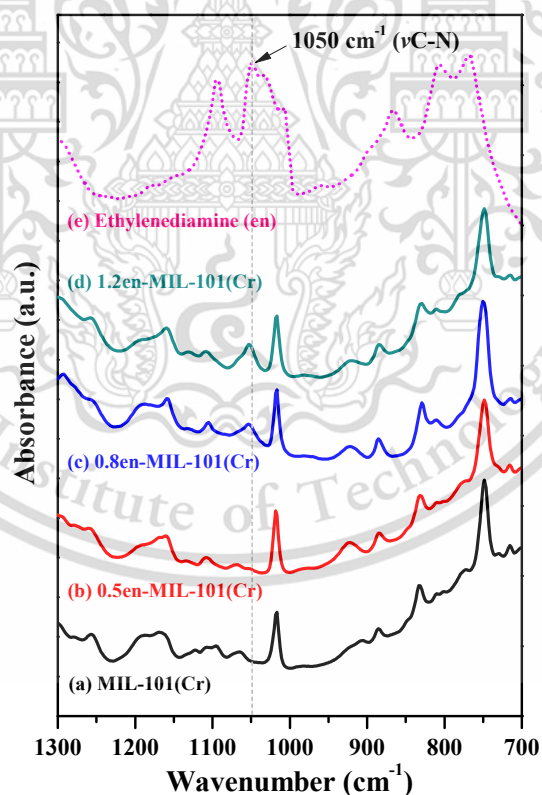


**Figure 6.6** FTIR spectra of (a) MIL-101(Cr), (b) 0.5en-MIL101(Cr), (c) 0.8en-MIL101(Cr), (d) 1.2en-MIL101(Cr) and (e) ethylenediamine (en)

Furthermore, the peak fitted Cr 2p spectra of the 0.5en-MIL-101(Cr) sample (Figure 6.7) also shifted from the typical binding energy of Cr<sup>3+</sup> (577.3 eV) to lower binding energy (576.8 eV). The corresponding red-shift of ~0.5 eV could be attributed to an interaction by the amino groups of ethylenediamine to the unsaturated sites at Cr<sup>3+</sup> nodes via N-Cr<sup>3+</sup> coordination. Again, this was consistent with the disappearance of the DMF, when ethylenediamine was introduced (Figure 6.4b). From the XPS and FTIR results, it is likely that the ethylenediamine replaces the coordinated solvent molecules as shown in scheme 6.1. The substitution by N-donor ligand at Cr<sup>3+</sup> nodes was mentioned elsewhere.<sup>10</sup> We have also reported an incorporation of acetyl pyridine at Cr<sup>3+</sup> nodes in MIL-101(Cr).<sup>11</sup>

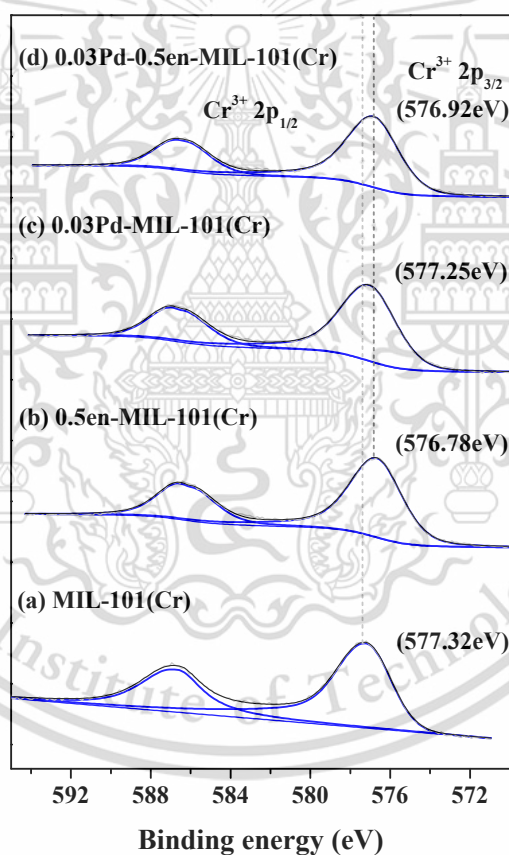
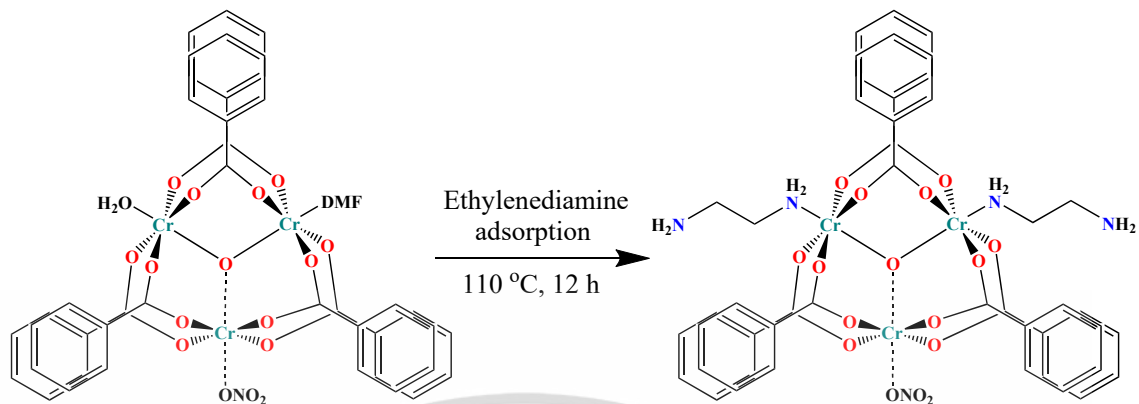


**Figure 6.7** High-resolution Cr 2p XPS spectra of (a) MIL-101(Cr), (b) 0.5en-MIL-101(Cr), (c) 0.03Pd-MIL-101(Cr) and (d) 0.03Pd-0.5en-MIL-101(Cr) samples



**Scheme 6.1** Ethylenediamine adsorption on the  $\text{Cr}^{3+}$  nodes of MIL-101(Cr)

#### 6.1.1.2 Anchoring $\text{Pd}^{2+}$ species on ethylenediamine-grafted-MIL-101(Cr)

When 0.03 mmol Pd/g was further incorporated into the MIL-101(Cr), either with or without ethylenediamine (0.5-1.2 mmol/g), a slight decrease in relative XRD intensity was observed (Figure 6.1b and Figure 6.5). This could be attributed to X-ray adsorption by the relatively large Pd nuclei, occupying in the MIL-101(Cr) micropores, especially at high Pd loading. A decrease in crystallinity was more pronounced after introducing 0.2 mmol Pd/g. This may be derived from partial collapse of the framework, presumably due to decarboxylation of the organic linker, catalyzed by Pd, in the presence of hydrogen. In line with this view, Pd loaded samples exhibited the decrease in surface area, pore volume and relative intensity of the characteristic carboxylate bands (from the organic linker), especially at 0.2 mmol Pd/g content (Table 6.1, entry 5–12, Figure 6.3b-c and Figure 6.8). In addition, the pores of these MOFs could be blocked by the loaded Pd, presumably Pd nanoparticles (Pd NPs).

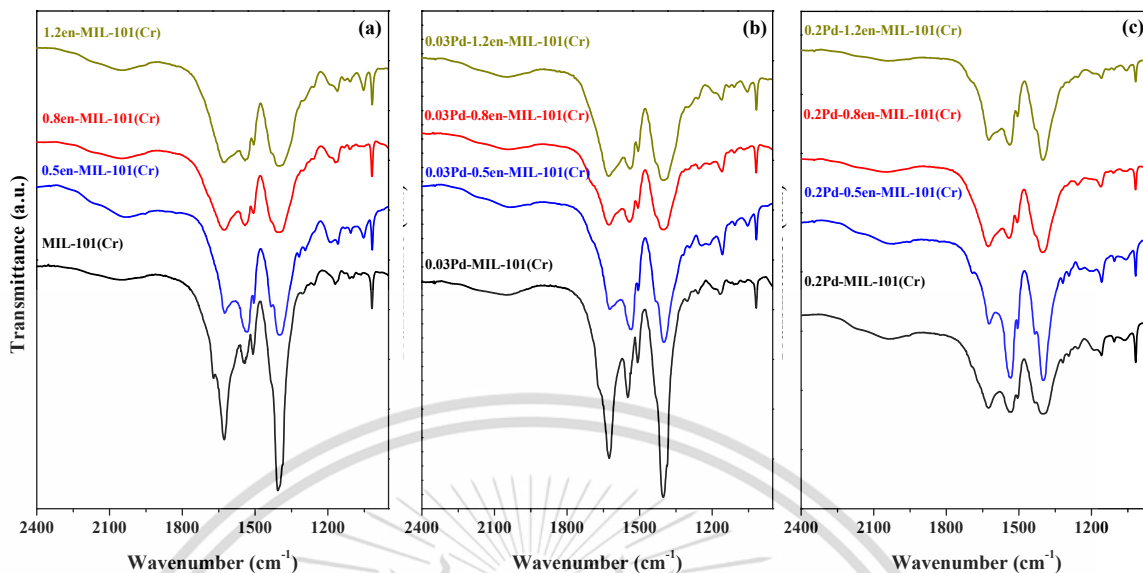


**Figure 6.8** FTIR spectra of (a) ethylenediamine-grafted MIL-101(Cr) with (b) 0.03 wt%Pd and (c) 0.2 wt%Pd loadings

The TEM images of the loaded 0.03Pd mmol/g in MIL-101(Cr) displayed the Pd NPs with an average size of  $\sim 1.8$  nm, which occupied in the MIL-101(Cr) cages (Figure 6.9). In contrast, with the same Pd loading, no Pd NPs was detected in the 0.03Pd-0.5en-MIL-101(Cr). This suggests that the presence of ethylenediamine may either (i) facilitate the dispersion of Pd NPs or even (ii) prevent the reduction of  $\text{Pd}^{2+}$  to Pd NPs, presumably by the strong Pd-N interaction.

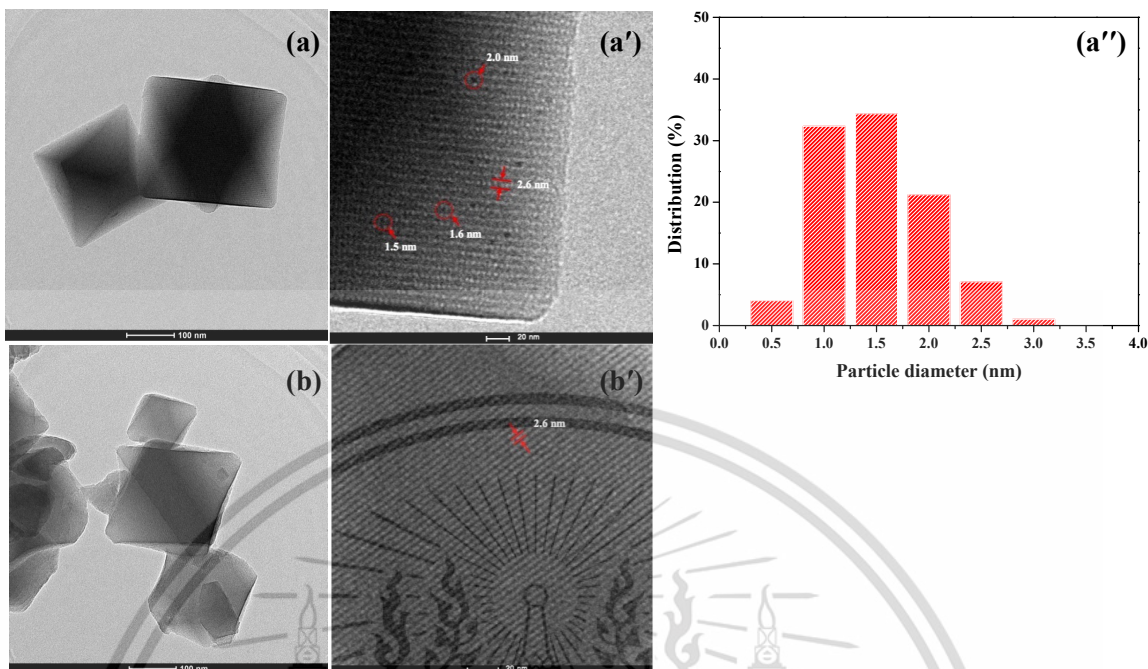


**Figure 6.9** TEM images and Pd size distribution of (a, a', a'') 0.03Pd-MIL-101(Cr) and (b, b') 0.03Pd-0.5en-MIL-101(Cr). Note that in b', no particle could be detected

In a supportive manner, Pd 3d XPS showed that only Pd<sup>2+</sup> species (338.0 eV) was observed in the 0.03Pd-0.5en-MIL-101(Cr) sample (Figure 6.10c), whereas Pd<sup>2+</sup> (337.3 eV) and Pd<sup>0</sup> (335.2 eV) were detected in the sample without ethylenediamine (Figure 6.10a-b). Moreover, the Pd<sup>2+</sup> binding energy, for the sample with ethylenediamine (0.03Pd-0.5en-MIL-101(Cr)), clearly shifted, as compared to that of 0.03Pd-MIL-101(Cr). This indicates the interaction between Pd<sup>2+</sup> and ethylenediamine (Pd-N),<sup>12</sup> as compared to Pd-O in the 0.03Pd-MIL-101(Cr). In line with this view, the N 1s binding energy of ethylenediamine in 0.03Pd-0.5en-MIL-101(Cr) also shifted to a value higher than that in the Pd-free sample (0.5en-MIL-101(Cr), Figure 6.4). This also suggests an electron donating effect, likely from ethylenediamine to the incorporated Pd<sup>2+</sup>. Accordingly, in 0.03Pd-0.5en-MIL-101(Cr), the Pd<sup>2+</sup> species could be anchored by the ethylenediamine, preventing reduction to Pd NPs even at 150 °C under 10%H<sub>2</sub>/Ar. Hence, no Pd NPs was observed by TEM (Figure 6.9b), since it could retain as Pd<sup>2+</sup>, due to the strong interaction with the ethylenediamine.

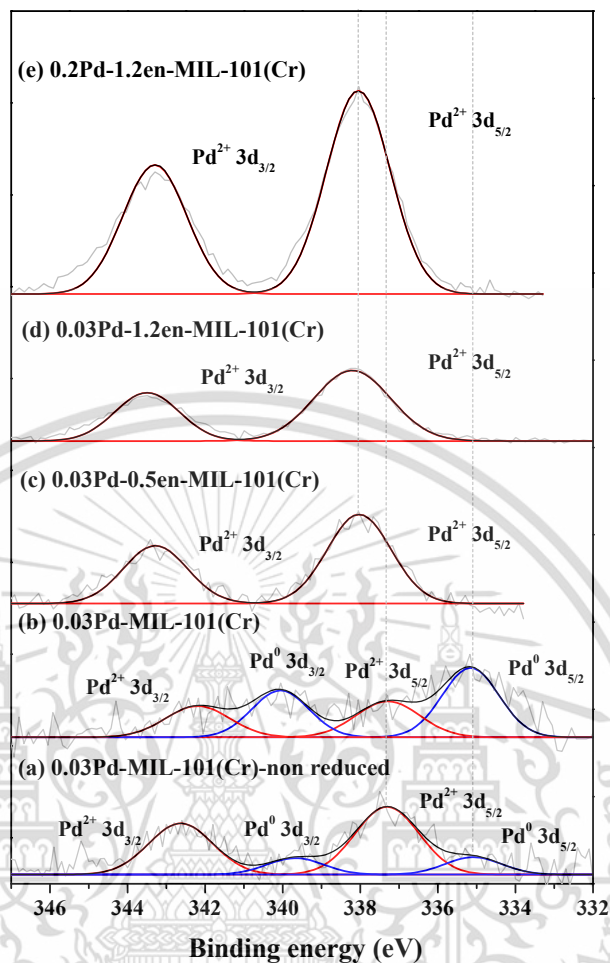


**Figure 6.10** High-resolution Pd 3d XPS spectra of (a) non-reduced 0.03Pd-MIL-101(Cr), (b) 0.03Pd-MIL-101(Cr), (c) 0.03Pd-0.5en-MIL-101(Cr), (d) 0.03Pd-1.2en-MIL-101(Cr) and (e) 0.2Pd-1.2en-MIL-101(Cr)

Upon increase of either ethylenediamine (0.5 to 1.2 mmol/g) or Pd content (0.03 to 0.2 mmol/g), binding energies of Pd<sup>2+</sup> and N remained unchanged (Figure 6.4, Figure 6.10d-e and Figure 6.11). Despite partial collapse of MIL-101(Cr) structure at high ethylenediamine and Pd loading, the Pd<sup>2+</sup> species was still stabilized in these samples. It is worth noting that ethylenediamine: Pd<sup>2+</sup> molar ratio always exceeded the stoichiometric value for all samples, even though the ethylenediamine content decreased after incorporation of Pd (0.03 and 0.2 mmol/g) (Table 6.1, entry 5-10).

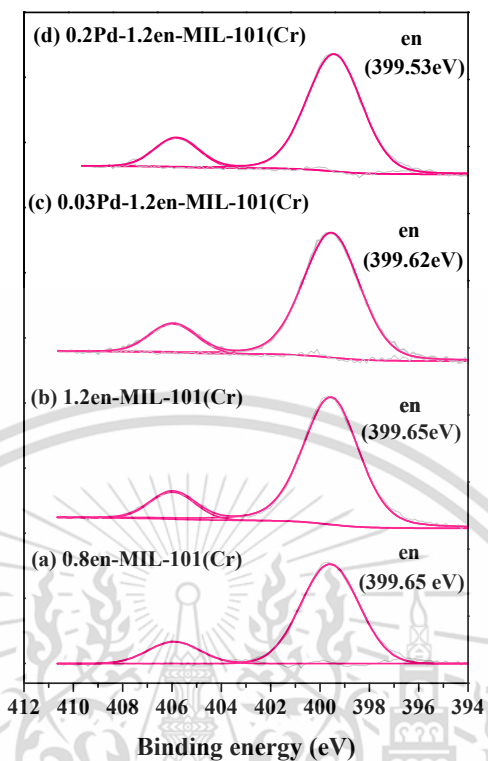


**Figure 6.11** High-resolution N 1s XPS spectra of (a) 0.8en-MIL-101(Cr), (b) 1.2en-MIL-101(Cr), (c) 0.03Pd-1.2en-MIL-101(Cr) and (d) 0.2Pd-1.2en-MIL-101(Cr) samples

Further evidence supporting the interaction of ethylenediamine with the incorporated Pd was obtained from Raman spectra (Figure 6.12). It can be seen that, when MIL-101(Cr) samples were loaded with either ethylenediamine ((x)en-MIL-101(Cr)) or Pd ((x)Pd-MIL-101(Cr)), only characteristic vibration of organic linkers and  $\text{Cr}^{3+}$  nodes, at  $1618\text{ cm}^{-1}$  ( $\nu(\text{C-O})_{\text{as}}$ ),  $1461\text{ cm}^{-1}$  ( $\nu(\text{C-O})_{\text{s}}$ ),  $1149\text{ cm}^{-1}$  ( $\nu(\text{C}=\text{C})$ ),  $873\text{ cm}^{-1}$  ( $\nu(\text{Cr-O})$ ) and  $495\text{ cm}^{-1}$  ( $\text{COO}^-$ ) deformation (Figure 6.12) were revealed.<sup>13</sup> However, new peaks at  $1350\text{ cm}^{-1}$  ( $\nu(\text{C-N})$ ) and  $595\text{ cm}^{-1}$  ( $\nu(\text{Pd-N})$ ) were pronounced, particularly in the samples with both ethylenediamine and  $\text{Pd}^{2+}$  (i.e. 0.2Pd-1.2en-MIL-101(Cr), Figure 6.12c). It is likely that the incorporated  $\text{Pd}^{2+}$  perturbs the electron density around the amino group of ethylenediamine, leading to a change in polarization of C-N bonds and a rise of Pd-N bonding. These peaks affirm a particular interaction of ethylenediamine with  $\text{Pd}^{2+}$ , as suggested earlier by XPS.

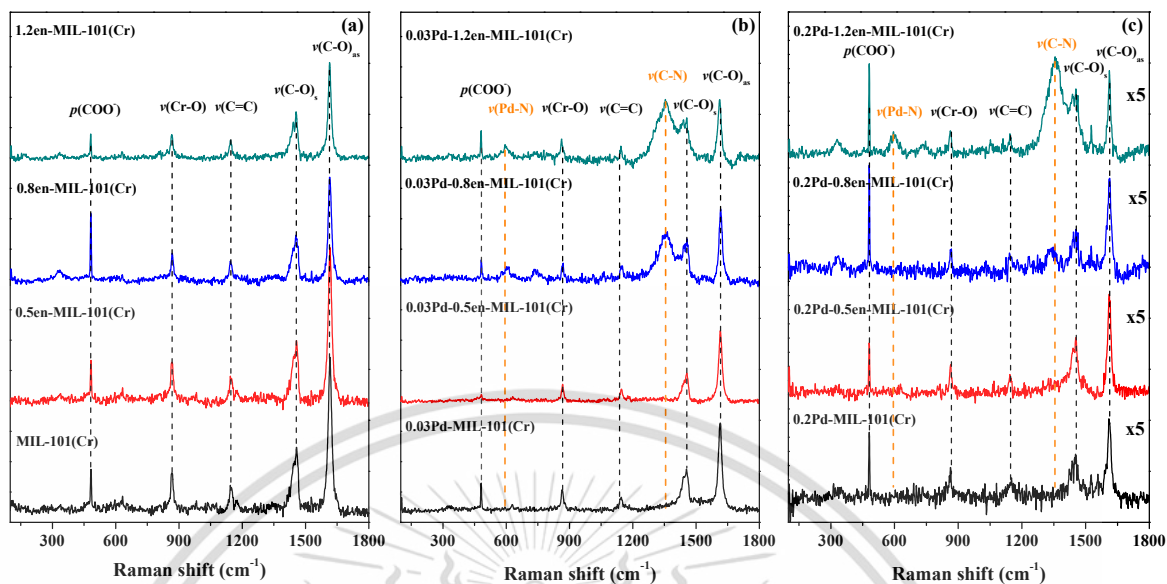


**Figure 6.12** Raman spectra of (a) ethylenediamine-grafted MIL-101(Cr) with (b) 0.03 wt%Pd and (c) 0.2 wt%Pd loadings

The strong interaction of  $\text{Pd}^{2+}$  with the ethylenediamine led to improved stability of this species, even though the samples were treated under 10%  $\text{H}_2/\text{N}_2$  at elevated temperature (up to 150 °C). This is deduced from Table 6.2 that absorption edge energy of the sample with ethylenediamine remained the same as  $\text{Pd}^{2+}$  standard (3174.2 eV), whereas others shifted towards that of Pd metal. From the *in situ* XANES reduction (Figure 6.13), the linear combination fitting (LCF, Figure 6.14) showed that  $\text{Pd}^{2+}$  species was retained for the sample with ethylenediamine (0.03Pd-1.2en-MIL-101(Cr)). While, at the same loading, 38 mol% Pd was reduced in the sample without ethylenediamine (0.03Pd-MIL-101(Cr)), and even more for 0.03Pd- $\text{SiO}_2$  (> 76% reduction). In the same trend, only 18 mol% Pd can be reduced for 0.2Pd-0.8en-MIL-101(Cr) sample (Figure 6.15), but greater proportions of metallic Pd were observed in samples without ethylenediamine (0.2Pd-MIL-101(Cr) – 70 mol% and 0.2Pd- $\text{SiO}_2$  – 83 mol%).

Table 6.2 Absorption edge energy of all samples under *in situ* reduction from 30 °C to 150 °C

|                                     | Temp (°C)   | Absorption edge energy (eV) |                    |                         |                         |                   |                        |
|-------------------------------------|-------------|-----------------------------|--------------------|-------------------------|-------------------------|-------------------|------------------------|
|                                     |             | 0.03Pd-1.2en-MIL-101(Cr)    | 0.03Pd-MIL-101(Cr) | 0.03Pd-SiO <sub>2</sub> | 0.2Pd-0.8en-MIL-101(Cr) | 0.2Pd-MIL-101(Cr) | 0.2Pd-SiO <sub>2</sub> |
| Activation                          | 150         | 3174.2                      | 3174.1             | 3173.3                  | 3174.2                  | 3173.6            | 3173.7                 |
|                                     | 30          | 3174.2                      | 3173.1             | 3173.4                  | 3174.2                  | 3173.5            | 3173.6                 |
| Reduction under H <sub>2</sub>      | 70          | 3174.2                      | 3173.2             | 3173.3                  | 3174.2                  | 3173.3            | 3173.4                 |
|                                     | 110         | 3174.2                      | 3173.1             | 3173.5                  | 3174.2                  | 3173.4            | 3173.5                 |
|                                     | 150         | 3174.2                      | 3173.0             | 3173.1                  | 3174.2                  | 3173.4            | 3173.5                 |
| Holding in H <sub>2</sub> at 150 °C | 150 (20min) | 3174.2                      | 3173.2             | 3173.4                  | 3174.2                  | 3173.2            | 3173.4                 |
|                                     | 150 (40min) | 3174.2                      | 3173.2             | 3173.4                  | 3174.2                  | 3173.3            | 3173.5                 |
|                                     | 150 (60min) | 3174.2                      | 3173.2             | 3173.3                  | 3174.2                  | 3173.3            | 3173.5                 |

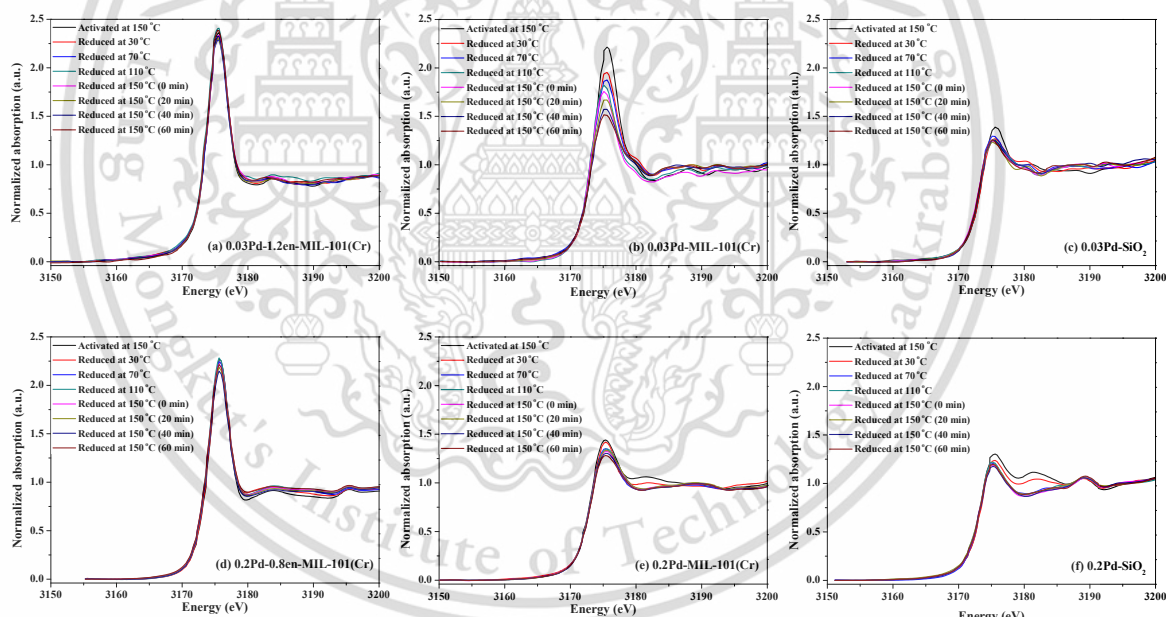


Figure 6.13 Normalized Pd L<sub>3</sub>-edge XANES spectra of (a)–(c) 0.03 wt%Pd over 1.2en-MIL-101(Cr), MIL-101(Cr) and SiO<sub>2</sub> samples and (d)–(f) 0.2 wt%Pd loaded over 0.8en-MIL-101(Cr), MIL-101(Cr) and SiO<sub>2</sub> samples after activation at 150 °C under N<sub>2</sub>, followed by reduction from 30 to 150 °C and holding at 150 °C for 20–60 min

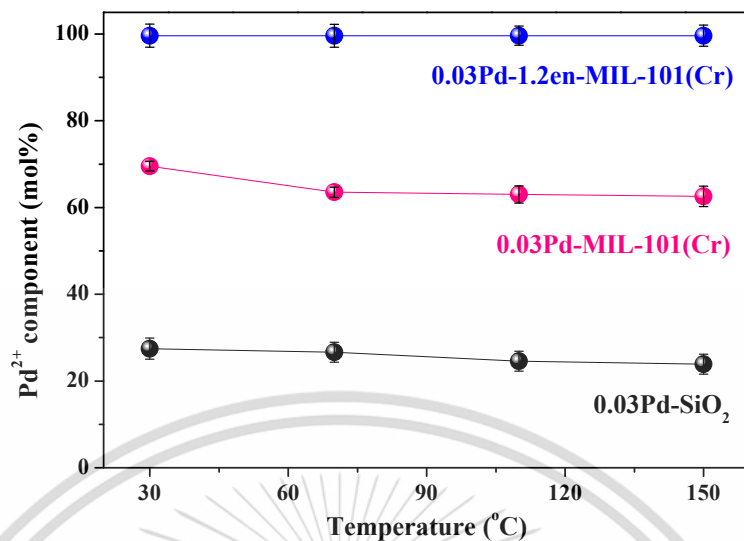


Figure 6.14 Pd<sup>2+</sup> component of 0.03Pd-1.2en-MIL-101(Cr), 0.03Pd-MIL-101(Cr), and 0.03Pd-SiO<sub>2</sub> upon *in situ* reduction from 30 °C to 150 °C under 10%H<sub>2</sub>/N<sub>2</sub>, obtained from linear combination fitting (LCF) of Pd L<sub>3</sub>-edge XANES (Figure 6.13) using metallic Pd foil and PdCOCl<sub>2</sub> as references

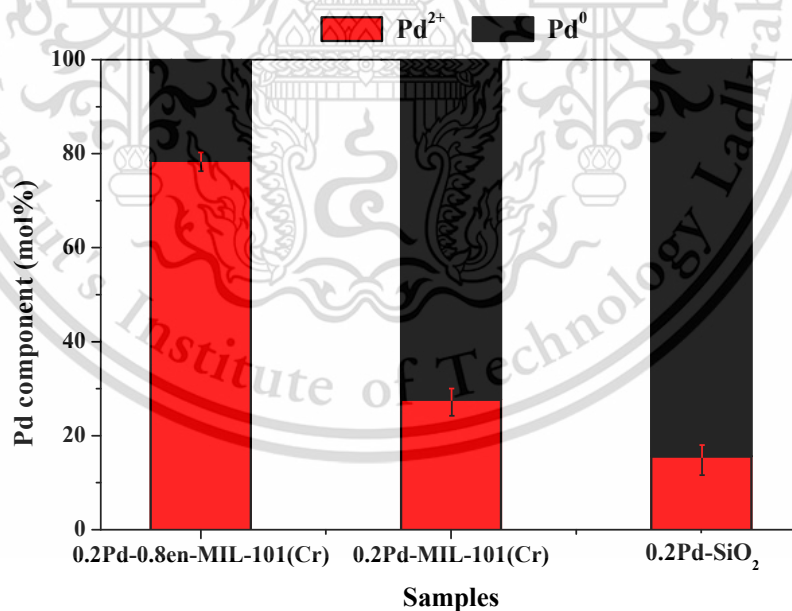


Figure 6.15 Pd component from Pd L<sub>3</sub>-edge XANES linear combination fitting of 0.2Pd-0.8en-MIL-101(Cr), 0.2Pd-MIL-101(Cr) and 0.2Pd-SiO<sub>2</sub> upon *in situ* reduction at 150 °C under 10% H<sub>2</sub>/N<sub>2</sub>

Despite further reduction at 150 °C for another 60 min, the Pd<sup>2+</sup> species was still maintained in 0.03Pd-1.2en-MIL-101(Cr) (Figure 6.16). In a different manner, the 0.03Pd-MIL-101(Cr) and 0.03Pd-SiO<sub>2</sub> samples were further reduced upon holding at 150 °C. Finally, up to 57 mol% Pd was readily reduced in 0.03Pd-MIL-101(Cr) and over 78 mol% metallic Pd was observed in 0.03Pd-SiO<sub>2</sub> (Figure 6.17). This clearly suggests that not only the strong Pd-N coordination but also the confinement, provided by the MIL-101(Cr) framework, could suppress the Pd reducibility and effectively stabilize the Pd<sup>2+</sup> species. It is worth noting that, even though Pd concentration was relatively low due to the dilution by boron nitride during the sample preparation, the misfit fractions, reported as R-factors, remained in an acceptable range of 0.007-0.05 (Table 6.3), suggesting that the results presented are precise and reliable.

**Table 6.3** R-factor of 0.03 wt%Pd over 1.2en-MIL-101(Cr), MIL-101(Cr) and SiO<sub>2</sub> samples and 0.2 wt%Pd loaded over 0.8en-MIL-101(Cr), MIL-101(Cr) and SiO<sub>2</sub> samples after linear combination fitting

|   | Temperature<br>(°C) | R-factor                     |                        |                         |                             |                       |                        |
|---|---------------------|------------------------------|------------------------|-------------------------|-----------------------------|-----------------------|------------------------|
|   |                     | 0.03Pd-1.2en-<br>MIL-101(Cr) | 0.03Pd-MIL-<br>101(Cr) | 0.03Pd-SiO <sub>2</sub> | 0.2Pd-0.8en-<br>MIL-101(Cr) | 0.2Pd-MIL-<br>101(Cr) | 0.2Pd-SiO <sub>2</sub> |
| Activation  | 150                 | 0.045                        | 0.007                  | 0.050                   | 0.046                       | 0.035                 | 0.037                  |
|   | 30                  | 0.045                        | 0.009                  | 0.043                   | 0.037                       | 0.048                 | 0.053                  |
| Reduction<br>under<br>10%H <sub>2</sub> /N <sub>2</sub> | 70                  | 0.045                        | 0.027                  | 0.044                   | 0.026                       | 0.045                 | 0.054                  |
|   | 110                 | 0.031                        | 0.040                  | 0.044                   | 0.028                       | 0.046                 | 0.051                  |
|   | 150                 | 0.038                        | 0.014                  | 0.045                   | 0.030                       | 0.044                 | 0.057                  |
|   | 150 (20 min)        | 0.043                        | 0.021                  | 0.036                   | 0.034                       | 0.051                 | 0.051                  |
| Hold at 150°C   | 150 (40 min)        | 0.045                        | 0.023                  | 0.041                   | 0.027                       | 0.059                 | 0.057                  |
|   | 150 (60 min)        | 0.034                        | 0.007                  | 0.050                   | 0.046                       | 0.034                 | 0.037                  |

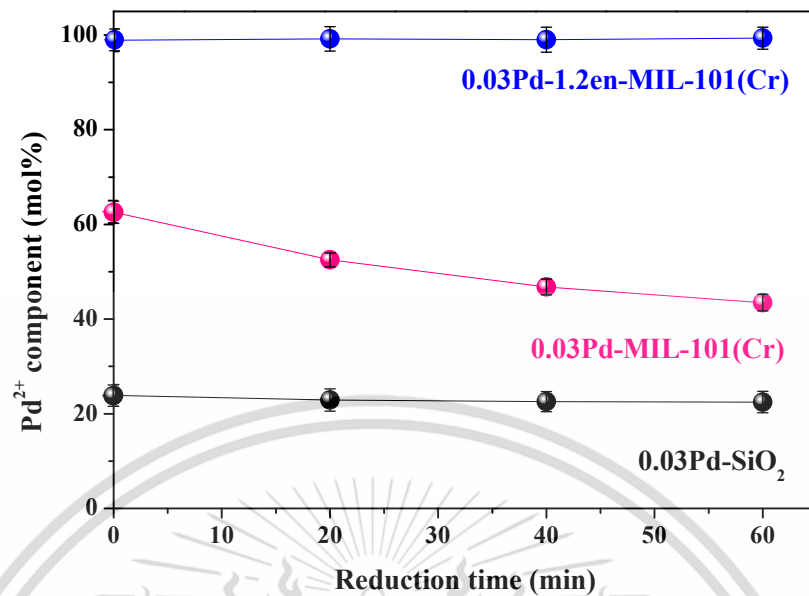


Figure 6.16 Pd<sup>2+</sup> component from Pd L<sub>3</sub>-edge XANES linear combination fitting of 0.03Pd-1.2en-MIL-101(Cr), 0.03Pd-MIL-101(Cr) and 0.03Pd-SiO<sub>2</sub> upon *in situ* reduction at 150 °C during 0–60 min under 10%H<sub>2</sub>/N<sub>2</sub>

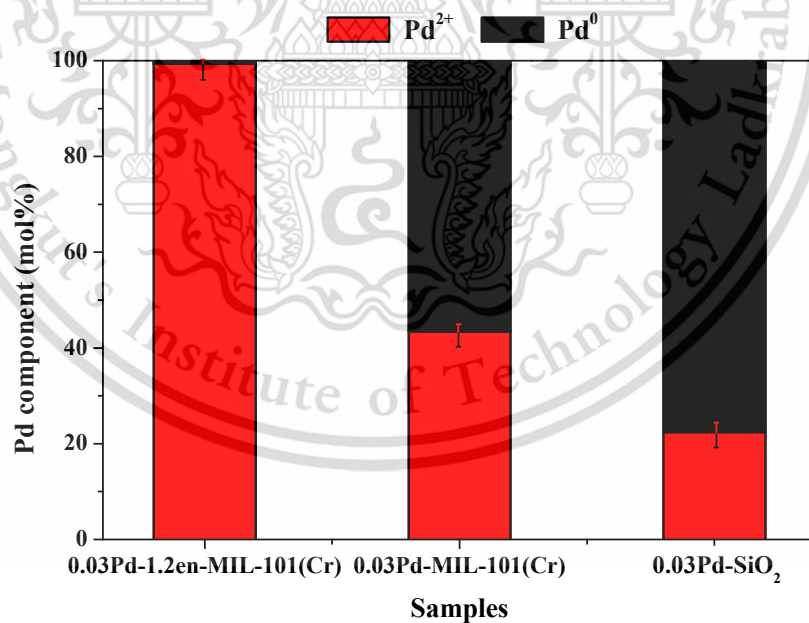
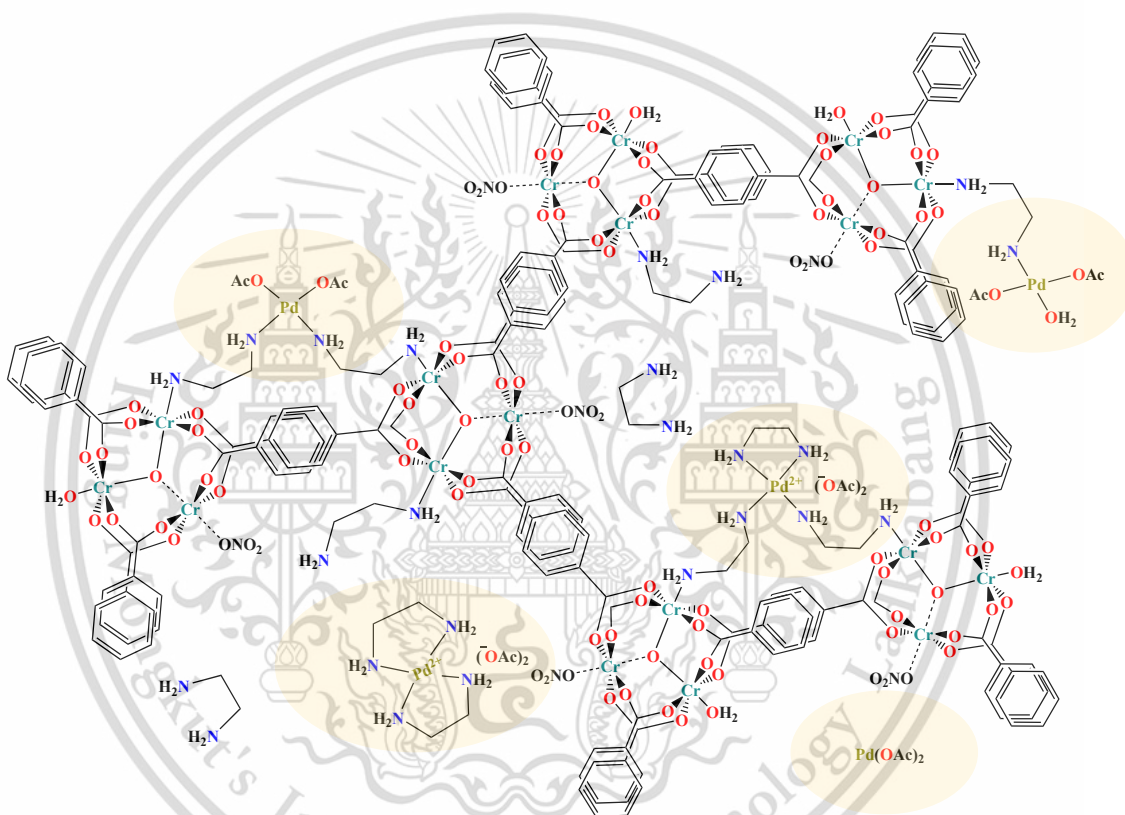


Figure 6.17 Pd component from Pd L<sub>3</sub>-edge XANES linear combination fitting of 0.03Pd-1.2en-MIL-101(Cr), 0.03Pd-MIL-101(Cr) and 0.03Pd-SiO<sub>2</sub> upon *in situ* reduction at 150 °C for 60 min under 10%H<sub>2</sub> in N<sub>2</sub>

From the above observation and spectroscopic results, the incorporated ethylenediamine could exist in the forms of (i) grafted ethylenediamine (interacting with the  $\text{Cr}^{3+}$  nodes) and/or (ii) occluded ethylenediamine (adsorbed in the cavities of MIL-101(Cr)). Moreover, the available amino group of ethylenediamine may also act as an anchoring site for  $\text{Pd}^{2+}$  species. Possible forms of the incorporated ethylenediamine and  $\text{Pd}^{2+}$  species are proposed, as shown in scheme 6.2.



Scheme 6.2 Possible forms of the incorporated ethylenediamine and  $\text{Pd}^{2+}$  species in MIL-101(Cr)

### 6.1.2 Catalytic testing

To better understand the effect of ethylenediamine, the Pd<sup>2+</sup> anchoring on ethylenediamine-grafted-MIL-101(Cr) catalysts were evaluated for oxidation of styrene, in which Pd<sup>2+</sup> is an active species. It can be seen from Table 6.4 that 0.03Pd-0.5en-MIL-101(Cr) offered a higher conversion (84%, entry 3), as compared to the sample without ethylenediamine (0.03Pd-MIL-101(Cr), 74% conversion, entry 1). This is presumably because the interaction of the ethylenediamine with the Pd<sup>2+</sup> could stabilize the active Pd<sup>2+</sup> species within the framework in the presence of H<sub>2</sub>O<sub>2</sub> under the acidic condition. In contrast, the incorporated Pd<sup>2+</sup> in the sample without ethylenediamine as an anchoring ligand is prone to be leached as free Pd<sup>2+</sup>, which is relatively less active (seen from a lower TOF of Pd(OAc)<sub>2</sub>, Table 6.4, entry 10). Hence, the 0.03Pd-MIL-101(Cr) offered an activity somewhat lower than the sample with ethylenediamine.

Table 6.4 Catalytic activities of Pd catalysts

| Entry | Sample                   | Conversion (%)                 |  |   | TOF (h <sup>-1</sup> ) for Styrene oxidation |
|-------|--------------------------|--------------------------------|--|---|--|
|       |                          | Styrene oxidation <sup>a</sup> | Phenylacetylene hydrogenation <sup>b</sup> | Heck C-C coupling reaction <sup>c</sup> |  |
| 1     | 0.03Pd-MIL-101(Cr)       | 74                             | 87   | Trace                                   | 24.7   |
| 2     | 0.03Pd-0.3en-MIL-101(Cr) | 91                             | -  | -                                       | 30.0   |
| 3     | 0.03Pd-0.5en-MIL-101(Cr) | 84                             | 55   | -                                       | 28.0   |
| 4     | 0.03Pd-0.8en-MIL-101(Cr) | 25                             | -  | -                                       | 8.3  |
| 5     | 0.03Pd-1.2en-MIL-101(Cr) | 22                             | -  | -                                       | 7.3  |
| 6     | 0.2Pd-MIL-101(Cr)        | 18                             | -  | 97                                      | 6.0  |
| 7     | 0.2Pd-0.5en-MIL-101(Cr)  | 46                             | -  | Trace                                   | 15.3   |
| 8     | 0.2Pd-0.8en-MIL-101(Cr)  | 74                             | -  | Trace                                   | 24.7   |
| 9     | 0.2Pd-1.2en-MIL-101(Cr)  | 82                             | -  | Trace                                   | 27.3   |
| 10    | Pd(OAc) <sub>2</sub>     | 44                             | -  | 99                                      | 14.7   |

<sup>a</sup>Styrene (1 mmol), 70% H<sub>2</sub>SO<sub>4</sub> (70 μL), 30% H<sub>2</sub>O<sub>2</sub> (6 mmol), MeCN (10 mL) and Pd (0.005 mmol) at 50 °C for 6 h

<sup>b</sup>Phenylacetylene (40 mmol), Ethanol (60 mL), Pd (0.4 μmol) at 30 °C for 0.5 h

<sup>c</sup>Iodobenzene (1 mmol), Styrene (1.5 mmol), K<sub>2</sub>CO<sub>3</sub> (1.5 mmol), DMF (4 mL) and Pd (0.005 mmol) at 120 °C for 6 h

In line with the above discussion, Figure 6.18 shows a significant decline in the activity when 0.03Pd-MIL-101(Cr) was reused (washed with acetonitrile and dried at 150 °C). This catalyst was no longer active (~7% styrene conversion) after three cycles, and the ICP analysis indicated that only 0.0013 mmol Pd/g was remained in the used 0.03Pd-MIL-101(Cr). Although some leaching was observed for 0.03Pd-0.5en-MIL-101(Cr) sample, the activity was preserved at 74% styrene conversion. This clearly suggests the ability of ethylenediamine to stabilize the Pd<sup>2+</sup>, as discussed earlier. It is worth noting that the decline in activity of the recycled 0.03Pd-0.5en-MIL-101(Cr) could attribute to the hydrolysis of some ethylenediamine from the Cr<sup>3+</sup> node upon the preceding reaction. This was further confirmed by noting that the ethylenediamine content was decreased from 0.48 to 0.35 mmol/g, providing 41% conversion after three cycles.

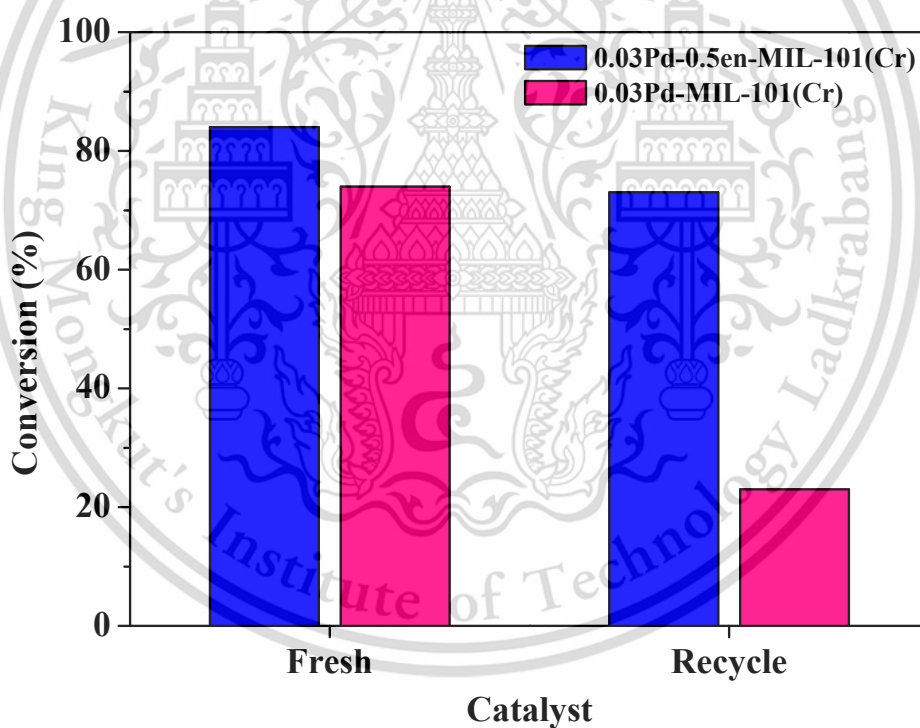


**Figure 6.18** Recycle of 0.03Pd-MIL-101(Cr) with or without ethylenediamine catalysts for oxidation of styrene

After several cycles of the reaction, no Pd particle was observed for 0.03Pd-0.5en-MIL-101(Cr) as evidenced by TEM (Figure 6.19). In contrast, larger Pd particles were found thoroughly on the surface of the sample without ethylenediamine (0.03Pd-MIL-101(Cr)). This emphasizes that the Pd<sup>2+</sup> in 0.03Pd-0.5en-MIL-101(Cr) can withstand the reduction by the feed. In a supportive manner, the 0.03Pd-0.5en-MIL-101(Cr) showed a lower activity for phenylacetylene hydrogenation (55% conversion), as compared to 0.03Pd-MIL-101(Cr) (87%, Table 6.4, entry 1, 3). Although Pd would be readily reduced under high pressure of H<sub>2</sub> at 1.0 MPa, relatively less active Pd<sup>0</sup> would be present in the sample with ethylenediamine. Again, this is because the ethylenediamine readily stabilizes Pd<sup>2+</sup> species and hinder their reduction to Pd<sup>0</sup>, as discussed earlier. In line with this view, the ethylenediamine grafted samples were virtually inactive in Heck coupling, for which metallic Pd is an active site<sup>14</sup> (Table 6.4, entry 6). Even with high Pd loading (0.2 mmol/g), ethylenediamine interacts strongly with the Pd<sup>2+</sup> species, presumably via coordinated covalent bonding (scheme 6.2). This interaction inhibits the reduction of Pd<sup>2+</sup> by the feed (styrene) to the active Pd metal in the Heck reaction. While, the 0.2Pd-MIL-101(Cr) and Pd(OAc)<sub>2</sub> showed almost complete conversion (Table 6.4, entry 6, 10). This is because the reduction of Pd<sup>2+</sup> was readily achieved for these samples: black particles were clearly visible after the reaction.

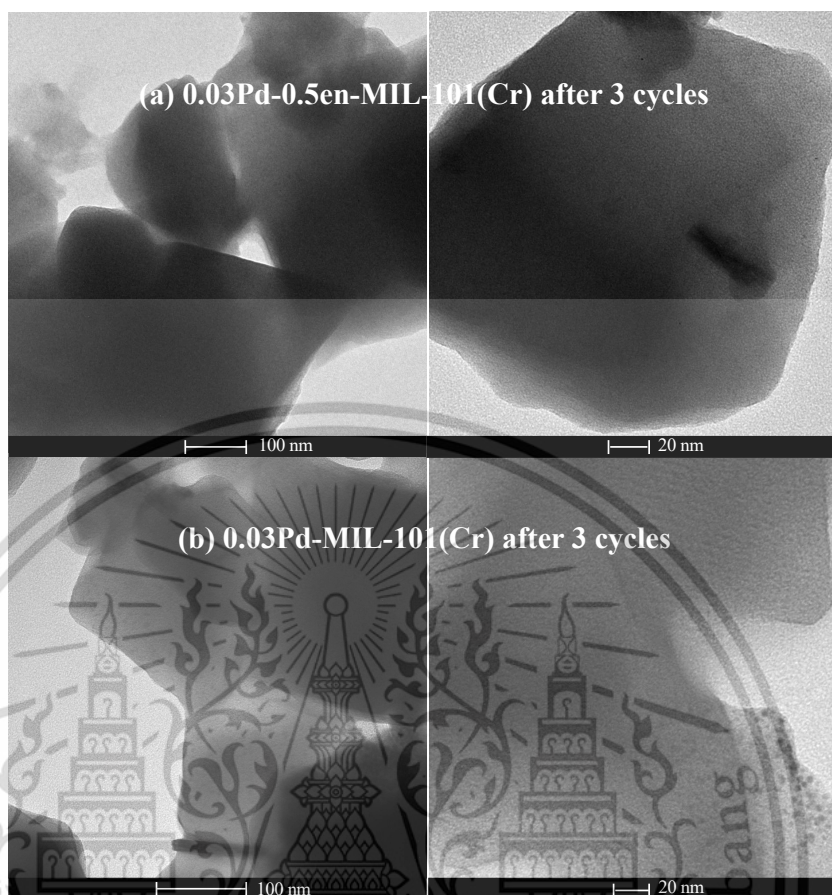


**Figure 6.19** TEM images of (a) 0.03Pd-0.5en-MIL-101(Cr) and (b) 0.03Pd-MIL-101(Cr) after used for three cycles of styrene oxidation

From the above results, it was clear that the ethylenediamine significantly affected styrene oxidization promoted by  $\text{Pd}^{2+}$ . This was supported by the significantly improved conversion (from 46% to 91%) and turnover frequency (TOF, from  $15.3 \text{ h}^{-1}$  to  $30.0 \text{ h}^{-1}$ ) as the ethylenediamine: $\text{Pd}^{2+}$  molar ratio increased from 1.8 to 10.0 (Figure 6.20). This is presumably because the ethylenediamine can readily inhibit reduction of  $\text{Pd}^{2+}$  to Pd metal, as typically observed in homogeneous reactions, despite the presence of oxidants, e.g.,  $\text{O}_2$  and  $\text{H}_2\text{O}_2$ .<sup>15</sup> Steinhoff and Stahl reported that the presence of pyridine prevented decomposition of Pd-alkoxide intermediate via  $\beta$ -hydride elimination to inactive Pd metal.<sup>16</sup> Consistent with this, the reaction using  $\text{Pd}(\text{OAc})_2$  as catalyst provided a lower TOF ( $14.7 \text{ h}^{-1}$ ) with Pd black suspension after a six-hour resident time (Table 6.4, entry 10).

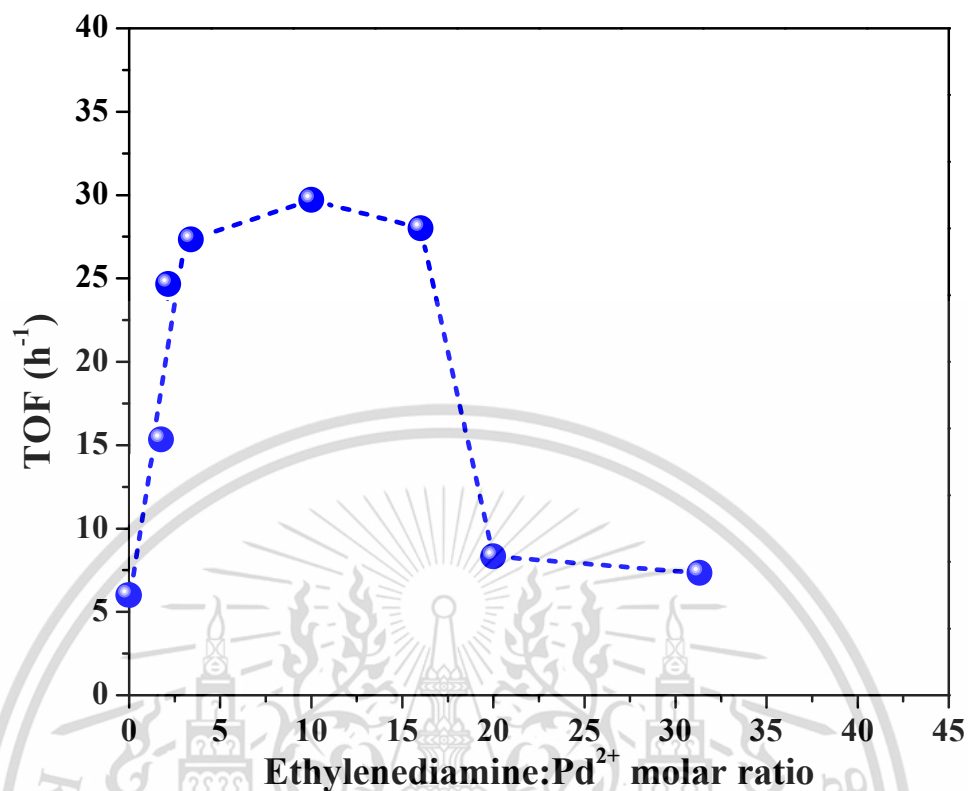


Figure 6.20 Effect of ethylenediamine: Pd<sup>2+</sup> molar ratio on the turnover frequency (TOF) of styrene oxidation

However, further an increase of the ethylenediamine: Pd<sup>2+</sup> molar ratio >10 led to a substantial decrease in the reaction rate (Table 6.4, entry 2–5, Figure 6.20). The excess amount of ethylenediamine may well competitively coordinate with Pd<sup>2+</sup> species, inhibiting association of the feed, i.e., styrene, as seen from the reaction using Pd(OAc)<sub>2</sub> as catalyst (Figure 6.21). In line with this view, Jiang et al. found that styrene oxidation was suppressed when excess chelating ligands were present.<sup>17</sup> Accordingly, it could be suggested in this work that the ethylenediamine: Pd<sup>2+</sup> molar ratio of 10 is optimum for high catalytic activity and stability.

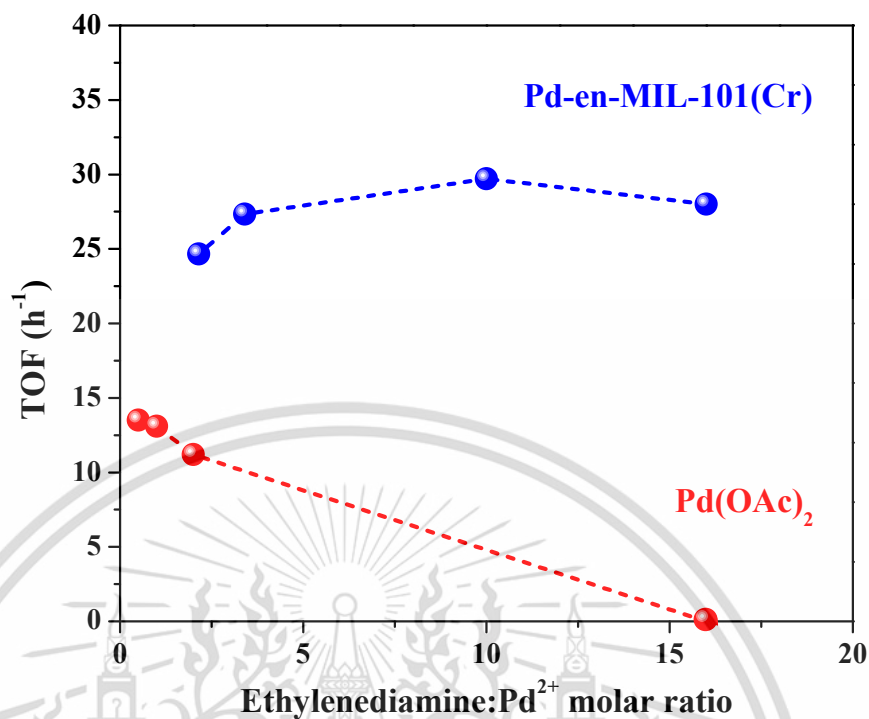


Figure 6.21 Effect of ethylenediamine on Pd activity of Pd-en-MIL-101(Cr) and Pd(OAc)<sub>2</sub>

Compared to other Pd<sup>2+</sup> catalysts reported in the literature (Table 6.5), the 0.03Pd-0.3en-MIL-101(Cr) offered much higher activity than the homogeneous Pd complex catalysts (Table 6.5, entry 2-3).<sup>18,19</sup> Although a comparable activity was obtained with the PdCl<sub>2</sub>/[C<sub>4</sub>mim][BF<sub>4</sub>] (Table 6.5, entry 4),<sup>20</sup> high CO<sub>2</sub> pressure was not required for the Pd<sup>2+</sup>-ethylenediamine grafted MOF catalyst. Moreover, our catalyst could be simply recovered and reused, as demonstrated previously. Among other heterogeneous Pd<sup>2+</sup> catalysts, the 0.03Pd-0.3en-MIL-101(Cr) also possessed a superior activity compared to the catalysts with SiO<sub>2</sub> or Al<sub>2</sub>O<sub>3</sub> supports (Table 6.5, entry 5-6).<sup>21,22</sup> Even though the single-site Pd<sup>2+</sup> species showed a higher TOF of 35.6 h<sup>-1</sup> (Table 6.5, entry 7), a relatively higher temperature (80 °C) was tested.<sup>23</sup> In comparison, the Pd<sup>2+</sup> anchoring on ethylenediamine-grafted-MIL-101(Cr) prepared in this work showed excellent activity, with possible recyclability, as mentioned earlier.

Table 6.5 Comparison of the catalytic activity of 0.03Pd-0.3en-MIL-101(Cr) with other catalysts reported in the literature for styrene oxidation

| Entry | Catalyst   | Condition   | Conversion (%) | TOF (h <sup>-1</sup> ) | Ref.      |
|-------|--|---|----------------|------------------------|-----------|
| 1     | 0.03Pd-0.3en-MIL-101(Cr)   | Styrene (2 mmol), Pd (0.5 mol%), H <sub>2</sub> O <sub>2</sub> (6 equiv.), MeCN at 50 °C for 6 h                          | 91             | 30.0                   | This work |
| 2     | (PBO)Pd(MeCN) <sub>2</sub> (OTf) <sub>2</sub>                                | Styrene (2.2 mmol), Pd (1 mol%), H <sub>2</sub> O <sub>2</sub> (5 equiv.), H <sub>2</sub> O/MeCN (1:1) at 27 °C for 24 h  | 92             | 3.8                    | 52        |
| 3     | [Pd(aPmic)(CH <sub>3</sub> CN) <sub>2</sub> ][BF <sub>4</sub> ] <sub>2</sub> | Styrene (1 mmol), Pd (5 mol%), H <sub>2</sub> O <sub>2</sub> (5 equiv.), MeCN at 45 °C for 12 h                           | 90             | 1.5                    | 53        |
| 4     | PdCl <sub>2</sub> /[C <sub>4</sub> mim][BF <sub>4</sub> ]                    | Styrene (100 mmol), Pd (0.5 mol%), H <sub>2</sub> O <sub>2</sub> (2.2 equiv.), CO <sub>2</sub> 20.68 atm at 50 °C for 5 h | 65             | 26.0                   | 54        |
| 5     | 2.5wt%Pd/2.5wt%Au/Al <sub>2</sub> O <sub>3</sub>                             | Styrene (1 mmol), Pd (9.4 mol%), H <sub>2</sub> O <sub>2</sub> (4 equiv.), scCO <sub>2</sub> 9 MPa at 120 °C for 3 h      | 68             | 2.4                    | 6         |
| 6     | Fe <sub>3</sub> O <sub>4</sub> @SiO <sub>2</sub> -APTES-Pd(OAc) <sub>2</sub> | Styrene (1 mmol), Pd (1 mol%), H <sub>2</sub> O <sub>2</sub> (3 equiv.), DMSO at 60 °C for 6 h                            | 78             | 13.0                   | 55        |
| 7     | Pd(II)-Y-bpydc <sub>0.8</sub> /bpdc <sub>0.2</sub>                           | Styrene (5 mmol), Pd (0.5 mol%), O <sub>2</sub> 1 atm, solvent-free at 80 °C for 5 h                                      | 89             | 35.6                   | 18        |

## 6.2 Conclusions

A highly stable Pd<sup>2+</sup> species was successfully prepared, within the ethylenediamine-grafted-MIL-101(Cr) sample, using sequential adsorption of ethylenediamine, followed by double solvent adsorption of Pd(OAc)<sub>2</sub>. The ethylenediamine readily interacts with the Cr<sup>3+</sup> nodes in MIL-101(Cr) via coordinative covalent bonding using one of the amino moieties, while the other acts as an anchoring site for Pd<sup>2+</sup>. The strong Pd<sup>2+</sup>-N coordination and the confinement of the MIL-101(Cr) framework could effectively suppress the reduction of Pd<sup>2+</sup> either by H<sub>2</sub> at elevated temperature (up to 150 °C) or by the feed during styrene oxidation. In addition, the presence of ethylenediamine as an anchoring ligand retards the leaching of the active Pd<sup>2+</sup> species during the reaction under oxidizing and acidic conditions. Although the addition of excess ethylenediamine and high loading of Pd<sup>2+</sup> affect the crystallinity of the MIL-101(Cr) framework, the Pd<sup>2+</sup> species anchoring on ethylenediamine-grafted-MIL-101(Cr) remains active. The catalyst with the ethylenediamine: Pd<sup>2+</sup> molar ratios of 10 offers optimum catalytic activity and stability for liquid-phase styrene oxidation, as compared to the previously reported Pd<sup>2+</sup> catalyst in the literature.

### 6.3 References

- (1) Ferey, G. A Chromium Terephthalate-Based Solid with Unusually Large Pore Volumes and Surface Area. *Science* **2005**, *309* (5743), 2040–2042.
- (2) Shafiei, M.; Alivand, M. S.; Rashidi, A.; Samimi, A.; Mohebbi-Kalhari, D. Synthesis and Adsorption Performance of a Modified Micro-Mesoporous MIL-101(Cr) for VOCs Removal at Ambient Conditions. *Chem. Eng. J.* **2018**, *341*, 164–174.
- (3) Maksimchuk, N. V.; Zalomaeva, O. V.; Skobelev, I. Y.; Kovalenko, K. A.; Fedin, V. P.; Kholdeeva, O. A. Metal–Organic Frameworks of the MIL-101 Family as Heterogeneous Single-Site Catalysts. *Proc. R. Soc. Math. Phys. Eng. Sci.* **2012**, *468* (2143), 2017–2034.
- (4) Hu, B.; Xue, Z.; Wang, H.; Cai, L.; Xiong, H.; Jiang, X.; Du, Z. Biomimetic Syntheses of Pure or Doped Metal Hydroxide Nitrate Thin Films by a Dual-Template Approach. *J. Mater. Chem.* **2009**, *19* (16), 2373–2379.
- (5) Erfaninia, N.; Tayebee, R.; Dusek, M.; Amini, M. M. Ethylene Diamine Grafted Nanoporous UiO-66 as an Efficient Basic Catalyst in the Multi-Component Synthesis of 2-Aminithiophenes: Ethylene Diamine Grafted UiO-66 as an Efficient Heterogeneous. *Appl. Organomet. Chem.* **2018**, *32* (5), e4307.
- (6) Vrtovec, N.; Mazaj, M.; Buscarino, G.; Terracina, A.; Agnello, S.; Arçon, I.; Kovač, J.; Zabukovec Logar, N. Structural and CO<sub>2</sub> Capture Properties of Ethylenediamine-Modified HKUST-1 Metal–Organic Framework. *Cryst. Growth Des.* **2020**, *20* (8), 5455–5465.
- (7) Maksimchuk, N.; Timofeeva, M.; Melgunov, M.; Shmakov, A.; Chesalov, Y.; Dybtsev, D.; Fedin, V.; Kholdeeva, O. Heterogeneous Selective Oxidation Catalysts Based on Coordination Polymer MIL-101 and Transition Metal-Substituted Polyoxometalates. *J. Catal.* **2008**, *257* (2), 315–323.
- (8) Yang, K.; Sun, Q.; Xue, F.; Lin, D. Adsorption of Volatile Organic Compounds by Metal–Organic Frameworks MIL-101: Influence of Molecular Size and Shape. *J. Hazard. Mater.* **2011**, *195*, 124–131.

- (9) Wickenheisser, M.; Jeremias, F.; Henninger, S. K.; Janiak, C. Grafting of Hydrophilic Ethylene Glycols or Ethylenediamine on Coordinatively Unsaturated Metal Sites in MIL-100(Cr) for Improved Water Adsorption Characteristics. *Inorganica Chim. Acta* **2013**, *407*, 145–152.
- (10) Chen, G.; Wu, S.; Liu, H.; Jiang, H.; Li, Y. Palladium Supported on an Acidic Metal–Organic Framework as an Efficient Catalyst in Selective Aerobic Oxidation of Alcohols. *Green Chem.* **2013**, *15* (1), 230–235.
- (11) Makmeesub, N.; Ritvirulh, C.; Choojun, K.; Chen, T.-H.; Poo-arporn, Y.; Resasco, D. E.; Sooknoi, T. Reversible Hydrogenation–Dehydrogenation of Acetylpyridine-Pd-MIL-101(Cr) for Chemical Hydrogen Storage. *Ind. Eng. Chem. Res.* **2020**, *59* (40), 17671–17679.
- (12) Ochoa, E.; Henao, W.; Fuertes, S.; Torres, D.; van Haasterecht, T.; Scott, E.; Bitter, H.; Suelves, I.; Pinilla, J. L. Synthesis and Characterization of a Supported Pd Complex on Carbon Nanofibers for the Selective Decarbonylation of Stearic Acid to 1-Heptadecene: The Importance of Subnanometric Pd Dispersion. *Catal. Sci. Technol.* **2020**, *10* (9), 2970–2985.
- (13) Jarrah, A.; Farhadi, S.  $K_6P_2W_{18}O_{62}$  Encapsulated into Magnetic  $Fe_3O_4$ /MIL-101 (Cr) Metal–Organic Framework: A Novel Magnetically Recoverable Nanoporous Adsorbent for Ultrafast Treatment of Aqueous Organic Pollutants Solutions. *RSC Adv.* **2018**, *8* (66), 37976–37992.
- (14) Jagtap, S. Heck Reaction—State of the Art. *Catalysts* **2017**, *7* (9), 267.
- (15) Nishimura, T.; Onoue, T.; Ohe, K.; Uemura, S. Palladium(II)-Catalyzed Oxidation of Alcohols to Aldehydes and Ketones by Molecular Oxygen. *J. Org. Chem.* **1999**, *64* (18), 6750–6755.
- (16) Steinhoff, B. A.; Stahl, S. S. Ligand-Modulated Palladium Oxidation Catalysis: Mechanistic Insights into Aerobic Alcohol Oxidation with the  $Pd(OAc)_2$ /Pyridine Catalyst System. *Org. Lett.* **2002**, *4* (23), 4179–4181.
- (17) Jiang, H.; Qiao, Q.; Gong, H.  $PdCl_2$  Catalyzed Oxidation of Styrene to Acetophenone under Mild Conditions. *Pet. Sci. Technol.* **1999**, *17* (9–10), 955–965.

- (18) Cao, Q.; Bailie, D. S.; Fu, R.; Muldoon, M. J. Cationic Palladium( II ) Complexes as Catalysts for the Oxidation of Terminal Olefins to Methyl Ketones Using Hydrogen Peroxide. *Green Chem.* **2015**, *17* (5), 2750–2757.
- (19) Saha, S.; Yadav, S.; Reshi, N. U. D.; Dutta, I.; Kunnikuruvan, S.; Bera, J. K. Electronic Asymmetry of an Annelated Pyridyl–Mesoionic Carbene Scaffold: Application in Pd(II)-Catalyzed Wacker-Type Oxidation of Olefins. *ACS Catal.* **2020**, *10* (19), 11385–11393.
- (20) Namboodiri, V. V.; Varma, R. S.; Sahle-Demessie, E.; Pillai, U. R. Selective Oxidation of Styrene to Acetophenone in the Presence of Ionic Liquids. *Green Chem.* **2002**, *4* (2), 170–173.
- (21) Wang, X.; Venkataramanan, N. S.; Kawanami, H.; Ikushima, Y. Selective Oxidation of Styrene to Acetophenone over Supported Au–Pd Catalyst with Hydrogen Peroxide in Supercritical Carbon Dioxide. *Green Chem.* **2007**, *9* (12), 1352.
- (22) Long, Y.; Zhao, Z.; Wu, L.; Luo, S.; Wen, H.; Wu, W.; Zhang, H.; Ma, J. Distinctive Ligand Effects of Functionalized Magnetic Microparticles Immobilizing Palladium Acetate as Heterogeneous Coordination Catalysts for Selective Oxidation of Styrene to Acetophenone. *Mol. Catal.* **2017**, *433*, 291–300.
- (23) Zhang, Y.; Wei, N.; Xing, Z.; Han, Z.-B. Functional Hexanuclear Y(III) Cluster-Based MOFs Supported Pd(II) Single Site Catalysts for Aerobic Selective Oxidation of Styrene. *Appl. Catal. Gen.* **2020**, *602*, 117668.

## Chapter 7

# Conclusions and Suggestions

### 7.1 Conclusions

As MOFs have an extraordinarily large internal surface area, uniform structure with extensive variety of chemical functionality. Therefore, this thesis has applied these strong points to upgrade MOFs for using in specific application. Improvement of selective gas separation of HKUST-1 in the HKUST-1/polymer MMM by using strong adsorption sites have been investigated in Chapter 4. Further, the strong adsorption sites of MIL-101(Cr) were modified by grafting with electron rich ligand that can function as chemical hydrogen storage (Chapter 5) and catalyst stabilizer (Chapter 6).

Chapter 4 investigates the polymer types and impact of HKUST-1 in HKUST-1/polymer MMM on H<sub>2</sub> and CO<sub>2</sub> permeability. The polymer membrane was fabricated by solution casting. The permeability of H<sub>2</sub> and CO<sub>2</sub> were investigated using single-gas permeation under atmospheric pressure. Due to its larger fractional free volume, the amorphous HIPS had H<sub>2</sub> diffusion more than the semicrystalline EVA. Moreover, the HIPS membrane's bulky phenyl group may interfere with the diffusion of large CO<sub>2</sub> molecules, producing lower CO<sub>2</sub> permeability and a greater H<sub>2</sub>/CO<sub>2</sub> permselectivity. Although the intermolecular interaction between CO<sub>2</sub> and the pendant acetate group increases CO<sub>2</sub> solubility in the EVA membrane, it was not considered for improving the H<sub>2</sub>/CO<sub>2</sub> permselectivity. Thus, the HIPS membrane was selected as the polymer matrix to prepare HKUST-1/HIPS MMM. The presence of HKUST-1 in the HIPS membrane influences H<sub>2</sub> permeability and H<sub>2</sub>/CO<sub>2</sub> permselectivity. Strong CO<sub>2</sub> adsorption sites at unsaturated Cu<sup>2+</sup> in the HKUST-1 paddle-wheel may impede CO<sub>2</sub> transport, making H<sub>2</sub> diffusion much faster than CO<sub>2</sub>. The loading of HKUST-1 in EVA, on the other hand, had no effect on H<sub>2</sub>/CO<sub>2</sub> permselectivity. It might be explained by polymer penetration blocking the HKUST-1 pores. The strong polymer-MOF interaction and high chain mobility of the rubbery EVA polymer presumably result in pore-blocking at the MOF particle's surface coating.

In Chapter 5, MIL-101(Cr) was successfully grafted with 3-acetylpyridine (AcP), which can function as reversible chemical hydrogen storage. The labile coordinated water at the  $\text{Cr}^{3+}$  nodes can be readily removed by heat treatment ( $150\text{ }^{\circ}\text{C}$ ), providing available unsaturated  $\text{Cr}^{3+}$  sites that can readily coordinate with N-ring of AcP. Moreover, the difference in polarity between the inner and outer surfaces of MIL 101(Cr) allows using the double solvent adsorption approach for Pd incorporation. This provides the potential to decrease the precursor migration and large particle agglomeration upon preparation. Since the carbonyl groups of AcP must interact with Pd in order to the chemical hydrogen storage. The cage-like structure of MIL 101(Cr) facilitates this need by increasing the potential for Pd NPs to interact intimately with the AcP. The chemical hydrogen storage of Pd-AcP-MIL-101(Cr) can occur through hydrogenation of the carbonyl group from AcP to the hydroxyl group, named 1-hydroxyethylpyridine (HEP), and dehydrogenation of the hydroxyl group from HEP back to the AcP one. Both processes can be catalytically driven by Pd NPs at atmospheric pressure. The hydrogen uptake and release can be regulated either by the operating temperature within the range of  $100\text{-}200\text{ }^{\circ}\text{C}$  or hydrogen partial pressure at a constant temperature. However, the operation at high temperature (over  $150\text{ }^{\circ}\text{C}$ ) could damage the MIL-101(Cr) crystallinity by heating cycle, affected to the hydrogen storage performance. The optimum temperature at  $150\text{ }^{\circ}\text{C}$  provided the consistent hydrogen storage of 0.08 wt% per cycle without loss of crystallinity.

Chapter 6 presents a highly stable  $\text{Pd}^{2+}$  species, anchoring on ethylenediamine-grafted-MIL-101(Cr) for using as a robust oxidation catalyst. The preparation of Pd-en-MIL-101(Cr) started with ethylenediamine adsorption, followed by double solvent adsorption of  $\text{Pd}^{2+}$  precursor. Ethylenediamine can readily interact with the unsaturated  $\text{Cr}^{3+}$  sites in MIL-101(Cr) nodes via coordinative covalent bonding using one of the amino moieties, while the other acts as an anchoring site for  $\text{Pd}^{2+}$ . Such amino moieties can facilitate  $\text{Pd}^{2+}$  dispersion and inhibit particle agglomeration during preparation. Further, strong  $\text{Pd}^{2+}$ -ethylenediamine coordination and confinement of MIL-101(Cr) framework can effectively suppress reduction of  $\text{Pd}^{2+}$  either by  $\text{H}_2$  at elevated temperature (up to  $150\text{ }^{\circ}\text{C}$ ) or by the feed (styrene) in Heck oxidative coupling. In addition, the presence of ethylenediamine as an anchoring ligand can also minimize the leaching of the active  $\text{Pd}^{2+}$

species during the reaction under oxidizing and acidic conditions. However, the increase ethylenediamine loading by using high ethylenediamine concentration (0.0015 %v/v per g of MIL-101(Cr)) damaged to the crystallinity, as the ethylenediamine has ligand field strength stronger than carboxylate of the organic linker, possibly leading to ligand substitution. In the same manner, high Pd<sup>2+</sup> loading (0.2 mmol/g, 2.0 wt%) also decreased the crystallinity due to decarboxylation of the organic linker, catalyzed by Pd, in the presence of hydrogen. Despite obtained partial loss of crystallinity at high ethylenediamine and Pd<sup>2+</sup> loading, the Pd<sup>2+</sup> species was still active. The ethylenediamine: Pd<sup>2+</sup> ratio affected significantly to styrene oxidization activity, stability and recyclability. As the ethylenediamine can readily inhibit reduction of Pd<sup>2+</sup> to Pd metal, despite the presence of oxidant. However, further increase in the ethylenediamine: Pd<sup>2+</sup> molar ratio over 16 led to a substantial decrease in the reaction rate, since ethylenediamine also competitively coordinates to Pd<sup>2+</sup> species, inhibiting association of the feed. Accordingly, the ethylenediamine: Pd<sup>2+</sup> molar ratio of 10 was optimum for high catalytic activity and stability.

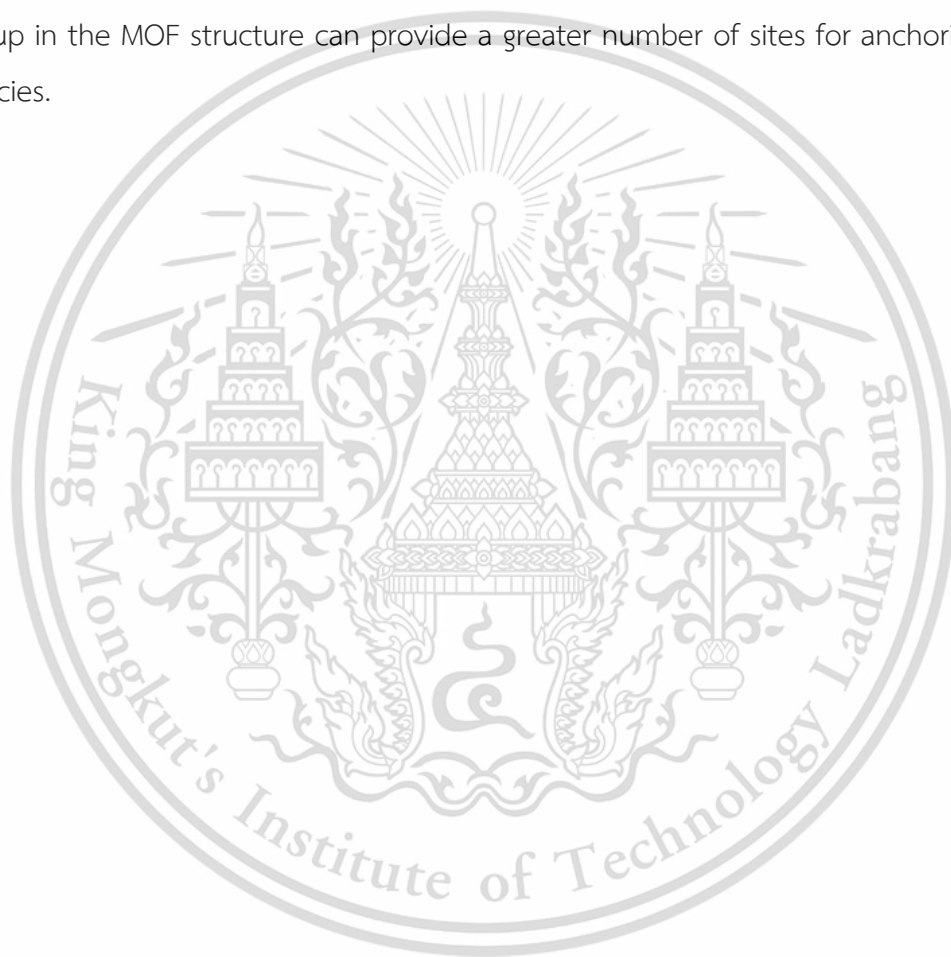
## 7.2 Suggestions

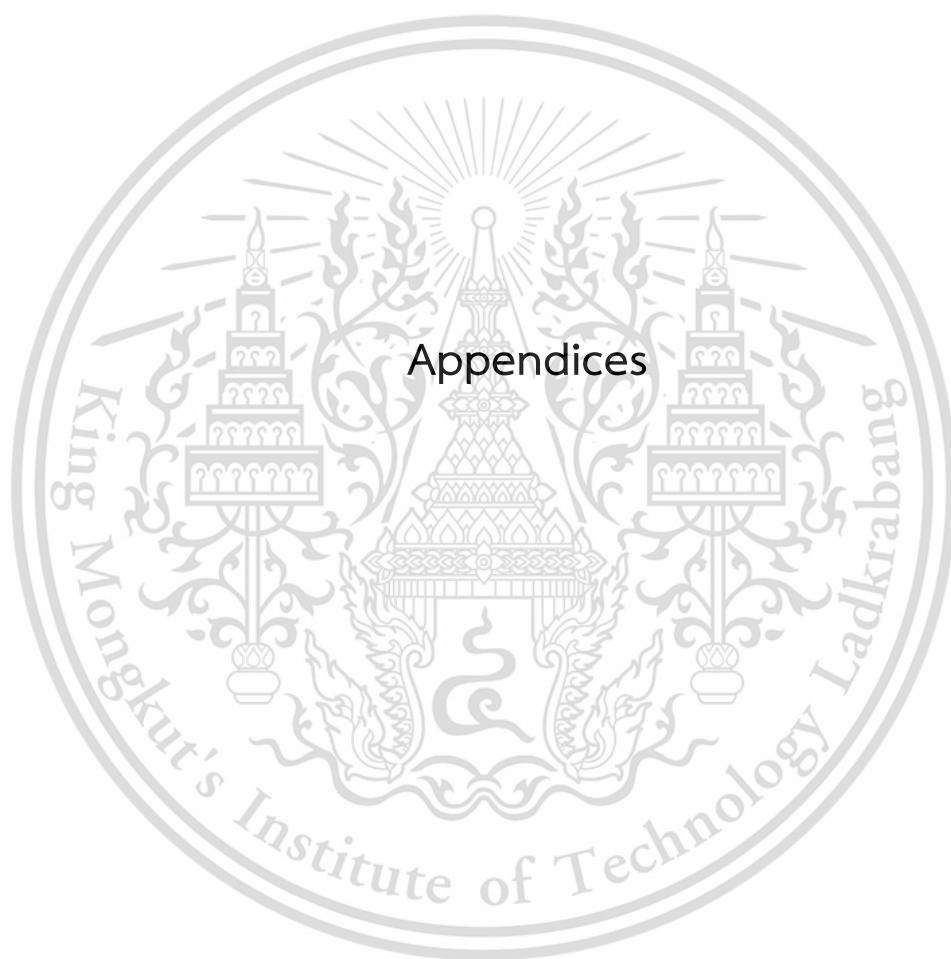
7.2.1 The post-synthetic modification of HKUST-1 with CO<sub>2</sub>-philic function such as ethylenediamine or pyridine compound can increase the strong adsorption sites for CO<sub>2</sub>, decreasing the CO<sub>2</sub> movement in the HKUST-1/polymer MMM. In addition, tuning the MOF structure by catenation or modifying MOF pore window by decreasing size lesser than the CO<sub>2</sub> molecules (0.33 nm) can create the CO<sub>2</sub> diffusion barrier in the MMM. In another way, polymer blending with non-crystalline glassy polymer or crosslinking the polymer chain can also increase the barrier segment to extend the tortuosity of the CO<sub>2</sub> diffusion path through the membrane, thereby reducing the CO<sub>2</sub> diffusivity. Furthermore, incorporating H<sub>2</sub>-philic metals such as Pd, Pt and Ru, into the HKUST-1 can improve the H<sub>2</sub> solubility and H<sub>2</sub>/CO<sub>2</sub> permselectivity of the HKUST-1/polymer MMM.

7.2.2 The amount of hydrogen storage in this study is limited by how many functional groups in the organic hydrogen carrier can undergo hydrogenation and dehydrogenation. In the case of AcP, only one carbonyl group can be performed. Thus,

the substance that has more carbonyl groups such as chloroquinone and aminoanthraquinone, is expected to have a greater hydrogen storage capacity. In addition, an increased number of grafting sites by attaching the organic hydrogen function at both metal nodes and organic linker of MOF can increase the loading of organic hydrogen carrier, thereby enhancing the H<sub>2</sub> uptake.

7.2.3 Post-synthetic modification of the organic linker (terephthalate) by amination or grafting at the MOF nodes with a multi-amino chelating agent to obtain more the amino group in the MOF structure can provide a greater number of sites for anchoring the Pd<sup>2+</sup> species.





This material is reserved for educational use only, not allowed for commercial use.

Forbidden to modify the content, and cite the document when use.

## Appendix A

### Temperature program condition

A1. *In situ* FTIR Temperature profiles for hydrogenation/dehydrogenation of Pd-AcP-MIL-101(Cr)

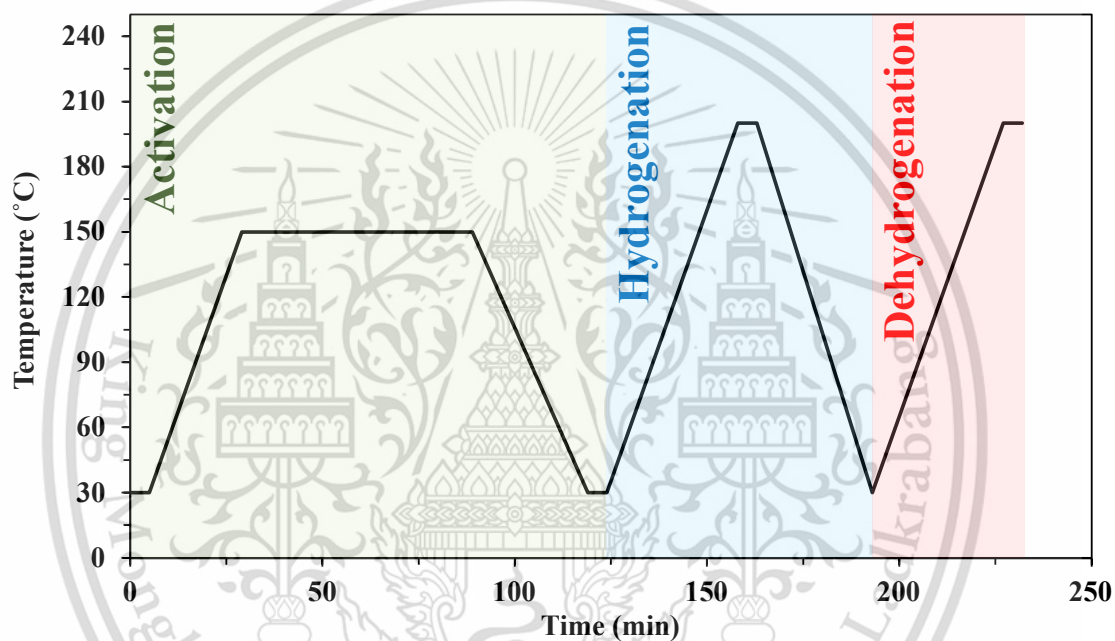


Figure A1 Temperature profile of *in situ* FTIR upon activation from 30 °C to 150 °C (5 °C/min) for 1 h, hydrogenation and dehydrogenation from 30 °C to 200 °C (5 °C/min). The data was recorded only hydrogenation and dehydrogenation zones with every 10 °C/spectra.

## A2. Temperature profile of *in situ* Pd L<sub>3</sub> edge XANES

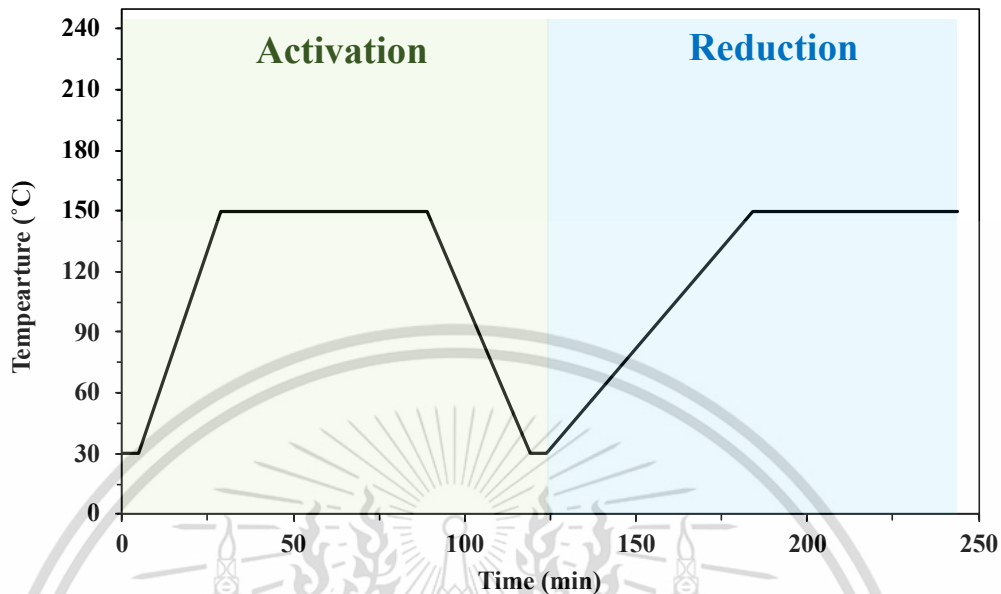


Figure A2 Temperature profile of *in situ* Pd L<sub>3</sub> edge XANES during reduction from 30 °C to 150 °C (5 °C/min) and holding at 150 °C for 20–60 min. The data was recorded in the reduction zone with every 20 min/spectra.

## A3. GC-oven temperature profile for styrene oxidation

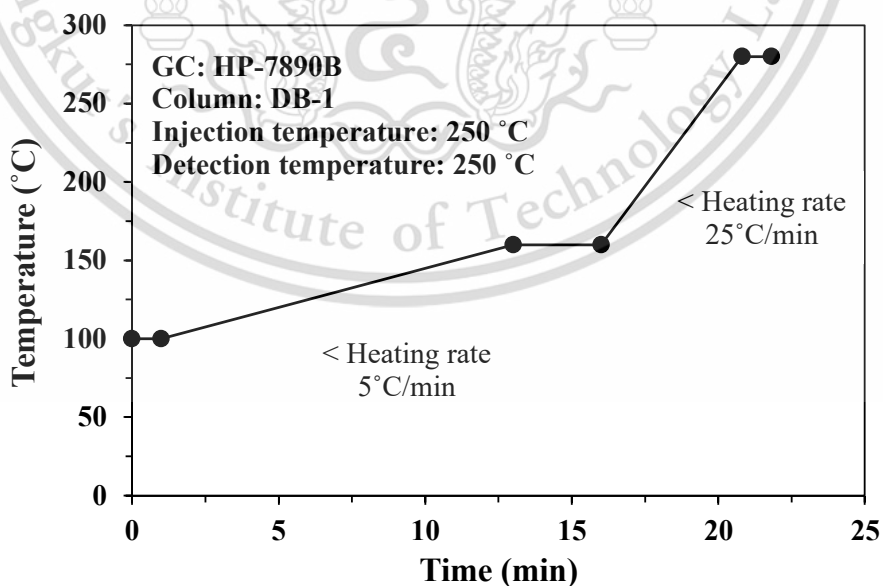


Figure A4 GC condition and oven temperature profile for styrene oxidation

## A4. GC-oven temperature profile for phenylacetylene hydrogenation

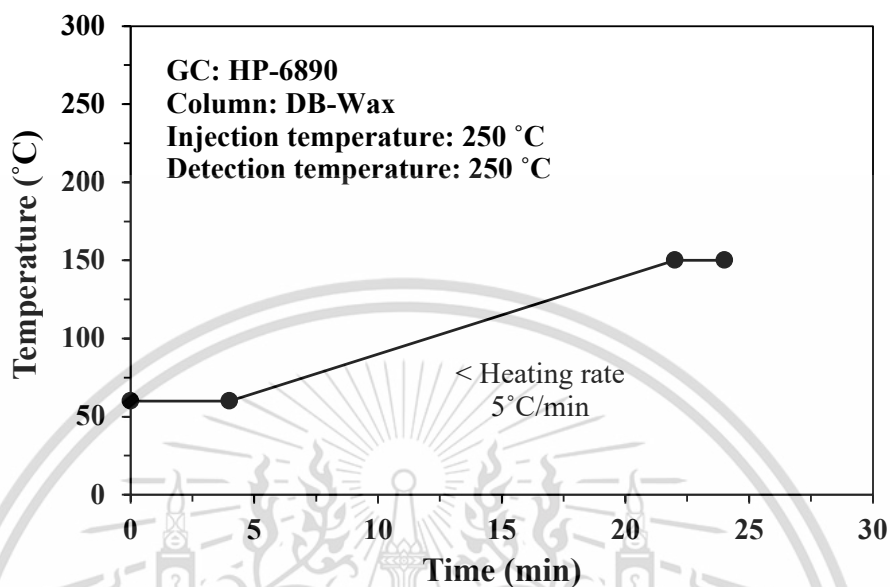


Figure A4 GC condition and oven temperature profile for phenylacetylene hydrogenation

## A5. GC-oven temperature profile for Heck reaction

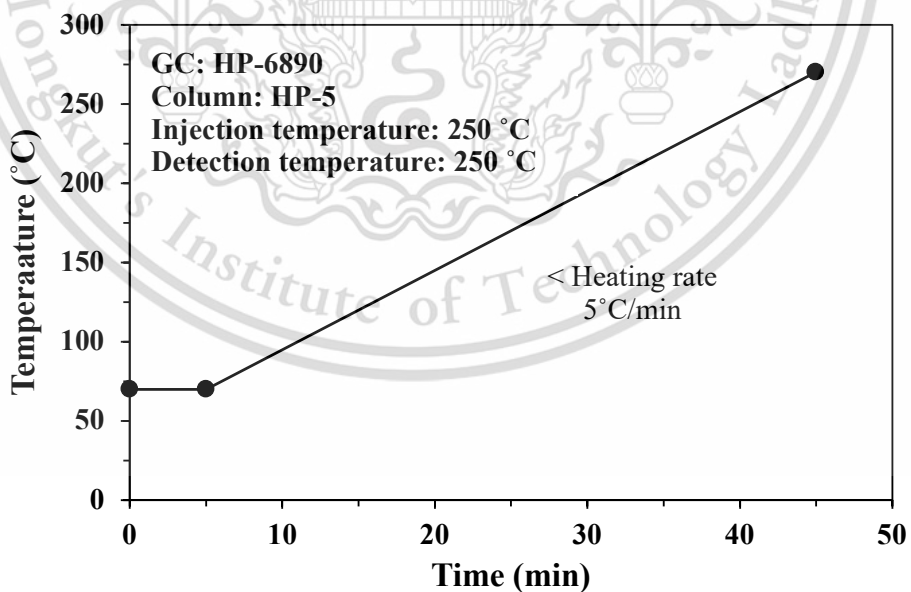


Figure A5 GC condition and oven temperature profile for Heck reaction

## Appendix B

### Spectra

#### B1. XANES spectra of standard $\text{PdOCl}_2$ and $\text{Pd(OAc)}_2$

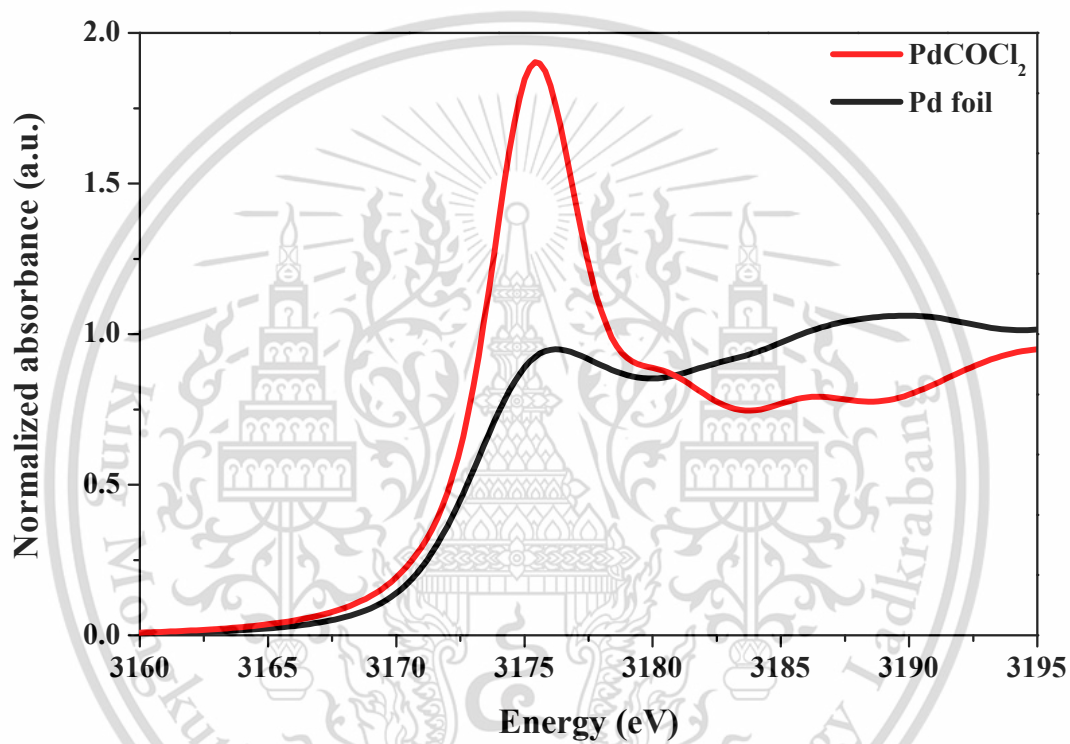


Figure B1 Pd  $L_3$ -edge XANES spectra of Pd foil and  $\text{PdCOCl}_2$  standards, recorded at room temperature

## Appendix C

### Calculation

#### C1. Quantitative analysis of H<sub>2</sub>-TPR

For correcting H<sub>2</sub>-TPR signal, the integrated peak (H<sub>2</sub> consumption/evolution) area needs to compare with a standard gas (e.g., 1% H<sub>2</sub>/Ar) that it has to be pulsed at the end of each run (Figure C1). However, the H<sub>2</sub>-TPRe experiment proceeds under different carrier gas (10%H<sub>2</sub>/Ar or Ar). Thus, 1%H<sub>2</sub>/Ar as a gas standard needs to be calibrated with a different condition.

**Hydrogen storage behavior experiment**, the carrier gas is 10%H<sub>2</sub>/Ar. The 1%H<sub>2</sub>/Ar standard will be calibrated with the hydrogen consumption from CuO reduction. The CuO reduction equation (equation C1) and their H<sub>2</sub>-TPRe chromatogram (Figure C1) show below.

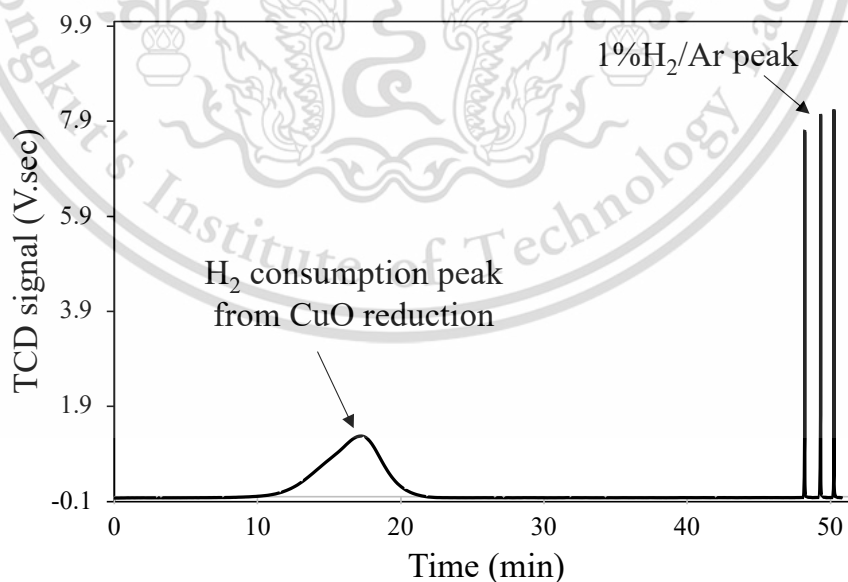


**Figure C1** H<sub>2</sub>-TPRe chromatogram of CuO reduction under 10%H<sub>2</sub>/Ar (at beginning, temperature start from 100 °C to 500 °C with heating rate 5 °C/min)

Since the stoichiometric reduction of CuO requires 1 mol of H<sub>2</sub>. To this calculation, 0.0045 g of CuO is selected for example. It resulted H<sub>2</sub> consumption peak with the area of 6.2858 V.sec.

$$\begin{array}{rcll}
 \text{From} & 1 \text{ mol}_{\text{CuO}} & = & 1 \text{ mol}_{\text{H}_2} \\
 & \text{mol}_{\text{H}_2} & = & 0.0045 / 79.545 \quad \text{g}/(\text{g}/\text{mol}) \\
 & & = & 5.65718 \times 10^{-5} \quad \text{mol} \\
 & & = & 56.57 \quad \mu\text{mol}
 \end{array}$$

Figure C2 shows that the relationship between CuO weight and amount of H<sub>2</sub> consumption is linear as expected.

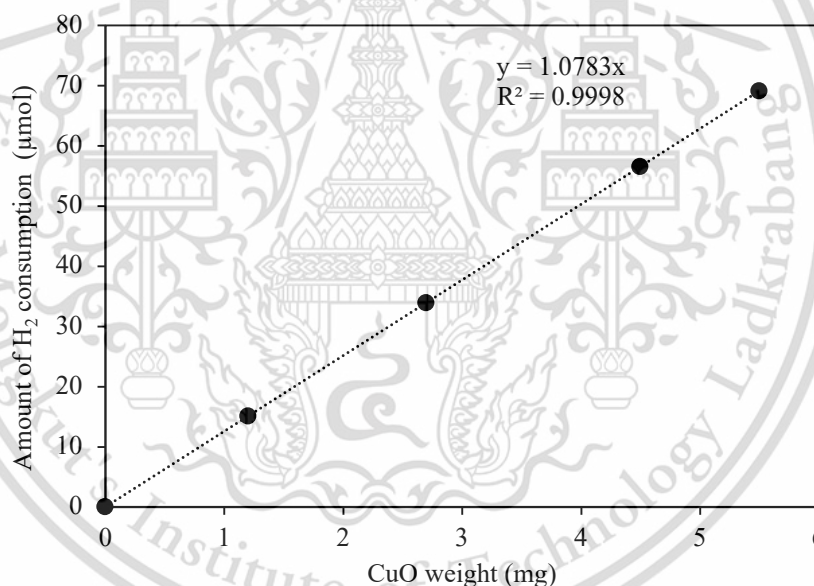


**Figure C2** Relationship between CuO weight and amount of H<sub>2</sub> consumption

To calculate the mol/pulse of 1%H<sub>2</sub>/Ar, the integrated value of 6.2858 V.sec from the H<sub>2</sub> consumption peak of CuO reduction could equilibrate to 5.65718 × 10<sup>-5</sup> mol. The average integrated 1%H<sub>2</sub>/Ar peak is 0.08898 V.sec/pulse.

$$\begin{aligned}
 \text{Thus, } \text{mol}_{1\% \text{H}_2/\text{Ar}} &= (\text{Integrated Area}_{1\% \text{H}_2/\text{Ar}} \times \text{mol}_{\text{CuO}}) / \text{Integrated Area}_{\text{CuO}} \\
 &= (0.008898 \times 5.65718 \times 10^{-5}) / 6.2858 \quad \text{mol/pulse} \\
 &= 8.0087 \times 10^{-7} \quad \text{mol/pulse} \\
 &= 0.8 \quad \mu\text{mol/pulse}
 \end{aligned}$$

## C2. Quantitative analysis of H<sub>2</sub>-TPRe

H<sub>2</sub>-TPRe experiment was used for investigation of hydrogen storage performance at different hydrogenation and dehydrogenation temperatures. The hydrogenation was carried out by using pure H<sub>2</sub> at different temperature, then dehydrogenation under Ar atmosphere. After obtained the sample signal, standard gas (1%H<sub>2</sub>/Ar) has to pulse at the end of each run.

**Hydrogen storage performance experiment**, the carrier gas is Ar pure. The 1%H<sub>2</sub>/Ar standard will be calibrated with the hydrogen evolution from NaBH<sub>4</sub> decomposition. The equation of NaBH<sub>4</sub> decomposition by temperature (equation C2) and their H<sub>2</sub>-TPRe chromatogram (Figure C3) present below;

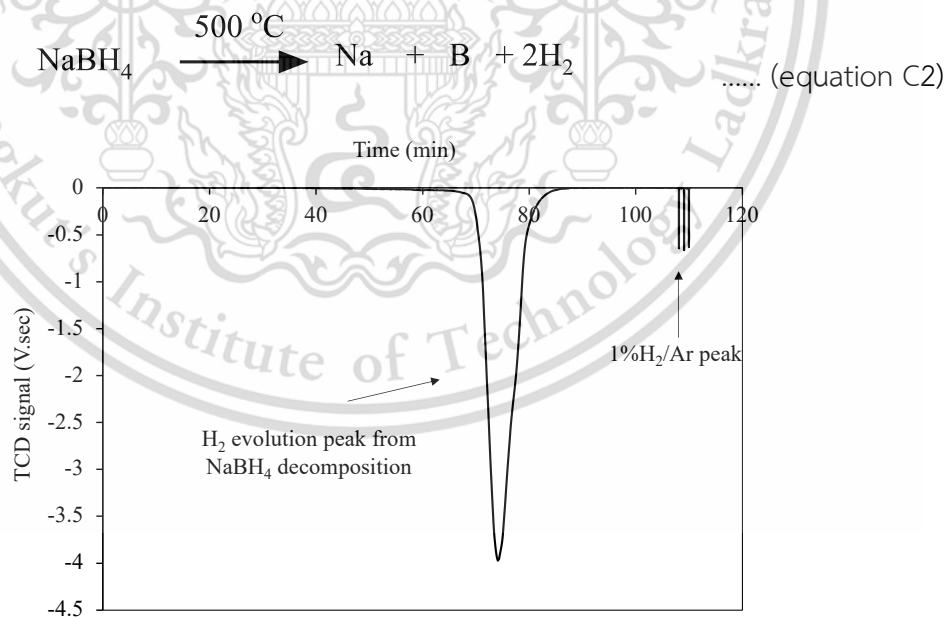
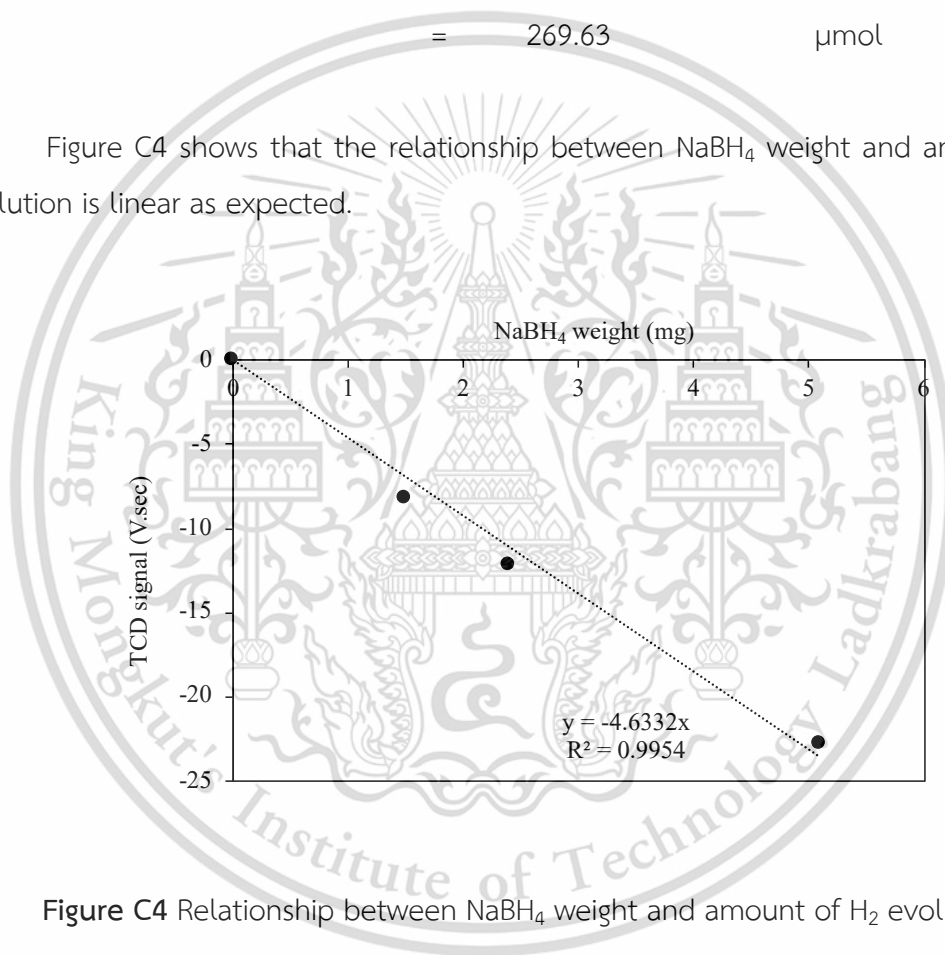


**Figure C3** decomposition profile of NaBH<sub>4</sub> under Ar from H<sub>2</sub>-TPRe chromatogram (at the beginning the temperature start from 75 °C to 550 °C with heating rate 5 °C/min)

Since, the  $\text{NaBH}_4$  decomposition releases 2 mol of  $\text{H}_2$ . To this calculation, 0.0051 g  $\text{NaBH}_4$  is selected for example. It resulted  $\text{H}_2$  evolution peak with the area of -22.7664 V.sec.

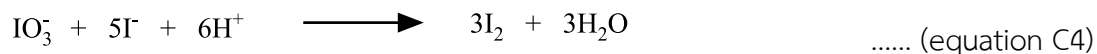
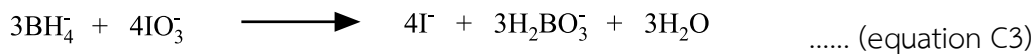
$$\begin{aligned}
 \text{From} \quad 1 \text{ mol}_{\text{NaBH}_4} &= 2 \text{ mol}_{\text{H}_2} \\
 \text{mol}_{\text{H}_2} &= (0.0051 \times 2) / 37.83 \quad \text{g/(g/mol)} \\
 &= 2.6963 \times 10^{-4} \quad \text{mol} \\
 &= 269.63 \quad \mu\text{mol}
 \end{aligned}$$

Figure C4 shows that the relationship between  $\text{NaBH}_4$  weight and amount of  $\text{H}_2$  evolution is linear as expected.



**Figure C4** Relationship between  $\text{NaBH}_4$  weight and amount of  $\text{H}_2$  evolution

However,  $\text{NaBH}_4$  is hygroscopic substance. It can degenerate readily by hydrolysis with humidity. Thus,  $\text{NaBH}_4$  purity needs to quantify using titration method with a solution of iodine. This method is based on oxidation of  $\text{BH}_4^-$  with an excess of  $\text{IO}_3^-$ , which is, after conversion of excess to  $\text{I}_2$ , back titrated using  $\text{S}_2\text{O}_3^{2-}$ . The procedure starts by adding  $\text{NaBH}_4$  in alkaline solution, to an excess of standard potassium iodate ( $\text{KIO}_3$ ). The stoichiometry shows in the following equation C3–C5:



Liberated  $\text{I}_2$  is then titrated with standard  $\text{S}_2\text{O}_3^{2-}$ :



After back titration with  $\text{S}_2\text{O}_3^{2-}$ , it was found that the  $\text{NaBH}_4$  purity is 26.09%. Thus, the adjusted hydrogen evolution from 1 mol  $\text{NaBH}_4$  could be.

$$\begin{aligned} \text{Actual mol}_{\text{NaBH}_4} &= \text{mol}_{\text{NaBH}_4} \times \% \text{purity} \\ &= (269.63 \times 26.09) / 100 \quad \mu\text{mol} \\ &= 70.346 \quad \mu\text{mol} \end{aligned}$$

To calculate the mol/pulse of 1%  $\text{H}_2/\text{Ar}$ , the integrated value of -22.7664 V.sec from the  $\text{H}_2$  evolution peak of  $\text{NaBH}_4$  decomposition could equilibrate to  $7.0346 \times 10^{-5}$  mol. The average integrated 1%  $\text{H}_2/\text{Ar}$  peak is -0.0066 V.sec/pulse.

$$\begin{aligned} \text{Thus, mol}_{1\% \text{H}_2/\text{Ar}} &= (\text{Integrated Area}_{1\% \text{H}_2/\text{Ar}} \times \text{mol}_{\text{NaBH}_4}) / \text{Integrated Area}_{\text{NaBH}_4} \\ &= (-0.0066 \times 7.0346 \times 10^{-5}) / -22.7664 \quad \text{mol/pulse} \\ &= 1.902 \times 10^{-8} \quad \text{mol/pulse} \\ &= 0.019 \quad \mu\text{mol/pulse} \end{aligned}$$

### C3. Calculation of gas permeability

Gas flux is defined as the rate of flow of a property per unit area. The rate of flow is derived from a proportion of integrated TCD peaks from sample to standard. The area is of the surface the property is flowing across.

$$\text{Flux} = \frac{(A_s/A_{\text{std}}) \times P_{\text{total}} \times F \times M_w}{R \times T \times 1000 \times S_{\text{area}} \times 60 \times \rho_{\text{H}_2}}$$

Where the unit of the flux is  $\text{cm}^3/\text{m}^2.\text{s}$ ,  $A_s$ , and  $A_{\text{std}}$  are peak areas of the sample and calibration gas,  $P$  is total pressure in permeation cell (atm),  $F$  is feed flow rate ( $\text{cm}^3/\text{min}$ ),  $M_w$  is molecular weight of feed ( $\text{g}/\text{mol}$ ),  $R$  is gas constant ( $\text{L.atm}/\text{K.mol}$ ),  $T$  is operate temperature (K),  $S_{\text{area}}$  is membrane area ( $\text{m}^2$ ). However, the pressure drop can generally arise when carrier gas swept permeated gas to the six-port valve (Figure 3.2). It can be measured by U-tube manometer.

$$\begin{aligned} P_{\text{total}} &= P_{\text{atmosphere}} + P_{\text{pressure drop}} \\ &= P_{\text{atmosphere}} + \rho g \Delta h_{\text{u tube}} \end{aligned}$$

Upon doing the permeation, if the water level increased 0.07 m. Thus, the calculation of total pressure shows below.

$$\begin{aligned} P_{\text{total}} &= 101325 \text{ Kg}/\text{m}.\text{s}^2 + (997 \text{ Kg}/\text{m}^3 \times 9.98 \text{ m}/\text{s}^2 \times 0.07 \text{ m}) \\ &= 102021.5 \text{ Kg}/\text{m}.\text{s}^2 \\ &= 1.0006 \text{ atm} \end{aligned}$$

2wt%HKUST-1/HIPS obtained 14.09 mV.sec for permeated  $\text{H}_2$  whereas 617.99 mV.sec for standard 1% $\text{H}_2/\text{Ar}$ . Feed ( $\text{H}_2$ ) flow rate is 30 mL/min.  $R$  constant is 0.08205 L.atm/K.mol. Active surface area is 0.0025  $\text{m}^2$ . Room temperature is 298 K.  $\text{H}_2$  density is  $8.988 \times 10^{-5} \text{ g}/\text{mL}$

$$\begin{aligned} \text{Thus, Flux}_{\text{H}_2} &= \frac{14.09 \times 1.0 \times 30 \times 2}{617.99 \times 0.08205 \times 298 \times 1000 \times 0.0025 \times 60 \times 8.988 \times 10^{-5}} \\ &= 4.15 \text{ mL}/\text{m}^2.\text{s} \end{aligned}$$

The gas permeation selectivity is defined as the ratio of the flux of two pure gases, measured separately under the same conditions.

$$\text{H}_2/\text{CO}_2 \text{ Selectivity} = \frac{\text{Flux}_{\text{H}_2}}{\text{Flux}_{\text{CO}_2}}$$

2wt%HKUST-1/HIPS has 4.15 of H<sub>2</sub> Flux and 0.42 of CO<sub>2</sub> flux. The calculation of H<sub>2</sub>/CO<sub>2</sub> Selectivity shows below.

$$\begin{aligned} \text{H}_2/\text{CO}_2 \text{ Selectivity} &= \frac{4.15}{0.42} \\ &= 9.88 \end{aligned}$$

#### C4. Quantitative analysis of reaction product

The quantitative analysis of products and feed was carried out by gas chromatography with flame ionization detector (GC-FID). The chromatogram was integrated to obtain the peak area. According to the certain injection volume (by on-line sampling loop) of sample to GC, the quantitative calculation is carried out by using absolute calibration curve with internal standard or percentage peak area methods, depending on the reaction.

##### Styrene oxidation

The calibration curve is used to translate the integration values given by the GC instrument into meaningful percentages that reflect actual mol% of standard samples. To generate the absolute calibration curve, standard samples of known molar or mass ratios are injected into the GC and the percentages reported by the instrument recorded. The graph in Figure C5 shows such a calibration curve for styrene (Sty), acetophenone (AcPh), benzaldehyde (BAL) and 1-phenyl ethanol (PhEOH) over internal standard toluene (Tol).

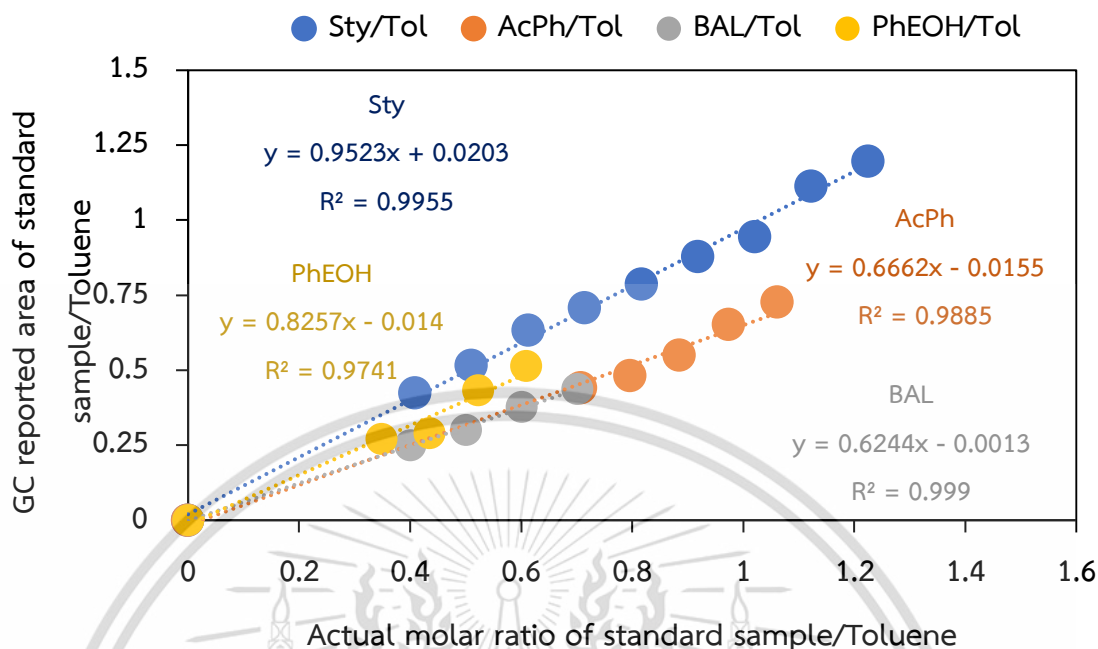


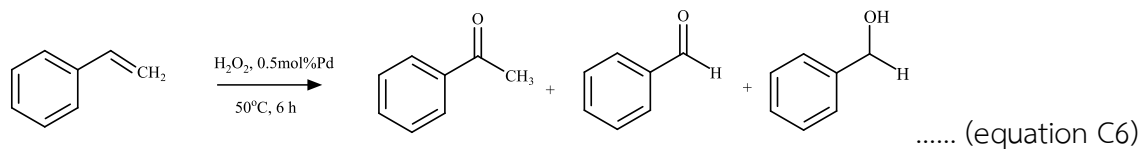
Figure C5 Correlation of actual molar ratio of standard sample/toluene and their GC reported area

To calculate the acetophenone %yield, the GC reported area of the sample have to divide with the area of toluene. This area ratio will be converted to the actual molar ratio of standard sample/toluene using the equation as depicted in Figure C5.

For example, the GC reported areas of the resulted solution for 0.03Pd-0.5en-MIL-101(Cr) produced acetophenone of 1683 mV.Sec and have internal standard toluene of 4442.8 mV.Sec. The AcPh/Tol area ratio is 0.3785. The molar ratio of Sty/Tol from blank is 1.039.

$$\begin{aligned}
 \text{Thus, Area ratio of AcPh/Tol} &= (0.6662 \times \text{Actual molar ratio of Sty/Tol}) - 0.0155 \\
 \text{Actual molar ratio of AcPh/Tol} &= (\text{Area ratio of AcPh/Tol} + 0.0155)/0.6662 \\
 &= (0.3785 + 0.0155)/0.6662 \\
 &= 0.5914
 \end{aligned}$$

According to the styrene oxidation, 1 mol of styrene can produce 1 mol of acetophenone following the equation C6.



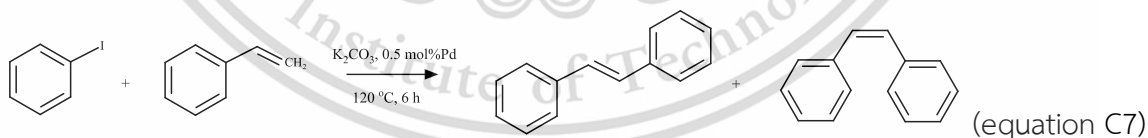
$$\begin{aligned}
 \text{So, \% AcPh Yield} &= (1 \times \text{molar ratio of AcPh/Tol} \times 100) / (\text{molar ratio of Sty/Tol})_{\text{Blank}} \\
 &= (0.5914 \times 100) / 1.0396 \% \\
 &= 56.88 \%
 \end{aligned}$$

To considerate the conversion, it is calculated by comparison between the remained styrene after reaction and the styrene from blank. For example, GC area reported the remained of Sty/Tol is 0.153, while blank is 1.003.

$$\begin{aligned}
 \% \text{ Conversion} &= ((\text{Area (Sty/Tol)}_{\text{Blank}} - \text{Area (Sty/Tol)}_{\text{Remain}} \times 100) / \text{Area (Sty/Tol)}_{\text{Blank}} \\
 &= ((1.003 - 0.153) \times 100) / 1.003 \% \\
 &= 84.74 \%
 \end{aligned}$$

#### Heck coupling reaction of iodobenzene and styrene

For this reaction, the conversion is counted by comparison area ratio of feed/internal standard before and after reaction. Iodobenzene (IB) is determined as limiting agent. The reaction is following in the equation C7.

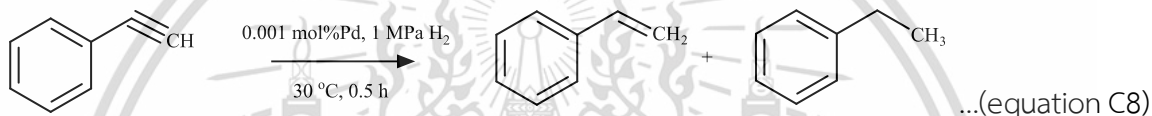


In this case, nitrobenzene (NB) is defined as internal standard. Thus, in term of calculation, whole feed and product areas have to be divided with the area of nitrobenzene. The GC area of IB/NB for blank is 1.4112. For example, after the reaction, 0.2Pd-MIL-101(Cr) converted the feed, resulted the remained GC area IB/NB ratio of 0.0369.

$$\begin{aligned}
 \text{So, } \% \text{ Conversion} &= ((\text{Area (IB/NB)}_{\text{Blank}} - \text{Area (IB/NB)}_{\text{Remain}}) \times 100) / \text{Area (IB/NB)}_{\text{Blank}} \\
 &= ((1.4112 - 0.0369) \times 100) / 1.4112 \quad \% \\
 &= 97.39 \quad \%
 \end{aligned}$$

### Phenylacetylene hydrogenation

The percentage peak area method (normalization) is considered to calculate the conversion or yield% for phenylacetylene hydrogenation, which the GC reported area of feed consumed or product component peak as a proportion of the total area of all detected peaks to analyze quantity. The reaction is described in equation C8.



$$\text{Conversion (\%)} = \frac{(\text{Total area} - \text{Area of feed remained}) \times 100}{\text{Total area}}$$

For example, in case of 0.03Pd-0.5en-MIL-101(Cr) catalyst

$$\begin{aligned}
 \text{Conversion (\%)} &= \frac{(2902.1 - 1307.8) \times 100}{2902.1} \quad \% \\
 &= 54.93 \quad \% \\
 &= 55 \quad \%
 \end{aligned}$$

### Calculation of turnover frequency (TOF)

The TOF is defined as the number of rotations of the catalytic cycle per unit of time. It is calculated as the number of molecules converted per active site per time as following.

$$\text{Turnover frequency (TOF)} = \frac{\text{Number of molecules converted (mol)}}{\text{Number of active sites (mol)} \times \text{Time of reaction (h)}}$$

For example, in case of styrene oxidation over 0.03Pd-0.5en-MIL-101(Cr) at 50 °C for 6 h and 1 mmol of styrene, 367 mg of the catalyst can convert 0.84 mmol of styrene at the period (derived from %conversion x number of styrene molecules before reaction). All Pd atom in the sample (0.03 mmol/g) assumes to be as a Pd<sup>2+</sup> active species.

$$\begin{aligned} \text{So, TOF} &= \frac{0.84 \times 10^{-3} \text{ (mol)}}{0.03 \times 10^{-3} \text{ (mol/g}_{\text{catalyst}}) \times 0.367 \text{ (g}_{\text{catalyst}}) \times 6 \text{ h}} \\ &= 12.71 \text{ h}^{-1} \\ &= 13 \text{ h}^{-1} \end{aligned}$$

### C5. Estimation of N content derived from NO<sub>3</sub><sup>-</sup> and AcP in MOF samples

It is suggested that the N content of MIL-101(Cr) is solely contributed from the NO<sub>3</sub><sup>-</sup> countered ion at the Cr<sup>3+</sup> nodes. However, since the N content is determined as wt%, this value would be decreased with the Pd loading as found in Table 4.1, entry 1 and 2. With a similar trend, the N content contributed from NO<sub>3</sub><sup>-</sup> can be estimated by plotting Pd loading vs N content of the sample with no AcP, as shown in Figure C6.

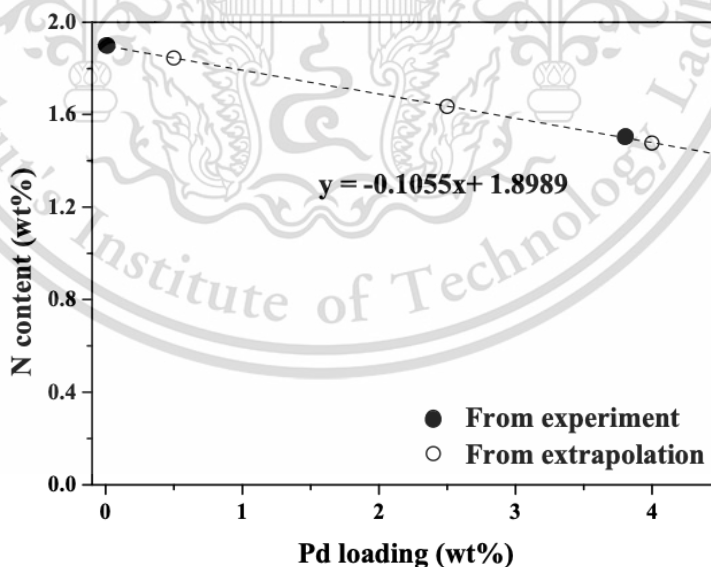


**Figure C6** Effect of Pd loading on observed N content from experiment (filled circle) and the estimated value (circle)

With this assumption, we could estimate that the AcP-grafted MIL-101(Cr) with Pd loading of 0.5, 2.5, and 4.0 wt% would possess N content derived from  $\text{NO}_3^-$  of 1.84, 1.63, and 1.47 wt%, respectively. We hence subtract the N content obtained by CHN analysis with these values and then calculated the N content dedicated from AcP as shown in Table C1.

Table C1 N content (wt%) from CHN analysis and estimated N content (wt%) for  $\text{NO}_3^-$  and AcP in MOF samples

| Sample                | N content (wt%)<br>from CHN<br>analysis | N content<br>(wt% $\text{NO}_3^-$ )<br>(Estimated) | N content<br>(wt% AcP)<br>(Calculated) | AcP loading<br>(wt%) |
|-----------------------|---|--|--|----------------------|
| MIL-101(Cr)           | 1.9                                     | -  | -                                      |                      |
| 4.0Pd-MIL-101(Cr)     | 1.5                                     | -  | -                                      |                      |
| AcP-MIL-101(Cr)       | 2.6                                     | 1.9  | 0.7                                    | 6.0                  |
| AcP-0.5Pd-MIL-101(Cr) | 2.4                                     | 1.845  | 0.555                                  | 4.8                  |
| AcP-2.5Pd-MIL-101(Cr) | 2.2                                     | 1.634  | 0.566                                  | 4.9                  |
| AcP-4.0Pd-MIL-101(Cr) | 1.9                                     | 1.476  | 0.424                                  | 3.7                  |

#### Calculation of AcP loading from estimated N content

From the calculated N content (wt%) from AcP, we can estimate the AcP loading as follow; For example, 0.5AcP-Pd-MIL-101(Cr)

$$\begin{aligned}
 \text{N content from AcP} &= 0.555 \quad \text{wt\%} \\
 &= 0.555 \quad \text{g}/100\text{g}_{\text{sample}} \\
 &= (0.555 \times 1000)/(14 \times 100) \quad \text{mmol}/\text{g}_{\text{sample}} \\
 &= 0.396 \quad \text{mmol}/\text{g}_{\text{sample}} \\
 \text{Hence, AcP loading} &= 0.396 \quad \text{mmol}/\text{g}_{\text{sample}} \\
 &= (0.396 \times 121) \quad \text{mg}/\text{g}_{\text{sample}} \\
 &= (47.916 \times 100)/1000 \quad \text{g}/\text{g}_{\text{sample}} \\
 &= 4.8 \quad \text{wt\%}
 \end{aligned}$$

## C6. Determination of ethylenediamine (en)

The amount of ethylenediamine in the sample can be determined by the total N content from CHN analysis (Table 6.1). However, in addition to ethylenediamine, this N content also consists of the nitrate counter anion and remained DMF, which cannot directly be measurable. The mol fraction from those N species can be calculated by the proportion of integrated peak area in N1s XPS (Figure 6.4).

Table C2 Mol fraction and ethylenediamine content in MIL-101(Cr), en-MIL-101(Cr), Pd-en-MIL-101(Cr) and Pd-MIL-101(Cr) samples

| Entry | Samples                  | Mol fraction <sup>a</sup> (%) |                              |    | Total N content <sup>b</sup> (wt%) | NO <sub>3</sub> <sup>-</sup> content (wt%) | en content        |                   |
|-------|--------------------------|-------------------------------|------------------------------|----|------------------------------------|--|-------------------|-------------------|
|       |                          | DMF                           | NO <sub>3</sub> <sup>-</sup> | en |                                    |  | (wt%)             | (mmol/g)          |
| 1     | MIL-101(Cr)              | 47                            | 53                           | -  | 1.9                                | 1.00                                       | -                 | -                 |
| 2     | 0.5en-MIL-101(Cr)        | -                             | 49                           | 51 | 3.2                                | 1.57                                       | 1.63              | 0.58              |
| 3     | 0.8en-MIL-101(Cr)        | -                             | 49                           | 51 | 4.0                                | 1.97                                       | 2.04              | 0.73              |
| 4     | 1.2en-MIL-101(Cr)        | -                             | 39                           | 61 | 5.3                                | 2.06                                       | 3.23              | 1.15              |
| 5     | 0.03Pd-0.5en-MIL-101(Cr) | -                             | 46                           | 54 | 2.5                                | 1.15                                       | 1.35              | 0.48              |
| 6     | 0.03Pd-0.8en-MIL-101(Cr) | -                             | -                            | -  | 3.4                                | 1.73 <sup>c</sup>                          | 1.67 <sup>c</sup> | 0.60 <sup>c</sup> |
| 7     | 0.03Pd-1.2en-MIL-101(Cr) | -                             | 43                           | 57 | 4.6                                | 1.96                                       | 2.62              | 0.94              |
| 8     | 0.2Pd-0.5en-MIL-101(Cr)  | -                             | -                            | -  | 2.1                                | 1.13 <sup>c</sup>                          | 0.97 <sup>c</sup> | 0.35 <sup>c</sup> |
| 9     | 0.2Pd-0.8en-MIL-101(Cr)  | -                             | -                            | -  | 2.2                                | 1.00 <sup>c</sup>                          | 1.20 <sup>c</sup> | 0.43 <sup>c</sup> |
| 10    | 0.2Pd-1.2en-MIL-101(Cr)  | -                             | 42                           | 58 | 3.3                                | 1.40                                       | 1.91              | 0.68              |
| 11    | 0.03Pd-MIL-101(Cr)       | 55                            | 45                           | -  | 1.6                                | 0.72                                       | -                 | -                 |
| 12    | 0.2Pd-MIL-101(Cr)        | -                             | -                            | -  | 1.3                                | -  | -                 | -                 |

<sup>a</sup>Calculated from integrated peak of N 1S XPS spectra, <sup>b</sup>CHN analysis and <sup>c</sup>Estimated content

### Calculation of ethylenediamine content

From XPS result, we can calculate ethylenediamine content as follow;

For example, 1.2en-MIL-101(Cr)

*From XPS analysis*

$$\begin{aligned}
 \text{N \%mol of nitrate} &= 39 \% \\
 \text{So, N \%mol of ethylenediamine} &= 100 - 39 \% \\
 &= 61 \%
 \end{aligned}$$

From CHN analysis

$$\begin{aligned}
 \text{Total N content} &= 5.3 && \text{wt\%} \\
 &= 5.3 && \text{g/100 } g_{\text{sample}} \\
 \\ 
 \text{N content of nitrate} &= (5.3 \times 39) / 100 && \text{g/100 } g_{\text{sample}} \\
 &= 2.1 && \text{g/100 } g_{\text{sample}} \\
 \text{N content of ethylenediamine} &= (5.3 \times 61) / 100 && \text{g/100 } g_{\text{sample}} \\
 &= 3.23 && \text{g/100 } g_{\text{sample}} \\
 \text{mmol of ethylenediamine} &= (3.2 \times 1000) / (14 \times 2) && \text{mmol/100}g_{\text{sample}} \\
 &= 115 && \text{mmol/100}g_{\text{sample}} \\
 &= 1.2 && \text{mmol/}g_{\text{sample}}
 \end{aligned}$$

#### C7. Determination of relative XRD intensities

The relative XRD intensities are defined as the intensity of modified-MIL-101(Cr) per the intensity of MIL-101(Cr) at the micropore region ( $2\theta = 3.3^\circ$ ).

$$\text{Relative XRD intensities (\%)} = \frac{\text{Intensity of modified-MIL-101(Cr)} \times 100}{\text{Intensity of MIL-101(Cr)}}$$

For example, in case of 0.2Pd-MIL-101(Cr), the peak intensity at ( $2\theta = 3.3^\circ$ ) of 0.2Pd-MIL-101(Cr) is 1122, while for the MIL-101(Cr) is 5910.

$$\begin{aligned}
 \text{Thus, relative XRD intensities (\%)} &= (1122 \times 100) / 5910 && \% \\
 &= 18.98 && \%
 \end{aligned}$$

## Author Biography

|                      |  |
|----------------------|--|
| <b>Name</b>          | Mr.Nuttapong Makmeesub   |
| <b>Date of Birth</b> | 18 March 1992  |
| <b>Address</b>       | 6/1, Tongnoi, Muang Nakhonpathom, Nakhonpathom, 73000  |
| <b>Education</b>     | (2014) Bachelor of Science in Industrial Chemistry GPA 3.60<br>King Mongkut's Institute of Technology Ladkrabang |
| <b>Scholarship</b>   | Royal Golden Jubilee Ph.D. Program (Grant No. PHD/0034/2557)   |

### Academic Publications

1. Reversible Hydrogenation/Dehydrogenation of Acetylpyridine-Pd-MIL-101(Cr) for Chemical Hydrogen Storage  
*Industrial & Engineering Chemistry Research*, 2020, 59, 40, 17671–17679
2. Highly stable Pd<sup>2+</sup> species anchoring on ethylenediamine-grafted-MIL-101(Cr) as a robust oxidation catalyst  
*Catalysis Science & Technology*, 2022, 12, 1824–1836